Quantum Nonlinearities in Strong Coupling Circuit QED

A dissertation submitted to
ETH ZURICH

for the degree of
Doctor of Sciences

presented by
JOHANNES M. FINK
Mag. rer. nat., University of Vienna
born December 21st, 1981
citizen of Austria

accepted on the recommendation of
Prof. Dr. Andreas Wallraff
Prof. Dr. Ataç İmamoğlu

2010

ABSTRACT

The fundamental interaction between matter and light can be studied in cavity quantum electrodynamics (QED). If a single atom and a single photon interact in a cavity resonator where they are well isolated from the environment, the coherent dipole coupling can dominate over any dissipative effects. In this strong coupling limit the atom repeatedly absorbs and emits a single quantum of energy. The photon and the atom loose their individual character and the new eigenstates are quantum superpositions of matter and light – so called dressed states.

Circuit QED is a novel on-chip realization of cavity QED. It offers the possibility to realize an exceptionally strong coupling between artificial atoms – individual superconducting qubits – and single microwave photons in a one dimensional waveguide resonator. This new solid state approach to investigate the matter-light interaction enables to carry out novel quantum optics experiments with an unprecedented degree of control. Moreover, multiple superconducting qubits coupled via intra-cavity photons – a quantum bus – are a promising hardware architecture for the realization of a scalable quantum information processor.

In this thesis we study in detail a number of important aspects of the resonant interaction between microwave photons and superconducting qubits in the context of cavity QED:

We report the long sought for spectroscopic observation of the $\sqrt{n}$ nonlinearity of the Jaynes-Cummings energy ladder where n is the number of excitations in the resonantly coupled matter-light system. The enhancement of the matter-light coupling by $\sqrt{n}$ in the presence of additional photons was already predicted in the early nineteen sixties. It directly reveals the quantum nature of light. In multi-photon pump and probe and in elevated temperature experiments we controllably populate one or multi-photon / qubit superposition states and probe the resulting vacuum Rabi transmission spectrum. We find that the multi-level structure of the superconducting qubit renormalizes the energy levels, which is well understood in the framework of a generalized Jaynes-Cummings model. The observed very strong nonlinearity on the level of single or few quanta could be used for the realization of a single photon transistor, parametric down-conversion, and for the generation and detection of individual microwave photons.

In a dual experiment we have performed measurements with up to three independently tunable qubits to study cavity mediated multi-qubit interactions. By tuning the qubits in resonance with the cavity field one by one, we demonstrate the enhancement of the collective dipole coupling strength by $\sqrt{N}$, where N is the number of resonant atoms, as predicted by the Tavis-Cummings model. To our knowledge this is the first observa-

tion of this nonlinearity in a system in which the atom number can be changed one by one in a discrete fashion. In addition, the energies of both bright and dark coupled multi-qubit photon states are well explained by the Tavis-Cummings model over a wide range of detunings. On resonance we observe all but two eigenstates to be dark states, which do not couple to the cavity field. The bright states on the other hand are an equal superposition of a cavity photon and a multi-qubit Dicke state with an excitation equally shared among the N qubits. The presented approach may enable novel investigations of super- and sub-radiant states of artificial atoms and should allow for the controlled generation of entangled states via collective interactions, not relying on individual qubit operations.

Finally, we study the continuous transition from the quantum to the classical limit of cavity QED. In order to access the quantum and the classical regimes we control and sense the thermal photon number in the cavity over five orders of magnitude and extract the field temperature given by Planck's law in one dimension using both spectroscopic and time-resolved vacuum Rabi measurements. In the latter we observe the coherent exchange of a quantum of energy between the qubit and a variable temperature thermal field. In the classical limit where the photon occupation of the cavity field is large, the quantum non-linearity is small compared to any coupling rates to the environment. Here the signature of quantization vanishes and the system's response is indistinguishable from the response of a classical harmonic oscillator. The observed transition from quantum mechanics to classical physics illustrates the correspondence principle of quantum physics as introduced by Niels Bohr. The emergence of classical physics from quantum mechanics and the role of decoherence in this process is an important subject of current research. In future experiments entanglement and decoherence at elevated temperatures can be studied in the context of quantum information.

KURZFASSUNG

Die grundlegende Wechselwirkung zwischen Materie und Licht kann in der Hohlraum-Quantenelektrodynamik (*cavity QED*) untersucht werden. Wenn ein einziges Atom und ein einzelnes Photon in einer Kavität interagieren, wo sie gut von Umgebungseinflüssen geschützt sind, kann die Dipolwechselwirkung über alle dissipativen Effekte dominieren. In diesem sogenannten Limit der starken Kopplung absorbiert und emittiert das Atom wiederholt ein einzelnes Energiequantum. Photon und Atom verlieren dabei ihren individuellen Charakter und die neuen Eigenzustände des Systems sind quantenmechanische Überlagerungen von Materie und Licht.

Schaltkreis-Quantenelektrodynamik (*circuit QED*) ist eine neuartige, auf einem Mikrochip integrierte Realisierung der Hohlraum-QED. Sie ermöglicht es, außergewöhnlich starke Kopplungen zwischen künstlichen Atomen, individuellen supraleitenden Quanten-Bits (Qubits) und einzelnen Mikrowellenphotonen in einem eindimensionalen Wellenleiterresonator zu realisieren. Dieser neue festkörperbasierte Ansatz die Materie - Licht Wechselwirkung zu studieren, ermöglicht die Durchführung von neuartigen Quantenoptikexperimenten mit beispielloser Kontrolle. Darüberhinaus können mehrere Qubits mit Hilfe von Photonen in der Kavität über einen so genannten Quantenbus gekoppelt werden. Dieser Ansatz ist einer der aussichtsreichsten für die Realisierung eines Quanteninformationsprozessors mit skalierbarer Hardwarearchitektur.

In dieser Doktorarbeit werden im Kontext der Hohlraum-Quantenelektrodynamik folgende wichtige Aspekte der resonanten Wechselwirkung zwischen Mikrowellenphotonen und supraleitenden Qubits untersucht:

Wir berichten von der seit langem angestrebten Beobachtung der $\sqrt{n}$ Nichtlinearität der *Jaynes-Cummings-Energieleiter*, wobei n die Anzahl der Anregungen im resonant gekoppelten Materie-Licht-System bezeichnet. Die Zunahme der Kopplung um den Faktor $\sqrt{n}$ in Anwesenheit von zusätzlichen Photonen wurde schon in den frühen 1960er Jahren vorausgesagt und offenbart direkt die Quantennatur des Lichts. Die Mehrniveaustruktur des supraleitenden Qubits sorgt bei diesem Experiment für einen zusätzlichen interessanten Aspekt, der im Rahmen eines verallgemeinerten Modells ausgezeichnet erklärt wird. Die beobachtete starke Nichtlinearität auf dem Niveau von einzelnen Quanten eignet sich für die Erzeugung von Mikrowellenphotonen und könnte benutzt werden, um einen Einzelphotonentransistor oder parametrische Abwärtskonvertierung zu realisieren.

In dem dazu dualen Experiment koppeln wir bis zu drei Qubits kollektiv mit einem einzelnen Photon und messen die erwartete $\sqrt{N}$ Skalierung der Kopplungsstärke, wobei N die Anzahl der Qubits bezeichnet. Die Nichtlinearität ergibt sich aufgrund des vergrößerten kollektiven Dipolmoments und wird durch das *Tavis-Cummings-Modell* erklärt. Wir

zeigen dieses Resultat erstmals in einem System, in dem die Atomzahl in diskreten Schritten kontrolliert verändert werden kann. In einem großen Bereich von Frequenzverstimmungen zwischen den Qubits und dem Photon stimmen die gefundenen Eigenenergien ausgezeichnet mit den so genannten Dicke-Zuständen überein. In Resonanz finden wir, dass mit Ausnahme von zwei hellen Zuständen alle Eigenzustände so genannte dunkle Zustände sind, die nicht an das Feld in der Kavität koppeln. Die hellen Zustände entsprechen gleich verteilten Superpositionen von einem Photon und den N Qubits. Der demonstrierte Ansatz ermöglicht neuartige Untersuchungen von sub- und superradianten Zuständen künstlicher Atome. Die gezeigte kollektive Wechselwirkung sollte außerdem eine kontrollierte Erzeugung von verschränkten Zuständen ermöglichen, die sich nicht auf individuelle Qubitoperationen stützt.

Zum Abschluss zeigen wir den kontinuierlichen Übergang vom quantenmechanischen zum klassischen Limit der Hohlraum-QED. Um beide Limits zugänglich zu machen, kontrollieren wir die mittlere thermische Photonenzahl n_{th} in der Kavität über einen Bereich von fünf Größenordnungen und extrahieren die effektive Temperatur des Mikrowellenfelds, die durch das Planck'schen Gesetz in einer Dimension gegeben ist, mittels spektroskopischen und zeitaufgelösten Vakuum-Rabi-Messungen. In den zeitaufgelösten Messungen beobachten wir die kohärente Wechselwirkung zwischen dem Qubit und einem niedrig besetzten thermischen Feld variabler Temperatur. Im klassischen Limit ist die Photonenzahlbesetzung des Feldes in der Kavität groß und die Quantennichtlinearität klein im Vergleich zu jeglichen Kopplungsraten zur Umgebung. In diesem Fall verschwindet die Signatur der Quantisierung und das Verhalten des Systems wird ununterscheidbar von dem eines klassischen harmonischen Oszillators. Der gefundene Übergang von der Quantenmechanik zur klassischen Physik zeigt das von Niels Bohr eingeführte Korrespondenzprinzip der Quantenphysik. Die Emergenz der klassischen Physik aus quantenmechanischen Gesetzen und die Rolle der Dekohärenz bei diesem Prozess, ist ein wichtiges Thema in der aktuellen Grundlagenforschung. In weiterführenden Experimenten kann, im Kontext der Quanteninformationstheorie, Verschränkung und Dekohärenz bei erhöhten Temperaturen untersucht werden.

CONTENTS

LIST OF PUBLICATIONS

This thesis is based in part on the following articles:

1. **J. M. Fink**, M. Göppl, M. Baur, R. Bianchetti, P. J. Leek, A. Blais and A. Wallraff. Climbing the Jaynes-Cummings ladder and observing its $\sqrt{n}$ nonlinearity in a cavity QED system. *Nature* **454**, 315-318 (2008)

2. **J. M. Fink**, R. Bianchetti, M. Baur, M. Göppl, L. Steffen, S. Filipp, P. J. Leek, A. Blais, A. Wallraff. Dressed collective qubit states and the Tavis-Cummings model in circuit QED. *Physical Review Letters* **103**, 083601 (2009)

3. **J. M. Fink**, M. Baur, R. Bianchetti, S. Filipp, M. Göppl, P. J. Leek, L. Steffen, A. Blais and A. Wallraff. Thermal excitation of multi-photon dressed states in circuit quantum electrodynamics. *Proceedings of the Nobel Physics Symposium on Qubits for Future Quantum Computers. Physica Scripta* **T137**, 014013 (2009)

4. **J. M. Fink**, L. Steffen, P. Studer, L. S. Bishop, M. Baur, R. Bianchetti, D. Bozyigit, C. Lang, S. Filipp., P. J. Leek and A. Wallraff. Quantum-to-classical transition in cavity quantum electrodynamics. *Physical Review Letters* **105**, 163601 (2010)

In addition, contributions have been made to the following articles:

5. P. J. Leek, **J. M. Fink**, A. Blais, R. Bianchetti, M. Göppl, J. M. Gambetta, D. I. Schuster, L. Frunzio, R. J. Schoelkopf and A. Wallraff. Observation of Berry's phase in a solid state qubit. *Science* **318**, 1889 (2007)

6. M. Göppl, A. Fragner, M. Baur, R. Bianchetti, S. Filipp, **J. M. Fink**, P. J. Leek, G. Puebla, L. Steffen, A. Wallraff. Coplanar waveguide resonators for circuit quantum electrodynamics. *Journal of Applied Physics* **104**, 113904 (2008)

7. A. Fragner, M. Göppl, **J. M. Fink**, M. Baur, R. Bianchetti, P. J. Leek, A. Blais and A. Wallraff. Resolving vacuum fluctuations in an electrical circuit by measuring the Lamb shift. *Science* **322**, 1357 (2008)

8. S.Filipp, P. Maurer, P. J. Leek, M. Baur, R. Bianchetti, **J. M. Fink**, M. Göppl, L. Steffen, J. M. Gambetta, A. Blais, A. Wallraff. Two-qubit state tomography using a joint dispersive read-out. *Physical Review Letters* **102**, 200402 (2009)

9. P. J. Leek, S. Filipp, P. Maurer, M. Baur, R. Bianchetti, **J. M. Fink**, M. Göppl, L. Steffen, A. Wallraff. Using sideband transitions for two-qubit operations in superconducting circuits. *Physical Review B* (Rapid Communications) **79**, 180511(R) (2009)

10. M. Baur, S. Filipp, R. Bianchetti, **J. M. Fink**, M. Göppl, L. Steffen, P. J. Leek, A. Blais, A. Wallraff. Measurement of Autler-Townes and Mollow transitions in a strongly driven superconducting qubit. *Physical Review Letters* **102**, 243602 (2009)

11. R. Bianchetti, S. Filipp, M. Baur, **J. M. Fink**, M. Göppl, P. J. Leek, L. Steffen, A. Blais and A. Wallraff. Dynamics of dispersive single qubit read-out in circuit quantum electrodynamics. *Physical Review A* **80**, 043840 (2009)

12. P. J. Leek, M. Baur, **J. M. Fink**, R. Bianchetti, L. Steffen, S. Filipp and A. Wallraff. Cavity QED with separate photon storage and qubit readout modes. *Physical Review Letters* **104**, 100504 (2010)

13. D. Bozyigit, C. Lang, L. Steffen, **J. M. Fink**, C. Eichler, M. Baur, R. Bianchetti, P. J. Leek, S. Filipp, M. P. da Silva, A. Blais, A. Wallraff. Antibunching of microwave frequency photons observed in correlation measurements using linear detectors. in print *Nature Physics* (2010)

14. R. Bianchetti, S. Filipp, M. Baur, **J. M. Fink**, C. Lang, L. Steffen, M. Boissonneault, A. Blais and A. Wallraff. Control and tomography of a three level superconducting artificial atom. in print *Physical Review Letters* (2010)

15. D. Bozyigit, C. Lang, L. Steffen, **J. M. Fink**, C. Eichler, M. Baur, R. Bianchetti, P. J. Leek, S. Filipp, M. P. da Silva, A. Blais, and A. Wallraff. Correlation measurements of individual microwave photons emitted from a symmetric cavity. submitted to *ICAP Proceedings, Journal of Physics: Conference Series* (2010)

16. S. Filipp, M. Göppl, **J. M. Fink**, M. Baur, R. Bianchetti, P. J. Leek, L. Steffen, A. Blais and A. Wallraff. Multi-mode mediated qubit-qubit coupling in a circuit QED setup. in preparation (2010)

BASIC CONCEPTS

INTRODUCTION

A first formulation of the quantum theory of light and matter was presented by Paul Dirac in the late 1920's [Dirac27, Fermi32]. He described the quantized electromagnetic field as an ensemble of harmonic oscillators and included interactions with electrically charged particles to compute the coefficient of spontaneous emission of radiation by an atom. Modern quantum electrodynamics (QED) has been pioneered by Richard Feynman, Freeman Dyson, Julian Schwinger and Sin-Itiro Tomonaga back in the late 1940's [Cohen-Tannoudji89]. They brought together the ideas of quantum mechanics, classical electrodynamics and special relativity and formulated a consistent relativistic quantum field theory (QFT) of electrodynamics. QED mathematically describes all phenomena involving charged particles by means of exchange of photons where both fields and particles are treated as discrete excitations of fields that are called field quanta. QED is among the most successful general and stringently tested theories to date. The success of QED also stimulated further successful QFTs such as quantum chromodynamics.

Modern quantum optics is the result of a fruitful union of QED and advanced experimental optical techniques [Feynman71, Gardiner91, Walls94, Mandel95, Scully97, Yamamoto99]. A remarkable example is the observation of the Lamb shift by Willis Lamb and Robert Curtis Retherford in 1947 [Lamb47, Bethe47]. The measured tiny difference between two degenerate energy levels of the hydrogen atom reveals its interaction with the virtual excitations of the vacuum field, which is a consequence of field quantization in QED. Lamb's observation was the precursor and stimulus for both modern QED which uses the concept of renormalization to eliminate vacuum induced infinite level shifts and the many spectacular quantum optics experiments that followed.

In spite of the close connection of QED and quantum optics many important phenomena such as stimulated emission, resonance fluorescence, lasing, holography and even the photoelectric effect [Wentzel26, Wentzel27] can be explained with a semiclassical theory where matter is treated quantum mechanically and radiation is described according to

Maxwell's equations. Even the Lamb shift, the Planck distribution of black-body radiation and the linewidth of a laser can be explained semiclassically if vacuum fluctuations are added stochastically to the otherwise classical field [Boyer75].

While the semiclassical understanding has remained a tempting concept in quantum optics, more advanced experimental methods allowed for many intriguing observations that unavoidably require the concept of the photon. In particular the observation of photon correlations by Hanbury Brown and Twiss [Brown56] and the subsequent systematic theoretical treatment of the quantum and classical properties of light [Glauber63b, Glauber63a] paved the way for modern quantum optics. In the same year, Jaynes and Cummings as well as Paul presented solutions for the interaction of a single atom and quantized radiation [Jaynes63, Paul63], an important theoretical model which today is routinely being studied in the field of cavity QED.

Observations that require the full machinery of the quantum theory of radiation in their explanation are non-classical photon correlations [Clauser74], photon antibunching [Kimble77], single photon anticorrelations [Grangier86], photon-photon interference [Ghosh87] and quantum beats [Scully97]. Moreover, early QED experiments in cavities showed collapse and revival of quantum coherence [Eberly80, Rempe87, Brune96] as a result of the predicted nonlinearity of the atom-photon coupling strength. The direct spectroscopic observation of this nonlinearity [Schuster08, Fink08] represents the first major result of this thesis, see Chapter 8. We also just reported the first demonstration of microwave frequency photon antibunching [Bozyigit10b].

1.1 QED in cavities

In cavity QED [Haroche89, Raimond01, Mabuchi02, Haroche06, Walther06, Ye08] atoms are coupled to photons inside a cavity with highly reflective walls. The cavity acts like a high finesse resonator which supports only a few narrow line-width standing wave modes. The mirrors therefore modify the mode structure of the cavity field and very effectively protect the intra-cavity atom from the electromagnetic environment at all off-resonant frequencies. Spontaneous emission is suppressed at these frequencies because the density of modes at which the atom could radiate is even inhibited for the occurrence of vacuum fluctuations. At the resonance frequency however, the mode density is large and the photon storage time is enhanced because an entering photon is reflected at the cavity mirrors many times before it leaves the cavity. Cavity QED therefore represents an open quantum system who's coupling to the environment can be engineered by choosing an appropriate reflectivity of the cavity mirrors. The cavity can be designed such that the mode volume is decreased considerably compared to free space. This leads to an increased electromagnetic field $\mathbf{E}$ for a given intra-cavity photon number n and in turn to an increased single atom - photon coupling. Small-volume large-quality resonators therefore enable to observe the coherent dynamics of a two state system, such as an atom, coupled to individual energy quanta of a single electromagnetic field mode.

This situation is well modeled by a spin which can only absorb and emit a single quantum of energy coupled to a harmonic oscillator which can give and receive an arbitrary number of quanta. In the electric dipole approximation, which is valid for long wavelengths compared to the size of the atom, and the appropriate gauge [Göppert-Mayer31,

Cohen-Tannoudji89] the electric dipole coupling is given by $g = \mathbf{E}\mathbf{d}$ with the dipole moment of the atom to first order $\mathbf{d} = e\mathbf{r}$ with charge e and dipole size $\mathbf{r}$. If $g \gg \kappa, \gamma$ with κ the rate at which photons leave the cavity and γ the rate at which the qubit looses its excitation to modes other than the resonator mode, the strong coupling regime of cavity QED is reached. In this limit, single photon coherent matter-light dynamics can be observed. The repeated coherent exchange of a field quantum between the (microscopic) atom and the (macroscopic) cavity is called vacuum Rabi oscillations.

In circuit QED [Blais04, Wallraff04, Schoelkopf08], where the atom is replaced by a superconducting circuit with an atom-like energy spectrum and the cavity by an electrical microwave resonator, the dipole coupling g is spectacularly increased due to two effects. Firstly, using an effectively one dimensional microwave resonator two of the three spatial dimensions are made much smaller than the wavelength of the field which decreases the mode volume dramatically and typically leads to an enhancement of up to $\sim 10^3$ of the electric field per photon. Secondly, the effective dipole moment of the superconducting circuit (a transmon type quibt) can be increased by a factor of up to $\sim 10^3$ compared to the largest known dipole moment atoms, e.g. Hydrogen atoms prepared in large quantum number Rydberg states, simply because of their macroscopic size.

Circuit QED allows to study in detail all facets of strong coupling cavity QED in a very controlled fashion and offers a number of new opportunities. The properties of artificial atoms can be engineered during fabrication, some of their parameters can be in-situ tuned and they remain fixed in space which implies a constant coupling strength. Circuit QED therefore has become a realistic platform to engineer a quantum information processor [Nielsen00, Ladd10] in the solid state. It solves an important task required in many implementations of quantum computation [Tanzilli05, Spiller06, Wilk07], i.e. it provides a fast interface between fixed solid state qubits with long coherence and quick operation times and flying qubits (photons) which can be sent to another circuit or chip [Wallraff04, Houck07, Majer07, Fink08, Hofheinz08, Hofheinz09, DiCarlo09, Bozyigit10c]. Moreover, circuit QED employs only conventional lithographic fabrication methods and in principle is based on a scalable hardware architecture that allows for an integrated design.

1.2 Outline of the thesis

We start with a general review and introduction to the basic concepts of circuit QED in Chapter 2. The microwave resonator and the superconducting charge qubit are the main building blocks of this on-chip cavity QED setup. The quantum description of these electrical circuits is discussed in Sections 2.1 and 2.2. The physics of their interaction is well described by a generalized Jaynes-Cummings Hamiltonian. This model is introduced step by step in Section 2.3. In addition, the dispersive limit which is particularly relevant for qubit state readout and coherent qubit state control is discussed.

After this theoretical part (Part I) we discuss in detail the required experimental techniques to successfully perform state of the art circuit QED experiments in Part II. We present the measurement setup built and used to characterize numerous resonator and qubit samples in Chapter 4. For additional technical aspects of the cryogenic microwave-frequency measurement setup refer to Appendix A. The design and nano-fabrication of

Josephson junction devices such as transmon qubits, tunable resonators and parametric amplifiers is yet another important part of this thesis and will be discussed in Chapter 5. For detailed fabrication recipes refer to Appendix B. At the end of this part, in Chapter 6, we discuss a typical set of important circuit QED sample characterization measurements. Before more sophisticated measurements can be envisaged, these experiments need to be conducted very carefully to determine the individual sample parameters every time a new sample is cooled down.

In the main part of this thesis (Part III) we quantitatively investigate the dependence of the large single-photon single-atom dipole coupling strength $g = \mathbf{E}\mathbf{d}$ on the photon number $n \propto \mathbf{E}^2$ in Chapter 8 and the number of qubits $N \propto \mathbf{d}^2$ in Chapter 9. In the presented spectroscopic vacuum Rabi splitting measurements we observe strong nonlinearities on the level of individual quanta. The observed $\sqrt{n}$ and $\sqrt{N}$ nonlinearities provide direct evidence for the quantization of the electromagnetic field and for the collective dynamics of up to three qubits entangled by the single photon. In Chapter 10 we study the strong coupling regime at large effective temperatures of the resonator field. As the number of thermal photons is increased, the signature of quantization is lost as expected from Bohr's correspondence principle. We quantitatively analyze this quantum-to-classical transition and demonstrate how to sense the effective cavity field temperature over a large range using both spectroscopic and time-resolved vacuum Rabi measurements.

REVIEW AND THEORY

Research in circuit QED broadly makes connections to the fields of quantum optics, atomic physics, quantum information science and solid state physics. As a result of the remarkably rapid progress during the last decade it has evolved from a theoretical idea to an established platform of quantum engineering.

The observation of coherent dynamics of a superconducting charge qubit by Y. Nakamura *et al.* in 1999 [Nakamura99] inspired many physicists to think about systems in which electromagnetic oscillators and superconducting qubits are coupled to form a novel type of solid state cavity QED system. It was suggested to use discrete LC circuits [Buisson01, Makhlin01], large junctions [Marquardt01, Plastina03, Blais03] and three dimensional cavities [Al-Saidi01, Yang03, You03] to observe coherent dynamics of qubits and photons. In 2004 A. Blais *et al.* [Blais04] suggested to couple a superconducting charge qubit to a coplanar waveguide resonator in order to realize an on-chip cavity QED system, see Fig. 2.1. It promised to be suitable to study strong coupling quantum optics and also has the potential for the successful implementation of a solid state quantum computer [Blais07]. Based on this proposal A. Wallraff *et al.* [Wallraff04] observed vacuum Rabi mode splitting, a hallmark experiment demonstrating strong coupling between a single qubit and a single photon for the first time in 2004. Coherent sideband oscillations between a flux qubit and an LC-resonator were also observed at that time [Chiorescu04]. For two introductory reviews on circuit QED see [Schoelkopf08, Wallraff08].

The observation of strong coupling was the outset for a remarkable number of novel solid state quantum optics and quantum computing experiments. A list of the important milestones is given here: observation of the quantum AC-Stark shift [Schuster05], demonstration of high qubit readout fidelities [Wallraff05], observation of vacuum Rabi oscillations [Johansson06] and photon number splitting of the qubit spectrum [Schuster07b], demonstration of a single photon source [Houck07], cavity sideband transitions [Wallraff07] and single qubit lasing [Astafiev07], observation of Berry's phase

[Leek07], coupling of two qubits via a cavity bus [Majer07, Sillanpää07], observation of the $\sqrt{n}$ nonlinearity of the Jaynes-Cummings ladder [Fink08], observation of the Lamb shift [Fragner08], cooling and amplification with a qubit [Grajcar08], controlled symmetry breaking in circuit QED [Deppe08], generation of Fock states [Hofheinz08] and arbitrary superpositions of Fock states [Hofheinz09], observation of collective states of up to 3 qubits [Fink09b], observation of Autler-Towns and Mollow transitions [Baur09], high drive power nonlinear spectroscopy of the vacuum Rabi resonance [Bishop09], demonstration of two qubit entanglement using sideband transitions [Leek09], demonstration of gates and basic two qubit quantum computing algorithms [DiCarlo09], violation of Bell's inequality [Ansmann09], demonstration of single shot qubit readout [Mallet09], implementation of separate photon storage and qubit readout modes [Leek10], measurement of the quantum-to-classical transition and thermal field sensing in cavity QED [Fink10], quantum non-demolition detection of single microwave photons [Johnson10], implementation of optimal qubit control pulse shaping [Motzoi09, Chow10a, Lucero10], preparation and generation of highly entangled 2 and 3-qubit states [Chow10b, Neeley10, DiCarlo10] and the first measurement of microwave frequency photon antibunching [Bozyigit10c, Bozyigit10b] using linear amplifiers and on-chip beam splitters.

Similarly, strong interactions have also been observed between superconducting qubits and freely propagating photons in microwave transmission lines. This includes the observation of resonance fluorescence [Astafiev10a], quantum limited amplification [Astafiev10b] and electromagnetically induced transparency [Abdumalikov10] with a single artificial atom. The rapid advances in circuit QED furthermore inspired and enabled the demonstration of single phonon control of a mechanical resonator passively cooled to its quantum ground state [O´Connell10].

We will now review the basics of circuit QED using transmon type charge qubits and coplanar waveguide resonators.

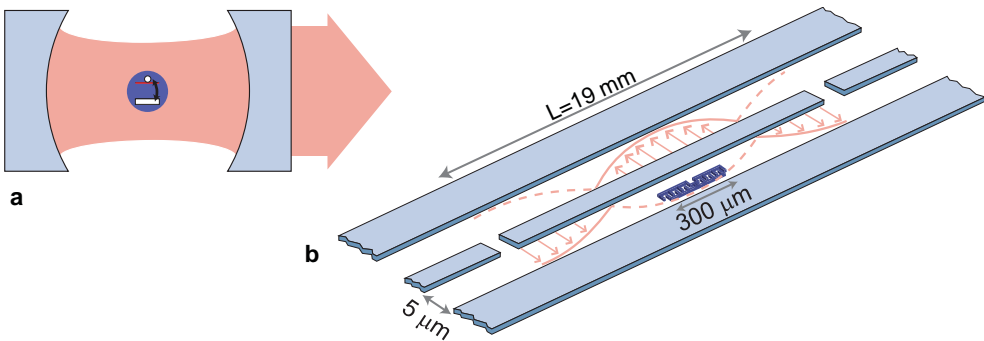Figure 2.1: **Schematic of an experimental cavity QED (a) and circuit QED (b) setup. a**, Optical analog of circuit QED. A two-state atom (violet) is coupled to a cavity mode (red). **b**, Schematic of the investigated circuit QED system. The coplanar waveguide resonator is shown in light blue, the transmon qubit in violet and the first harmonic of the standing wave electric field in red. Typical dimensions are indicated.

2.1 On-chip microwave cavity

Most circuit QED setups are using 1D transmission line resonators with quality factors reaching $Q \sim 10^5 - 10^6$ as a cavity. Coplanar waveguide (CPW) resonators can be fabricated with a simple single layer photo-lithographic process using gap or finger capacitors to couple to input and output transmission lines, see Figs. 2.1 and 2.2. The coplanar geometry resembles a coaxial line with the ground in the same plane as the center conductor. CPWs allow to create well localized fields in one region of the chip, e.g. where the qubit is positioned, and less intense fields in another region, e.g. where the dimensions should match with the printed circuit board (PCB). In contrast to circuits based on microstrip lines, this is possible at a fixed impedance simply by maintaining the ratio of the center conductor width to the ground to center conductor gap width, [Pozar93, Simons01]. Their distributed element character helps avoiding uncontrolled stray conductances and inductances which allows to design high quality circuits up to well above 10 GHz. For a detailed discussion of the properties of coplanar waveguide resonators refer to [Göppl08].

2.1.1 Coplanar waveguide resonator

The fundamental mode ($m = 1$) resonance frequency of a CPW of length l, capacitance per unit length C_l and inductance per unit length L_l is given as $\nu_{\mathrm{r},1} = \nu_{\mathrm{ph}}/(2l)$ with the phase velocity $\nu_{\mathrm{ph}} = 1/\sqrt{L_l C_l} = c/\sqrt{\epsilon_{\mathrm{eff}}}$. Here is c the speed of light in vacuum and $\epsilon_{\mathrm{eff}} \sim 5.9$ the effective permittivity of the CPW which depends of the CPW geometry and the relative permittivity ϵ_1, see Fig. 2.2. The resonance condition for the fundamental standing wave harmonic mode is fulfilled at a wavelength $\lambda_1 = 2l$ and the characteristic impedance is $Z_0 = \sqrt{L_l/C_l} \sim 50\Omega$. For nonmagnetic substrates ($\mu_{\mathrm{eff}} = 1$) and neglecting kinetic inductance, L_l depends (similar to C_l) on the CPW geometry only. Using conformal mapping techniques [Simons01], one can determine $L_l = \mu_0 K(k_0')/(4K(k_0))$ and $C_l = 4\epsilon_0 \epsilon_{\mathrm{eff}} K(k_0)/K(k_0')$, where ϵ_0 is the vacuum permittivity and K denotes the complete elliptic integral of the first kind with the arguments $k_0 = w/(w + 2s)$ and $k_0' \sqrt{1 - k_0^2}$.

The resonator is symmetrically coupled to input and output transmission lines with capacitance C_κ with typical values in the range of 10 fF to 50 fF realized with gap or finger
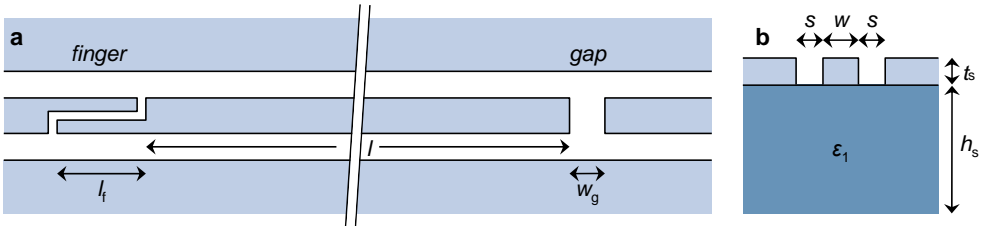
Figure 2.2: **Coplanar waveguide resonator geometry. a,** Top view of a CPW resonator of length l with finger capacitor of length l_{f} (left) and gap capacitor of width w_{g} (right). **b,** Cross section of a CPW resonator design. Center conductor of width w and lateral ground plane (light blue) spaced by two gaps of width s. The metallization is either evaporated Aluminum or etched Niobium of thickness $t_{\mathrm{s}} \sim 200$ nm patterned in a standard single layer photo-lithographic process. As a substrate 2 inch wavers of c-cut sapphire with a thickness of $h_{\mathrm{s}} = 500~\mu m$ and relative permittivity $\epsilon_1 \sim 11$ were used (dark blue).

capacitors, see geometries in Fig. 2.2. Due to this coupling we need to distinguish between the internal quality factor of the resonator $Q_{\text{int}} = m\pi/2\alpha l$ for the considered harmonic mode m and the external quality factor $Q_{\text{ext}} = m\pi/(4Z_0)(1/(C_\kappa^2 R_L \omega_{\text{r,m}}^2) + R_L)$ obtained from a LCR-model mapping, see [Göppl08]. While the former accounts for dissipative photon losses via dielectric, radiative and resistive interactions taken into account by the attenuation constant α, the latter is related to the input and output coupling of photons which depends on C_κ and the real part of the load impedance of the input and output transmission lines $R_L \sim 50\,\Omega$.

The loaded quality factor Q_L can directly be measured in a resonator transmission measurement. It is given as a combination of the internal and external quality factors $1/Q_L = 1/Q_{\text{int}} + 1/Q_{\text{ext}}$. The coupling coefficient is defined as $g_{\text{CPW}} = Q_{\text{int}}/Q_{\text{ext}}$ and the expected deviation of the peak transmission power from unity is given by the insertion loss $\text{IL} = g_{\text{CPW}}/(g_{\text{CPW}} + 1)$, or in decibel $\text{IL}_{\text{dB}} = -10\log(g_{\text{CPW}}/(g_{\text{CPW}} + 1))\,\text{dB}$. All presented experiments were done in the over-coupled regime where $g_{\text{CPW}} \gg 1$, $\text{IL} \approx 1$ and $\text{IL}_{\text{dB}} \approx 0$.

The rate of photon loss κ is related to the measured quality factor as $Q_L = \omega_r/\kappa$ for the Lorentzian shaped transmission power spectrum

$$P(\nu) = \frac{P_r}{1 + \left(\frac{\nu - \nu_r}{\kappa/(4\pi)}\right)^2}. \tag{2.1}$$

The photon storage time of the considered cavity mode is simply given as

$$\tau_{\text{n}} = 1/\kappa \tag{2.2}$$

with $\kappa/2\pi$ the full width at half maximum of the resonant transmission peak power $P_r = \text{IL} \cdot P_{\text{in}}$ where P_{in} is the probe power applied directly at the resonator input. The phase shift of the transmitted microwave with respect to the incident wave can also be measured and is given by [Schwabl02]

$$\delta(\nu) = \tan^{-1}\left(\frac{\nu - \nu_r}{\kappa/(4\pi)}\right). \tag{2.3}$$

On resonance and for $g_{\text{CPW}} \gg 1$ the average photon number n inside the cavity is directly proportional to the power applied at its input

$$P_{\text{in}} \approx P_r \approx n\hbar\omega_r\kappa, \tag{2.4}$$

valid for a coherent input tone and a symmetrically coupled resonator without insertion loss. In order to populate the resonator with a single photon on average we therefore require a microwave power of only $\sim 10^{-18}\,\text{W}$ at the resonator input for typical values of κ.

2.1.2 Transmission matrix model

In contrast to lumped element oscillators, distributed element resonators carry multiple harmonic resonance modes. Their full spectrum can be calculated using a transmission matrix model, see [Pozar93], where each component of a microwave network is represented by a 2 x 2 matrix. The product of these matrices gives an overall ABCD matrix which

can be used to calculate the transmission coefficient S_{21} of the network. The ABCD matrix of a symmetrically coupled transmission line resonator is defined by the product of an input-, a transmission-, and an output matrix as

$$\begin{pmatrix} A & B \\ C & D \end{pmatrix} = \begin{pmatrix} 1 & Z_{in} \\ 0 & 1 \end{pmatrix} \begin{pmatrix} t_{11} & t_{12} \\ t_{21} & t_{22} \end{pmatrix} \begin{pmatrix} 1 & Z_{out} \\ 0 & 1 \end{pmatrix}, \tag{2.5}$$

with input and output impedances $Z_{in} = Z_{out} = 1/(i\omega C_\kappa)$. The transmission matrix parameters are defined as $t_{11} = t_{22} = \cosh(l(\alpha + i\beta))$, $t_{12} = Z_0 \sinh(l(\alpha + i\beta))$ and $t_{21} = (1/Z_0)\sinh(l(\alpha + i\beta))$ with a typical attenuation constant $\alpha \sim 2.4 \cdot 10^{-4}$ and the phase propagation constant $\beta = \omega_m / v_{ph}$. The entire resonator transmission spectrum is then simply calculated as

$$S_{21} = \frac{2}{A + B/R_L + CR_L + D}, \tag{2.6}$$

where R_L is the real part of the load impedance, accounting for all outer circuit components.

2.1.3 Circuit quantization

Here we address the description of a (non-dissipative) lumped-element circuit known from electrical engineering in the quantum regime, for details see Refs. [Devoret97, Blais04, Burkard04, Bishop10a]. An electrical circuit is a network of nodes that are joined by two-terminal capacitors and inductors, see e.g. Fig. 2.3. Each component a carries the current $i_a(t)$ and causes a voltage drop $v_a(t)$. The corresponding charges and fluxes, which are more convenient to derive the Hamiltonian, are given by $Q_a(t) = \int_{-\infty}^{t} i_a(t')dt'$ and $\Phi_a(t) = \int_{-\infty}^{t} v_a(t')dt'$, where it is assumed that any external bias is switched on adiabatically from $t = -\infty$. Most relevant devices, such as the transmission line resonator used in this thesis, can be modeled by combinations of capacitative $v_a = f(Q_a)$ and inductive $i_a = g(\Phi_a)$ circuit elements. The classical Hamiltonian of the entire circuit may be derived using the Lagrangian formulation $L(\phi_1, \dot{\phi}_1, ...) = T - V$ with T the energy of the capacitive and V the energy of the inductive components. The quantum Hamiltonian is then retrieved by replacing the classical variables by the corresponding quantum operators obeying the commutation relation $[\phi_m, q_m] = i\hbar$ with ϕ_m the flux and q_m the charge of the node m.

An important example is the quantization of the parallel LC oscillator, see Fig. 2.3 a, which has only one active node and one ground. The Lagrangian is $L(\phi, \dot{\phi}) = C\dot{\phi}^2/2 - $
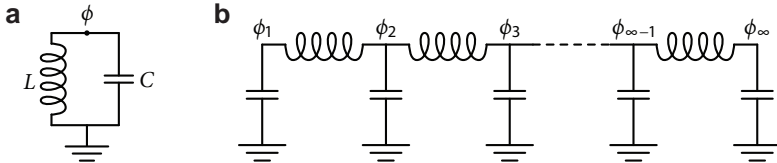
Figure 2.3: **LC circuits. a**, The parallel LC oscillator with one active node ($m = 1$) and corresponding node flux $\phi_1 = \phi$ at the top and the ground node at the bottom of the diagram. **b**, The transmission line resonator modeled as an infinite chain of LC oscillators with open-circuit boundary conditions.

$\phi^2/2L$ and by defining the charge as the conjugate momentum of the node flux $q = \partial L/\partial\dot\phi$ and applying the Legendre transform $H(\phi, q) = \dot\phi q - L$ we obtain the Hamiltonian $H = q^2/2C + \phi^2/2L$. In analogy to the Hamiltonian of a particle in a harmonic potential and the direct mappings $p \to q$, $x \to \phi$ and $\omega_{\rm r}^2 \to 1/(LC)$ we can quantize it in the usual way as

$$H = \hbar\omega_{\rm r}\left(a^\dagger a + \frac{1}{2}\right), \tag{2.7}$$

by introducing the annihilation operator $a = 1/\sqrt{2\hbar Z}(\phi + iZq)$ obeying $[a, a^\dagger] = 1$ with $\phi = \sqrt{\hbar Z/2}(a + a^\dagger)$, $q = -i\sqrt{\hbar/(2Z)}(a - a^\dagger)$, the characteristic impedance $Z = \sqrt{L/C}$ and the angular resonance frequency $\omega_{\rm r}$.

A distributed element transmission line can be treated as the continuum limit of a chain of LC oscillators [Pozar93], see Fig. 2.3 b. The effective Lagrangian $L(\Phi_1, \dot\Phi_1, ...) = \sum_{m=1}^\infty C_m\dot\Phi_m^2/2 - \Phi_m^2/2L_m$ describes an infinite number of uncoupled LC oscillators with effective capacitances $C = C_m = C_l l/2$, effective inductances $L_m = 2lL_l/(m^2\pi^2)$ and resonance frequencies $\omega_m = mv_{\rm ph}\pi/l$. The quantum Hamiltonian of the transmission line cavity is then given as

$$H = \hbar\sum_m \omega_{r,m}\left(a_m^\dagger a_m + \frac{1}{2}\right), \tag{2.8}$$

where m is the harmonic mode number. In many cases it is sufficient to characterize the behavior of the circuit only in the vicinity of a particular frequency where the Hamiltonian reduces to the single mode Hamiltonian Eq. (2.7). Near resonance of the chosen mode with frequency $\omega_{\rm r}$ the mapping to the simple single LC or single LCR model provides a sufficient understanding of the CPW resonator.

2.2 Superconducting quantum bits

A quantum bit or qubit is a quantum system with a two-dimensional Hilbert space and represents the unit of quantum information [Nielsen00]. In contrast to a classical bit to which the state space is formed only by the two basis states 0 and 1, a qubit can be prepared in any one of an infinite number of superposition states $|\psi\rangle = \alpha|0\rangle + \beta|1\rangle$ of the two basis states $|0\rangle$ and $|1\rangle$ with the normalization $\alpha^2 + \beta^2 = 1$. It is very useful to think of a sphere with radius 1, the Bloch sphere, where the two poles represent the two basis states and the collection of points on its surface represent all possible pure states $|\psi\rangle$ of the qubit. The concept of quantum information promises insights to the fundamentals of physics [Deutsch85, Landauer91, Zurek03, Lloyd05], an exponential speedup of certain complex computational tasks [Feynman82, Deutsch92, Grover96, Shor97] and has become a substantial motivation and driving force for the research in the fields of information theory, computer science, quantum optics, AMO physics, cavity QED, solid state physics and nanotechnology.

The experimentalist needs to implement the idealized qubit concept in an actual physical system [DiVincenzo00, Nielsen00, Ladd10]. Like most other quantum systems that are used to implement qubits (with exception of the spin-1/2 systems), superconducting circuits in principle have a large number of eigenstates. If these states are sufficiently nonlinearly distributed in energy, one can unambiguously choose two as the basis states $|g\rangle$ and $|e\rangle$ of the physical qubit.

In order to achieve high fidelity state preparation we need be able to reliably initialize one of the two basis states, typically the ground state $|g\rangle$. This can be achieved if the thermal occupation of the qubit is negligibly small such that $k_B T \ll h\nu_{g,e}$. For high fidelity state control, the two qubit states $|g\rangle$ and $|e\rangle$ need to be sufficiently long lived compared to manipulation times. This implies on the one hand the need for strong coupling to control and readout elements, and on the other hand close to perfect protection from any coupling to the environment. The latter requires not only the suppression of any dissipative loss but necessitates also an efficient protection from spontaneous emission which is triggered by vacuum fluctuations [Houck08, Reed10b]. Both can induce unwanted transitions between the qubit levels and therefore limit the energy relaxation time $T_1 = 1/\gamma_1$ of the excited state $|e\rangle$. Similarly, in order to maximize the coherence time $T_2 = 1/\gamma = 1/(1/(2T_1) + 1/T_\phi)$, with $T_\phi = 1/\gamma_\phi$ the pure dephasing time, any interactions between the qubits and its environment need to be minimized [Ithier05].

2.2.1 Charge qubits

The transmission-line shunted plasma oscillation qubit [Koch07b, Schreier08, Houck08], in short *transmon*, is based on the Cooper pair box (CPB) which is the prototype of a qubit based on superconducting electronic circuits [Büttiker87, Bouchiat98, Nakamura99, Vion02]. The basis states of the CPB qubit are two charge states defined by the number of charges on a small superconducting island which is coupled to a superconducting reservoir via a Josephson tunnel junction that allows for coherent tunneling of Cooper pairs. The Josephson tunnel junction, see Fig. 2.4 a and b, consists of two electrodes connected by a very thin (~ 1 nm) insulating barrier which acts like a non-dissipative nonlinear inductor according to the Josephson effect [Josephson62, Tinkham96]. The transmon type qubit is a CPB where the two superconductors are also capacitatively shunted in order to decrease the sensitivity to charge noise, while maintaining a sufficient anharmonicity for selective qubit control [Koch07b], see Fig. 2.4 c and d. Other actively investigated superconducting qubit types include the RF-SQUID (prototype of a flux qubit) and the current-biased junction (prototypal phase qubit), for a review see [Devoret04, Zagoskin07, Clarke08].

The Hamiltonian of the transmon or CPB can be shown to be [Büttiker87, Devoret97, Bouchiat98, Makhlin01]

$$H = 4E_{\text{C}}(\hat{n} - n_{\text{g}})^2 - E_{\text{J}}\cos\hat{\varphi}, \tag{2.9}$$

where the first term denotes the energy associated with excess charges on the island and the second term is the energy associated with the Josephson coupling between the two islands. The latter can be understood as a measure for the overlap of the Cooper pair wavefunctions of the two electrodes. The symbols $\hat{n} = -\hat{q}/(2e)$ and $\hat{\varphi} = \hat{\phi}2e/\hbar$ denote the number of Cooper pairs transferred between the islands and the gauge-invariant phase difference between the superconducting electrodes, respectively. $\hat{\varphi}$ is a compact variable that satisfies $\psi(\hat{\varphi} + 2\pi) = \psi(\hat{\varphi})$ and the commutation relation between the conjugate variables is given as $[\hat{\varphi}, \hat{n}] = -i$. The effective offset charge on the island in units of the Cooper pair charge $2e$ may be controlled via a gate electrode (V_g) capacitively coupled to the island (C_g) such that $n_{\text{g}} = Q_{\text{r}}/(2e) + C_g V_g/(2e)$ with Q_{r} an environment induced offset charge, e.g. from 1/f charge noise or quasi-particle poisoning.

The charging energy

$$E_C = e^2/(2C_\Sigma) \tag{2.10}$$

is the energy needed in order to charge the island with an additional electron. It solely depends on the total capacitance $C_\Sigma = C_g + C_S$, given as the sum of the the gate capacitance C_g and the transmon specific shunt capacitance C_S, see Fig. 2.4. The latter also includes the junction capacitance C_J and other relevant parasitic capacitances, see Section 5.1 for a detailed analysis of an actual qubit design. For typical transmon qubit designs C_S is chosen such that the charging energy is reduced significantly to the range $200\,\mathrm{MHz} \lesssim E_C/h \lesssim 500\,\mathrm{MHz}$. Its lowest value is limited by the minimal anharmonicity of the transmon levels required for fast single qubit gates. The upper value on the other hand is determined by the intended suppression of charge noise sensitivity at typical qubit transition frequencies, see Subsection 2.2.2 for details.

The second characteristic energy of the circuit is the Josephson energy E_J which is the energy stored in the junction as a current passes through it, similar to the energy of the magnetic field created by an inductor. In the case of the Josephson junction no such field is created however and the energy is stored inside the junction. If the current through the junction is smaller than the critical current of the junction I_c, there is no associated voltage drop rendering it the only known dissipationless and nonlinear circuit element. By choosing a split junction design, see Fig. 2.4 c and d, the Josephson energy can be tuned by applying a magnetic field to the circuit which threads an external magnetic flux ϕ through the dc-SQUID formed by the two junctions [Tinkham96]

$$E_J(\phi) = E_{J_{max}}|\cos{(\pi\phi/\phi_0)}| \tag{2.11}$$

for the simple case of two identical junctions and $\phi_0 = h/(2e)$ the magnetic flux quantum. Both the charging energy and the maximum Josephson energy

$$E_{J_{max}} = \phi_0 I_c/(2\pi) \tag{2.12}$$
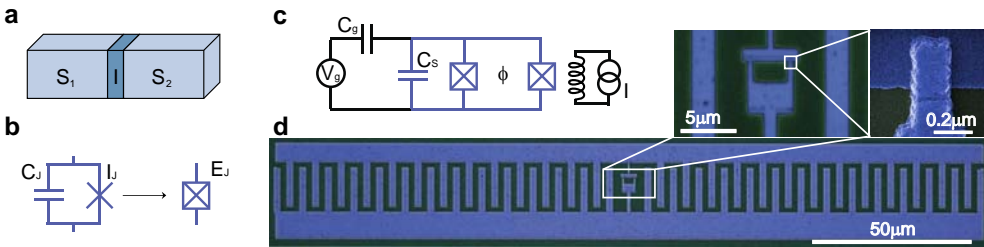
Figure 2.4: **Josephson junction and transmon charge qubit. a**, A Josephson tunnel junction consisting of two superconducting electrodes S_1 and S_2 connected via a thin insulating barrier I. **b**, Circuit representation of the junction. The Josephson element is represented by a cross and the junction capacitance C_J is taken into account by the boxed cross. **c**, Circuit diagram of the transmon qubit (shown in blue) consisting of two superconducting islands (top and bottom leads) shunted with a capacitor C_S and connected by two Josephson junctions (boxed crosses) thus forming a DC-SQUID loop. The top island can be voltage (V_g) biased via the gate capacitor C_g. In order to induce an external flux ϕ in the SQUID loop a current (I) biased coil is used (shown in black). **d**, Colorized optical image of a transmon qubit. It is made of two layers of aluminum (blue) of thicknesses 20 nm and 80 nm on a sapphire substrate (dark green). The SQUID loop of size 4 μm by 2 μm and one of the two Josephson junctions of size 200 nm by 300 nm (colorized SEM image) are shown on an enlarged scale.

with I_c the critical current of the Josephson junctions are fabrication parameters that depend on the circuit geometry and the details of the tunnel barriers respectively, see Chapter 5 for details.

2.2.2 Transmon regime

The qubit Hamiltonian can be solved exactly in the phase basis using Mathieu functions [Devoret03, Cottet02], see Fig. 2.5 for the energy level diagram. For numerical simulations it is equivalent to solve the Hamiltonian by exact diagonalization in a truncated charge basis

$$H = 4E_C \sum_{j=-N}^{N} (j - n_g)^2 |j\rangle\langle j| - E_J \sum_{j=-N}^{N-1} (|j+1\rangle\langle j| + |j\rangle\langle j+1|), \qquad (2.13)$$

where the number of charge basis states that need to be retained in order to obtain an accurate result, $2N + 1$, depends on the ratio E_J/E_C and on the transmon eigenstate $l \in \{0, 1, 2, 3, ...\}$ (or equivalently $l \in \{g, e, f, h, ...\}$) of interest. Typically, $N \sim 10$ charge basis states are sufficient to obtain a good accuracy for the lowest few energy levels in the transmon regime where $20 \lesssim E_J/E_C \lesssim 100$.

In this limit we can also find analytic expressions. Approximately, the eigenenergy of the state l is given as [Koch07a]

$$E_l \simeq -E_J + \sqrt{8E_J E_C}\left(l + \frac{1}{2}\right) - \frac{E_C}{12}(6l^2 + 6l + 3), \qquad (2.14)$$

valid for the first few levels l and large values of the ratio $E_J/E_C \gg 1$. The $|g\rangle$ to $|e\rangle$ level transition frequency of the transmon is therefore simply given as

$$\nu_{ge} \simeq (\sqrt{8E_J E_C} - E_C)/h. \qquad (2.15)$$
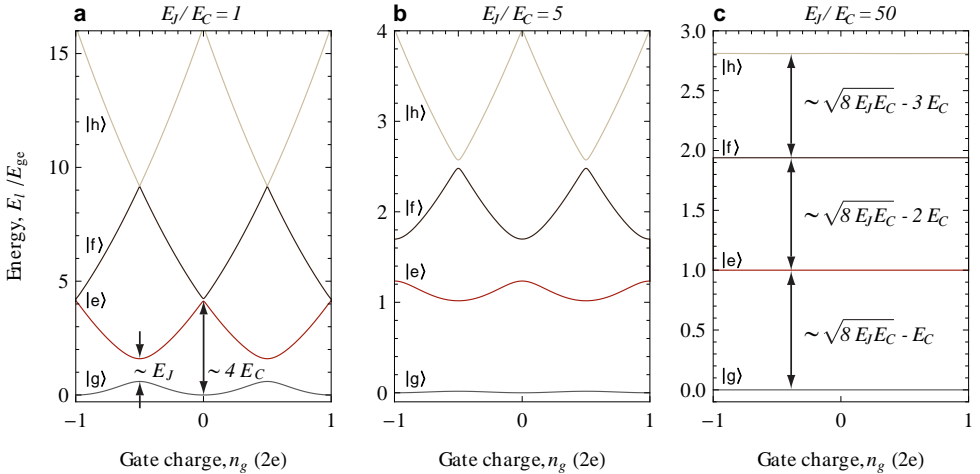
Figure 2.5: **Energy level diagram of the Cooper pair box and the transmon.** Calculated eigenenergies E_l of the first four transmon levels $|g\rangle$, $|e\rangle$, $|f\rangle$ and $|h\rangle$ as a function of the effective offset charge n_g for different ratios $E_J/E_C = 1, 5, 50$ in panels **a**, **b** and **c**. Energies are given in units of the transition energy E_{ge}, evaluated at the degeneracy point $n_g = 0.5$ and the zero point in energy is chosen as the minimum of the ground state level $|g\rangle$.

The anharmonicity of the transmon levels $\alpha \equiv E_{\mathrm{ef}} - E_{\mathrm{ge}}$, which can limit the minimal qubit manipulation time, decreases only slowly with increasing $E_{\mathrm{J}}/E_{\mathrm{C}}$ and is approximately given as $\alpha \simeq -E_{\mathrm{C}}$, see Fig. 2.5 c. The energy dispersion of the low energy eigenstates l with respect to charge fluctuations on the other hand $\epsilon_l \equiv E_l(n_{\mathrm{g}} = 1/2) - E_l(n_{\mathrm{g}} = 0)$ approaches zero rapidly [Koch07a]

$$\epsilon_l \simeq (-1)^l E_{\mathrm{C}} \frac{2^{4l+1}}{l!} \sqrt{\frac{2}{\pi}} \left(\frac{E_{\mathrm{J}}}{2E_{\mathrm{C}}} \right)^{\frac{l}{2}+\frac{3}{4}} e^{-\sqrt{8E_{\mathrm{J}}/E_{\mathrm{C}}}} \tag{2.16}$$

with the ratio $E_{\mathrm{J}}/E_{\mathrm{C}}$, see Fig. 2.5 a-c. A DC-gate bias V_{g} for qubit control, as shown in Fig. 2.4 c, is therefore obsolete in the transmon regime. This abandonment of charge control has dramatically improved the stability of the qubit energy levels, which in many CPB devices is limited by 1/f charge noise and randomly occurring quasi particle tunneling events. The new design has furthermore significantly improved the dephasing times of superconducting charge qubits [Schreier08] by effectively realizing the charge noise insensitive 'sweet spot' of the CPB [Vion02] at any charge bias point. It is important to note that, in contrast to its insensitivity to low frequency noise, the transmon matrix elements for resonant level to level transitions are even increased compared to the CPB, see Subsection 2.3.3.

2.2.3   Spin-1/2 notation

The qubit Hamiltonian Eq. (2.13) can also be rewritten in the basis of the transmon states $|l\rangle$ which gives

$$H = \hbar \sum_l \omega_l |l\rangle\langle l|. \tag{2.17}$$

Introducing the atom transition operators $\sigma_{ij} = |i\rangle\langle j|$, Eq. (2.17) can be written as $H = \hbar \sum_l \omega_l \sigma_{ll}$. In case only two transmon levels are relevant we can make use of the notation used to describe a spin-1/2 particle. With the relations $\omega_{\mathrm{a}} = \omega_{\mathrm{ge}} = \omega_{\mathrm{e}} - \omega_{\mathrm{g}}$, $\sigma_{\mathrm{gg}} + \sigma_{\mathrm{ee}} = 1$ and the Pauli matrix notation $\sigma_z = \sigma_{\mathrm{gg}} - \sigma_{\mathrm{ee}} = |g\rangle\langle g| - |e\rangle\langle e|$ the two state transmon Hamiltonian simplifies to the spin-1/2 particle Hamiltonian [Scully97]

$$H = \frac{1}{2}\hbar\omega_{\mathrm{a}}\sigma_z. \tag{2.18}$$

The transmon qubit pseudo-spin can be represented by a vector on the Bloch sphere and its dynamics is governed by the Bloch equations [Allen87], widely used in the description of magnetic and optical resonance phenomena.

Although the spin-1/2 model is a sufficient description for the transmon qubit in many cases, optimal control techniques are required for short qubit control pulses with a bandwidth comparable to the anharmonicity [Motzoi09, Chow10a, Lucero10]. The two-state model is also not appropriate if the transmon is strongly coupled to a field mode, see Section 2.3, which is occupied by more than a single photon on average $n, n_{\mathrm{th}} \gtrsim 1$, see Chapters 8 and 10.

2.3 Matter – light coupling

In this section we address the physics of superconducting circuits coupled to photons in a microwave resonator. Before going into the details in the context of circuit QED, we start with the description of matter-light interactions in the more general context of quantum electrodynamics in Subsection 2.3.1. The dipole coupling Hamiltonian is then used to introduce the famous Jaynes-Cummings model which describes atoms coupled to cavity photons in Subsection 2.3.2. In Subsection 2.3.3 we show that a superconducting artificial atom in a microwave resonator also realizes Jaynes-Cummings physics and introduce a generalized model taking which takes into account the multiple states of the transmon. In Subsection 2.3.4 we address the physics of coherent qubit state control and readout in the dispersive limit of circuit QED.

2.3.1 Atom-field interaction

The quantitative description of the interaction of matter and radiation is a central part of quantum electrodynamics. The minimal coupling Hamiltonian

$$H_{\min} = \frac{1}{2m}\left(\mathbf{p} - e\mathbf{A}(\mathbf{r},\mathbf{t})\right)^2 + eU(\mathbf{r},t) + V(r), \tag{2.19}$$

describes an electron in an electromagnetic field with the vector and scalar potentials $\mathbf{A}(\mathbf{r},t)$ and $U(\mathbf{r},t)$, the canonical momentum operator $\mathbf{p} = -i\hbar\nabla$ and $V(r)$ an electrostatic potential (e.g. the atomic binding potential). It can be derived from the Schroedinger equation of a free electron

$$\frac{-\hbar^2}{2m}\nabla^2\psi = i\hbar\frac{d\psi}{dt}, \tag{2.20}$$

and the additional requirement of local gauge (phase) invariance [Cohen-Tannoudji89, Scully97], such that both the electron wave functions $\psi(\mathbf{r},t)$ and also $\psi(\mathbf{r},t)e^{i\chi(\mathbf{r},t)}$ are valid solutions. Here the arbitrary phase $\chi(\mathbf{r},t)$ is allowed to vary locally, i.e. it is a function of space and time variables. While the probability density $P(\mathbf{r},t) = |\psi(\mathbf{r},t)|^2$ of finding an electron at position $\mathbf{r}$ and time t remains unaffected by the phase change, Eq. (2.20) is no longer satisfied and needs to be modified. It can be shown that the new Schroedinger equation

$$H_{\min}\psi = i\hbar\frac{d\psi}{dt} \tag{2.21}$$

with the minimal coupling Hamiltonian Eq. (2.19) satisfies local phase invariance and covers the physics of an electron in an electromagnetic field. In the dipole approximation, valid for long wavelength compared to the size of the particle, and the radiation gauge [Göppert-Mayer31, Scully97, Cohen-Tannoudji98, Yamamoto99, Woolley03] the minimal coupling Hamiltonian of an electron at position $\mathbf{r}_0$ given in Eq. (2.19) can be simplified to $H = p^2/(2m) + V(r) + H_{\text{int}}$. Here the interaction part

$$H_{\text{int}} = -e\mathbf{r}\mathbf{E}(\mathbf{r}_0,t) \tag{2.22}$$

represents the well known dipole coupling Hamiltonian with the dipole operator $\mathbf{d} = e\mathbf{r}$.

2.3.2 Jaynes-Cummings model

The physics of cavity QED with superconducting circuits [Blais04] is very similar to the physics of cavity QED using natural atoms [Haroche06]. By making use of the previously found expression for the resonator field Eq. (2.7) the spin-1/2 particle Eq. (2.18) and the electron field interaction term Eq. (2.22), we will now introduce the full quantum model for the interaction of a two state system with quantized radiation in a cavity.

Using the atom transition operators $\sigma_{ij} = |i\rangle\langle j|$, we can reexpress the dipole operator in Eq. (2.22) as $\mathbf{d} = \sum_{i,j} M_{ij}\sigma_{ij}$ with the electric-dipole transition matrix element $M_{ij} = e\langle i|\mathbf{r}|j\rangle$. The electric field of mode m with unit polarization vector $\hat{\epsilon}_m$ at the position of the atom is given as $\mathbf{E} = \sum_m \mathscr{E}_m \hat{\epsilon}_m (a_m + a_m^\dagger)$ with the photon creation and annihilation operators $a^\dagger$ and a. When the field is confined to a finite one-dimensional cavity with volume V the zero point electric field is $\mathscr{E}_m = \sqrt{\hbar\omega_m/(\epsilon_0 V)}$. In the case of just two atomic levels $|g\rangle$ and $|e\rangle$ and only one electromagnetic field mode the interaction Hamiltonian reduces to

$$H_{\text{int}} = \hbar g(\sigma_{\text{ge}} + \sigma_{\text{eg}})(a + a^\dagger),\tag{2.23}$$

with the single photon dipole coupling strength $g = g_{\text{ge}} = -M_{\text{ge}}\hat{\epsilon}_k \mathscr{E}/\hbar$.

By introducing the Pauli matrix notation where $\sigma_+ = \sigma_{ge} = |g\rangle\langle e|$ and $\sigma_- = \sigma_{eg} = |e\rangle\langle g|$ and by combining the interaction Hamiltonian Eq. (2.23) with the single mode cavity Hamiltonian Eq. (2.7) and the two state qubit Hamiltonian Eq. (2.18) we get

$$\mathscr{H} = \hbar\omega_r\left(a^\dagger a + \frac{1}{2}\right) + \frac{1}{2}\hbar\omega_a \sigma_z + \hbar g(\sigma_+ + \sigma_-)(a + a^\dagger)\tag{2.24}$$

fully describing all aspects of the single mode field interacting with a single two level atom or qubit without dissipation.

The two energy conserving terms $\sigma_- a^\dagger$ ($\sigma_+ a$) describe the process where the atom is taken from the excited to the ground state and a photon is created in the considered mode (or vice versa). The two terms which describe a simultaneous excitation of the atom and field mode (or simultaneous relaxation) are energy nonconserving. In particular when the coupling strength $g \ll \omega_r, \omega_a$ and the two systems are close to degeneracy $\omega_r \sim \omega_a$ the latter terms can be dropped, which corresponds to the rotating-wave approximation. More specifically this approximation holds as long as the energy of adding a photon or adding a qubit excitation is much larger than the coupling or the energy difference between them $(\omega_r + \omega_a) \gg g, |\omega_r - \omega_a|$. The resulting Hamiltonian is the famous Jaynes-Cummings model

$$\mathscr{H}_{JC} = \hbar\omega_r\left(a^\dagger a + \frac{1}{2}\right) + \frac{1}{2}\hbar\omega_a \sigma_z + \hbar g(\sigma_+ a + a^\dagger \sigma_-),\tag{2.25}$$

which describes matter-field interaction in the dipole and rotating wave approximations [Jaynes63]. It is analytically solvable and represents the starting point for many calculations in quantum optics.

Close to resonance ($\omega_r \sim \omega_a$) the photon number state $|n\rangle$ and the atom ground and excited states $|g\rangle$ and $|e\rangle$ are no longer eigenstates of the full Hamiltonian. The interaction term lifts their degeneracy and the new eigenstates are superpositions of qubit and cavity states $|n, \pm\rangle = (|g\rangle|n\rangle \pm |e\rangle|n-1\rangle)/\sqrt{2}$, where the two maximally entangled symmetric and antisymmetric superposition states are split by $\sqrt{n}2g\hbar$, see level diagram in Fig. 2.6 a. An

atom in its ground state resonantly interacting with one photon in the cavity will therefore flip into the excited state and annihilate the photon inside the cavity $|g,1\rangle \rightarrow |e,0\rangle$ and vice versa. This process was named vacuum Rabi oscillation and occurs at a frequency $\sqrt{n}\,g/\pi$. The term vacuum refers to the fact that the process also happens with an initially empty cavity $n = 0$ where the vacuum fluctuations of the cavity field trigger the relaxation of the atom. Systems that show several vacuum Rabi cycles before either the photon decays with rate κ or the atom decays into a mode other than the resonator mode at rate γ are said to be in the strong coupling limit of cavity QED where $g \gg \kappa, \gamma$. In circuit QED systems it is comparatively easy to realize this limit, see Chapter 8.

In the dispersive limit where the detuning $\Delta = |\omega_a - \omega_r| \gg g$ no atomic transitions occur. Instead, virtual photons mediate dispersive interactions which lead to level shifts proportional to g^2/Δ of the coupled system, see Fig. 2.6 b. The Hamiltonian in this regime can be approximated using second order time dependent perturbation theory of the Jaynes Cummings Hamilonian Eq. (2.25). Expanding the terms into powers of g/Δ yields [Haroche92, Gerry05]

$$H \approx \hbar\left(\omega_r + \frac{g^2}{\Delta}\sigma_z\right)\left(a^\dagger a + \frac{1}{2}\right) + \frac{\hbar\omega_a}{2}\sigma_z, \tag{2.26}$$

which illustrates the qubit state dependent shift of the resonator with the new oscillation frequency $\tilde{\omega}_r = \omega_r \pm g^2/\Delta$. This resonator frequency change is detectable in a
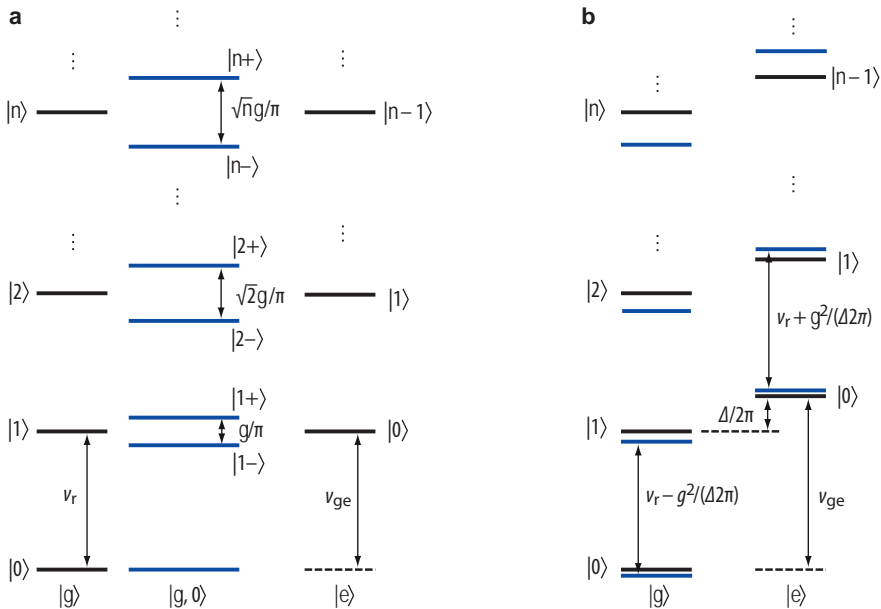
Figure 2.6: **Jaynes-Cummings dressed states energy level diagram.** The uncoupled product states (black lines) $|g,n\rangle$ (left) and $|e,n\rangle$ (right) are given in frequency units $\nu = E/h$. **a,** The resonant dipole coupled states $|n\pm\rangle$ (blue lines) are split in frequency by $\sqrt{n}g/\pi$. **b,** In the detuned case where $|\Delta| \gg g$ the energy levels (blue lines) are state dependently shifted to lower ($|g\rangle$) or larger ($|e\rangle$) frequencies by $(n+1/2)g^2/(2\pi\Delta)$.

time-resolved cavity transmission measurement and allows to perform a quantum non-demolition (QND) measurement of the atom state. Rearranging the terms in Eq. (2.26) yields

$$H \approx \hbar\omega_{\mathrm{r}}\left(a^{\dagger}a+\frac{1}{2}\right)+\frac{\hbar}{2}\left(\omega_{\mathrm{a}}+\frac{2g^2}{\Delta}a^{\dagger}a+\frac{g^2}{\Delta}\right)\sigma_z, \tag{2.27}$$

and crosses out the dual effect of the dispersive interaction. Here the atomic transition frequency is shifted by the photon number dependent AC-Stark shift $2g^2 a^{\dagger}a/\Delta$ and the constant Lamb shift g^2/Δ. The former can e.g. be used to perform a QND measurement of the photon number state inside the cavity [Brune94, Gleyzes07, Guerlin07, Baur07, Johnson10].

2.3.3 Transmon – photon coupling

In this thesis we experimentally explore the above described Jaynes-Cummings physics by integrating a transmon qubit into a coplanar microwave cavity as shown in Fig. 2.1 b. In such a solid state setting it is more natural to express the dipole coupling in terms of voltages instead of electric fields. As discussed in Subsection 2.2.2 the transmon is insensitive to a change in the DC gate voltage bias V_{g}, see Fig. 2.5. The qubit does however couple to an AC electric field which arises due to photons populating the cavity. If the transmon is positioned at the maximum of a considered standing wave electric field mode with resonance frequency ω_{r} we can express the corresponding AC gate voltage as

$$\hat{V}_{\mathrm{g}} = \sqrt{\frac{\hbar\omega_{\mathrm{r}}}{2C}}(a+a^{\dagger}) = \mathcal{V}(a+a^{\dagger}), \tag{2.28}$$

where we have used $\hat{V}_{\mathrm{g}} = q/C$ with q proportional to the charge operator introduced to quantize the LC-oscillator (Subsection 2.1.3). Here C is the capacitance and Z the characteristic impedance of the resonator such that $\omega_{\mathrm{r}} = 1/\sqrt{LC}$ and $Z = \sqrt{L/C}$ is fulfilled and $\mathcal{V}$ denotes the rms vacuum voltage of the LC oscillator[1] similar to the zero point electric field $\mathcal{E}$ in Subsection 2.3.2.

The quantum gate voltage Eq. (2.28) is related to the gate charge as $\hat{n}_{\mathrm{g}} = C_g\hat{V}_g/(2C)$. If we substitute this in the electrostatic part of the charge qubit Hamiltonian Eq. (2.9) and expand the square we obtain a coupling term $H \propto -4E_c C_g \hat{V}_g \hat{n}/e$ which contains the charge qubit state $\hat{n}$ as well as the quantum field oscillator state $\hat{V}_g$. This relation can be simplified as

$$H = 2\hbar g(a+a^{\dagger})\hat{n} \tag{2.29}$$

with the single qubit single photon coupling strength

$$g = \frac{C_g}{C_{\Sigma}}\frac{e\mathcal{V}}{\hbar}. \tag{2.30}$$

The ratio $\beta = C_{\mathrm{g}}/C_{\Sigma} \in \{0, 1\}$ is the coupling capacitance divided by the total capacitance of the qubit. It accounts for the division of voltage in the CPB – the fact that part of the

---

[1]$\mathcal{V}$ can for example be derived by equating the electric field part of the zero point energy with the electrostatic energy in the resonator $\hbar\omega_{\mathrm{r}}/4 \equiv C\mathcal{V}^2/2$.

voltage $\hat{V}_g$ drops e.g. from the resonator center conductor to the qubit island, see Section 5.1 for details. $2\hbar g$ therefore represents the energy needed to move one Cooper pair across a portion β of the rms vacuum voltage fluctuations $\mathcal{V}$ in the resonator. For only two qubit states, valid for example at the charge degeneracy point of the CPB, we can replace the charge operator with the Pauli spin operator $\hat{n} \rightarrow \sigma_x/2$. If we now also apply the rotating wave approximation, which neglects the rapidly rotating terms $a^\dagger \sigma_+$ and $a\sigma_-$, we recover the Jaynes-Cummings Hamiltonian for the qubit photon coupling

$$H = \hbar g (a\sigma_+ + a^\dagger \sigma_-). \tag{2.31}$$

More generally for a multilevel system, such as the transmon qubit, the coupling strength between the levels i and j does also depend on the transition matrix element

$$g_{ij} = 2\beta e\mathcal{V} \langle i|\hat{n}|j \rangle /\hbar. \tag{2.32}$$

In the asymptotic limit where $E_J/E_C \gg 1$ the matrix elements can be examined with a perturbative approach [Koch07b]

$$|\langle l+1|\hat{n}|l \rangle| \approx \sqrt{\frac{l+1}{2}} \left(\frac{E_J}{8E_C} \right)^{1/4}, \tag{2.33}$$

and for all non-nearest neighbor transitions ($|k| > 1$) the matrix element $|\langle l+k|\hat{n}|l \rangle|$ approaches zero rapidly. Employing the rotating wave approximation we obtain a generalized Jaynes-Cummings Hamiltonian which takes into account multiple transmon levels l [Koch07b]

$$H_{JC} = \hbar\omega_r \left(a^\dagger a + \frac{1}{2} \right) + \hbar \sum_l \omega_l |l\rangle\langle l| + \left(\hbar \sum_l g_{l,l+1} |l\rangle\langle l+1|a^\dagger + \text{H.c.} \right). \tag{2.34}$$

Interestingly, the maximal dimensionless qubit-photon coupling g/ω_r depends only on resonator specific geometric and dielectric constants if the transition matrix element is neglected. There exists therefore a relation between the relative coupling strength of a single superconducting qubit and the fine structure constant approximately given as [Devoret07, Koch07b]

$$g/\omega_r \sim 4\beta\sqrt{\alpha/\epsilon_r}, \tag{2.35}$$

with $\alpha = e^2/(4\pi\epsilon_0 \hbar c)$. The maximal coupling strength of a single qubit is therefore on the order of $g/\omega_r \sim 0.1$ for realistic values of the dielectric constant. Note however that this limit is only valid for a half wave transmission line resonator. In addition, an inductively coupled superconducting qubit can in principle easily exceed this bound [Devoret07, Bourassa09, Niemczyk10, Forn-Díaz10]. The same is true if multiple qubits are collectively coupled to the resonator field.

2.3.4 Dispersive limit: Qubit control and readout

The dispersive coupling of atoms and photons detuned by $\Delta = |\omega_a - \omega_r| \gg g$ was already introduced in Subsection 2.3.2. The dispersive Hamiltonian, see Eqs. 2.26 and 2.27, in principle also applies to circuit QED. There is however an interesting quantitative difference.

Due to the large coupling strength as well as the multi-level structure of the transmon, a substantially different (typically much larger) dispersive shift term is obtained.

This enabled not only the observation of the quantum AC-Stark shift [Schuster05], which is very useful to obtain a calibration for the mean cavity photon number as a function of the applied microwave probe power, see Section 6.4. In circuit QED it has furthermore been demonstrated that the AC-Stark shift per photon can become much larger than the qubit line width. This allows to spectroscopically infer the cavity photon number distribution [Gambetta06, Schuster07b]. In addition, it has been observed that the Lamb shift can even exceed the former in some cases [Fragner08].

Dispersive shifts   The dispersive frequency shift between a multilevel qubit and the resonator ($\chi \sim g^2/\Delta$ in Subsection 2.3.2) can be calculated as $\chi = \chi_{01} - \chi_{12}/2$ where $\chi_{ij} = g_{ij}^2/(\omega_{ij} - \omega_{\mathrm{r}})$ and $\omega_{ij} = \omega_j - \omega_i$ for multilevel circuits [Koch07b]. For large detunings this shift can therefore be approximated as

$$\chi \approx -\frac{g^2 E_{\mathrm{C}}/\hbar}{\Delta(\Delta - E_{\mathrm{C}}/\hbar)} \tag{2.36}$$

in the transmon regime.   Due to the reduced anharmonicity also virtual transitions through excited transmon states need to be taken into account. This leads to a renormalization of both the qubit $\omega_{\mathrm{ge}}' = \omega_{\mathrm{ge}} + \chi_{\mathrm{ge}}$ and cavity $\omega_{\mathrm{r}}' = \omega_{\mathrm{r}} - \chi_{\mathrm{ef}}/2$ frequencies due to their interaction. ω_{r}' is then shifted by $+\chi$ or $-\chi$ depending on the qubit state $|g\rangle$ or $|e\rangle$, see Fig. 2.7, and ω_{ge}' is shifted by $+2\chi$ per cavity photon. We can write the effective Hamiltonian as

$$H \approx \frac{1}{2}\hbar\omega_{\mathrm{ge}}'\sigma_{\mathrm{z}} + (\hbar\omega_{\mathrm{r}}' + \hbar\chi\sigma_{\mathrm{z}})a^{\dagger}a. \tag{2.37}$$

For small positive detunings $\Delta \lesssim E_{\mathrm{C}}/\hbar$ much larger (and positive) frequency shifts can be obtained. This so called straddling regime of circuit QED has been identified as an interesting parameter region for an efficient single shot qubit readout [Srinivasan10].

Qubit readout   For a dispersive QND qubit readout the qubit state dependent shift of the cavity resonance frequency by $+\chi$ or $-\chi$ is detected in a time-resolved resonator transmission measurement [Wallraff05, Bianchetti09], see Fig. 2.7. We apply a continuous coherent microwave tone at a frequency ω_{m} to the resonator starting at the time $t = 0$. Including the measurement drive into the dispersive Hamiltonian Eq. (2.37) and expressing it in a frame rotating at the measurement frequency leads to

$$H_{\mathrm{m}} = \frac{1}{2}\hbar\omega_{\mathrm{ge}}'\sigma_{\mathrm{z}} + (\hbar\omega_{\mathrm{r}}' - \hbar\omega_{\mathrm{m}} + \hbar\chi\sigma_{\mathrm{z}})a^{\dagger}a + \hbar\epsilon_{\mathrm{m}}(t)(a^{\dagger} + a), \tag{2.38}$$

where $\epsilon_{\mathrm{m}}(t)$ is the time dependent amplitude of the measurement tone. Measuring the radiation transmitted through the cavity by heterodyne detection we can infer a complex valued signal

$$S(t) = \sqrt{Z\hbar\omega_{\mathrm{m}}\kappa}\,\langle a(t)\rangle\,, \tag{2.39}$$

which gives us access to the time evolution of the expectation value of the annihilation operator, where Z is the characteristic impedance of the system. This signal is different
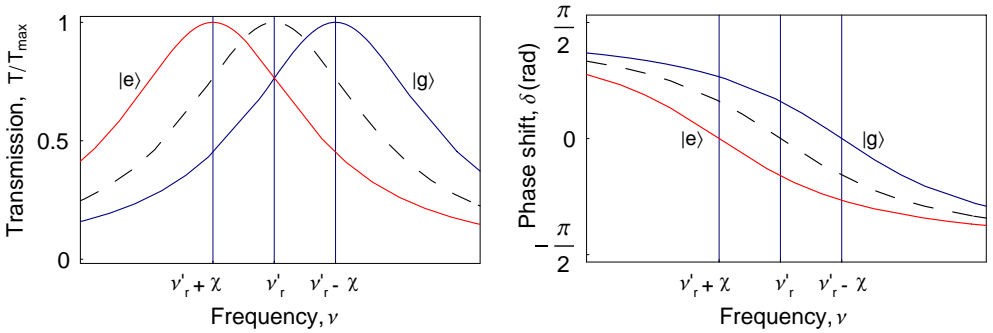
Figure 2.7: **Calculated qubit state dependent resonator spectrum. a**, Calculated transmission amplitude according to Eq. (2.1) and **b,** relative phase shift of the transmitted microwave according to Eq. (2.3) for a moderate dispersive shift $|\pm\chi| \sim \kappa/2$. The solid lines represent the spectrum of the cavity for the qubit being in the ground state $|g\rangle$ (blue) or the excited state $|e\rangle$ (red).

for the qubit in the $|g\rangle$ or in the $|e\rangle$ state, see also Section 6.5, and can be calculated by solving the cavity Bloch equations [Bianchetti09]. By comparing the measurement with the theoretical prediction the population of the excited state

$$P_{\mathrm{e}} = (\langle \sigma_{\mathrm{z}} \rangle + 1)/2 \qquad (2.40)$$

can be extracted. The frequency of the measurement drive is chosen typically close to the resonator frequency $\omega_{\mathrm{m}} = \omega'_{\mathrm{r}}$ or the qubit ground state resonator frequency $\omega_{\mathrm{m}} = \omega'_{\mathrm{r}} - \chi$, because the effect of the dispersive shift is strongest in this frequency range. This dispersive readout scheme has been shown to enable full quantum state tomography of multiple qubits [Filipp09, Leek09, DiCarlo09] in joint measurements. In addition this scheme was extended to readout the quantum state of multiple levels of an artificial atom [Bianchetti10b]. It was furthermore demonstrated that even single shot readout of up to three qubits [Reed10a, DiCarlo10] is possible by measuring at the bare cavity frequency $\omega_{\mathrm{m}} = \omega_{\mathrm{r}}$ with a very high average photon number. This scheme relies on the nonlinearity provided by the Jaynes-Cummings energy ladder [Boissonneault10, Bishop10b]. However, in contrast to a weak dispersive readout it is likely not of the QND type.

Qubit control   Coherent control of the qubit state is achieved by applying a microwave tone at the qubit transition frequency ω'_{a} when the qubit is strongly detuned from the resonator. Although most of the radiation is reflected at the resonator input port, according to Eq. (2.1) a small part will enter the resonator and drive qubit transitions at the Rabi frequency $\Omega/(2\pi) = \sqrt{n_{\mathrm{d}}} g/\pi$, where n_{d} is the number of drive photons inside the resonator.[2] For large detunings of the drive frequency ω_{d} from the resonance frequency $\Delta_{\mathrm{d}} \equiv \omega'_{\mathrm{r}} - \omega_{\mathrm{d}} \gg \kappa/2$ the average number of drive photons is given as $n_{\mathrm{d}} \approx (\epsilon_{\mathrm{d}}/\Delta_{\mathrm{d}})^2$. The coherent driving field can be considered as a classical field with an amplitude $\epsilon_{\mathrm{d}}(t)$ and a

---

[2]Alternatively, a charge gate line can be used to provide local access to drive the qubit, see Fig. 4.2.

frequency ω_d which leads to the following effective Hamiltonian [Blais07]

$$H_d = (\hbar\omega_r' - \hbar\omega_d)a^\dagger a + \frac{1}{2}\left(\hbar\omega_{ge}' - \hbar\omega_d + 2\hbar\chi a^\dagger a\right)\sigma_z + \frac{1}{2}\hbar\Omega(t)\sigma_x, \qquad (2.41)$$

with the Rabi frequency $\Omega(t) = 2\epsilon_d(t)g/\Delta_d$. This control parameter allows to rotate the qubit state vector on the Bloch sphere around the x-axis, or by shifting the phase of the drive signal by $\pi/2$ also around the y-axis. The overall rotation around the x-axis is characterized by the Rabi angle $\theta_R = \int \Omega(t)dt$. By applying a pulse of suitable amplitude and length such that $\theta_R = \pi$ the qubit can be excited from the ground to the excited state. For arbitrary Rabi angles the final qubit state reads

$$|\psi\rangle = \cos(\theta_R/2)|g\rangle + \sin(\theta_R/2)|e\rangle, \qquad (2.42)$$

which can be prepared and readout in a time-resolved Rabi oscillation experiment, see Section 6.5.

3

CONCLUSION

The physics of cavity QED with superconducting circuits is very similar to the physics of cavity QED using natural atoms. There are however also a number of substantial differences.

The most obvious difference is a dramatically increased single-photon single-atom coupling strength g. This very strong coupling regime of cavity QED allows for a number of experimental investigations of matter-light interaction effects only amendable to theoretical consideration up to now. Additionally, the artificial atom stays inside the resonator under all circumstances without changing its position or coupling, also e.g. if very high drive powers are applied. As a consequence it is much easier to investigate the large photon number regime as well as multi-qubit interactions without the need of introducing effective coupling constants.

In contrast to cavity QED where the dipole moment constitutes a fixed property of a given atom, the effective dipole moment of the superconducting qubit can be adjusted by design, fabrication and by using in-situ bias currents. If relatively harmonic qubits like the transmon are used it turns out that the multi-level physics is in general more relevant compared to traditional cavity QED. This brings about both a number of additional difficulties, e.g. in high fidelity state preparation, but also new and interesting multi-level physics.

Interestingly, even the comparatively much shorter qubit state lifetimes add to the new experimental quality in many cases since they allow for a drastically increased repetition rate of the experiments on the order of ~ 100 kHz. The long time stability of charge noise insensitive transmon qubits combined with efficient data acquisition and averaging methods then allows for long time averaging and the acquisition of low noise, high resolution data sets.

P A R T **ii**

EXPERIMENTAL PRINCIPLES

Be it a 'trapped' microwave photon or the position of a single electron out of hundreds of billions in a small piece of aluminum; the topic of this part are the experimental techniques required to explore such a single quantum in a solid-state microchip circuit. Technological challenges include ultra low power microwave frequency measurement and control at millikelvin temperatures, see Chapter 4 and Appendix A, as well as design and fabrication of micro- and nanometer sized circuits discussed in Chapter 5 and Appendix B. Necessary sample characterization measurements are discussed in Chapter 6 before the main experimental results are presented in Part III.

MEASUREMENT SETUP

Typical energy level splittings of superconducting Josephson junction devices are in the microwave frequency range. The technology required for experiments at frequencies of a few GHz is well established due to its applications in radio-astronomy and wireless telecommunication. However, as we intend to study coherent physical effects on the level of a single quantum of energy, we have to efficiently control and analyze microwave signals at extremely low powers $< 10^{-18}$ W. In addition, the experimental setup, see Fig. 4.1, needs to be cooled to ultra-low temperatures < 20 mK in order to suppress any thermal excitations and prepare the system in its quantum ground state. These requirements imply the need for appropriate wiring, electromagnetic shielding and careful filtering at ultra-low temperatures, as well as careful mixing techniques, high sampling rates and a full characterization of the RF-equipment in use. For a complete circuit diagram of the experimental setup see Fig. 4.1 a.

At the beginning of this chapter, in Section 4.1, we will introduce the superconducting microchip sample, discuss its main design parameters and explain how it is integrated into the measurement setup. In order to control and readout the qubit and cavity states of such a sample three main ingredients are required. In Section 4.2 the signal synthesis part is discussed, where DC bias and phase coherent microwave signals are generated and pulse modulated before they enter the dilution refrigerator, see Fig. 4.1 a top left. The cryogenic part of the circuit constitutes the second main building block and is discussed in Section 4.3. In this part of the setup the generated signals are filtered and attenuated before they interact with the qubit. Subsequently, the transmitted measurement tone is amplified and the cables are routed back to room temperature, see lower part of Fig. 4.1 a. Finally, in Section 4.4, we will explain how the amplified microwave tone is down-converted to frequencies that can be sampled, averaged and post-processed digitally, see top right part in Fig. 4.1 a.

4.1   Microchip sample

A number of qubits with varying parameters and layouts have been designed and fabricated for the experiments presented in this thesis and Refs. [Fink09a, Fink09b, Fink10, Leek10, Bianchetti10b, Bozyigit10c, Bozyigit10b, Lang10]. One of the fabricated chips is depicted as an example in Fig. 4.2 a and b.
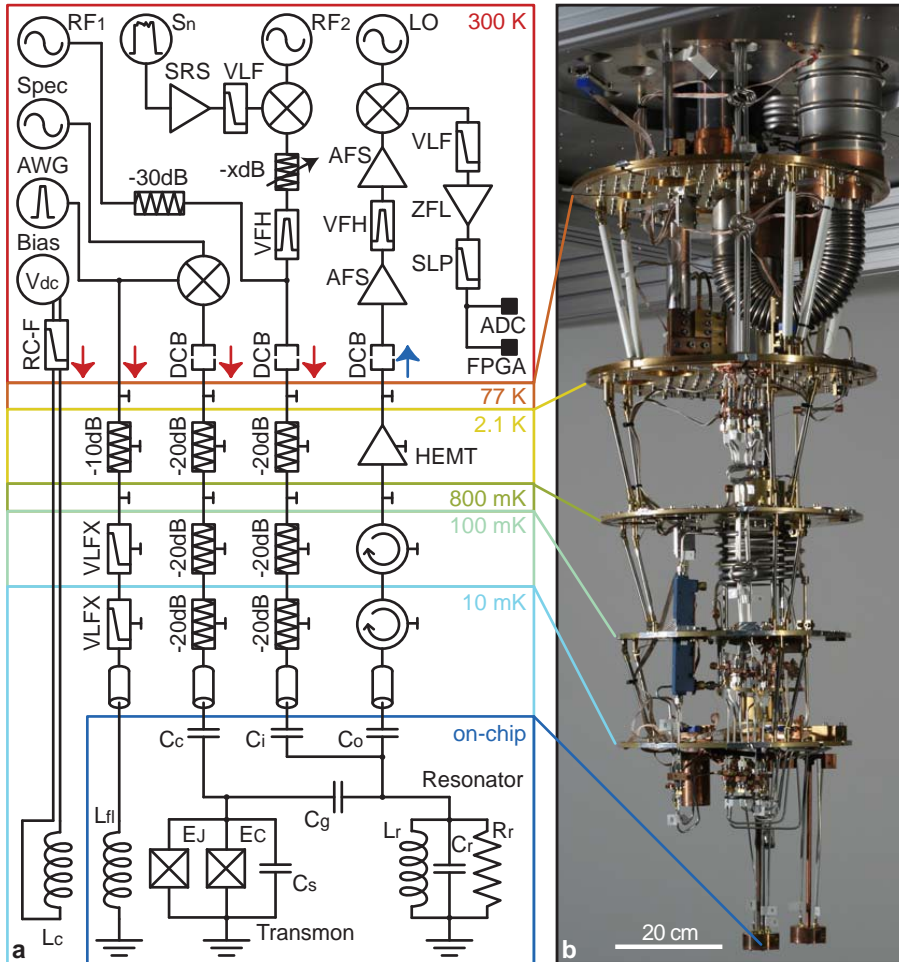
Figure 4.1: **Exemplary measurement & control circuit (a) and cryogenic part of the setup (b). a**, The transmon (bottom, middle) is controlled via a superconducting coil L_c, an on-chip flux bias line with large bandwidth L_{fl} and an on-chip microwave frequency charge gate line C_c (from left to right). The transmon is also coupled via C_g to the $L_r C_r R_r$ modeled resonator (bottom right) coupled to input and output lines via C_i and C_o respectively. Different temperature stages are indicated with color. See text for details. **b**, Cryogen free dilution refrigerator from *Vericold*, equipped with two complete measurement circuits as shown in a. Different temperature stages are indicated.

4.1.1 Superconducting circuit

The wave-guide structures, such as the coplanar resonator (green) in Fig. 4.2, qubit control lines (violet) and additional components such as microwave beam splitters (red) with a typical minimal feature size of $\sim 4\ \mu m$ are fabricated in a standard photo-lithographic process. Different chip designs with varying geometries and coupling parameters are patterned on a polished 2 inch c-cut sapphire wafer of thickness $500\,\mu m$. This is done either by reactively etching a magnetron sputtered Niobium thin film of thickness ~ 150 nm or alternatively by evaporation of an aluminum thin film of thickness ~ 200 nm. Details of this process, which was not part of this thesis, can be found in Refs. [Frunzio05, Schuster07a, Göppl08, Göppl09]. In contrast to thin film aluminum resonators, circuits made of Niobium can be characterized in the superconducting state at liquid helium temperatures. In addition, their visibility in the electron microscope is much better due to its larger atomic weight compared to aluminum. This is relevant for the accurate alignment of qubit structures in the following nano fabrication steps. For details of microwave beam splitter design and characterization refer to Refs. [Frey08, Henzen08, Littich09] and for details of the design of local charge gate and flux bias lines refer to [Steffen08].

The three main design parameters of the coplanar waveguide resonator are the resonance frequency ν_r determined by the length of the resonator, the quality factor Q determined by the size of the chosen gap or finger capacitors and finally the impedance of the circuit which is determined by the ratio of the center conductor width to the size of the gap between the center conductor and the ground planes (designed to be $\sim 50\ \Omega$), see Subsection 2.1.1. In order to obtain the desired resonator frequency, the resonator is usually shaped in the form of a meander, see Fig. 4.2 a (green), which does not harm the low
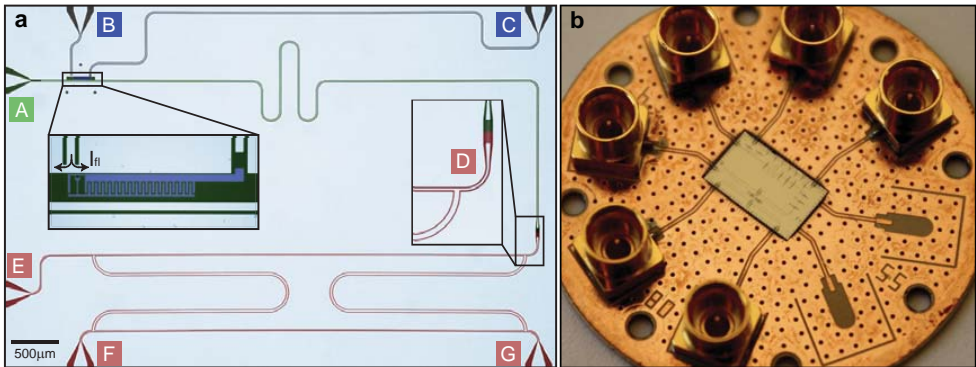
Figure 4.2: **Fabricated exemplary microchip sample. a**, The sapphire chip of size 7x4.2 mm^2 with patterned aluminum thin film was used in [Bozyigit10b, Bozyigit10a, Lang10]. Indicated is the resonator in green with input port A and the qubit in violet (enlarged inset) equipped with control lines for DC current pulses via port B and RF pulses via port C. Also shown is the high capacitance resonator output port (enlarged inset) which at the same time represents the input port D of an on-chip beam splitter (red) with vacuum port E and outputs F and G. For design of beam splitters and local qubit control lines see [Frey08, Henzen08, Littich09] and [Steffen08] respectively. **b**, Printed circuit board with diameter 30 mm containing the glued and wire bonded chip shown in panel a. Also shown is the PCB without (bottom right) and with soldered surface mount SMP connectors that connect to ports G, F, E, A, B, C (clockwise from bottom).

loss transmission properties as long as the curvature is much less than the gap size of the waveguide [Simons01, Wang09]. For large external quality factors the gate capacitors are designed just as a gap in the center conductor. In order to get high coupling on the other hand, the capacitance can be made almost arbitrarily large by designing finger capacitors, where the minimum spacing is set by the minimal feature size of the optical lithography process. The center conductor width was chosen to be 10 μm and, together with the gap, tapered smoothly at the edges of the chip to a width of about 300 μm in order to be able to connect the chip to the PCB, using wire bonds, with a minimum amount of unwanted reflections.

After cutting the waver into chips of size 2x7, 4.2x7, or 6.4x7 mm^2 with the dicing saw *DAD 321* from *Disco*, the qubits (violet) are fabricated. These are made using double layer resist electron beam lithography with a typical minimal feature size of ~ 100 nm. This is followed by double angle shadow evaporation of two aluminum thin films including a controlled oxidation step. Again there are three main design parameters, namely the two characteristic energies: Josephson energy E_J and charging energy E_C as well as the qubit photon coupling strength g, see Sections 2.2 and 5.1. Virtually all desired combinations of these parameters can be implemented with an appropriate geometry and fabrication. Fabrication and design of Josephson junction devices is covered in detail in Chapter 5 and relevant recipes are given in Appendix B.

4.1.2 Printed circuit board

The printed circuit board (PCB), see Fig. 4.2 b, provides the necessary interface between the microchip and the rest of the measurement circuit. Its main design consideration is the suppression of parasitic resonances due to impedance mismatches. One action is to periodically contact the bottom ground plane with the top ground strips of the PCB with copper vias, suppressing any modes between these two planes up to over 15 GHz. No vias could be fabricated in the silicon substrate of the chip, however the chips were taken to be small enough so the cutoff frequency of such modes are much higher than the operation frequencies. In order to keep the impedance mismatch due to different dielectric constants small, a PTFE - woven fiberglass - ceramic filled laminate *AD1000* of thickness 0.5 mm from *Arlon* was used as a dielectric. It has a low loss tangent of tan δ ~ 0.0023 and a large dielectric constant of ~ 10.2 at 10 GHz, which allows for a compact design of the conductor backed coplanar PCB wave guides. Electrodeposited copper is used for the front and back metallization of thickness 17.5 μm and 70 μm respectively. The two metal films are connected by a large number of copper *vias* of diameter 300 μm which are arranged with a spacing of 1 mm in order to minimize stray resonances. The boards are designed with a cutout to hold different chip sizes and fabricated at *Hughes Circuits Inc*. Common minimal PCB feature sizes are on the order of 100 μm with typical tolerances of ~ ±75 μm. For further details of PCB design refer to [Schmidlin08].

Right angle surface mount SMP connectors *19S102-40ML5* with good performance up to about 20 GHz from *Rosenberger* are heat gun soldered to the PCB using leaded solder paste *SC170* from *Solder Chemistry*. After the soldering, the PCB is cleaned in an ultrasonic bath with citric acid (1:1 in H_2O) and IPA for about ~ 3 minutes each. The chips are then glued and carefully aligned in the PCB cutout under an optical microscope. A thin layer of PMMA (thinned with about 4% chlorbenzene) is used as a glue that dries typically within ~ 20 minutes.

4.1.3 Wire bonds

The device is contacted with aluminum wires of thickness $\sim 30~\mu$m using the wire bonder *7476E* from *Westbond*. About 2-3 bonds were used to contact each waveguide launcher. All chip ground planes were contacted to the PCB ground at the circumference with about 5-10 bonds per millimeter. Typical bond wire configurations are shown in Fig. 4.3 a. Short bonds are more difficult to achieve but generally preferred as they have smaller inductance and therefore improved high frequency properties.

In addition, on-chip bonds were used for more complicated designs where the ground plane is divided into several parts due to the presence of bias lines or different beam splitter paths, see Fig. 4.3 a. In such a case superconducting interconnects between the ground planes are needed in order to avoid spurious resonances of the circuit. One quite successful strategy was to simply connect all on-chip ground planes by as much superconducting bonds as easily possible on the limited space available. In particular, multiple connections between both sides of the resonator reduce the occurrence of so called odd modes [Simons01]. If these bonds are used on either side of a qubit however, a closed superconducting loop around the qubit is formed. In this case a decreased coupling to an externally applied B-field bias has been observed. This effect is probably due to screening currents through the loop formed by the bond wires which needs to be taken into account. A new air bridge process is under development and should replace the sometimes difficult on-chip bonding process in the future.

4.1.4 Sample mount, coils and shielding

The main design parameter for the sample mount is once more the suppression of any electromagnetic stray fields as well as any unwanted reflections due to impedance mis-
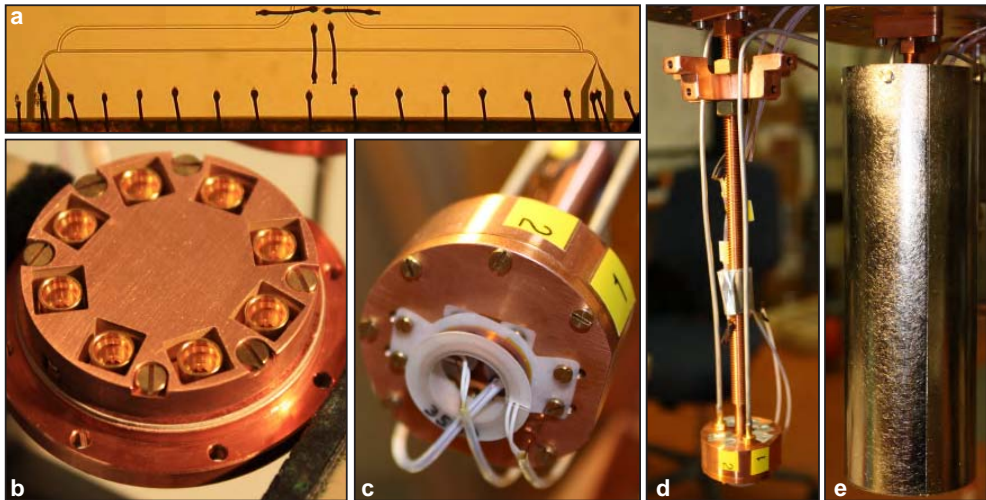
Figure 4.3: **Chip and sample mounting. a**, Section of the wire bonded chip. **b**, Sample cover and bottom part of the sample holder. **c**, Closed sample holder containing three superconducting coils. **d**, Mounted sample holder with shield holder (top). **e**, Mounted double-walled magnetic shielding.

matches in the connections of the circuit. A sample mount made from solid copper, as shown in Fig. 4.3, was used to protect the chip from interference with electromagnetic fields. In order to end up with nicely sealed box and provide good contact between the bottom ground plane of the PCB and the sample holder, suitable bullet connectors were used to connect the semi rigid coaxial lines to the surface mount connectors. In order to minimize the volume for parasitic modes a sample cover was used, see Fig. 4.3 b, to fill the empty volume between PCB and sample box optimally, see Ref. [Marx09] for details.

At the outside of the copper box a milled blind hole houses two small superconducting coils with diameter of ~5 mm for selective magnetic field biasing of the qubits. In addition a third larger coil with diameter of ~18 mm was installed on top of the small ones, see Fig. 4.3 c. The used wire was *SC-T48B-M0.026mm* from *Supercon* with an outer diameter of 36 μm with ~100 turns per layer and ~70 layers implemented. The bias lines were common twisted pairs with RC filters at room temperature. Suitable filters at cryogenic temperatures would be an improvement for future experiments. For further details of the superconducting coils and the used filters refer to Subsection 4.3.4 and [Bianchetti10a].

The sample holder is fixed to the base plate of the dilution refrigerator using a long threaded rod with spanner flat. The rod is also used to height adjustably mount the double walled magnetic shields made from tempered *Cryoperm 10* of thickness 1 mm from *Vacuumschmelze*, which is soft magnetic at low temperatures, see Fig. 4.3 d and e. All copper parts below 4 K are made using oxygen-free copper in order to ensure reasonable heat conduction and thermalization even at temperatures of only a few millikelvin. As a side effect the vacuum properties are also improved.

4.2   Signal synthesis

Most experiments presented in Chapter 8 are based on spectroscopic measurements where phase coherent continuous wave (CW) tones of variable power are used as input signals. For time-resolved qubit manipulation however, see Section 6.5 and Chapter 10, phase sensitive pulsed microwave signals are required. In both cases, a number of trigger signals and an accurate synchronization is absolutely necessary to ensure successful and reliable operation of the experiment.

4.2.1   Microwave generation, control and synchronization

Microwave frequency signal generators *PSG E8257C* and *PSG E8257D* from *Agilent* were used to provide classical phase coherent signals[1] of up to 20 GHz, see RF1, RF2 and Spec signal sources as shown in Fig. 4.1 a top. In order to be able to modulate the amplitude of these tones with nanosecond resolution, arbitrary waveform generators *AWG520* or *AWG5014* from *Tektronix* are used to generate envelope pulses with a sampling rate of 1 GS/s on up to four independent channels and 4 additional digital markers, see AWG in Fig. 4.1 a top left. The digital markers are used to define and control the sequence of each measurement by triggering the output of microwave sources and data acquisition cards at the beginning of every measurement with typical repetition rates of 10 to 50 kHz, limited

---

[1]Phase noise in CW mode: -115 dBc/Hz at 100 kHz offset in the relevant frequency range of 3.2 GHz to 10 GHz.

by the qubit relaxation time T_1. Pulse sequences are designed in *Mathematica* and transferred into the memory of the AWG via an ethernet connection. Apart from the pattern file transfer, all communication between the measurement and control computer and the discussed devices is done via their GPIB-interface where *Labview* software is used to automate the measurement procedures. Long term phase stability and synchronization is achieved by phase locking all signal generators, AWGs and acquisition cards with an ultra low phase noise 10 MHz Rubidium frequency standard *SRS FS745* from *Stanford Research Systems.*

4.2.2 Quadrature modulation

To apply microwave pulses phase sensitively to the qubit, e.g. via the charge bias line, an *IQ* quadrature mixer *IQ-0714M* from *Marki Microwave* was used to modulate the output of the spectroscopy generator, see $\otimes$ symbol in Fig. 4.1 a top left. Such a device has a LO (local oscillator) input, two separate IF (intermediate frequency) inputs I and Q (DC-500 MHz) and one RF (radio frequency) output. The LO input is split with a power divider into two signals. One of them is directly multiplied with the I input while the other is first phase shifted by -90 degree (for RF>LO) before being multiplied with the Q input. Those two branches are finally combined again at the RF output.

Mathematically the amplitudes of the in-phase carrier I and the quadrature phase carrier Q, which are applied at the I and Q inputs of the mixer, are interpreted as the two Fourier components

$$I = \frac{2}{T} \int_T S_{\text{IF}}(t) \cos(\omega_{\text{IF}} t) \, dt \tag{4.1}$$

$$Q = \frac{2}{T} \int_T S_{\text{IF}}(t) \sin(\omega_{\text{IF}} t) \, dt \tag{4.2}$$

of the IF signal

$$S_{\text{IF}}(t) = A \cos(\omega_{\text{IF}} t + \phi) = I \cos(\omega_{\text{IF}} t) - Q \sin(\omega_{\text{IF}} t), \tag{4.3}$$

where T is any chosen period interval e.g. $0 - 2\pi$. We can therefore represent the state of the sine wave $S_{\text{IF}}(t)$ by a vector in a complex plane with I on the real axis and Q on the imaginary axis. Amplitude and phase of the IF signal are encoded in the two quadratures I and Q as

$$A = \sqrt{I^2 + Q^2} \quad \text{and} \quad \phi = \tan^{-1}\left(\frac{I}{Q}\right). \tag{4.4}$$

We can therefore adjust both the amplitude and phase of the RF signal simply by changing the voltages applied to the I and Q ports of the mixer. The angular intermediate frequency $\nu_{\text{IF}} = \pm(\nu_{\text{RF}} - \nu_{\text{LO}})$ can now be chosen to be either zero (homodyne mode or direct modulation), or finite (heterodyne mode, or sideband modulation). In the direct modulation scheme a DC pulse applied e.g. to the Q input port will cause the LO input signal to be transmitted with a phase shift of 90 degrees. Using a finite intermediate frequency two sidebands at frequencies $\nu_{\text{RF}} = \nu_{\text{LO}} \pm \nu_{\text{IF}}$ are transmitted. In the ideal case the RF amplitude scales linearly with the IF amplitude and if both IF inputs are set to ground no signal is transmitted through the mixer.

In reality, the finite LO to RF isolation of the mixer can be a substantial problem for high fidelity state preparation as the qubit is weakly driven even if there is no pulse applied. In case of direct modulation the best strategy was to use an AWG marker similar to a backup switch, gating the microwave sources shortly before and after each pulse. Here a pin diode is used in the microwave source to switch on and off the signal with an on/off ratio of well above 80 dB. In accordance with the specifications of the signal generators being externally pulse modulated in such a procedure, a rise and fall time of the backup pulses are however limited to ~ 6 ns each. An even better strategy is to use single sideband modulation of the microwave pulses at an intermediate frequency of typically 100 MHz. In this case the remaining leakage of the LO signal is detuned from the RF pulse (and the qubit transition frequency) which improves the fidelity of the qubit state preparation. In both modulation schemes it is required to apply and calibrate DC bias voltages at the IF ports of the mixer in order to maximally suppress the leakage of the carrier signal and guarantee phase conservation and a linear dependence of input and output powers, see [Schmidlin09] for details of mixer calibration.

4.2.3   Generation of Gaussian noise

For the experiments presented in Chapter 10 a variable amplitude noise source with a constant frequency spectrum in a bandwidth ~ ±100 MHz centered at the ~ 6.5 GHz resonator mode is needed. The arbitrary waveform generator *AWG520* provides a quasi-random (gaussian) noise source output S_n with a sampling rate limited bandwidth of 500 MHz, see top of Fig. 4.1 a. In order to up-convert this signal to the frequency of the resonator mode, the tone is mixed with the local oscillator RF2, see Fig. 4.1. In order to maximally suppress the coherent carrier tone leakage, the noise signal was amplified twice by 14 dB with the 350 MHz preamplifier *SR445A* from *Stanford Research Systems* which allows to make use of the full linear IF-input range of the mixer. Furthermore, calibrated constant DC voltages on the I and Q ports of the mixer were applied to further suppress carrier leakage.

The resulting tone is then attenuated with two USB programmable step attenuators *DA8-30* from *Weinschel Associates* with a maximal attenuation of 31.5 dB in steps of 0.5 dB from DC to 8 GHz, which were operated in series. In order to restrict the bandwidth of the upconverted noise tone to the required frequency range a 105 MHz low pass filter (VLF) from *Minicircuits* was used before the mixer. In order to suppress any harmonics as a result from the mixing, also a bandpass filter (VHF) from *Minicircuits* was employed. Usage of 3 dB attenuators between each active component helps to reduce reflections and improve the flatness of the noise spectrum. The noise tone is then added to the measurement tone, RF1 in Fig. 4.1 a, with a standard resistive power splitter from *Minicircuits*.

4.3   Cryogenic setup

In this subsection we discuss some important aspects of the dilution refrigerator, the part of the measurement setup providing low operating temperatures for the circuits. The generated signals need to be filtered, attenuated and after interaction with the sample, amplified and routed back to the data analysis circuit at room temperature. The main design consideration for the wiring of a cryostat as shown in Figures 4.1 and 4.4 is to minimize the amount of heat and Johnson noise that reaches the sample, which requires careful

thermalization of all lines. At the same time the attenuation on the input side and the attenuation on the output side as well as the amplifier noise needs to be minimized to be able to apply large field amplitudes and ensure good signal to noise ratio during data acquisition respectively. It is also important to ensure that the heat loads at different stages of the cryostat do not harm its proper operation. Furthermore, high quality microwave frequency components, such as coaxial lines, connectors and circulators are required.

4.3.1 Dilution refrigerator

In order to perform experiments at $10 - 20$ mK, three new dilution refrigerators were installed, equipped and maintained by the *QuDev* team during the past 4 years. These include a conventional *Kelvinox 400HA* and a cryogen free *Triton 200* dilution refrigerator from *Oxford Instruments* and another cryogen free system *DR200* from *Vericold Technologies*. All of which are specified with a base temperature of < 10 mK which was confirmed by nuclear-orientation thermometry.

Prior to their installation sensitive vibration measurements with μg resolution by means of geophone sensors have been carried out. The suppression of vibrations is essential to reach ultra low and stable base temperatures, see Appendix A. Furthermore, measurements of the electromagnetic spectrum in the laboratory up to low GHz frequencies have been carried out in order to characterize the amount of parasitic e.m. fields that could possibly interfere with the experiments implemented later on. In the first test run, without the necessary wiring installed, we could reach a stable base temperature of <5 mK was reached in the Kelvinox 400HA. After the cables were in place a temperature of ~ 10 mK was typical.

For general principles of cryostat design and operation refer to [Pobell06], [Enss05], or [White02] and for rather technical details like pumping line layout and the necessary vacuum techniques, see Appendix A and [Roth76]. For the development of efficient vibration isolation of pumping lines [Richardson88] and [Kirk78] were very helpful, see also Appendix A.

4.3.2 Microwave input

We generate high power and high frequency signals at room temperature, but, according to Eq. (2.4) and typical values of κ, require only ~ -145 dBm (~ 10^{-18} W) for measurement and typically not more than ~ -60 dBm to drive qubit transitions with a Rabi period of a few nanoseconds. The necessary drive power depends on the qubit to charge gate line coupling via capacitor C_c, see Fig. 4.1. If the resonator input is used for qubit driving most of the drive tone is reflected and the necessary drive power therefore depends on the drive to resonator frequency detuning Δ_d, as discussed in Subsection 2.3.4. Typically we therefore use a fixed attenuation of -30 dB right after the measurement signal generation, RF in Fig. 4.1 a, as a protection and no room temperature attenuation on the qubit drive line, Spec in Fig. 4.1 a.

After generation and initial attenuation the microwave tones are routed to the cryogenic part of the setup using standard 50 Ω impedance semi rigid UT85 coaxial lines from *Rosenberger Micro-Coax* equipped with SMA connectors from *AMP*. SMA DC-blocks *8039* from *Inmet* are used to isolate the microwave generator device ground form the cryostat ground, see DCB's in Fig. 4.1 a. In fact every connection to the cryostat including the vacuum lines are DC isolated except for one single well defined grounding cable in order to

avoid the occurrence of ground loops. Standard SMA vacuum feedthroughs *34_SMA-50-0-3/111_NE* from *Huber and Suhner*, see Fig. 4.4 a, are then employed at the 300 K plate of the dilution refrigerator.

Also inside the fridge semi rigid coaxial lines were used. Each of them was bent at least once between every temperature stage such that the mechanical stress acting on the connectors is reduced. This can be a problem for long sections of cables and in particular if the inner and outer conductors thermalize differently.[2] Standard SMA connectors from *AEP* (male with dielectric) and *SGMC* (female without dielectric) were soldered according to the manufacturers connector mounting instructions. The cable preparation before soldering turned out to be a crucial point in order to achieve the connector specifications with typically less than 20 dB reflection (voltage standing wave ratio (VSWR) smaller than ~ 1.2) in the range from DC to 20 GHz. In Fig. 4.4 b a nicely stipped UT-85 stainless steel cable with a very smooth and flat stripped dielectric is shown. During soldering it was important to use not too much solder flux and evaporate it entirely during soldering, as residual solder flux can corrode the solder tin such that the connection breaks under the stress cause e.g. by thermal expansion of the cables. In the case of copper mantled cables even water based flux was used. This also helps to avoid electrical shorts induced by residual flux between the inner and outer conductor.

At GHz frequencies $1/f$ noise is usually a minor issue. In contrast, Johnson noise generated by the thermal motion of charge carriers in the conductor, is the dominant noise source at temperatures above 100 mK. The voltage noise power spectral density in this regime can be estimated to be linear with the temperature T and the resistance R as $S_{v^2}(\omega) = 4k_\mathrm{B}TR$. Since the required signal powers are very low, the most effective way to suppress thermal radiation is to attenuate the signal together with the noise. In order to reduce the room temperature thermal noise, at $\sim 300\,$K, down at liquid helium temperatures, at $\sim 4\,$K, it is therefore sufficient to install a cryogenic attenuator providing 20 dB, this is a factor of 100, of attenuation.

For the necessary attenuation between liquid He temperature and base temperature, the consideration with a linear temperature dependance is not valid anymore. For this section of wire the radiation spectrum of a one dimensional black body was calculated and analyzed, particularly the radiation in the frequency band the experiments are operated at. In order to suppress thermal radiation from temperatures higher than the base temperature, a 20 dB attenuator at 100 mK and at base temperature each were installed, see Fig. 4.1 a. For lower attenuation on the base plate of the cryostat slightly elevated cavity temperatures $> 70\,$mK were observed and characterized, see Chapter 10.

Even larger attenuations would on the other hand reduce the maximal field amplitudes and thus the minimal qubit Rabi rotation times achievable. If this was compensated with larger input powers, the resulting heat load due to dissipation at the base temperature attenuation may become an issue. Additional frequency dependent attenuation is provided by the coaxial cables, see Table 4.1, as well as the insertion loss of the connectors and other components.

---

[2]The linear thermal expansion coefficient of both stainless steel and copper is $\alpha_\mathrm{th} \approx 17 \cdot 10^{-6}\,\mathrm{m/(m \cdot K)}$.

4.3.3 Heat loads

In order to find a good tradeoff between low heat conductance and low electric loss different coaxial cables were employed, see Table 4.1. The used materials for ground / center conductor were low loss silver and tin plated copper / copper at room temperature (UT-85-TP), medium loss stainless steel / copper from 2.1 K to room temperature (UT-85-SS), which is typically only used on the signal output side, and relatively lossy stainless steel / stainless steel semi rigid cables (UT-85-SS-SS) for any connections between different temperature stages inside the dilution refrigerator. Connections within a given temperature stage are always made of the low loss coaxial lines.

Frequency [GHz]	UT85-TP [dB/m]	UT85-SS [dB/m]	UT85-SS-SS [dB/m]
0.5	-0.45	-1.02	-2.92
1	-0.64	-1.46	-4.13
5	-1.51	-3.33	-9.32
10	-2.21	-4.79	-13.26
20	-3.29	-6.94	-18.91

Table 4.1: **Cable attenuation.** Specified frequency dependent attenuations of one meter of semi rigid coaxial cable used in the experimental setup.

The signal attenuation method for thermal noise reduction only works if the coaxial lines are well thermalized with each temperature stage. In addition, every thermalization minimizes the heat load at the next lower temperature stage. Therefore, all cables are thermalized at every temperature with copper braces, see heat sinks indicated by symbol ⊣ in Fig. 4.1 a. Since the teflon dielectric in the coaxial lines has extremely low thermal conductance this only thermalizes the outer conductor. Therefore, the only points where the center conductor can be thermally anchored to the surrounding temperature is at the position of the attenuators, filters, amplifiers and circulators. Typical heat sinking of outer
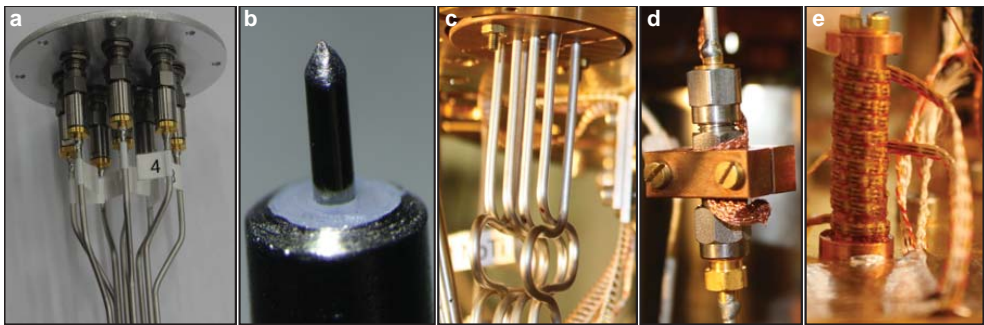
Figure 4.4: **Cabling and thermalization at cryogenic temperatures. a,** Eight cables mounted to the cryostat input port plate using vacuum feedthroughs. **b,** Stripped semirigid stainless steel cable prepared for connector soldering. **c,** Clamped and heat sunk cables inside the cryostat. Thermalization of the outer conductor using oxygen free copper braces. **d,** Thermalization of the inner conductor by heat sinking a connected attenuator using a copper clamp and braids. **e,** Heat sunk twisted pair loom glued to copper post with GE-varnish.

eight conductors and an attenuator by means of copper clamps and a solder flux free copper braid is indicated in Fig. 4.4 c and d respectively.

This cabling strategy was confirmed to be compatible with the typical maximal heat loads of the three fridges for up to 16 coaxial lines per cryostat. The total thermal heat load at every temperature stage was estimated by considering shield and center conductor separately, assuming every thermalization to be perfect and calculating the resulting total heat load with $\dot{Q} = A/L \int_{T_1}^{T_2} \lambda(T)\, dT$ where A is the cross section, L the length, $\lambda(T)$ the temperature dependent heat conductivity of the material and T_1 and T_2 the temperatures of the considered fridge stage and the next higher temperature stage without intermediate thermalization, respectively. Instead of explicitly integrating $\lambda(T)$ one can directly subtract two heat conductivity integrals $\Theta = \int_0^T \lambda\, dT$ given in W/m and available for example from *Lakeshore Cryogenics*, see also Ref. [Pobell06]. For typical combinations of temperatures mean values of $\bar{\lambda}(T_1, T_2)$ in W/(m·K) are also available and can be used without the need for integration, see Table 4.2 and Ref. [White02]. At very low temperatures the heat conductivity of pure metallic elements highly depends on small traces of chemical impurities and physical defects, therefore these values may vary quite a lot and are given in brackets. Typical cross section areas of the coaxial cable shield and center conductor were 1.6 mm^2 and 0.2 mm^2, respectively.

Material	300-77 K	300-4 K	77-4 K	4-1 K	1-0.1 K
do. copper	190	160	80	5	(1)
el. copper	410	570	980	200	(40)
st. steel	12.3	10.3	4.5	0.2	0.06

Table 4.2: **Thermal conductivities.** Temperature dependent mean thermal conductivities of phosphorus deoxidized copper (typically used for bars, rods and pipes), electrolytic tough pitch copper (typically used in spools of wire) and stainless steel (18/8) in W/(m·K), from [White02].

Typical values for the cooling power available at the different temperature stages, see Fig. 4.1 b, of the installed cryostat are $\sim 5 - 10$ μW at ~20 mK, typical ~ 400 μW at the 100 mK stage (specified), estimated 100 - 300 mW at the 1.5, 2.1 or 4 K stages of the Kelvinox, Triton and Vericold dilution refrigerators respectively. At the 4 K stage of the conventional fridge the cooling power is only limited by the maximal evaporation rate of liquid Helium and in the case of cryogen free systems the cooling power provided by the pulse tube cooler is 4 and 2 W respectively. Note that here also the twisted-pair copper wires, typically used for DC bias between room temperature and ~ 2.1 K, can contribute considerably to the total heat flow $\dot{Q}$.

4.3.4   DC bias input

The split transmon qubit transition frequency can be controlled by applying a magnetic field which threads a flux through the SQUID loop thus changing the phase difference across the two Josephson junctions, see Section 2.2. In our setup we make use of superconducting coils with large inductance to generate a constant offset flux bias and also on-chip flux lines for rapid flux bias changes on a typical timescale of 3-5 nanoseconds.

Due to field focusing effects and the large mutual inductance between the coil with inductance on the order of 0.8 H and qubit with loop sizes of up to 4x4 μm^2, currents of

some tens of micro amperes were sufficient to induce single flux quanta. We used a *Yokogawa* voltage source and an RC-filter with a 3 dB cutoff frequency of $<< 50\,\text{Hz}$ and a total resistance of 32 kΩ at room temperature to bias the coils, see Fig. 4.1 a top left. For details refer to [Bianchetti10a]. The voltage source output is differential and isolated in order to keep the cryostat on just one well defined ground.

The wiring between a home made breakout box and the superconducting coils was done with electromagnetically shielded twisted pairs and shielded connectors from *Lemo* at room temperature. Standard twisted pair looms made of copper, between room temperature and 2.1 K, and NbTi for temperatures below 2.1 K were employed inside the cryostat. Connections inside the cryostat were done using *micro sub-D* connectors. Resistive connectors are avoided in the low temperature part of the coil wiring to avoid heating. All wires were thermally anchored at every temperature stage by wrapping them around a copper post and fixing them with *GE varnish* (*C5-101*) from *Oxford Instruments*, see Fig. 4.4 e.

The on-chip flux bias lines are operated by applying short voltage pulses with a bandwidth of ∼ 500 MHz directly via one of the AWG outputs, see Fig. 4.1 a top left. The voltage translates to a current via the characteristic impedance of the circuit which is dominated by the 10 dB attenuator and the impedance of the transmission line. Once the current pulse I_fl reached the sample via the on-chip flux line, it passes by the qubit SQUID loop and induces a flux. Finally it enters the ground plane where it is dissipated on the PCB, see left inset in Fig. 4.2 a. For details of flux and charge line design refer to [Steffen08].

The flux line cabling and thermal anchoring is similar to the one used for the microwave frequency inputs. However, since large attenuation in DC bias lines would lead to heating, two *VLFX* 300 MHz low pass filters from *Minicircuits*, see Fig. 4.1 a, are used to suppress thermal noise at the relevant frequencies.

Several pulse imperfections have been identified and need to be corrected. First of all, occurring DC offsets on the order of up to ±10 mV deviation from 0 V need to be corrected by adding an external DC voltage to the active port of the AWG. A pulse shaping procedure was furthermore implemented in order to correct temporal distortions introduced by the AWG itself, the low pass filters, and the semi rigid coaxial transmission line connectors. The correct pulse modulation was inferred from a characterization measurement of the signal transfer function of the signal generating system at room temperature and without a sample. For details refer to Appendix A in [Bozyigit10a].

4.3.5 Microwave output

After interaction with the sample, signal powers corresponding to less than a single microwave photon energy per mean cavity photon lifetime are to be measured. In order to achieve their detection in the presence of thermal photons and amplifier noise, which is typically larger than the signal itself, any losses need to be minimized along the output line. An additional damping of the signal before the first amplifier by say −3 dB requires 4 times more averaging to realize the same signal to noise ratio (SNR), see [Pozar93].

In order to protect the sample also from noise that could enter the resonator from the output side e.g. input noise from the first amplifier, the signal is directed through two circulators from *Pamtech* or alternatively two isolators from *Raditech Inc.* In the case of the circulators one of the three ports is terminated with a well thermalized 50 Ω cryogenic termination, which makes the circulator acting similar to a one-way microwave valve. These

devices provide an isolation of typically 20 dB each in the reverse direction while transmitting the microwaves with only little loss of < 0.5 dB in the forward direction, see Fig. 4.1 a.

Due to the low loss requirements the cables between sample and the first amplifier were made of superconducting coaxial cables based on a Niobium-Titanium alloy. These have a very low electric loss below the critical temperature comparable to the UT-85 coaxial cables. In contrast to the copper cables there is almost no thermal heat conductivity through the superconductor however. Since these cables were not suitable for soldering, appropriate SMA connectors were crimped with the *Universal Compression Crimp Tool Kit* from *AMP*.

A good amplifier is the key hardware ingredient in order to be able to detect ultra low power signals. Together with a large gain, an ideal amplifier also provides a low noise temperature and a large dynamic range over a large bandwidth. High electron mobility transistor (HEMT) amplifiers offer a superb compromise of all these requirements. The InP HEMTs employed in our setup were manufactured by the *Sander Weinreb* group at *Caltech* and by the *Low noise factory* at Chalmers. These devices have a typical gain of 30 - 40 dB, a large dynamic range with a 1 dB compression point at ~ -10 dB and most importantly a characteristic noise temperature of only $\sim 2.5 - 4$ K in a bandwidth of typically $4 - 8$ GHz. The low noise amplifiers (LNA) are operated with a stable (< 10 mV) and carefully adjustable voltage supply (± 3 V) for drain and gate biases, which was made in house[3], see Refs. [Puebla08, Bolesch10] for further details.

An amplifier noise temperature of $T_a = P_n/(k_B B_n)$ with the noise power P_n and the relevant bandwidth B_n of only 2.6 K is specified for the HEMT amplifier, a value which is among the lowest one can obtain with conventional transistor based amplification techniques. T_a can also be thought of as the number of thermal photons n_a added at the input of an otherwise perfect amplifier expressed as a temperature via Planck's law in one dimension $n_a = 1/[\exp(\hbar\omega/k_B T_a) - 1]$. At typical microwave photon frequencies of 6 - 7 GHz this corresponds to adding 6 - 9 thermal photons before the amplification of signal plus noise by 4 orders of magnitude. For successful detection a cascade of amplifiers with a total amplification of ~ 14 orders of magnitude is required. The few noise photons at the output of the first amplifier are therefore amplified by almost another 100 dB.

For a chain of amplifiers the total noise temperature is given by Frii's law

$$T_a = T_{a,1} + \frac{T_{a,2}}{G_1} + \frac{T_{a,3}}{G_1 G_2} + ... \tag{4.5}$$

with the individual amplifier gain G_i and the noise temperature $T_{a,i}$ of the i's amplifier. For a sufficiently large G_1 the signal to noise ratio (SNR) which depends on the total T_a is therefore governed by the noise temperature of the first amplifier $T_{a,1}$ only. In fact, the effective system noise temperature relative to the resonator output port has been measured [Bozyigit10b] to be on the order of 17 K. This value is considerable larger than expected from the thermal occupation of the resonator field, which for the latest damping configuration is on the order of $T_r < 70$ mK, see Subsection 8.3.3 for a characterization of the background resonator field temperature. The larger effective noise temperature of the

---

[3]Note that the DC voltage source wiring resistance should not become a notable fraction of the amplifiers internal drain resistance in order to be able to source the intended source-drain and bias currents with the specified voltages that were optimized to give the minimal noise temperature.

amplification chain is therefore attributed to cable and insertion losses of 5.8 dB between the resonator output port and the low noise amplifier.

Due to Frii's law it is not necessary to be exceptionally worried about signal loss once the microwave tone has been amplified with the LNA. Standard lossy stainless steel coaxial lines and in some instances the medium loss copper/stainless lines are used to route the microwave tone back to room temperature. At the cryostat output plate another DC block isolates the experiment from the active components that follow, i.e. two *Miteq* amplifiers with a measured total gain of 59 dB. This gain includes an extra 3 dB attenuator for the reduction of reflections between the amplifiers as well as two filters from *Minicircuits* which form a bandpass that is positioned in between the two amplifiers in order to not saturate the second amplifier with noise in unused frequency bands. In Section 4.4 we review how the weak coherent measurement tone, which corresponds to only a few photons populating the resonator on average, is extracted from the noise dominated signal.

4.4 Data acquisition

All measurements presented in this thesis are measurements of the cavity transmission. Employing a heterodyne detection scheme [Walls94, Wallraff04] we can detect the measurement photons which are phase coherent with a local oscillator while averaging out all uncorrelated noise photons. In order to be able to fully analyze GHz frequency signals digitally, it is convenient to use analog down-conversion. We used the IQ mixer *IRM0408LC2Q* from *Miteq* in which the measurement signal is mixed with a separately generated phase coherent and phase locked local oscillator signal, see LO in Fig. 4.1 a. The LO signal is typically offset by ν_{IF} = 10 - 25 MHz from the measurement frequency, which allows for convenient digital sampling of the I and Q quadratures of the down converted signal at frequency ν_{IF}. After another stage of amplification with a *Minicircuits* amplifier (24 dB gain) the signal has an amplitude in the millivolts range. Another low-pass filter from *Minicircuits* is used to reduce high frequency noise and suppress aliasing by removing frequency components above the Nyquist frequency set by the data acquisition sampling rate [Bozyigit08, Lang09, Bozyigit10a]. After that, the down-converted measurement tone is digitized and averaged with an ADC data acquisition card, see Fig. 4.1 a.

The PCI acquisition board from *Aquiris* with a maximum sampling rate of 1 GS/s on each of two channels, has fast AD converters and an on-board FPGA hard-coded to average the acquired signals in real time. This is particularly interesting as it is extremely large amounts of data that can be acquired in very short time at the high sampling rates used in these experiments. When we make use of the provided averaging optimization, which is sufficient for studying ensembles of qubit states, the data transfer time becomes negligible compared to the acquisition time for numbers of averages $\gtrsim$1000.The architecture of the board and the available memory of 2 Mpoints (24 bit accumulation memory per channel), allowed for a maximum of 2^{16} averages at the full sampling rate, i.e. 1 GS/s per channel or 2 GS/s on one channel with a resolution of 8 bit. Alternatively an FPGA programmable *Xilinx Xtreme DSP* board was used [Bozyigit08, Lang09]. It only features a sampling period of 10 ns on two channels but can be programmed to perform arbitrary operations on the measurement data prior to averaging. This allows to very efficiently acquire and statis-

tically analyze large amounts of individual single shot measurements, required for single shot qubit readout and field tomography, see [daSilva10, Bozyigit10b].

Once the two quadratures are acquired we typically extract the phase and amplitude information of the transmitted measurement signal. For the case of a homodyne measurement, where the local oscillator is taken to be at the same frequency as the measurement signal, the analog hardware mixed the signal down to DC already. We can simply substitute the measured DC values of I and Q into the formulas Eq. (4.4) in order to determine amplitude and phase of the measurement tone. Homodyne measurement is the method of choice when high time resolution is required. The resolution is just limited by the sampling rate of the ADC board and the bandwidth of the IQ mixer, i.e. 500 MHz in our case. Every nanosecond we acquired a value for I and Q providing amplitude and phase. Such a procedure was implemented e.g. to precisely analyze the timing of our DC modulation pulses used for the up-conversion.

Although the DC signals are easy to handle they are much more prone to 1/f noise, slow drifts and offsets. For the regular measurements therefore, we realized a heterodyne data acquisition procedure with an IF frequency of typically $\nu_{\mathrm{IF}} = 10 - 25$ MHz. One can now think about using either one or both of the two quadratures to reconstruct amplitude and phase digitally. In order not to be that sensitive to offsets and imbalances in the IQ mixer or the rest of the amplification chain it turned out to be an effective method only to sample one of the two quadratures. This goes along with some reduction of bandwidth. While using both channels one is just limited by the bandwidth of the IQ mixer (similar to the homodyne acquisition), using only one channel means being limited by the chosen IF frequency. In a process called *single channel digital homodyne*, see [Schuster07a], we acquire and digitally integrate a full IF period of just one IF channel and extract the two Fourier coefficients given in Eq. (4.1) and Eq. (4.2), which in turn yields amplitude and phase using Eq. (4.4). In our case, with $\nu_{\mathrm{IF}} = 25$ MHz and the ADC sampling rate being 2 GS/s, we acquire a total of 80 data points yielding only one data point of amplitude and phase. The detection bandwidth is therefore set by the IF frequency with a period of 40 ns. This detection bandwidth is still larger than the typical cavity bandwidth $\sim \kappa$ and was therefore found to be appropriate for the experiments implemented in this thesis.

DESIGN AND FABRICATION OF JOSEPHSON JUNCTION DEVICES

In this section the design and the essential aspects of the thin film fabrication of superconducting transmon qubits are summarized. In addition, the fabrication of SQUIDS for parametric amplifiers is briefly discussed. Reasonable values for the desired Josephson energy are between 30 and 100 GHz in the case of qubits and above 1 THz for parametric amplifiers. Sub-micron ~ 150 nm x 150 nm to micron sized junctions with a tunnel barrier thickness of some atomic layers (1 - 2 nm) were fabricated with electron beam lithography and shadow evaporation and oxidation of aluminum thin films.

5.1 Qubit design

In order to be able to faithfully design and predict the qubit parameters prior to their fabrication and measurement a detailed simulation was carried out. While the charging energy E_C and the qubit / resonator coupling strength g basically depend on the geometry of the circuit only, the maximal Josephson energy $E_{J_{max}}$ depends exponentially on the thickness of the tunnel barrier and therefore requires some fine tuning and feedback from the fabrication process. In case of sufficiently small charging energies, i.e. when the junction capacitance C_J is only a small fraction of the geometric part of the transmon shunt resistance C_S, g and E_C can be designed independently of the required and fabricated $E_{J_{max}}$.

5.1.1 Charging energy and voltage division

Both E_C and the qubit-photon coupling g depend on the network of capacitances formed by the qubit and the resonator. We use the electrostatic solver provided in the software package *Ansoft Maxwell* to simulate a 3 dimensional model of our intended qubit design,

see Fig. 5.1 a. In such a model typically a box of size 500μm by 500μm by 500μm which contains the relevant parts of the chip is considered. The dielectrics and metals such as sapphire, vacuum and aluminum as well as different electrostatic potentials between 0 and 1 V are assigned to each independent part of the circuit. The circuit model effectively consists of only 4 electrodes, i.e. the two ground planes shown in blue, the resonator center conductor shown in red, the qubit reservoir shown in light blue and the qubit island shown in violet, see Fig. 5.1 a. The electrostatic solver then tries to find the capacitance matrix that contains all mutual capacitances C_{ij} between the four electrodes $i, j \in \{1, 2, 3, 4\}$ using finite element techniques.

Typical values such as the ones extracted for the circuit shown in Fig. 5.1 a are[1] $C_{12} = 25.8\,$fF, $C_{13} = 5.6\,$fF, $C_{23} = 27.7\,$fF, $C_{24} = 3.7\,$fF and $C_{34} = 6.7\,$fF. In contrast, the capacitance between the ground planes and the resonator center conductor C_{14} is typically in the low pF range. In this limit where $C_{14} \gg C_\mathrm{g}, C_\mathrm{S}$ one can verify that the reduced Cooper pair box network as shown in Fig. 5.1 c is equivalent to the full transmon network shown in Fig. 5.1 b by introducing the effective shunt

$$C_\mathrm{S} = C_{23} + C_\mathrm{J} \tag{5.1}$$

and gate capacitances

$$C_\mathrm{g} = \frac{(C_{34} + C_{13})(C_{24} + C_{12})}{C_{34} + C_{13} + C_{24} + C_{12}}. \tag{5.2}$$

The qubit charging energy is then simply given by $E_\mathrm{C} = e^2/(2C_\Sigma)$ with $C_\Sigma = C_\mathrm{g} + C_\mathrm{S}$. The voltage division

$$\beta = V_\Sigma/V_\mathrm{g} = C_\mathrm{g}/C_\Sigma \tag{5.3}$$

$$= \frac{(C_{12} + C_{24})(C_{13} + C_{34})}{C_{23}C_{24} + C_{13}(C_{23} + C_{24}) + (C_{23} + C_{24})C_{34} + C_{12}(C_{13} + C_{23} + C_{34})} \tag{5.4}$$

is the fraction of the voltage that drops across the junction V_J if the voltage V_g is applied between resonator and ground. For a systematic approach involving a full network analysis see appendix A in [Koch07a].

The qubit's ground to first excited state transition couples to a resonant photon with the vacuum Rabi frequency

$$2g/(2\pi) = 4\beta e\mathcal{V}\sqrt{\frac{1}{2}}\left(\frac{E_J}{8E_C}\right)^{1/4}\frac{1}{h} \tag{5.5}$$

where

$$\mathcal{V} = \sqrt{\hbar m\omega_r/(2C_\mathrm{r})} \tag{5.6}$$

is the resonator rms zero point voltage, $C_\mathrm{r} = \epsilon_\mathrm{r}\pi/(2\omega_\mathrm{r}Z_0)$ the effective resonator capacitance, $\nu_\mathrm{r} = \omega_\mathrm{r}/(2\pi)$ the fundamental resonator frequency, $Z_0 = 50\,\Omega$ the resonator impedance, $\epsilon_\mathrm{r} \approx 5.9$ the effective dielectric constant of the resonator and $E_\mathrm{J} \approx (m\nu_\mathrm{r} +$

---

[1]Note that the capacitance C_{14} obtained from such a simulation is not correct since only a small part of the resonator and ground planes is considered.
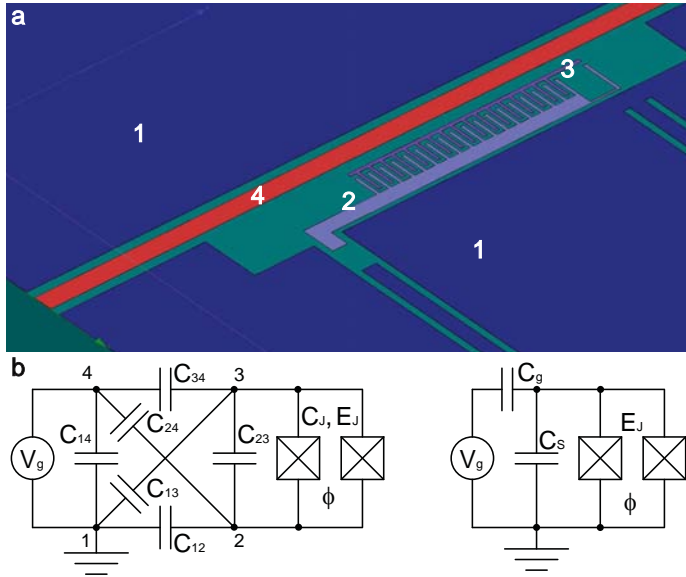
Figure 5.1: **Simulation for qubit parameter design. a**, Screen shot of an *Ansoft Maxwell 3D* electrostatic simulation of an exemplary qubit design. The four electrodes, i.e. ground (blue), reservoir (light blue), island (violet) and resonator (red) are assigned to the indices $i, j = 1, 2, 3$ and 4. **b**, Equivalent circuit diagram comprising all mutual capacitances. **c**, Reduced equivalent circuit diagram of the qubit, similar to the one shown in Fig. 2.4 c.

$E_C)^2/(8E_C)$ the Josephson energy of the qubit when in resonance with the resonator mode m, see also Sections 2.1 and 2.2.

We find very good agreement of this model and a number of fabricated and characterized devices by taking into account a capacitance of both junctions on the order of $C_J \sim 3 - 10\,\text{fF}$. The junction capacitance depends on the size and thickness of the junction and is therefore directly related to the chosen Josephson energy. This dependence could be integrated into our model for future device simulations. While the prediction of the charging energy is typically very accurate with an error of $< 5\,\%$, the predicted qubit coupling strength tends to be lower by $0 - 20\,\%$ compared to the actually measured values. The relative deviation between simulation and measurement is found to be increased for larger couplings. Despite a number of approximations in the presented simple model, i.e. reduced circuit model, finite element solving with a typical specified error of $< 2\%$ in the total energy, estimated junction capacitance, finite resolution in fabrication, analytic approximations of transition matrix element and transition frequency and simplified calculation of the resonator capacitance using an effective dielectric constant, it works sufficiently well for most applications of designing new qubits in the typical parameter range of the transmon and the Cooper pair box.

5.1.2 Josephson energy

The Josephson energy of the transmon E_J is in situ tunable by threading a flux ϕ through the DC-SQUID according to Eq. (2.11). The maximal Josephson energy $E_{J_{max}}$ obtained for

integer ϕ/ϕ_0 on the other hand is a junction property that very sensitively depends on its size, thickness and material. Numerous test junctions were fabricated under varying conditions and analyzed in order to optimize the fabrication parameters such that an intended Josephson energy can reproducibly be realized. In this section we point out the important relations to understand and control this qubit parameter.

According to Josephson's first relation [Josephson62], the DC Josephson equation

$$I_s = I_c \sin\varphi, \tag{5.7}$$

a tunneling current I_s of Cooper pairs flows through a thin insulating junction that connects two superconductors without an externally applied voltage. In Eq. (5.7) I_c is the maximal super current that the junction can support before it turns normal conducting and $\varphi = \varphi_2 - \varphi_1$ is the relative phase difference[2] between the two electrodes containing Cooper pairs in their lowest energy state each described by a single wave function

$$\psi(\mathbf{r}) = \sqrt{\rho(\mathbf{r})}e^{i\varphi_{1,2}(\mathbf{r})}, \tag{5.8}$$

with the charge density ρ and the individual condensates quantum phases $\varphi_{1,2}$. If a voltage is built up across the junction, the relative phase φ evolves in time according to the AC-Josephson relation

$$\frac{\partial\varphi}{\partial t} = \frac{2\pi}{\Phi_0}\,V, \tag{5.9}$$

with Φ_0 being the flux quantum $\Phi_0 = h/(2e) \approx 2.07 \cdot 10^{-15}\ \mathrm{Tm}^2$. After integration one obtains the voltage-phase relation

$$\varphi(t) = \varphi_0 + \frac{2\pi}{\Phi_0}\,V\,t \tag{5.10}$$

where φ_0 is an integration constant. Substituting Eq. (5.10) into Eq. (5.7) one observes that the Josephson-current is oscillating sinusoidal with amplitude I_c and Josephson-frequency

$$\nu_J = \frac{V}{\Phi_0}, \tag{5.11}$$

where 1 μV corresponds to about 500 MHz. The energy $h\nu_J$ represents the energy that is needed to transfer one Cooper pair across the junction.

Is the externally applied current lower than the critical current I_c there is no voltage drop across the junction, which means that there is in principle no energy dissipated in the contact. Nevertheless, there is energy stored in the Josephson-junction. In order to apply a current I_s that current has to be ramped up starting from $I_s = 0$. During this time the phase φ changes according to Eq. (5.7) hence giving rise to a voltage across the contact, Eq. (5.10). When integrating the product $\int I_s(t)V(t)dt$ over that time one obtains the Josephson coupling energy

$$E_J(\varphi) = E_{J_{max}}(1 - \cos\varphi), \tag{5.12}$$

---

[2]In the presence of external magnetic fields the gauge invariant phase difference needs to be taken into account here.

which denotes the energy due to the overlap of the two wavefunctions of the Cooper pair condensates and the Josephson energy

$$E_{J_{max}} = \frac{\Phi_0 I_c}{2\pi},$$ (5.13)

is directly proportional to the critical current I_c.

The critical current is a measure of how strongly the two phases are coupled through the tunnel junction. Accordingly, I_c is proportional to the area of the tunnel barrier A and it is useful to define the critical current density $J_c = I_c/A$. It can further be shown that J_c scales approximately exponentially with the insulator thickness d of a superconductor insulator superconductor (SIS) junction $I_c \propto e^{-d}$. The latter dependence is used to control the critical current in the fabrication process by changing the oxide layer thickness, see Section 5.2. Typical values of the fabricated devices lie between $I_c \sim 20$ nA, i.e. $E_{J_{max}}/h \sim 10$ GHz for the small qubit junctions of size 200 by 250 nm^2 and $I_c \sim 4$ μA, i.e. $E_{J_{max}}/h \sim 2$ THz for larger SQUID junctions of up to 2.5 by 1.5 μm^2 used for tunable resonators. The typical current densities are then in the range of 20 to 50 A/cm^2, for the 3 qubit experiments presented in Chapter 9 accidentally even up to 400 A/cm^2.

The temperature dependence of the critical current is given by [Ambegaokar63]

$$I_c R_n = \frac{\pi \Delta(T)}{2e} \tanh\left(\frac{\Delta(T)}{2k_B T}\right),$$ (5.14)

where R_n denotes the junction's electrical resistance in its normal state, T the temperature of the material and $\Delta(T)$ the superconducting energy gap. For $T \to 0$ the relation can be simplified as

$$I_c R_n = \frac{\pi \Delta(0)}{2e},$$ (5.15)

where according to BCS theory [Bardeen57] the superconducting energy gap is related to the critical temperature of aluminum $T_c = 1.176$ K as $\Delta(0) = 1.76 k_B T_c$. Using Eq. (5.15) and Eq. (5.13) we can therefore easily determine I_c and $E_{J_{max}}$ for $T \ll T_c$ simply by measuring the electrical resistance of the junction at room temperature

$$E_{J_{max}} = \frac{R_q}{R_n} \frac{\Delta(0)}{2}.$$ (5.16)

Here we have introduced the resistance quantum $R_q = h/4e^2$. Depending on the actual critical temperature of the material in use, we can estimate the Josephson energy expressed as a frequency in GHz from the normal state resistance in kΩ as $E_{J_{max}}/h \lesssim 140$ GHz kΩ/R_n.

In Fig. 5.2 we plot Josephson energy values obtained from qubit spectroscopy at a temperature < 20 mK, see Section 6.4, as a function of room temperature resistance (conductance) measurements obtained on nominally identical test chips fabricated simultaneously. A fit (red line) yields a conversion factor close to its theoretical value $E_{J_{max}}/h \approx 120^{+30}_{-20}$ GHz kΩ/R_n. The stated imprecision is indicated by blue lines. Experimental deviations from the expected superconducting gap energy have also been reported previously, see for example Refs. [Bouchiat98, Steinbach01, Court08] and references therein.
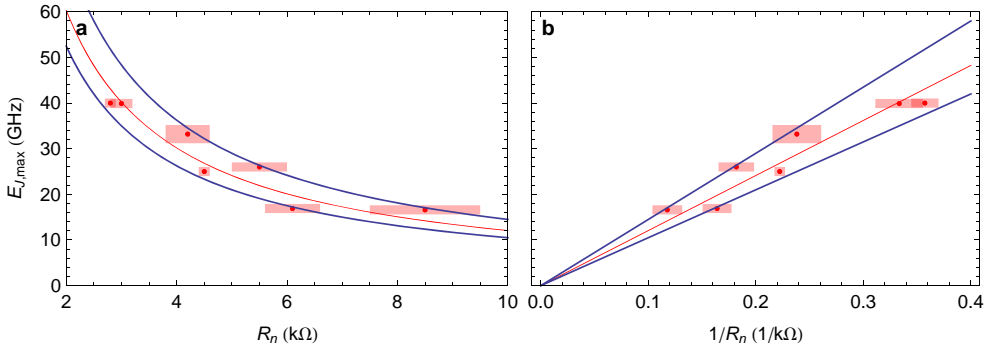
Figure 5.2: **Josephson energy versus normal state resistance (a) and calculated conductance (b).** Spectroscopically measured Josephson energies of seven qubit samples versus measured normal state resistances of seven test chips fabricated simultaneously (red dots). Junction aging, see Fig. 5.8, between the normal state resistance measurement and the qubit cool-down is taken into account in the shown data. The size of the error bars (red rectangles) is determined by statistical variations of the normal state resistances and Josephson energies on the same chip, imprecision of the available spectroscopy data as well as expected systematic imprecisions of the junction aging estimation and slightly varying junction sizes due to different lithography, development and substrate wavers.

5.2   Fabrication process

Qubit fabrication is a central cornerstone of experimental circuit QED. Reproducible device parameters and long coherence times can only be obtained with a robust and carefully conducted fabrication process. In this subsection we describe the fabrication of superconducting qubits with the main steps being chip preparation, electron beam exposure, development, thin film shadow evaporation, oxidation and liftoff. These steps are indicated in Fig. 5.3 and are discussed in detail in the following. For fabrication recipes refer to Appendix B. All described fabrication steps were conducted in the cleanroom FIRST at ETH Zurich.

5.2.1   Chip preparation

Chip cleaning

Similar to any other clean room process, it is important to start with a clean substrate. This is even more true for nano-fabrication of thin film Josephson junctions since their critical current can strongly be influenced by the surface roughness of the substrate. The qubit fabrication is the second major process step after photolithography and subsequent dicing, therefore the sapphire substrate surface can contain resist residues and debris which are difficult to observe optically without careful analysis, e.g. by means of an atomic force microscope. Our first step, which was found to improve the fabrication reproducibility substantially, is therefore to remove organic residues and photoresists in an O_2 plasma asher. This is followed by rinsing the chip with hot acetone and isopropanol in an ultrasonic bath, see Appendix B for details.

Resist deposition

The bilayer resist for electron beam lithography is spun onto the chip directly after the cleaning procedure. Due to very small chip sizes of ~ 2 mm by 7 mm and the relatively large resist thickness required, this can be a delicate issue. Before spinning, the chip is baked on a hot plate at 120°C in order to remove water molecules present in the cleanroom atmosphere. We use a pure copolymer of methyl methacrylate and methacrylic acid, or P(MMA-MAA) in short, thinned in 4% ethyl lactate as the first resist layer of thickness 630 ± 10 nm, see Fig. 5.3 a. This layer is very sensitive to direct, secondary and backscattered electron deposition during lithography. It is rapidly developed in isopropanol (IPA) and basically serves as a spacer between the substrate and the second resist layer allowing for a large undercut of up to $1 \, \mu$m to be realized, see Fig. 5.3 a-d. After spinning, the chip is baked for 5 minutes at 180°C on a hot plate.

This is followed by spinning a layer of low sensitivity but high resolution ploymethyl methacrylate resist with a large molecular weight of 950000 (PMMA 950k) on top of the copolymer. In order to improve the resolution, which can be limited by beam broadening due to secondary (forward scattered) electrons, a small thickness of only 115 ± 10 nm is used. The two layers are then baked for 15 minutes on a hotplate.

Exposed PMMA is developed using methyl isobutyl ketone (MIBK). It is not as sensitive as the copolymer, which in the end limits the speed of the exposure, but provides a much higher resolution and thus is used to define the geometry of the aluminum structures. The copolymer on the other hand is basically overexposed (and over developed) and therefore forms a large undercut of up to $1 \, \mu$m after development. The undercut size is controlled by choosing an appropriate exposure dose. Their combination therefore allows for the formation of free standing bridges necessary for the shadow evaporation technique.
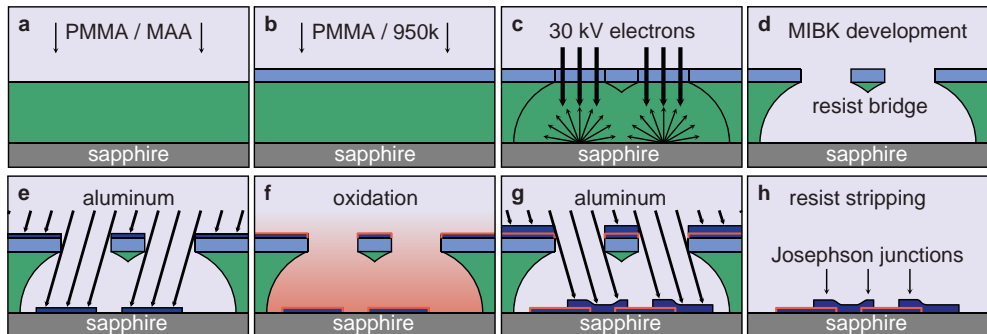
Figure 5.3: **Thin-film nano fabrication. a**, Copolymer of thickness 630 nm is spun on the sapphire substrate. **b**, After baking, a PMMA 950k layer of thickness 115 nm is spun on top of the first layer and post-baked. **c**, Electron beam lithography of qubits, junctions and SQUIDS using 30 kV electrons. **d**, Development of the exposed resist with MIBK in isopropanol (1:3). **e**, Evaporation of aluminum of thickness 20 nm at a growth rate of 0.5 nm/s at an angle of typically $0°$ to $-45°$ (from vertical direction). **f**, Aluminum oxidation with $Ar - O_2$ (85% - 15%) gas mixture for 1 to 30 minutes at typically 9 Torr. **g**, Shadow evaporation of aluminum of thickness 80 nm at a rate of 0.5 nm/s and at an angle of typically $20°$ to $45°$. **h**, Resist liftoff in 50°C hot acetone for 30 to 120 minutes. Figure adapted from [Göppl09].

In rare cases it can happen that the bottom layer does not adhere to the clean and smooth sapphire surface during spinning. To avoid this problem it turned out to be a good strategy to wait for 5 to 10 seconds between the resist deposition and spinning. Another solution would be slower spinning speeds and a more gentle spinner acceleration. This would however also affect the resulting edge bead which we tried to minimize by using relatively large spinning speeds of 3000 to 4000 rpm and short ramp up times. Typical edge bead widths are on the order of $500\,\mu$m. Much larger or smaller width indicate that the resist thickness is too large or too small. The substantial chip area covered by the edge bead is not used for subsequent electron beam lithography.

5.2.2   Electron beam lithography

In a positive resist electron beam lithography (EBL) process, patterns are formed through the photo scission of the polymer backbone by exposure to a beam of high energy electrons, see 5.3 c. In the subsequent development process the exposed lower molecular weight resist is removed chemically, see 5.3 d. In our qubit fabrication process we use the *RAITH150* electron beam writer providing electron energies of up to 30 keV. The relevant steps of EBL and the system specific parameters are described below.

Charge layer

Electron beam lithography on an insulating substrate such as sapphire can be problematic because the electrons deposited in the process of lithography can not easily escape from the exposed surface area. This causes local electrostatic charging effects which lead to distortions and shifts in the exposed patterns. We therefore deposit a 10 nm thick layer of aluminum on top of the double layer resist using an electron beam evaporator[3] from *Plassys Bestek*. This layer facilities the quick discharge of the deposited electrons during exposure. We furthermore contact the charge layer with the sample holder from the top using small copper clamps in order to assure a firm contact to ground. The lithography is not noticeably affected by the additional aluminum layer, as it is basically transparent for the 30 kV electrons used. Its use turned out to be very important in particular when sapphire chips without any previous metallization are processed. See Appendix B for a detailed chip preparation recipe.

File preparations

The geometry of the qubits, SQUIDS and test structures is drawn in the *RAITH* specific *GDSII editor* software[4]. A dose factor in the range of 3-5 is assigned to every square area in the designed structures where the total dose is the multiple of the dose factor and the chosen base dose of $100\,\mu$C/cm^2. The zero coordinate was typically taken to be the center of the on-chip alignment marks or the middle of the chip in case of empty test chips without a previous photolithography process. If alignment marks are available we make use of a semi automatic beam based write-field alignment. The positions of these marks, typically four crosses at the edges of a square of size 300μm by 300μm, need to be indicated, the RAITH software specific *layer 63* needs to be assigned to the squares indicating these

---

[3]In general it is not suggested to use an electron beam evaporator for this task since electrons and x-rays in the evaporation chamber could partly expose the resist. We did not find this an issue however.

[4]Certainly the geometries can also be imported from a different CAD software.

positions and finally, also the number of averages for the automatic alignment mark scan needs to be set in the geometry file.

For samples fabricated throughout this thesis no proximity correction was implemented. Instead, we make use of undercut boxes, i.e. additional areas exposed at a low dose of typically $100\,\mu$C/cm^2, in order to increase the undercut at that specific position if needed. The typical bridge dimensions of the fabricated transmon qubit samples are 100 nm by 200 nm which, depending on the exposure dose, leads to a single Josephson junction width of ~ 250 nm, see Fig. 5.4 f. The SQUID sizes were chosen between minimally 1 μm by 1 μm and maximally 4.5 μm by 4.5 μm, depending on the intended inductive coupling to coils and flux bias lines, see Fig. 5.5 d and e.

Dose tests
The ideal dose and the requirement of additional undercut boxes needs to be verified in a dose test series. The resulting structures can then be inspected using an scanning electron microscope (SEM) either directly after development or after shadow evaporation. A few typical examples of SEM imaged test Cooper pair box (CPB) like structures are depicted in Fig. 5.4. Panel a (and d) shows a developed CPB structure with nicely resolved edges corresponding to a well chosen exposure dose of typically 400 to 450 μC/cm^2 and a
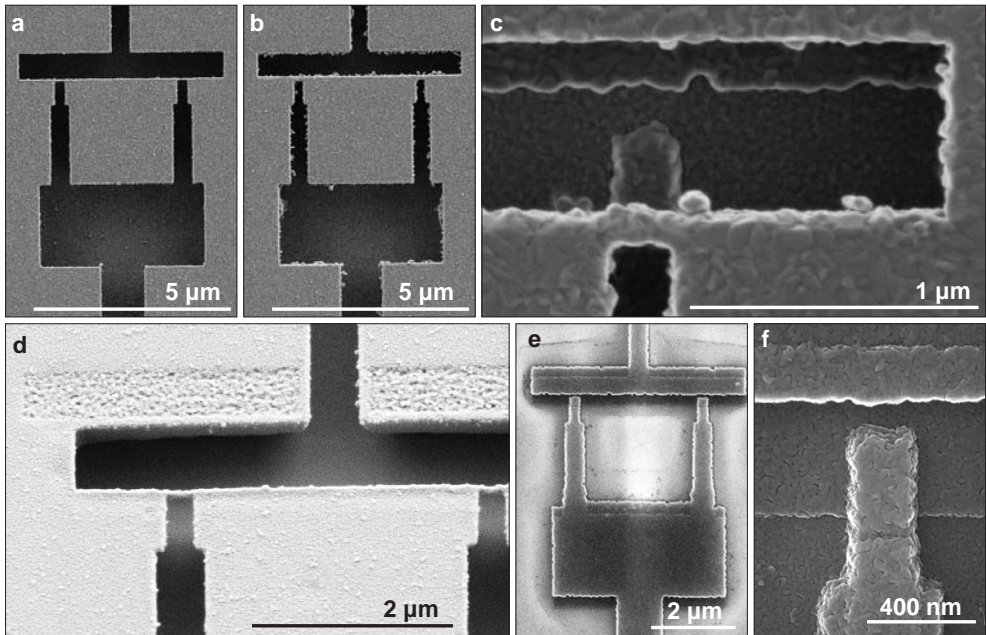
Figure 5.4: **SEM inspection of resist and junctions. a**, Developed resist exposed with appropriate dose. **b**, Developed resist exposed with too small dose. **c**, Exposed resist after shadow evaporation exposed with to small dose. **d**, Free standing bridges of the developed resist. **e**, Finished double layer aluminum structure after resist stripping (only panel imaged without the use of a charge layer). **f**, Single Josephson junction.

correct development time. Panels b and c on the other hand indicate the effect of a too low dose. In such a case the resist edges are not smooth which leads to rough aluminum edges after evaporation, see panel c. Additionally large amounts of resist residues can remain at exposed areas on the substrate. Panel d shows a nice example of developed resist imaged under an angle of 35°. Here one can see the two free standing bridges of width and thickness < 100 nm and length ∼ 300 nm. Also visible is the undercut box that was placed above the exposed vertical bar and leads to some additional resist surface roughness.

In case of a too large dose the undercut size increases and the bridge width shrinks until it becomes too fragile and breaks down, which results in a shorted Josephson junction. In panel e a CPB test structure after development, evaporation and resist liftoff is shown. The shadow, visible on the sapphire substrate in the vicinity of the evaporated aluminum, indicates the size of the undercut and is likely due to indirect (diffusive) deposition of aluminum during evaporation. In panel f a close up of one of the two well resolved Josephson junctions of size 250 nm by 300 nm is shown. Note, in all panels but panel e a 5 − 10 nm thin layer of aluminum was evaporated on the structures under 45° and rotation prior to their imaging in order to reduce electrostatic charging problems during SEM imaging.

Exposure preparations
Every qubit fabrication, see Fig. 5.5 a and b, was accompanied by the simultaneous fabrication of a monitor chip, see Fig. 5.5 c-e, of size 5 mm by 5 mm. This chip is used for initial focus and write-field alignment and most importantly room temperature Josephson junction resistance measurements to estimate the maximal Josephson energies.

Both chips are prepared identically and loaded on the waver sample holder. The resist on the surface of the test chip is scratched a few times close to one of its corners to facilitate focusing on the otherwise blank sapphire chip. The charge layer of both chips are contacted to ground using top clamps close to the edge of the chips. After the load lock is evacuated, the high voltage electron source is ramped all the way up to 30 kV and the 10 μm aperture is chosen, the previously saved electron beam optics aperture and stigmatism correction values are loaded and the write-field size of 500 μm^2 is set (720000 fold magnification). Next, the faraday cup positions used to measure the total beam current right before exposure are corrected and the lower left corner of the test chip is approached carefully with the laser controlled sample holder stage.

At this position the origin of the chip coordinate system is set such that $(U,V) = (0,0)$ corresponds to the center of the monitor chip. After a rough angle correction at the lower edge of the chip, an initial focussing step is performed on a suitable dirt particle or scratch. Aperture, stigmatism and focus need to be adjusted iteratively until features of size < 30 nm are easily resolvable. The edge of a larger dirt particle is a suitable feature in order to perform a number of manual stage based write-field alignments with increasing stage displacements and decreasing scan area sizes. In this procedure one and the same feature is scanned at three displaced positions of the stage by deflection of the electron beam. The resulting positions are then used to adjust the occurring shifts, zooms and rotations of the electron beam deflection coordinate system with respect to the stage or chip coordinates.

In order to further improve the electron beam optics the so called contamination dot technique is employed next. The coarsely focused beam is concentrated onto the resist
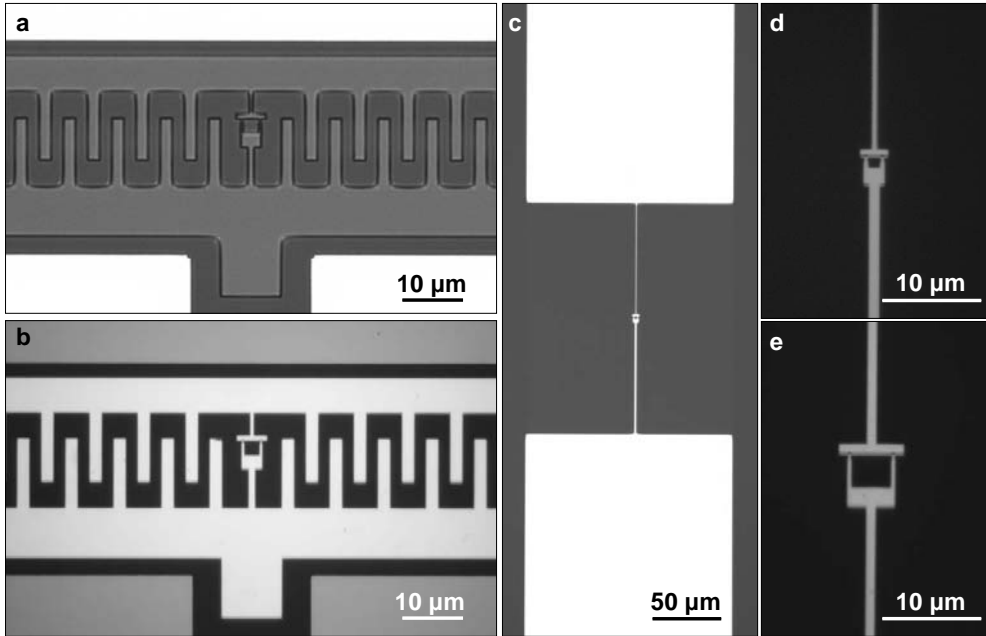
Figure 5.5: **Optical microscope inspection of resist, qubit and monitor chips. a**, Imaged resist after exposure and development of a typical qubit structure embedded in an aluminum resonator. **b**, Evaporated qubit structure after liftoff, embedded in a niobium resonator. **c**, Typical CPB test structure contacted to DC probing pads for 4 point resistance measurements. **d**, Enlarged view of the contacted CPB with a small (and large in panel e) SQUID loop.

surface for a short time, typically on the order of 5 seconds. Residual gas molecules are cracked by the incoming electrons and become visible as a circular dot on the resist surface. This dot is used as a reference point to further optimize focal length, astigmatism correction and aperture alignment until a circular dot of size $\leq 30\,\text{nm}$ is obtained. The contamination dot should be burned in the vicinity of the planned exposure region, typically $200 - 300\,\mu\text{m}$ away. Any sort of imaging of the exposure region or other critical areas like resonator gaps needs to be avoided however.[5]

Once the beam and stage coordinate systems are aligned and the beam properties are optimized, the exposure dose needs to be calibrated before the exposure is initialized. This is done by focussing the beam to the closest Faraday cup and measuring the total flux of deposited electrons. Typical beam current values are $27\,\text{pA}$ and $5\,\text{nA}$ for the two used apertures of size $10\,\mu\text{m}$ and $120\,\mu\text{m}$. The intended area dose D as a function of the beam current I_b is given as

$$D = \frac{I_\text{b} T}{S^2}, \tag{5.17}$$

---

[5]In the presence of charging effects or in case the resist was spun already a few days prior to its exposure, such that the out-gasing of solvents is reduced, it can be very hard to obtain a high quality contamination dot with good visibility. In such a case it often helps to try to burn dots at various different coordinates of the chip. If this does not help the charging layer, its grounding or the resist itself need to be checked.

where T is the exposure time or dwell time. The exposure area given as the square of the step size S is typically chosen to be a single pixel, i.e. $S \sim 8\,\text{nm}$ for the chosen write-field of size $500\,\mu m$. The typical beam speed given as $v = S/T$ is then on the order of $v \sim 3.5\,\text{mm/s}$ with a dwell time of $T \sim 10\,\mu s$. Large features such as the DC probing pads were exposed with the large $120\,\mu m$ aperture, see pads of size $150^2\,\mu m^2$ Fig. 5.5 c. Here the step size was chosen to be up to 19 pixel, i.e. $S \sim 150\,\text{nm}$ and although typically the dwell time should not be much shorter than a microsecond and the beam speed should not exceed about 10 mm/s, we went up to 70 mm/s of beam speed in order to minimize the writing time of these particularly simple and coarse structures.

Exposure

The geometries prepared in the *GDSII editor* need to be organized in a position list where the size of the working field is typically set to be the size of the write-field (if no stitching is needed). Furthermore we define which layer will be exposed and at what UV coordinates the given structure should be centered at. On the test chip we usually create a position list with 16 evenly spaced copies of the contacted junction test patterns as shown in Fig. 5.5 c. First the CPB patterns are exposed. This is followed by a change of aperture and without any further focusing steps the square shaped DC probing pads are written. Note, that the beam current needs to be measured and the dwell time as well as the step size need to be adjusted when the aperture is switched.

Some of the exposure details have been adjusted in order to improve the stabilization of the beam during exposure on the insulating substrate. We introduced a waiting time of 20 ms during which the beam is blanked between each primitive (each box). Additionally a flyback factor of 0.15 was set. It defines the settling time between each written line as multiple of the waiting time and the flyback factor. Also the dynamic compensation of beam drag effects was turned on. All other exposure settings are chosen as recommended in the *RAITH manual*. The typical writing time for the monitor chip is on the order of an hour.

The subsequent exposure procedure of the actual qubit sample is very similar to the one already described. One difference is that we need to carefully align the qubits with respect to the resonator. Therefore after the rough origin and angle correction at one of the chip corners a careful 3 point alignment on three far separated outer alignment marks is carried out in order to align the stage and chip coordinates. In particular if the resonator (and the alignment marks) are made of an aluminum thin film it can be very difficult to find the first alignment mark due to the low atomic weight aluminum compared to the usually used niobium [6]. Independent of the material it is crucial to have a good knowledge where to find all required marks such that no critical parts of the chip are exposed accidentally. It also helps to have determined the focus and beam correction settings already on the test chip. These are typically not changed when switching to the resonator chip which is of the same thickness.

Once the chip alignment is finished, the contamination dot technique is employed again. This time it is carried out directly on one of the inner alignment marks which are centered at the corners of a square of size $150\,\mu m$ that is centered at the qubit cutout. This

---

[6]Initial alignment could also be done using 10 kV electrons in case the visibility is too low. This was not required for the work described in this thesis however.

is reasonable since the alignment marks are on the same focal plane as the qubit gap (no metallization). This time typically only a few adjustments are required in order to burn a circular dot of diameter $\sim 20 - 30$ nm.

Before the exposure is initialized, an additional and more accurate beam based write-field alignment is performed. In this version of beam calibration the electron beam scans three different inner alignment marks which allows to adjust for remaining small rotations, zooms and shifts between the chip coordinates and the beam deflection coordinates, without moving the stage. In practice this last alignment step is done by duplicating the qubit pattern in the position list two times. For the first two copies we set the RAITH specific layer for alignment marks (*layer 63*) as the exposure layer. Once the exposure is started first the alignment marks are scanned and manually corrected. This is done at least twice and directly followed by the exposure of the actual qubit pattern.

Fabrication of large junctions

Large SQUIDs and SQUID arrays for parametric amplifiers, see Fig. 5.6, are prepared, exposed and developed similar to the qubit and test chips presented earlier. In order to achieve large junction areas (and larger Josephson energies) the free standing bridges need to be longer however. This requires some extra tests in order to assure their mechanical stability. We have found that a bridge width to length aspect ratio of 1 to 10 is possible but starts to become problematic. If the bridge width on the other hand is chosen too large,
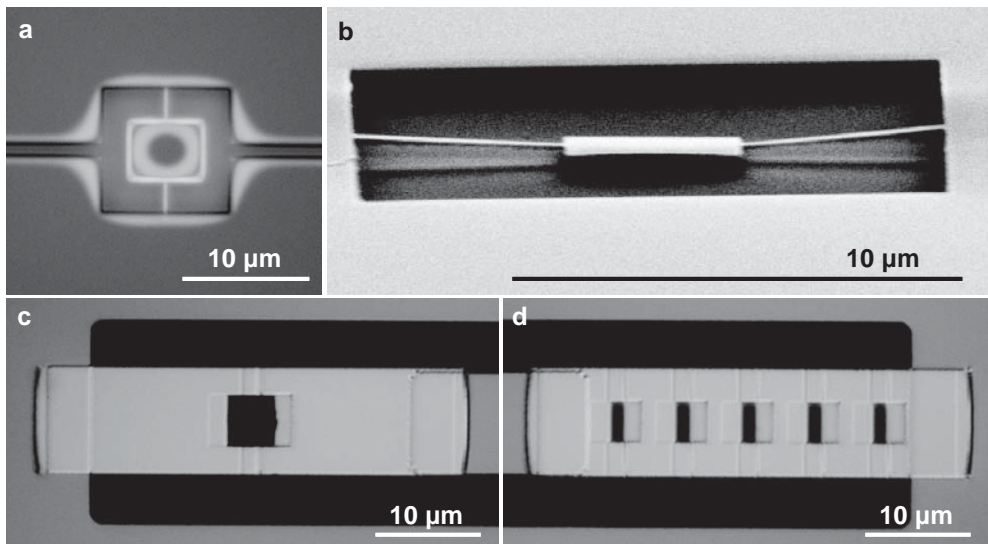
Figure 5.6: **Optical and SEM images of SQUIDs and SQUID arrays used for parametric amplifiers. a**, Optical image of developed resist for a DC measurement test SQUID. White areas indicate the region of the undercut. **b**, SEM picture of developed resist for a very large test SQUID imaged under at an angle of only 15°. The two free standing bridges have the dimensions of $4.5\,\mu$m by ~ 300 nm by ~ 110 nm (exposure dose $300\,\mu$C/cm^2). **c** and **d**, Differential interference contrast microscope images of a single SQUID (c) and a SQUID array (d) contacting the short end of a $\lambda/4$ resonator, thus forming a parametric amplifier that can be operated in reflection.

typically > 400 nm, the resist directly below the bridge is not entirely cleared off during development. Free standing bridges of up to 4.5 μm length and ~ 300 nm width (exposure width of 400 nm) and minimal SQUID loop sizes of 2.5 μm by 4.5 μm have been fabricated, see Fig. 5.6. An extreme example is depicted in Fig. 5.6 b where the entire support structure, i.e. the resist SQUID loop, is lowered due to a too large undercut. Such a change in distance from the substrate in combination with the large evaporation angles of $\pm 45°$ used for these SQUIDs can lead to trapezoidal Josephson junctions.

The images in Fig. 5.6 b and c have been obtained using the Nomarski prism. This enables to see also the lower aluminum film and therefore the overlap and size of the junction area (area between the two faint vertical lines). The optimal dose was found to be somewhat lower than for the typical qubit designs, i.e. ~ 300 μC/cm^2 in contrast to the usually used 350 − 400 μC/cm^2, which is expected due to the proximity effect.

5.2.3   Development

After electron beam exposure the aluminum charge layer is removed using sodium hydroxide (NaOH) solved in water (10 %). The aluminum etch is stopped after about 30 seconds by rinsing the chip in water. After very carefully blow drying the chip with the nitrogen gas (N_2) it is useful to check if all aluminum is removed. Optionally one can already check the exposed structure in the optical microscope. Here it helps to use the Normarski prism for differential interference contrast microscopy which is most sensitive to the slightly different optical depth of the exposed resist. In the second step the bilayer resist is developed using a mixture of MIBK:IPA (1:3) which provides a very high selectivity, i.e. low sensitivity (high resolution, low throughput) of the PMMA layer and high sensitivity (low resolution, high throughput) of the copolymer layer. After 50 seconds of careful moving in the developer the exposed resist is removed and the copolymer typically shows an undercut on the order of 500 nm or more, see Figs. 5.3 d, 5.5 a and 5.6 a.

If the undercut is too large it limits the lower bound of attainable SQUID sizes and similarly thin structures like the gaps between the transmon finger capacitors. In such a case it was found to be most useful to reduce the electron beam area dose in the vicinity of these structures. The PMMA development is stopped by rinsing in IPA for 10 seconds and blow drying with the N_2 gun.

5.2.4   Shadow evaporation and oxidation

The shadow evaporation technique is an established process known and used for many years [Dolan88]. It still remains the most suitable process to obtain nanometer sized Josephson junctions but requires some extra care to obtain reproducible results. Figure 5.3 e-g captures the essentials of the process.

Equipment

We use an electron beam evaporator *MEB550* from *Plassys Besteck* for our process. If maintained properly it features a stable evaporation and deposition rate of high purity aluminum (5N) in the range between 0.2 and at least 1 nm/s. The load lock is separated from the main evaporation chamber which reduces pump down times considerably and allows for a controlled oxidation without breaking the chamber vacuum. The load lock can controllably be vented with N_2, O_2, *Ar* and a gas mixture of argon and oxygen up to

a chosen constant pressure or flow rate. The sample holder can fully automatically be rotated (360° from arbitrary zero) and tilted ($\sim \pm 60°$ from load, etch or deposition positions) during and between evaporations. Amongst others the machine also features an ion gun source for milling oxides and cleaning substrates.

Preliminary steps
The first step is to mount the sample together with the monitor chip with the resist bridges well aligned in the center of the specially designed sample holder. The sample holder is then mounted in the load lock and rotated such that the resist bridges are well aligned with the tilt axis of the sample holder stage. The rest of the process is largely automated by writing evaporation recipes. Typically it contains the following steps.

The load lock is pumped down to pressures $< 2 \cdot 10^{-6}$ Torr in approximately 30 minutes. Then the chamber and load lock are switched to process mode where the pneumatically controlled valve between them is opened and the load lock pressure is further reduced to $< 5 \cdot 10^{-7}$ Torr supported by the cryogenic chamber pump. The time for pump down is limited by the amount of humidity that is acquired at the load lock surfaces. It therefore strongly depends on the time the load lock was kept open. In order to improve the reproducibility of the junction oxidation we then purge the ArO_2 stainless steel line connecting the pressurized gas bottle with the load lock by venting the load lock with ArO_2 gas up to a pressure of 10 Torr which is again followed by the same pump down procedure.

If an electrical contact between the resonator and the aluminum layers forming the SQUID is required, such as in the case of the parametric amplifiers shown in Fig. 5.6 b and c, a short ($\pm 45°$, 4 seconds each) and intense (500 V beam voltage / 5 mA beam current, 40 V acceleration voltage, 35 V discharge voltage) use of ion gun milling in a flow controlled 3.8 sccm Ar atmosphere (chamber pressure $5 \cdot 10^{-5}$ Torr) was used to partly remove the niobium oxide layer of the resonator surface. Since the etch rate of PMMA is substantially larger than the oxide etch rate, longer milling times have been found to collapse the resist bridges. Although it is unlikely that a substantial part of the niobium oxide (or resist scum) is removed during such a short etching time, this process has been found to reliably establish a DC contact. Without the ion milling treatment on the other hand a DC contact could not be established.

In the standard qubit fabrication process no such surface treatment was typically used. In principle it would however be advisable to use one of the established descumming techniques such as O_2 plasma ashing, UV ozone cleaning or ion milling[7] at this point in order to improve the quality and reproducibility of the Josephson junctions. It has furthermore been shown [Koppinen07] that plasma ashing can reduce the effect of junction aging, see Subsection 5.3.2. The effect on coherence times of qubit samples would need to be checked however after different treatments. While all of these techniques have been tried at least once, no conclusive results could be obtained concerning their compatibility and usefulness. A more systematic analysis needs to be done in order to determine process parameters that reliably improve the substrate surface without harming any of the fragile and thin resist bridges. A moderate O_2 plasma ashing for 10 s at 50 W or a more intense ashing in combination with wider resist bridges > 100 nm would be reasonable starting points for further improvements.

---

[7]The latter two can be done directly inside the evaporator just before evaporation.

Deposition and oxidation

After these preliminary steps the material *Alpure*, this is the aluminum supply reserved for qubit evaporations only, is selected by rotation of the crucible stack. The electron gun is switched on and operated at a constant voltage of ~ 9.5 kV. Then the beam current is slowly ramped up to 100 mA where it stays for about one minute in order to slowly heat up the aluminum and also to manually fine tune the alignment of the electron beam to the center of the material. The chosen beam pattern is simply a single point at a medium gain setting of 15, a number which is proportional to the beam spot size. This is most appropriate for a stable evaporation of aluminum which melts before its evaporation. After heating, the beam current is ramped up to typically $280 - 300$ mA.

At this point we measure the deposition rate by tracking the resonance frequency of a crystal oscillator which slightly changes its mass and resonance frequency of ~ $5 - 6$ MHz during deposition. In order to obtain an accurate rate, the specific weight of the material and the tooling factor, which depends on the specific geometry of the crystal mount position, needs to be determined and calibrated. A software based *PID controller* is employed to feedback control the rate to typically (0.5 ± 0.05) nm/s. Then the substrate shutter is opened and a counter integrates the acquired film thickness until the target value of typically 20 nm or 15 nm for the first aluminum layer is reached. In the case of qubit fabrication this layer is deposited under an angle of $0°$ from the direction perpendicular to the chip surface. In case of large junctions used for parametric amplifiers a deposition angle of up to $-45°$ and thicknesses of up to 30 nm are used to compensate the angle dependent deposition rate, see Fig. 5.3 e.

The static oxidation is initialized by closing the valve between chamber and load lock followed by controlled venting of the load lock with a gas mixture of 85% argon and 15% oxygen.[8] The gas inlet pressure is adjusted to about 0.5 bar at the bottle overpressure valve and subsequently reduced with a needle valve such that the chosen load lock pressure of 9 Torr is reached within about 1 minute. At higher gas inlet speeds the final oxidation pressure is not reliably met and at even lower speeds the inlet and pump out times become a substantial fraction of the total oxidation time. The critical current of the fabricated junctions is then controlled by choosing oxidation times in the range between 2 minutes (parametric amplifiers) and 30 minutes (low transition frequency qubits).

It is important to note that the typically employed pirani/penning pressure gauges are calibrated for gases of molecular mass similar to that of air, i.e. O_2 and N_2. This gives a nonlinear dependence for other gases like *Ar* particularly in the range of pressures > 1 mbar where the pirani gauge relies on the thermal conductivity which is reduced for heavier molecules. Instead, an absolute pressure gauge based on the capacitance measurement of a membrane, a *Baratron gauge*, calibrated for arbitrary gases up to 10 Torr is employed.

After the oxidation the pump down procedure is started again. This is followed by tilting the sample holder to the opposite angle, i.e. $+20°$ or $+45°$ for qubits or paramps respectively. Then the second aluminum layer of thickness 80 nm or 85 nm is deposited, see Fig. 5.3 g. Again, in case of large evaporation angles this thickness is increased to ~ 150 nm to compensate the angle dependent deposition rate. One reason for choosing the

---

[8]The reduced oxygen partial pressure of the gas mixture allows for longer oxidation times for a given Josephson critical current. This decreases the effect of slightly variable gas inlet and pump down times and avoids the danger connected with pumping pure oxygen.

first layer substantially thinner than the second is that this way the top layer thickness does not substantially vary at the transition from substrate to aluminum overlap, see Fig. 5.4 f. Secondly, for very thin films on the order of 15 to 10 nm, the superconducting gap energy is expected to be modified which would enable to engineer quasi-particle traps [Court08]. If the gap energy of the superconducting qubit island could be increased, tunneling of quasi particles from the reservoir would be suppressed. Such an effect of the film thickness on qubit coherence times could be studied in the future.

Directly after the second aluminum deposition the load lock is vented with pure oxygen up to 10 Torr and the aluminum structure is oxidized for 15 minutes. This step is intended to generate a uniformly distributed passivation layer of clean aluminumoxide on top of the structure before the sample is exposed to atmosphere.

5.2.5   Resist stripping and liftoff

When the thin film aluminum shadow evaporation is finished the remaining resist needs to be stripped from the sapphire chip. We used the least invasive technique based on hot (50°C) acetone only. Due to the large undercut and a comparably large resist thickness this usually works quite well. In order to facilitate the aluminum layer liftoff we mount the sample surface vertically in a teflon mount and use a stirrer with ~ 300 rpm rotation speed to move the acetone across the chip surface. After 1-2 hours a clean acetone filled pipette was used to carefully blow off the aluminum layer. Ideally the film lifts off in one piece only.

Before the chip is dried it is necessary to check that all aluminum came off, in particular it needs to be checked if the SQUID centers stripped properly. It is difficult to remove residual metal once the chip is dry. Therefore the chip is placed in a shallow vessel filled with some IPA and placed under the optical microscope.[9] After rinsing in IPA and blow drying, the chips are ready for inspection[10], optical microscope imaging, bonding and measurement at cryogenic temperatures. See Figs. 5.4 e, f, 5.5 b-e and 5.6 c, d for finished Josephson junction devices and refer to Appendix B for more details of the process. The monitor chip on the other hand is now ready for DC junction resistance measurements in order to determine the junction critical currents and their scatter.

5.3   Room-temperature characterization

5.3.1   DC resistance measurements

We use the DC prober *PM8* from *Karl Süss* in order to determine the room temperature resistance of DC contacted test Josephson junction SQUIDs, see Fig. 5.5 c-e. The four point

---

[9]Problems with this liftoff process typically indicate an issue with either the resist layer or the exposure details. Most likely it is a too large exposure dose that leads to large undercuts such that part of the top resist layer collapses. In case the liftoff problem is only marginal, residuals of the metal film can be removed using short periods (1-10 s) of ultrasonic power (power level 2) in an acetone bath. Note however that this procedure can potentially lift off parts of the qubit from the sapphire substrate.

[10]While SEM inspection has been found to be a harmful for the Josephson junctions, O_2 plasma ashing did not affect the room temperature resistance of a set of fabricated test junctions. Such an additional cleaning step could be useful to remove resist residues in the vicinity of the junctions that could possibly harm the energy relaxation times of the qubits. There is however no final conclusion about the effectiveness of such a process step yet.

measurement is done by carefully placing two probe needles on each probing pad of size 150 by 150 μm^2. The current voltage characteristic is then determined by supplying a current between 10 nA and 60 nA and measuring the voltage drop across the junctions. From a linear model fit we extract the junction resistances R_n in the low $k\Omega$ range. One of the test structures is fabricated with shorted junctions in order to extract part of the measured resistance which is not due to the junctions. Additionally the shorted test structure is useful to bring the four probe needles on the same potential before the actual junctions, which are very sensitive to voltage discharges[11], are measured. In order to be able to measure the much smaller resistance of these shorted junctions and also of the large critical current junctions used for parametric amplifiers, larger currents of 1 μA to 6 μA are supplied. As a rule of tumb the measurement currents should not exceed the critical current of the Josephson junctions.

Figure 5.7 depicts the results of a series of resistance measurements on a typical set of chips that have been fabricated over the period of four month. Each of these chips contains up to 12 double junction test structures and was oxidized for a variable time τ_{oxi} between 7 and 30 minutes. All junctions were approximately of size 0.05 μm^2 each and oxidized at a pressure of 9 Torr in the argon-oxygen gas, see Subsection 5.2.4. We observe a monotonic increase in the normal resistance for larger oxidation times. The error bars indicate the statistical error of the mean value of all test structures on a single chip. The red line in Fig. 5.7 a is an empirical nonlinear model fit

$$R_n(\tau_{oxi}) = A(\tau_{oxi} + \tau_0)^{2/3}, \tag{5.18}$$

with $A = 0.534^{+0.06}_{-0.03}\,\mathrm{k\Omega/min}^{2/3}$ and $\tau_0 = 1\,\mathrm{min}$ accounts for the gas inlet and pump out times. The accuracy and reproducibility is expected to be limited by variations in the junction size which is directly proportional to R_n and therefore A. The blue lines in Fig. 5.7 a indicate the confidence region due to changes in A. The normal resistance R_n is related to the maximal Josephson energy of the SQUID via Eq. (5.16), see Fig. 5.7 b. Using Eq. (2.15) we show the expected qubit ground to excited state transition frequencies for typical charging energies in Fig. 5.7 c. According to these measurements the expected reproducibility is on the order of $\nu_{ge} \pm 500\,\mathrm{MHz}$.

5.3.2   Junction aging

The results shown in Fig. 5.7 have been obtained by measuring the normal state junction resistance within one hour after evaporation and liftoff. Once at atmosphere the Josephson junctions are found to slowly increase their normal state resistance over time, an effect which is called junction aging. There is at least two possible mechanisms responsible for this kind of effect. First, the junctions are expected to oxidize further when they are exposed to air, in particular at the circumference of the formed junctions. The significance of such a process is therefore dependent on the area to circumference ratio of the junctions. In such a scenario it would be expected that junctions with a close to saturated oxidation layer, i.e. low critical current density and low Josephson energy, should age slower compared to very thin junctions. This type of aging can easily be stopped by storing the finished samples e.g. in an evacuated or oxygen free environment [Nahum93].

---

[11]In order not to damage the junctions, it is furthermore suggested to not turn on or off the prober light source, or alternatively not to use it at all during the measurements.
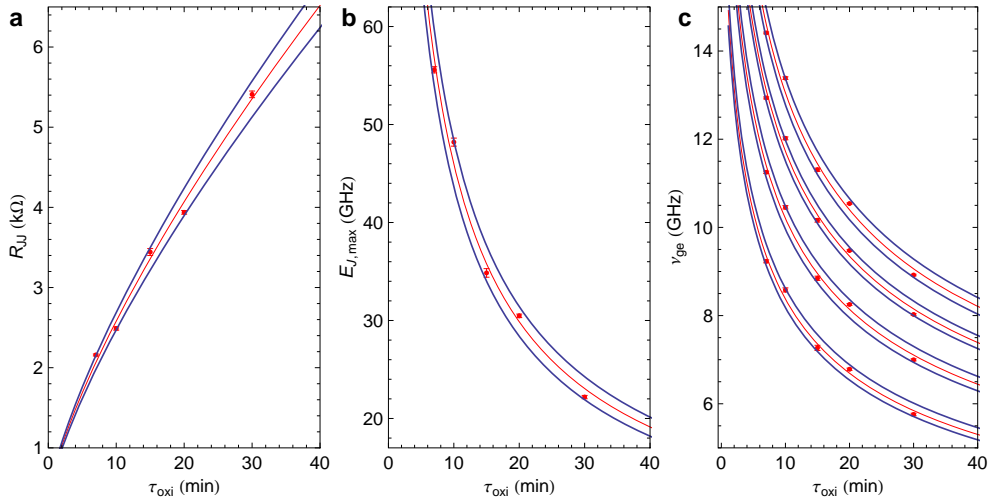
Figure 5.7: **Transmon Josephson junction oxidation measurements. a**, Measured normal state resistance of up to 12 double junctions of approximately equal size (0.05 μm^2 each) on 5 different chips and error of the plotted mean value. Each chip was oxidized for variable time τ_{oxi} at 9 Torr using argon oxygen gas. The red line is a nonlinear model fit to Eq. (5.18) and the blue lines indicate the region of expected reproducibility. **b**, Calculated Josephson energies using Eq. (5.16) (conversion factor of 120) with fit and expected variation. **c**, Calculated qubit transition frequencies using Eq. (2.15) for typical charging energies of 200, 300, 400 and 500 MHz (from bottom to top), a fit in red and region of expected reproducibility between the two blue lines.

There is however a second mechanism that could be significantly contribute to the observed post oxidation aging process. It is believed that the AlO_x barrier that is formed during fabrication is rich of oxygen and only slowly relaxes to the stable Al_2O_3 by a diffusive mass transport from the oxygen rich surface to the underlying aluminum [Jeurgens02]. Such a process would depend on the sample temperature and a stabilization of junction resistances has indeed been achieved by annealing the junctions at temperatures above 350°C in vacuum [Koppinen07]. Another approach to reduce the effect of aging is to use a double oxidation scheme [Holmqvist08]. In order to suppress changes on existing samples, storage at liquid nitrogen temperatures should stop such a diffusive aging process.

We also observe the effect of aging and find good agreement with a simple square root dependence

$$R_n(\tau_{age}) = R_{n,0} + \alpha_{age}\sqrt{\tau_{age}}, \tag{5.19}$$

for the same 5 test chips, see Fig. 5.8 a and b. τ_{age} denotes the time between fabrication and measurement and $R_{n,0}$ is the initial normal resistance measured directly after the liftoff process shown in Fig. 5.7. The longest time scale aging measurement was done 3 month after fabrication. This measurement could also be explained reasonably well using Eq. (5.19). For even longer times we would however expect a saturation of the oxide layer thickness and therefore a slow down of aging. The extracted α_{age} are plotted in Fig. 5.8 c. We find that the rate of post oxidation α_{age} increases approximately linearly with
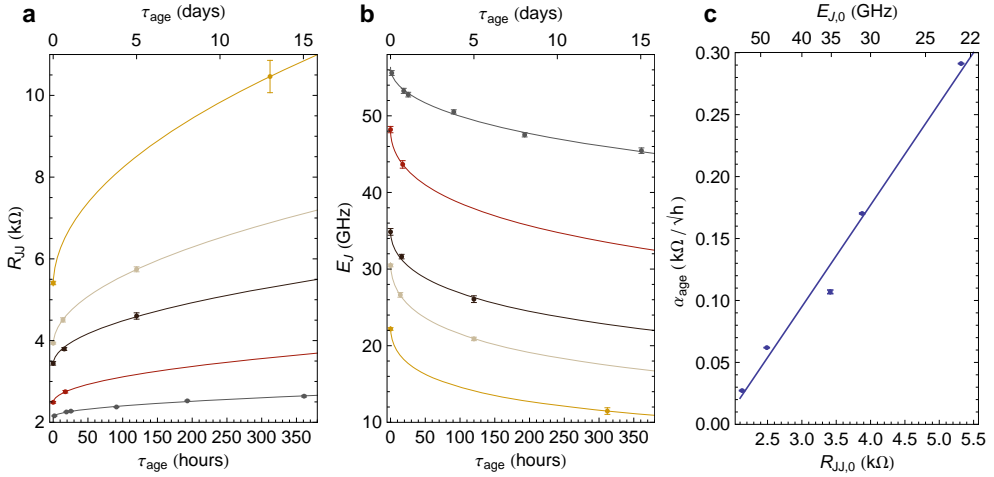
Figure 5.8: **Aging of transmon Josephson junctions. a**, Measured normal state resistances at time τ_{age} after fabrication and fit to Eq. (5.19). **b**, Calculated Josephson energy. **c**, Extracted aging speed versus initial normal state resistance and linear fit (line).

the initial Josephson junction normal resistance over the investigated parameter range as $\alpha_{\text{age}} \approx -0.15\,\text{k}\Omega/\sqrt{\text{h}} + 0.08\,R_n/\sqrt{\text{h}}$.

The methods and models discussed in this section can be used as a reference and calibration for further sample fabrication with controlled sample parameters. For a detailed step by step fabrication recipe refer to Appendix B. In case further improvements, such as an additional resist descumming step is implemented, the presented oxidation and post oxidation dependences are likely to be affected as well.

SAMPLE CHARACTERIZATION

After the long list of steps required to fabricate the device and install the measurement setup, it is a thrilling experience when a new sample is finally cooled down in the dilution refrigerator. While the RF chip design has typically already been tested at liquid helium temperatures, the qubit parameters such as Josephson energies and coherence times can only be accurately determined at ultra-low temperatures. The basic properties of the sample need to be carefully quantified before more elaborated experiments can be done. In the following we will briefly review a typical set of circuit QED characterization measurements. Typically these experiments need to be done iteratively with an increasing level of control and precision.

6.1 Resonator spectrum

The first step is to measure the transmission spectrum of the resonator. This includes the determination of the resonance frequencies and quality factors of the different resonator harmonics. Additionally, a transmission spectrum across the full detection bandwidth should be recorded in order to identify spurious modes.[1] If the sample is processed on a new waver it is furthermore advisable to test and characterize the loss properties of the niobium thin film. The internal quality factor can be determined by measuring the transmission of an under-coupled resonator that is processed on the same waver, see for example Ref. [Göppl09].

The resonator transmission of a weakly driven and damped harmonic oscillator exhibits a Lorentzian line shape according to Eq. (2.1) and an associated phase shift between

---

[1] Note that in a transmission measurement only those modes can be identified which couple to the resonator input and output ports. Spurious modes which couple to the qubit but not to the resonator need to be identified in a qubit spectroscopy measurement.

the transmitted and incoming wave as given in Eq. (2.3). In order to measure the transmission shown in Fig. 6.1 a, a constant input power of -30 dBm is applied with the RF1 signal generator, see the measurement setup Fig. 4.1. The transmitted amplitude is then measured versus frequency. More precisely, the I and Q voltage quadratures of the transmitted signal are sampled at a rate of one sample per ns for 40 μs separately, see Section 4.4 for details, and averaged on the order of 10^4 times for each data point. We then calculate the transmission power $P(\nu) = (I^2 + Q^2)/R$, with $R = 50\ \Omega$ being the characteristic impedance of the measurement circuit.

Figure 6.1 a-d depicts the measured relative microwave transmission power $T^2/T_{\max}^2$, where $T = \sqrt{I^2 + Q^2}$ is the measured absolute voltage transmission amplitude, in the vicinity of the harmonic modes $m = 1, 2, 3$ and 4. The red line is a fit to a Lorentzian model as given in Eq. (2.1). The quality factors and resonance frequencies of these overcoupled harmonic resonator modes are indicated. The used sample is shown in Fig. 9.2. From earlier measurements, see [Göppl08], we would expect a monotonic decrease of the quality factor, which is not observed in this sample. There is no final conclusion if the qubits, spurious modes, or another parameter is responsible for the observed quality factors. A measurement of the transmission amplitude over the full spectral range of the experimental setup, see Fig. 6.1 e, shows that there is only one visible spurious resonance at ~ 8.8 GHz. This resonance mode is expected to be either due to a resonance matching condition of the sample holder geometry or, more likely, the resonance of a so called slot line or odd mode of the coplanar waveguide, [Pozar93, Simons01]. In order to suppress this resonance superconducting on-chip bonds connecting the two coplanar waveguide ground planes are used in more recent samples, in the future micro fabricated air bridges will be used.

In general during the first resonator measurements there will be dispersive or even resonant interactions with qubits if they are present in the resonator. These interactions
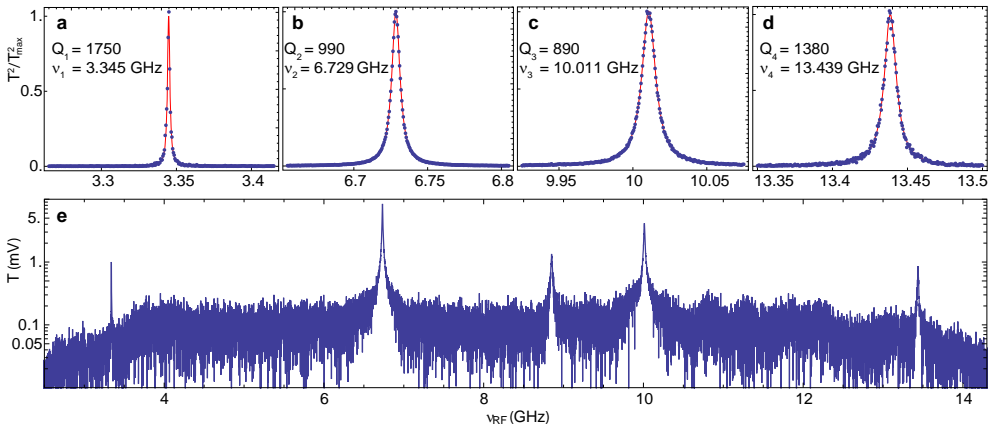
Figure 6.1: **Resonator characterization. a - d**, Measured power transmission spectrum of the fundamental (a) and first three harmonic modes (b-d) of the coplanar waveguide resonator shown in Fig. 9.2 and Lorentzian fits (red) plotted over an identical frequency range of 150 MHz. **e**, Measured transmission amplitude T over the entire detection bandwidth plotted on a logarithmic scale.

renormalize the resonance frequency and also alter the transmission line-shape. The measurements shown in Fig. 6.1 were however conducted with the qubit's transition frequencies maximally detuned from the resonator resonance frequencies. In this case the interaction of the qubit with the resonator is quite small and the bare resonator properties can be approximated. A more precise way would be to determine the bare resonator frequency by carefully measuring the qubit induced shifts versus qubit-resonator detuning, see for example Ref. [Bianchetti10b]. Another way to infer the bare resonator frequency is to go to the limit of very large coherent or incoherent radiation field powers, see Chapter 10 and Ref. [Reed10a, Bishop10b, Boissonneault10].

6.2 Flux periodicity

A good strategy to quickly estimate the qubit ground to excited state transition frequency is to investigate the dependence of the resonator frequency shift versus flux applied to the qubit which tunes its transition frequency. In Fig. 6.2 we present two measurements similar to the ones shown in Fig. 6.1 a-d. Here the resonator spectrum is measured for different applied flux bias values controlled by changing a DC current through one of the superconducting coils shown in Fig. 4.3 c. The strong coherent single qubit single photon interaction leads to avoided crossings whenever the qubit transition frequency crosses the resonator frequency. It is important to conduct this measurement with measurement powers corresponding to not much more than a single intra-resonator photon on average in order to resolve a clear avoided crossing, see Chapters 8 and 10.

Figure 6.2: **Resonator flux response. a**, Resonator transmission (red is high and blue is low transmission) versus flux bias of a single qubit. The violet line indicates ground to first excited state transition frequency according to Eq. (6.1). **b**, Similar measurement in the presence of three qubits (violet, red and yellow lines) as a function of external flux bias.

For the devices fabricated and measured in the framework of this thesis it is a good approximation to assume that the qubit transition frequency follows the simple absolute cosine dependence of the Josephson energy of a symmetric SQUID. Using Eq. (2.15) and Eq. (2.11) we find

$$\nu_{\text{ge}} \simeq \left(\sqrt{8 E_{\text{J}_{\text{max}}} |\cos(\pi(\phi + \phi_{\text{off}})/\phi_0)| E_{\text{C}}} - E_{\text{C}} \right) / h, \qquad (6.1)$$

for the ground to first excited state qubit transition frequency ν_{ge} as a function of flux ϕ (violet lines in Fig. 6.2 a). From this relatively simple measurement we can infer not only the flux coupling, i.e. the flux quantum ϕ_0 in units of the bias voltage (or bias current) applied to the coil but also the offset flux ϕ_{off} associated with that very qubit. We furthermore can infer the approximate maximal transition frequency $\nu_{\text{ge,max}}$ at $\phi/\phi_0 = 0$ and using Eq. (6.1) determine the Josephson energy E_{J} for an arbitrary ϕ if the charging energy E_{C} is known. The accuracy of determining $\nu_{\text{ge,max}}$ is drastically increased if the flux response of additional resonator modes is measured.

We would like to stress that this characterization method is particularly useful to understand the considerably more complex transmission spectrum of a resonator coupled to multiple qubits. In Fig. 6.2 b we have depicted a resonator measurement which shows the flux dependent interaction of three qubits A, B and C as a function of external flux bias $\phi_{0,A}$. All three qubits couple on a similar level to the large coil A that was used for this measurement. Using Eq. (6.1) for every qubit we can explain the value of applied flux at which each splitting is observed, see violet, yellow and red lines in Fig. 6.2 b.

There are however also a number of limitations to this convenient way of inferring the flux couplings and qubit parameters. One problem is that the cross couplings are typically not large enough to thread entire flux quanta through the qubit SQUID loop. Also, the accuracy of determining the maximal transition frequency and therefore the maximal Josephson energy is limited. Finally, the charging energy needs to be inferred from a seperate experiment. All of these points can be solved and improved doing careful qubit spectroscopy measurements, see Section 6.4.

6.3   Dipole coupling strengths

The qubit resonator dipole coupling strength is another important parameter to be extracted from resonator transmission measurements. By focussing on one of the avoided crossings, see Fig. 6.3 a, similar to the ones seen in Fig. 6.2, we observe the vacuum Rabi mode splitting spectrum when the qubit transition frequency is in resonance with the resonator frequency, see Fig. 6.3 b. On resonance the separation of the two Lorentzian peaks is minimal and corresponds to twice the single-photon single-atom dipole coupling strength. Absorption and emission of single quantum of energy happens at this splitting frequency $2g/(2\pi)$.

It is interesting to investigate the scaling of the coupling strength extracted from the Rabi splitting with the harmonic mode number m of the resonator, see Fig. 6.3 c. According to Eq. (5.5) we expect a larger coupling to higher frequency resonator modes due to the increased zero point electric field which is proportional to $\sqrt{m}$, see Eq. (5.6). There is

however a second contribution which increases the coupling strength at higher frequencies even further. When the qubit is tuned in resonance with higher harmonic modes the Josephson energy and thus the effective dipole moment is changed, see Eqs. (2.33) and (5.5). If we make use of Eq. (6.1) and consider only qubit frequencies resonant with the resonator harmonics $\nu_{ge} = \nu_1 m$, we arrive at an expression that is approximately proportional to m

$$\hbar g = \mathbf{E} \cdot \mathbf{d} \approx \sqrt{\frac{\hbar m \omega_1}{2 C_r}} \cdot 2 e \beta \sqrt{\frac{m \omega_1 + E_C}{16 E_C}}. \tag{6.2}$$

Experimentally, see blue dots in Fig. 6.3 c, we find such an approximately linear dependence when extracting the minimal peak separation in 4 measurements similar to the one shown in Fig. 6.3 a and b. Comparing the analytic solution Eq. (6.2), see blue line in Fig. 6.3 c, to an exact numerical diagonalization of the truncated Hamiltonian Eq. (2.34) (red line) we find only a small correction at higher mode numbers.

It may be interesting to draw a comparison to cavity QED with natural atoms at this point. The possibility to change both the transition frequency and the effective dipole moment over a very large range is one aspect that is novel. It is furthermore also the order of magnitude of the effective dipole moment which is very different to conventional cavity QED setups. For typical single photon resonator fields on the order of $13 \, \text{mV/m}$, which corresponds to a voltage of $0.5 \, \mu\text{V}$ dropping across the $30 \, \mu\text{m}$ gap, and a moderate voltage division factor $\beta \sim 0.25$ we arrive at an effective dipole moment of $d \sim 1 \cdot 10^{-24} \, \text{Cm}$. This corresponds to about $2 \cdot 10^6$ Debye and is a $\sim 10^5$ fold increase compared to large dipole moment molecules and still an increase of up to $\sim 10^3$ compared to atoms in highly excited Rydberg states.

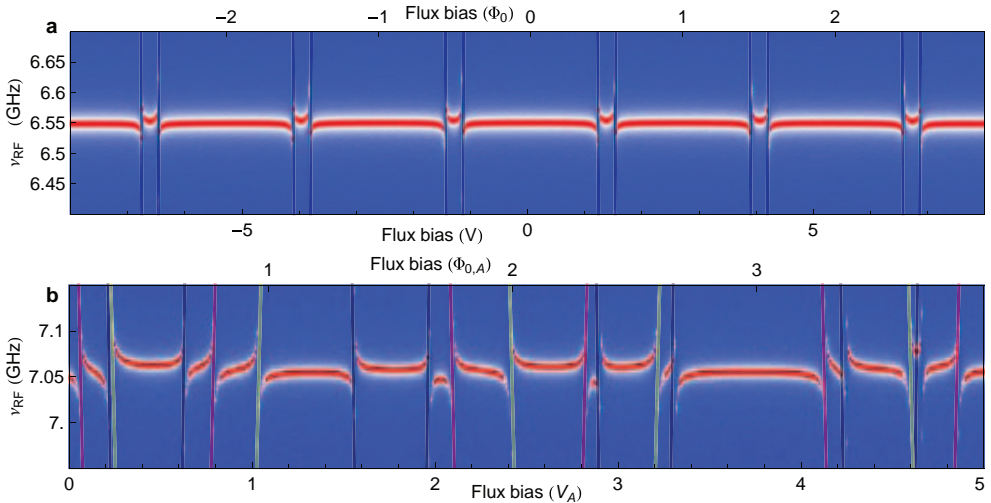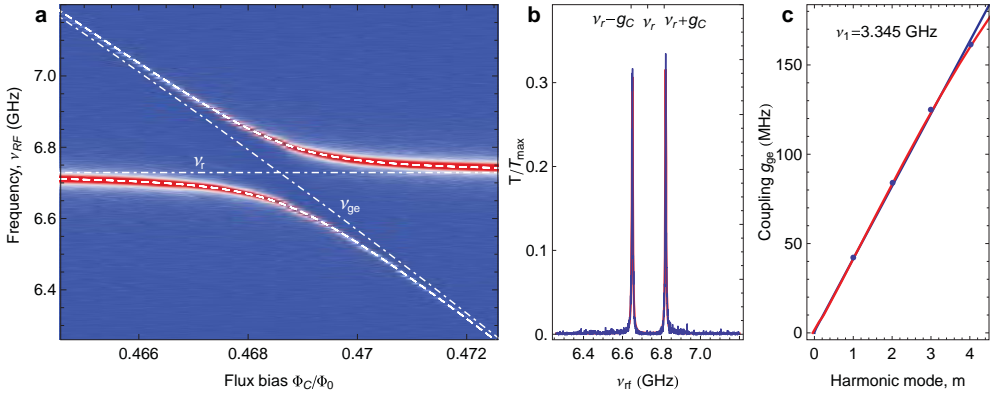

Figure 6.3: **Vacuum Rabi splitting. a**, Resonator transmission (red is high and blue is low transmission) versus flux bias of a single qubit. The white dash dotted lines indicate the qubits ground to first excited state transition and the uncoupled resonator frequency respectively. The white dashed lines correspond to the dressed state eigenenergies obtained by numerically solving the Jaynes-Cummings Hamiltonian. **b**, Cavity transmission as a function of probe frequency for the flux value with minimal separation of the two transmission peaks (blue) and fit to two Lorentzians (red). The frequency splitting $2g/(2\pi)$ corresponds to twice the dipole coupling energy $\hbar g$. **c**, Measured (blue dots) dependence of the vacuum Rabi mode splitting on the harmonic mode index m. Lines are calculated using Eq. (6.2) (blue) and an exact numerical diagonalization of the truncated Hamiltonian Eq. (2.34) (red).

This new domain of cavity QED allows for the careful investigations of the photon number and qubit number scaling of the resonant qubit - photon interaction. If on average more than one coherent or thermal photon is present in the considered resonator mode, the presented vacuum Rabi mode splitting measurements are strongly altered. In terms of sample characterization this property can for example be used to calibrate the number of photons in the resonator. These and related effects due to changes in the number of coupled qubits are studied in Chapters 8, 9 and 10.

6.4   Qubit spectroscopy

Spectroscopic qubit measurements are an important tool in circuit QED. Spectrally resolving both, the ground to first and also the first to second excited state transitions of the transmon, directly reveals the charging and Josephson energies and fully determines the qubit spectrum. Additionally, the flux coupling including all cross couplings can be determined with good accuracy. The photon number dependent shift of the transmon level splitting, i.e. the AC Stark shift, furthermore represents a useful effect to calibrate the number of photons in the resonator [Schuster05]. Qubit spectroscopy has also been used to investigate dressed state [Schuster07b] and side band transitions [Wallraff07] and also the Lamb shift [Fragner08]. In addition, spurious resonator modes which do not couple to the input and output transmission lines can only be characterized via spectroscopy of the qubit. Finally, also the sometimes present two level fluctuators coupling to a qubit level transition [Simmonds04, Neeley08, Lisenfeld10] and also possibly occurring slow transition frequency fluctuations due to flux instabilities [Koch07b] can be analyzed in detail.

For the dispersive qubit spectroscopy and readout we use a second microwave tone $\nu_{\rm spec}$, see setup in Fig. 4.1. If $\nu_{\rm spec}$ is in resonance with a qubit transition and one of the two involved states is populated, the resonant tone induces a change in the qubit state. This is however only noticeable if the drive rate (Rabi frequency) is comparable to the intrinsic qubit decay [Schuster05]. The state change then induces a state dependent shift by $\pm\chi$ of the renormalized bare resonator resonance frequency, see Subsection 2.3.4. By measuring the resonator transmission at a fixed frequency, e.g. the resonator frequency with the qubit is in its ground state, we detect this shift as an amplitude and phase change in the measured resonator transmission. Note that in case the flux bias is changed, the new optimal measurement frequency needs to be determined for each flux setting. For further details refer to Subsection 2.3.4 and Refs. [Schuster05, Wallraff05, Schreier08, Bianchetti09, Bianchetti10b, Reed10a, Bishop10b, Boissonneault10].

In Fig. 6.4 we present three typical spectroscopic sample characterization measurements. We demonstrate the easiest way to extract the Josephson and charging energies of the transmon in the far detuned dispersive regime in panel a. In order to increase the precision of this measurement and in order to also infer the maximal Josephson energy a flux dependent transmon spectroscopy is demonstrated. Working at elevated cavity photon numbers such a measurement can also reveal individual cavity photon number (Fock) states if the qubit dipole strength is sufficiently large, see panel b. In panel c we show a typical photon number calibration measurement conducted in the far detuned dispersive regime.
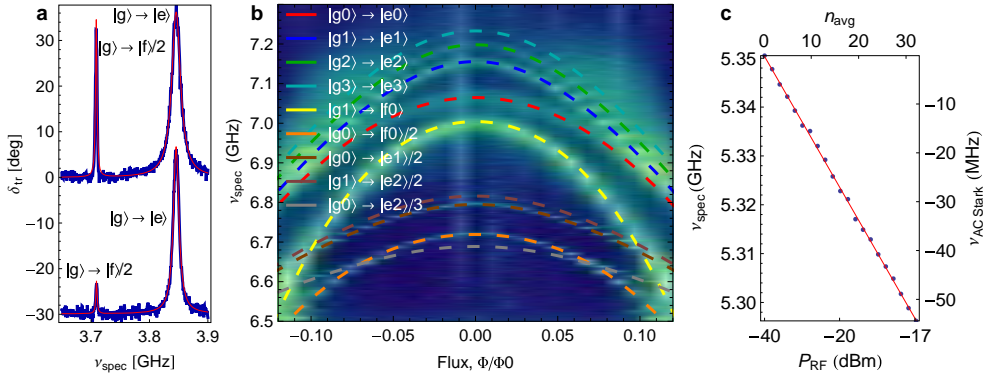
Figure 6.4: **Transmon spectroscopy. a**, Phase shift of the fixed frequency cavity transmission measurement tone as a function of applied spectroscopy frequency for two different spectroscopy powers (blue) and fit to two Lorentzians (red). In the lower power measurement (trace offset by -30 deg) only the transmon ground to first excited state transition is clearly visible. As the spectroscopy power is increased also the two photon ground to second excited state transition is clearly resolved. **b**, Amplitude of the measurement tone as a function of flux bias and spectroscopy frequency where blue is high transmission and green is low transmission. If both the measurement tone and the spectroscopy tone powers are increased, many transitions are observed. In the very strong coupling regime different photon number states are clearly resolved (number splitting) as indicated in the legend. **c**, Measured and fitted qubit ground to excited state transition frequency versus measurement power in the far detuned dispersive regime. The cavity photon number dependent AC Stark shift of the qubit transition frequency provides a photon calibration for the applied cavity input power, in this case $P_{n=1} \approx -32\,\text{dBm}$.

6.4.1 Charging energy

In Fig. 6.4 a we show a measurement of the qubit state dependent phase shift of the cavity transmission as a function of the applied spectroscopy frequency and a fit to two Lorentzians. At intermediate spectroscopy power, i.e. the measurement which is offset by -30 deg, the qubit $|g\rangle$ to $|e\rangle$ transition is already broadened and there is a weakly driven second transition visible in the spectrum. If the spectroscopy power is further increased the second transition becomes clearly visible. The additional spectroscopic line at lower frequency corresponds to a two photon process driving the transmon population between the states $|g\rangle$ and $|f\rangle$.

By fitting the two transmission peaks with two Lorentzian functions, see [Schuster05, Schreier08], we can extract the two transition frequencies ν_{ge} and $\nu_{gf}/2$. For typical values of E_J/E_C the anharmonicity of the transmon [Koch07a] is $\alpha = \nu_{ge} - \nu_{gf} = 2(\nu_{ge} - \nu_{gf}/2) \sim 1.2\,E_C$, which directly gives us an estimate for the charging and, using Eq. (2.15), also the Josephson energy. For an exact value we solve the Cooper pair box hamiltonian Eq. (2.13) exactly, e.g. analytically in the phase basis. The measured two values fully determine the qubit Hamiltonian with the two free parameters E_J and E_C.

In this measurement scheme any AC Stark shifts of the one and two photon transition are neglected. To reduce this effect, measurements like the one presented in Fig. 6.4 a should be taken in the far detuned regime and with a very low measurement power, ideally corresponding to less than a single photon in the resonator on average. An even better strategy is to implement pulsed qubit spectroscopy where the measurement tone is only turned on directly after the excitation of the qubit with a long saturation pulse at frequency

ν_{spec}, see also Subsection 6.5. This scheme enables to excite the qubit in the absence of resonator photons and AC Stark shifts. To avoid the need for large spectroscopy powers one can alternatively use a pump and probe spectroscopy scheme. In such a scheme low power spectroscopy tones at frequencies ν_{ge} and ν_{spec} are used to populate the $|e\rangle$ state with a pump power dependent probability and probe the single photon $|e\rangle$ to $|f\rangle$ transition directly.

6.4.2 Flux dependence, dressed states and number splitting

In circuit QED the qubit photon coupling strength can be large enough such that even in the dispersive regime it is difficult to talk about uncoupled qubit or cavity states only. In Fig. 6.4 b we present a spectroscopy measurement versus flux bias at elevated measurement and spectroscopy powers. While such a data set is much more difficult to analyze than one obtained with lower powers or one where both drive and measurement tones are pulsed, it in the end contains also more useful information. For solving the flux dependent eigenenergies we numerically solve the multilevel Jaynes-Cummings Hamiltonian in the charge basis Eq. (2.34) by exact diagonalization.

In addition to the transition observed in panel a, i.e. $|g0\rangle \rightarrow |e0\rangle$ where the number now indicates a tensor product with the photon number state in the Fock basis $|n\rangle$, we also observe the $|g1\rangle \rightarrow |e1\rangle$, $|g2\rangle \rightarrow |e2\rangle$ and very faint $|g3\rangle \rightarrow |e3\rangle$ transitions in Fig. 6.4 b. The observation of spectroscopic number splitting in the 'strong dispersive coupling regime' [Schuster07b], is an incarnation of the AC Stark shift and has only been observed in circuit QED due to the very large coupling strength attainable. In addition we observe the two photon side band transition $|g0\rangle \rightarrow |e1\rangle/2$, its number split pendant $|g1\rangle \rightarrow |e2\rangle/2$ and the second order three photon sideband transition $|g0\rangle \rightarrow |e2\rangle/3$, see also [Wallraff07, Leek09]. All of these states are mainly dependent on the transmon ground to excited state transition energy and the qubit photon coupling strength g_{ge}.

States containing 2 or more quanta of energy are however shifted in frequency due to the presence of the additional transmon states $|f\rangle, |h\rangle, ...$ and an accurate fit would not be possible without including them in the model. Most sensitive to the qubit parameters E_{J} and E_{C} are however transitions that directly involve higher energy transmon states such as the $|g0\rangle \rightarrow |f0\rangle/2$ already presented in panel a and its number split single photon equivalent $|g1\rangle \rightarrow |f0\rangle$, see Fig. 6.4 b. We argue that fitting a measurement such as the one presented in Fig. 6.4 b represents the most precise and complete way to determine all relevant sample parameters, i.e. all free variables in the Jaynes-Cummings Hamiltonian Eq. (2.34), i.e. ν_{r}, g_{ge} and $\nu_{\mathrm{ge}}(\phi)$, which is a function of E_{C}, $E_{\mathrm{J_{max}}}$, ϕ and the flux periodicity ϕ_0.

6.4.3 AC-Stark shift photon-number calibration

There is one remaining parameter that has not been discussed in enough detail yet. This is the average number of photons that populate the cavity due to the applied resonant and coherent measurement tone. We can calibrate the average number of photons in the resonator n_{avg} in a far detuned dispersive AC Stark shift measurement [Schuster05, Gambetta06]. Far dispersive refers to the regime where the individual photon number split qubit lines can not be resolved anymore, i.e. if the shift per photon $2\chi \ll \gamma_2$ or in case of a strong spectroscopy drive where the qubit line is broadened $2\chi \ll \Omega_{\mathrm{Rabi}}/(2\pi)$.

The measurement as shown in Fig. 6.4 c is obtained by extracting the ground to excited state transition frequency ν_{spec} from a Gaussian line fit for different applied measurement powers P_{RF}.

We observe an AC Stark shifted qubit transition frequency with a linear dependence $\nu_{\mathrm{ge}}(n_{\mathrm{avg}}) = \nu_{\mathrm{ge}}(0) + 2\chi n_{\mathrm{avg}}$ on the applied measurement power (blue dots). The detuning Δ dependent qubit shift per photon of 2χ, see Eq. (2.37), can either directly be measured by probing the cavity frequency for different qubit drive powers, it can approximately be calculated with Eq. (2.36), or exactly by solving the Hamiltonian Eq. (2.34) for $n = 0$ and $n = 1$. For the measurement presented in Fig. 6.4 c the relevant parameters are $\Delta/(2\pi) = -1.088\,\mathrm{GHz}$, $g/(2\pi) = 54\,\mathrm{MHz}$ and the calculated AC Stark shift per photon of $2\chi/(2\pi) \approx -1.69\,\mathrm{MHz}$ using the relation Eq. (2.36). From the linear fit shown in Fig. 6.4 c we conclude that a coherent measurement power of $P_{\mathrm{n=1}} \approx -32\,\mathrm{dBm}$ populates the cavity with on average a single photon.

In case of a symmetrically over-coupled resonator with a negligible insertion loss, the microwave power applied to the input of the resonator is related to the average resonator photon number, see Subsection 2.1.1 as $P_{\mathrm{RF}} = n_{\mathrm{avg}}h\nu_{\mathrm{r}}\kappa$ where $1/\kappa$ is the mean photon lifetime in the resonator. This relation, see also Eq. (2.4), together with the AC Stark shift calibration directly yields the attenuation along the input line of the experimental setup. The total attenuation extracted in this way was found to be consistent with the expected frequency dependent damping coefficients. These are typically not exactly known at ultra-low temperatures due to a variation of attenuation with temperature.

6.5   Rabi oscillations

Time-resolved Rabi oscillations, see Fig. 6.5, are an important characterization measurement which demonstrates full coherent control of a single qubit [Nakamura01, Vion03, Wallraff05, Allen87]. Well calibrated Rabi π pulses are furthermore a necessary prerequisite for the vacuum Rabi oscillation measurements presented in Chapter 10, for the single photon source used in [Bozyigit10c, Bozyigit10b] and also for any other of our experiments more closely related to quantum information processing [Leek07, Leek09, Leek10, Bianchetti09, Bianchetti10b].

The pulse sequence of the presented Rabi oscillation measurement is depicted in the inset of Fig. 6.5 c. We apply an amplitude modulated square shaped coherent microwave pulse which is resonant with the qubit ground to excited state transition frequency of variable length Δt. This is followed by a long measurement pulse in resonance with the resonator frequency at time $t = 5\,\mu\mathrm{s}$. This scheme enables to excite the qubit in the absence of resonator photons which would induce an AC Stark shift or dressed dephasing, [Boissonneault08]. Similar to the spectroscopic experiments presented above, the transmitted measurement tone experiences a phase shift depending on the prepared qubit state and the prepared qubit state is a function of the applied Rabi pulse length or amplitude, see Subsection 2.3.4.

In Fig. 6.5 a we show the measured phase response as a function of time and the applied Rabi pulse length Δt. In this density plot red color corresponds to a large negative phase shift of the transmitted tone and blue to the case where the transmitted tone does
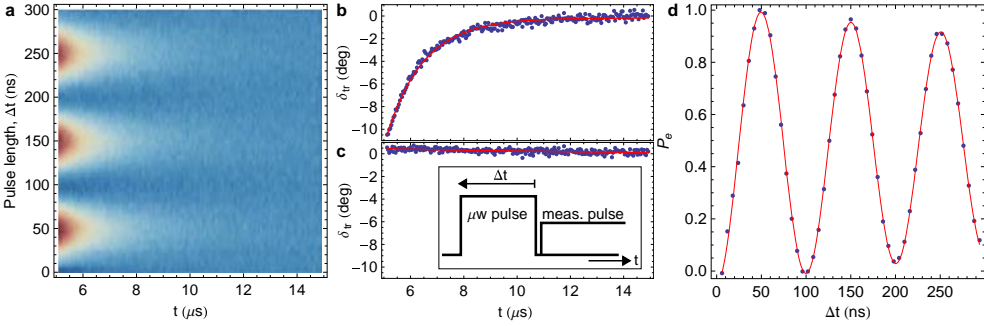
Figure 6.5: **Rabi oscillations. a**, Phase shift of the pulsed measurement tone as a function of time and applied Rabi pulse length (red is large negative phase shift). **b**, Maximal phase response versus time for a Rabi pulse length corresponding to a full ground to excited state qubit rotation by π (dots) and exponential fit (red). The fitted T_1 time is $1.4\,\mu$s. **c**, Same measurement as in panel b for a 2π pulse. Inset shows the used pulse sequence. **d**, Extracted excited state population versus applied Rabi pulse length (dots) and exponential cosine fit (red).

not see a phase shift due to the qubit. In panels c and d the phase response corresponding to a rotation of the qubit state vector by π and 2π is depicted (dots). Note that the measured phase is not a well defined quantity before the measurement pulse is applied. Therefore, the two field quadratures are analyzed and fitted to a full cavity Bloch model in current experiments, see Ref. [Bianchetti09] for details.

An exponential fit to the π pulse response (panel c) yields an energy relaxation time of $T_1 = 1/\gamma_1 \approx 1.4\,\mu$s. By taking the area below the π pulse phase response as a calibration for a qubit excited state population $P_e = 1$ we can extract the qubit population for all measured pulse length Δt, see Fig. 6.5 d (dots). A similar technique has been used to determine the population of single qubit states in Refs. [Wallraff05, Bianchetti09], entangled qubit states in Refs. [Filipp09, Leek09] and multi level system states in Ref. [Bianchetti10b].

The Rabi oscillations are fitted (red line) using an exponentially decaying cosine with the Rabi frequency $\Omega/(2\pi) \approx 10\,$MHz and a decay constant of $\tau_{\mathrm{Rabi}} \approx 1.3\,\mu$s. In the limit of strong driving the Rabi decay is related to energy relaxation and pure dephasing rates as $1/\tau_{\mathrm{Rabi}} = (3\gamma_1 + 2\gamma_\phi)/4$, see [Allen87, Bianchetti09]. Accordingly, we obtain a pure dephasing time $T_\phi = 1/\gamma_\phi \approx 1.9\,\mu$s and a coherence time of $T_2 = 1/(1/(2T_1) + 1/T_\phi) \approx 1.1\,\mu$s. This is a remarkably long T_2 time in current experiments. In order to confirm this number a Ramsey type experiment would be suitable.

Time-resolved quit measurements were not the main focus of this thesis, we refer the reader to [Bianchetti09, Bianchetti10b] for details of the dispersive qubit readout. For an explicit measurement of the qubit coherence in Ramsey and spin echo measurements refer to [Steffen07, Fink07, Bianchetti10a]. Pulsed qubit spectroscopy is a useful tool to measure the qubit transition frequency in the absence of resonator photons, which avoids spurious effects such as number splitting, side-band transitions and dressed dephasing. It can be implemented simply by probing the resonator response after a long ($\Delta t \gg T_1, T2$) qubit saturation pulse for different frequencies ν_{spec}, see e.g. [Göppl09]. For flux-pulsed spectroscopy or time-resolved vacuum Rabi oscillations, see Chapter 10, it is furthermore important to carefully characterize the pulsed flux response, see [Bozyigit10c].

CONCLUSION

In this chapter we have reviewed the relevant experimental techniques required to obtain the main results presented in Chapters 8, 9 and 10 of this thesis.

While most of the characterization measurements presented in the previous section would have been called novel only a few years ago, now they form a set of established techniques to quickly learn about all aspects of a new circuit QED sample. Similarly, the experimental setup has advanced e.g. by using cryogen free dilution refrigerators that are easy to operate and offer an unprecedented amount of space for the cold experimental setup. Another example is the development of the data acquisition system, which now in principle allows for the implementation of microwave field tomography and real time feedback algorithms, [Bozyigit08, Lang09, Bozyigit10a].

The field of circuit QED is developing rapidly at all ends indeed.[1] Setting up a quantum processor that can solve a given task more quickly than a classical computer remains an extremely challenging goal however, and the potential scalability of quantum electronic circuits still needs to be demonstrated. This could e.g. be done by integrating and coherently controlling many qubits in a single resonator, controllable couple grids of resonators with embedded qubits [Helmer09], or scale up the system size by making use of alternative tunable coupling techniques that do not require microwave resonators [Bialczak10]. It will be interesting to see if this task can be achieved without degrading the single qubit performance.

Rather than tackling this ambitions goal, the measurements presented in the following chapters aim at harnessing the new possibilities of circuit QED to study some of the most basic quantum optical effects. This includes an investigation of the nature of matter light interaction on the level of individual quanta as well as an exploration of the transition from the quantum to the classical regime of an open quantum system.

---

[1]Refer to the introduction of Chapter 2 for a detailed list of recent progress in circuit QED.

P A R T **III**

MAIN RESULTS

In this part of the thesis we quantitatively investigate the strong dipole coupling strength between individual artificial atoms and single photons. As discussed in Section 2.3, the single-photon single-qubit interaction can be modeled by the electric dipole coupling energy $g\hbar = \mathbf{Ed}$ of a single particle with dipole moment $\mathbf{d}$ subject to an electric field $\mathbf{E}$.

According to quantum mechanics the energy of the electromagnetic field is quantized in the photon number n. Because the field amplitude E is proportional to the square root of its energy, the dipole coupling strength $g\hbar = \mathbf{Ed}$ is expected to scale with $\sqrt{n}$ as the number of photons is increased. In the bottom left part of the energy level diagram in Fig. 7.1 we indicate the resonant dressed states of one qubit and up to two photons $|1, \pm\rangle$ and $|2, \pm\rangle$ split by $2\sqrt{n}g\hbar$. In Chapter 8, see also Refs. [Fink08, Fink09a], we probe the indicated level transitions (blue vertical arrows) between these states with two weak coherent probe tones. The observed discrete and nonlinearly spaced excitation energies of this strongly coupled multi-photon / qubit molecule is a direct consequence of the quantization of the electromagnetic field.

While the quantization of matter in terms of the number of atoms, or in our case the number of qubits, N is not under debate, it is interesting to show that multiple qubits can be collectively coupled such that they need to be described as a single quantum system.
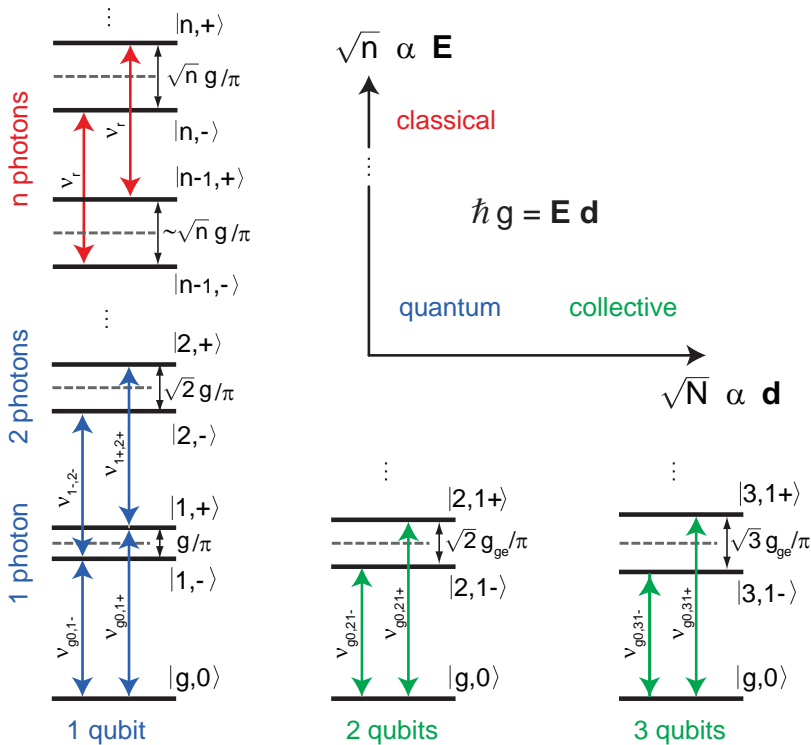
Figure 7.1: **Quantum, collective and classical regimes of cavity QED.** Dipole coupled dressed states (black lines) of $n = 0, 1, 2, ...$ photons in resonance with $N = 1, 2, 3$ qubits given in frequency units. Bare qubit and cavity states (dashed lines) and allowed transitions (colorized vertical arrows) are indicated.

Quantum mechanics predicts that the magnitude of the collective dipole moment d in such a case scales with the square root of the number of atoms. In a dual experiment to the previous one, see Chapter 9 and Ref. [Fink09b], we observe this square root nonlinearity by probing the level transitions indicated by green vertical arrows in Fig. 7.1 in the presence of one, two and three qubits. The increased splitting by $\sqrt{N}$ is clear evidence for the collective interaction of up to three qubits entangled by a single photon.

It has been a long standing goal to observe these quantum nonlinearities on the level of only a few quanta. Due to the excellent control and the large dipole coupling strength g in our circuit QED setup, we could demonstrate the expected $\sqrt{n}$ and $\sqrt{N}$ nonlinearities independently for up to 3 photons and up to 3 qubits.

In addition to these experiments which explore the quantum and the collective regime of matter-light interaction we have also studied the regime of very large photon numbers in Chapter 10 and Ref. [Fink10], see Fig. 7.1. In this limit, the relative nonlinearity between two neighboring dressed state doublets disappears, see level transitions indicated by red vertical arrows in Fig. 7.1, and the level spectrum is that of a classical harmonic oscillator. We observe this gradual disappearance of the $\sqrt{n}$ nonlinearity by increasing the number of thermal photons, or equivalently the effective temperature of the resonator field. We study this transition from the quantum to the classical regime of cavity QED with a quantitative model and demonstrate how to sense the effective cavity field temperature in spectroscopic and time-resolved vacuum Rabi measurements.

OBSERVATION OF THE JAYNES-CUMMINGS $\sqrt{n}$ NONLINEARITY

The already very active field of cavity quantum electrodynamics (QED), traditionally studied in atomic systems [Raimond01, Mabuchi02, Walther06], has recently gained additional momentum by the advent of experiments with semiconducting [Reithmaier04, Yoshie04, Peter05, Hennessy07, Englund07] and superconducting systems [Wallraff04, Chiorescu04, Johansson06]. In these solid state implementations, novel quantum optics experiments are enabled by the possibility to engineer many of the characteristic parameters at will. In cavity QED, the observation of the vacuum Rabi mode splitting is a hallmark experiment aimed at probing the nature of matter-light interaction on the level of a single quantum. However, this effect can, at least in principle, be explained classically as the normal mode splitting of two coupled linear oscillators [Zhu90]. It has been suggested that an observation of the scaling of the resonant atom-photon coupling strength in the Jaynes-Cummings energy ladder [Walls94] with the square root of photon number n is sufficient to prove that the system is quantum mechanical in nature [Carmichael96].

8.1 Introduction

In early experiments the quantization of the electromagnetic field was observed in cavity QED with Rydberg atoms by measurements of collapse and revival [Rempe87]. Similarly, the $\sqrt{n}$ scaling of the atom/photon coupling strength with the number of photons n has been observed in the time domain by measuring n photon Rabi oscillations using coherent states [Brune96] and Fock states [Varcoe00, Bertet02].

In the frequency domain the $\sqrt{n}$ scaling can be extracted from spectroscopic cavity transmission measurements. Initial attempts employing pump and probe spectroscopy

with alkali atoms [Thompson98] were inconclusive. In a recent experiment however the two-photon vacuum Rabi resonance was resolved using high power nonlinear spectroscopy [Schuster08]. At the same time, we observed this quantum nonlinearity by measuring the spectrum of two photons and one artificial atom in circuit QED [Fink08]. In our measurements the originally proposed pump and probe spectroscopy scheme [Thompson98] was used. Similarly the n photon Rabi mode splitting was studied using multi-photon transitions up to $n = 5$ [Bishop09].

In the dispersive regime the photon number splitting of spectroscopic lines provides similar evidence for the quantization of microwave radiation in circuit QED [Schuster07b]. Further experimental progress in the time domain has enabled the preparation and detection of coherent states [Johansson06], photon number states [Hofheinz08] and arbitrary superpositions of photon number states [Hofheinz09] in circuits. Using Rydberg atoms quantum jumps of light have been observed [Gleyzes07, Guerlin07] and Wigner functions of Fock states have been reconstructed [Deleglise08].

These experiments demonstrate the quantum nature of light by measuring the nonlinear $\sqrt{n}$ scaling of the dipole coupling strength with the discrete number of photons n in the Jaynes-Cummings model [Carmichael96].

In this thesis, we report a direct spectroscopic observation of this characteristic quantum nonlinearity. Measuring the photonic degree of freedom of the coupled system, our measurements provide unambiguous, long sought for spectroscopic evidence for the quantum nature of the resonant atom-field interaction in cavity QED. We explore atom-photon superposition states involving up to two photons, using a spectroscopic pump and probe technique. The experiments have been performed in a circuit QED setup [Blais04], in which ultra strong coupling is realized by the large dipole coupling strength and the long coherence time of a superconducting qubit embedded in a high quality on-chip microwave cavity. Circuit QED systems also provide a natural quantum interface between flying qubits (photons) and stationary qubits for applications in quantum information processing and communication (QIPC) [Nielsen00].

8.1.1 The Jaynes-Cummings model

The dynamics of a two level system coupled to a single mode of an electromagnetic field is described by the Jaynes-Cummings Hamiltonian

$$\hat{\mathcal{H}}_0 = \hbar\omega_{ge}\hat{\sigma}_{ee} + \hbar\omega_r\hat{a}^\dagger\hat{a} + \hbar g_{ge}(\hat{\sigma}_{ge}^\dagger\hat{a} + \hat{a}^\dagger\hat{\sigma}_{ge}). \tag{8.1}$$

Here, ω_{ge} is the transition frequency between the ground $|g\rangle$ and excited state $|e\rangle$ of the two level system, ω_r is the frequency of the field and g_{ge} is the coupling strength between the two. $\hat{a}^\dagger$ and $\hat{a}$ are the raising and lowering operators acting on the photon number states $|n\rangle$ of the field and $\hat{\sigma}_{ij} = |i\rangle\langle j|$ are the corresponding operators acting on the qubit states. When the coherent coupling rate g_{ge} is larger than the rate κ at which photons are lost from the field and larger than the rate γ at which the two level system looses its coherence, the strong coupling limit is realized.

On resonance ($\omega_{ge} = \omega_r$) and in the presence of n excitations, the new eigenstates of the coupled system are the symmetric $(|g, n\rangle + |e, n-1\rangle)/\sqrt{2} \equiv |n+\rangle$ and antisymmetric $(|g, n\rangle - |e, n-1\rangle)/\sqrt{2} \equiv |n-\rangle$ qubit-photon superposition states, see Fig. 8.1. For $n = 1$, these states are equivalently observed spectroscopically as a vacuum Rabi mode
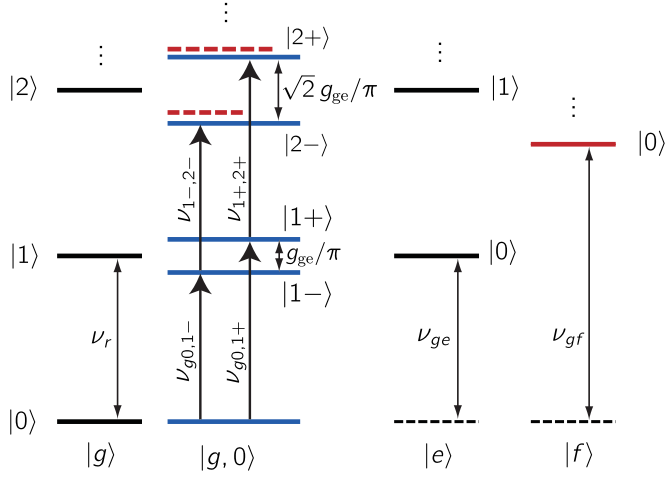
Figure 8.1: **Level diagram of a resonant ($v_r = v_{ge}$) cavity QED system.** The uncoupled qubit states $|g\rangle, |e\rangle$ and $|f\rangle$ from left to right and the photon states $|0\rangle, |1\rangle, ..., |n\rangle$ from bottom to top are shown. The dipole coupled dressed states are shown in blue and a shift due to the $|f, 0\rangle$ level is indicated in red. Pump $v_{g0,1-}, v_{g0,1+}$ and probe $v_{1-,2-}, v_{1+,2+}$ transition frequencies are indicated accordingly.

splitting [Thompson92, Wallraff04, Boca04, Reithmaier04, Yoshie04, Peter05, Hennessy07, Englund07] or in time-resolved measurements as vacuum Rabi oscillations [Brune96, Varcoe00, Bertet02, Johansson06, Hofheinz08] at frequency $2g_{ge}$. The Jaynes-Cummings model predicts a characteristic nonlinear scaling of this frequency as $\sqrt{n}2g_{ge}$ with the number of excitations n in the system, see Fig. 8.1. This quantum effect is in stark contrast to the normal mode splitting of two classical coupled linear oscillators, which is independent of the oscillator amplitude.

Since the first measurements of the vacuum Rabi mode splitting with, on average, a single intra-cavity atom [Thompson92] it remains a major goal to clearly observe this characteristic $\sqrt{n}$ nonlinearity spectroscopically to prove the quantum nature of the interaction between the two-level system and the radiation field [Zhu90, Carmichael96, Thompson98]. In time domain measurements of vacuum Rabi oscillations, evidence for this $\sqrt{n}$ scaling has been found with circular Rydberg atoms [Brune96] and superconducting flux qubits [Johansson06] interacting with weak coherent fields. Related experiments have been performed with one and two-photon Fock states [Varcoe00, Bertet02]. We now observe this nonlinearity directly using a scheme similar to the one suggested in Ref. [Thompson98] by pumping the system selectively into the first doublet $|1\pm\rangle$ and probing transitions to the second doublet $|2\pm\rangle$. This technique realizes efficient excitation into higher doublets at small intra cavity photon numbers avoiding unwanted AC Stark shifts occurring in high drive [Bocquillon09] and elevated temperature experiments, see Refs. [Fink09a, Fink10] and Chapter 10.

In a different regime, when the qubit is detuned by an amount $|\Delta| = |\omega_{ge} - \omega_r| \gg g_{ge}$ from the cavity, photon number states and their distribution have recently been observed using dispersive quantum non-demolition measurements in circuit QED [Schuster07b] and also in Rydberg atom experiments [Guerlin07].

8.1.2 Experimental setup

In our experiments, in the resonant regime a superconducting qubit playing the role of an artificial atom is strongly coupled to photons contained in a coplanar waveguide resonator in an architecture known as circuit QED [Blais04, Wallraff04]. We use a transmon [Koch07a, Schreier08], which is a charge-insensitive superconducting qubit design derived from the Cooper pair box (CPB) [Bouchiat98], as the artificial atom. Its transition frequency is given by $\omega_{\mathrm{ge}}/2\pi \simeq \sqrt{8E_{\mathrm{C}}E_{\mathrm{J}}(\Phi)} - E_{\mathrm{C}}$ with the single electron charging energy $E_{\mathrm{C}} \approx 0.4\,$GHz, the flux controlled Josephson energy $E_{\mathrm{J}}(\Phi) = E_{\mathrm{J,max}}|\cos{(\pi\Phi/\Phi_0)}|$ and $E_{\mathrm{J,max}} \approx 53.5\,$GHz, as determined in spectroscopic measurements. The cavity is realized as a coplanar resonator with bare resonance frequency $\nu_{\mathrm{r}} \approx 6.94\,$GHz and decay rate $\kappa/2\pi \approx 0.9\,$MHz. Optical images of the sample are shown in Fig. 8.2 a. The large dimension of the qubit in the quasi one dimensional resonator provides a very large dipole coupling strength g_{ge}. A simplified electrical circuit diagram of the setup is shown in Fig. 8.2 b.

8.2 Coherent dressed states spectroscopy

The system is prepared in its ground state $|g,0\rangle$ by cooling it to temperatures below $20\,$mK in a dilution refrigerator. We then probe the energies of the lowest doublet $|1\pm\rangle$ measuring the cavity transmission spectrum T and varying the detuning between the qubit transition frequency ν_{ge} and the cavity frequency ν_{r} by applying a magnetic flux Φ, see Fig. 8.3 a. The measurement is performed with a weak probe of power $P \approx -137\,$dBm applied to the input port of the resonator populating it with a mean photon number of $\bar{n} \approx 1.6$ on resonance when the qubit is maximally detuned from the resonator. P is calibrated in a dispersive AC Stark shift measurement [Schuster05]. At half integers of a flux quantum Φ_0, the qubit energy level separation ν_{ge} approaches zero. At this point the bare resonator spectrum peaked at the frequency ν_r is observed, see Fig. 8.3 b. We use the measured maximum transmission amplitude to normalize the amplitudes in all subsequent measurements. At all other detunings $|\Delta| \gg g_{\mathrm{ge}}$ the qubit dispersively shifts [Koch07a] the cavity frequency ν_{r} by $\chi \simeq -g_{\mathrm{ge}}^2 E_{\mathrm{C}}/(\Delta(\Delta - E_{\mathrm{C}}))$.
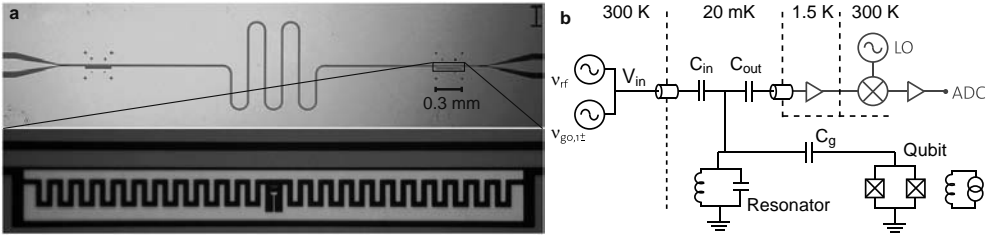
Figure 8.2: **Sample and experimental setup. a**, Optical images of the superconducting coplanar waveguide resonator (top) with the transmon type superconducting qubit embedded at the position indicated. On the bottom, the qubit with dimensions $300 \times 30~\mu\mathrm{m}^2$ close to the center conductor is shown. **b**, Simplified circuit diagram of the experimental setup, similar to the one used in Ref. [Wallraff04]. The qubit is capacitively coupled to the resonator through C_{g} and the resonator, represented by a parallel LC circuit, is coupled to input and output transmission lines via the capacitors C_{in} and C_{out}. Using ultra low noise amplifiers and a down-conversion mixer, the transmitted microwave signal is detected and digitized.

8.2.1 Vacuum Rabi splitting

Measuring cavity transmission T as a function of flux bias Φ in the anti-crossing region yields transmission maxima at frequencies corresponding to transitions to the first doublet $|1\pm\rangle$ in the Jaynes-Cummings ladder as shown in Fig. 8.3 c. On resonance ($\Delta = 0$), we extract a coupling strength of $g_{\text{ge}}/2\pi = 154\,\text{MHz}$, see Fig. 8.3 d, where the linewidth of the individual vacuum Rabi split lines is given by $\delta_{\nu 0} \approx 2.6\,\text{MHz}$. This corresponds to a transmission peak separation g_{ge}/π of over 100 linewidths $\delta_{\nu 0}$, clearly demonstrating that the strong coupling limit is realized [Wallraff04, Schoelkopf08]. Solid white lines in Figs. 8.3 (and 8.4) are numerically calculated dressed state frequencies with the qubit and resonator parameters as stated above, being in excellent agreement with the data. For the calculation, the qubit Hamiltonian is solved exactly in the charge basis. The qubit states $|g\rangle$ and $|e\rangle$ and the flux dependent coupling constant g_{ge} are then incorporated in the Jaynes-Cummings Hamiltonian Eq. (8.1). Its numeric diagonalization yields the dressed states of the coupled system without any fit parameters.
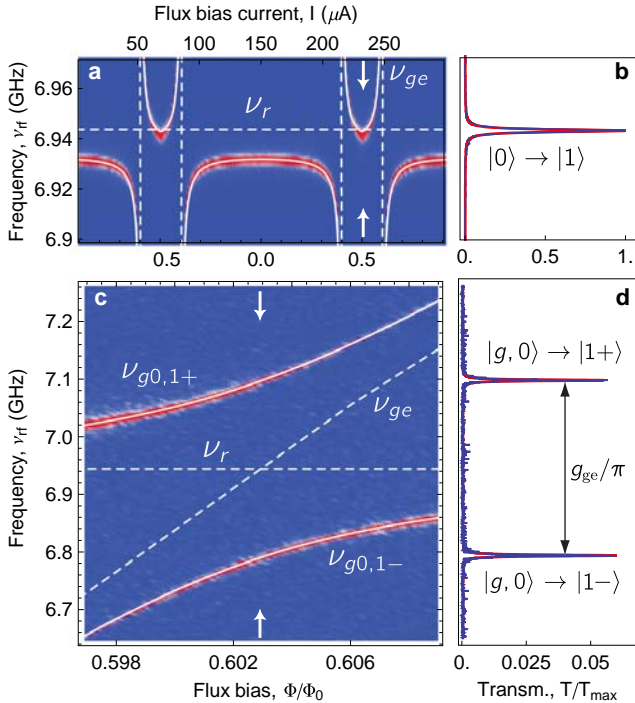
Figure 8.3: **Vacuum Rabi mode splitting with a single photon. a**, Measured resonator transmission spectra versus external flux Φ. Blue indicates low and red high transmission T. The solid white line shows dressed state energies as obtained numerically and the dashed lines indicate the bare resonator frequency ν_r as well as the qubit transition frequency ν_{ge}. **b**, Resonator transmission T at $\Phi/\Phi_0 = 1/2$ as indicated with arrows in panel **a**, with a Lorentzian line fit in red. **c**, Resonator transmission T versus Φ close to degeneracy. **d**, Vacuum Rabi mode splitting at degeneracy with Lorentzian line fit in red.

8.2.2 Two photon vacuum Rabi splitting

In our pump and probe scheme we first determine the exact energies of the first doublet $|1\pm\rangle$ at a given flux Φ spectroscopically. We then apply a pump tone at the fixed frequency $\nu_{g0,1-}$ or $\nu_{g0,1+}$ to populate the respective first doublet state $|1\pm\rangle$. A probe tone of the same power is then scanned over the frequency range of the splitting. This procedure is repeated for different flux controlled detunings. The transmission at the pump and probe frequencies is spectrally resolved in a heterodyne detection scheme.

Populating the symmetric state $|1+\rangle$, we observe an additional transmission peak at a probe tone frequency that varies with flux, as shown in Fig. 8.4 a. This peak corresponds to the transition between the symmetric doublet states $|1+\rangle$ and $|2+\rangle$ at frequency $\nu_{1+,2+}$. Similarly, in Fig. 8.4 c where the antisymmetric state $|1-\rangle$ is populated we measure a transmission peak that corresponds to the transition between the two antisymmetric doublet states $|1-\rangle$ and $|2-\rangle$ at frequency $\nu_{1-,2-}$. The transmission spectra displayed in Figs. 8.4 b and d recorded at the values of flux indicated by arrows in Figs. 8.4 a and c show that the distinct transitions between the different doublets are very well resolved with separations of tens of linewidths. Transitions between symmetric and antisymmetric doublet states are not observed in this experiment, because the flux-dependent transition matrix elements squared are on average smaller by a factor of 10 and 100 for transitions $|1+\rangle \rightarrow |2-\rangle$ and $|1-\rangle \rightarrow |2+\rangle$, respectively, than the corresponding matrix elements between states of the same symmetry.

The energies of the first doublet $|1\pm\rangle$, split by g_{ge}/π on resonance, are in excellent agreement with the dressed states theory (solid red lines) over the full range of flux Φ controlled detunings, see Fig. 8.5. The absolute energies of the second doublet states $|2\pm\rangle$ are obtained by adding the extracted probe tone frequencies $\nu_{1-,2-}$ and $\nu_{1+,2+}$ to the applied pump frequencies $\nu_{g0,1-}$ or $\nu_{g0,1+}$, see blue dots in Fig. 8.5. For the second doublet, we observe two peaks split by $1.34\, g_{ge}/\pi$ on resonance, a value very close to the expected $\sqrt{2} \sim 1.41$. This small frequency shift can easily be understood, without any fit parameters, by taking into account a third qubit level $|f,0\rangle$ which is at frequency $\nu_{gf} \simeq 2\nu_{ge} - E_C$
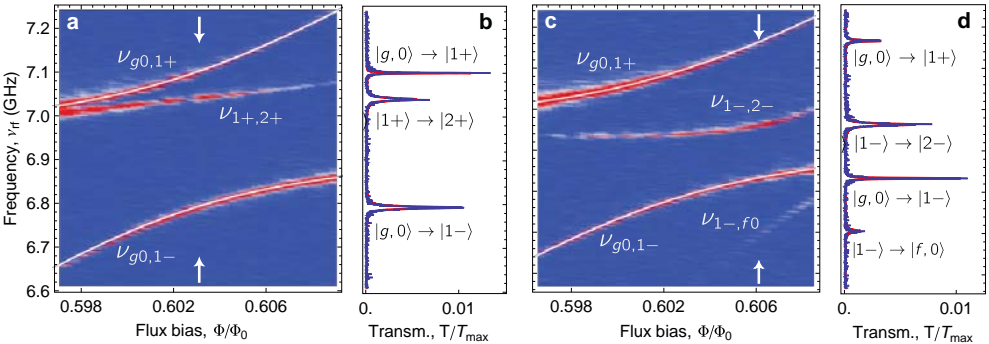
Figure 8.4: **Vacuum Rabi mode splitting with two photons. a,** Cavity transmission T as in Fig. 8.3 with an additional pump tone applied to the resonator input at frequency $\nu_{g0,1+}$ populating the $|1+\rangle$ state. **b,** Spectrum at $\Delta = 0$, indicated by arrows in **a. c,** Transmission T with a pump tone applied at $\nu_{g0,1-}$ populating the $|1-\rangle$ state. **d,** Spectrum at $\Phi/\Phi_0 \approx 0.606$ as indicated by arrows in **c.**
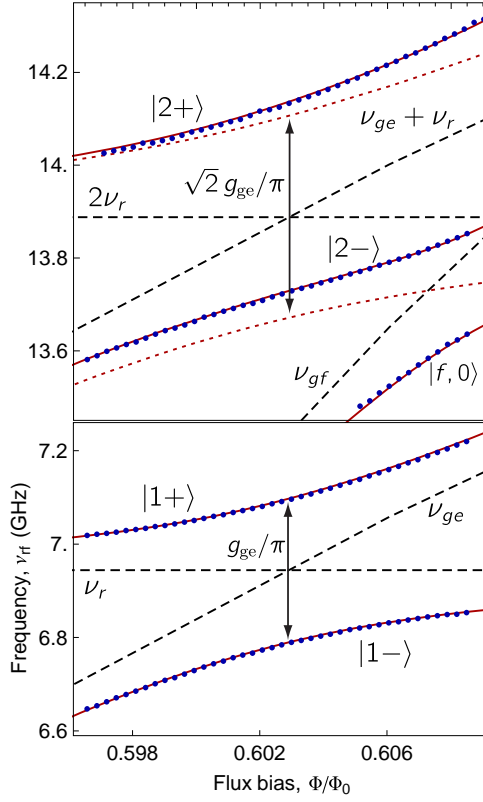
Figure 8.5: **Experimental dressed state energy levels.** Measured dressed state energies (blue dots) reconstructed by summing pump and probe frequencies, compared to the calculated uncoupled cavity and qubit levels (dashed lines), the calculated dressed state energies in the qubit two-level approximation (dotted) and to the corresponding calculation including the third qubit level (solid red lines).

for the transmon type qubit [Koch07a], just below the second doublet states $|2\pm\rangle$. In order to find the energies of the dressed states in the presence of this additional level we diagonalize the Hamiltonian $\hat{\mathcal{H}} = \hat{\mathcal{H}}_0 + \hat{\mathcal{H}}_1$, where $\hat{\mathcal{H}}_1 = \hbar\omega_{\text{gf}}\hat{\sigma}_{\text{ff}} + \hbar g_{\text{ef}}(\hat{\sigma}^{\dagger}_{\text{ef}}\hat{a} + \hat{a}^{\dagger}\hat{\sigma}_{\text{ef}})$ and $g_{\text{ef}}/2\pi \approx 210\,\text{MHz}$ (obtained from exact diagonalization) denotes the coupling of the $|e\rangle$ to $|f\rangle$ transition to the cavity. The presence of the $|f,0\rangle$ level is observed to shift the antisymmetric state $|2-\rangle$, being closer in frequency to the $|f,0\rangle$ state, more than the symmetric state $|2+\rangle$, see Figs. 8.1 and 8.5, leading to the small difference of the observed splitting from $\sqrt{2}$. The $|f,0\rangle$ state, being dressed by the states $|g,2\rangle$ and $|e,1\rangle$, is also directly observed in the spectrum via the transition $|1-\rangle \rightarrow |f,0\rangle$ at frequency $\nu_{1-,f0}$, see Fig. 8.4 c. This is in excellent agreement with the dressed states model, see Fig. 8.5. For comparison the dressed states split by $\sqrt{2}g_{\text{ge}}/\pi$ in the absence of the $|f,0\rangle$ state are shown as dotted red lines in Fig. 8.5.

Our experiments clearly demonstrate the quantum nonlinearity of a system of one or two photons strongly coupled to a single artificial atom in a cavity QED setting. Both sym-

metric and antisymmetric superposition states involving up to two photons are resolved by many tens of linewidths.

8.3   Weak thermal excitation

In this section we investigate the resonant interaction between a single transmon-type multilevel artificial atom and weak thermal fields. We explore up to three photon dressed states of the coupled system in a linear response heterodyne transmission measurement, similar to the one presented in Section 8.2. The results are also in good quantitative agreement with the generalized Jaynes-Cummings model. Our data indicates that the role of thermal fields in resonant cavity QED can be studied in detail using superconducting circuits. Note that a different sample was used for the measurements presented in this section.

8.3.1   Sample parameters

For the experiments presented here we use a transmon type qubit, which is a charge-insensitive superconducting qubit design derived from the Cooper pair box [Bouchiat98], as the artificial atom [Koch07a, Schreier08]. Its transition frequency is given by $\omega_{g,e}/2\pi \simeq \sqrt{8E_C E_J(\Phi)} - E_C$ with the single electron charging energy $E_C/h \approx 0.232\,\text{GHz}$, the flux controlled Josephson energy $E_J(\Phi) = E_{J,\text{max}}|\cos(\pi\Phi/\Phi_0)|$ and $E_{J,\text{max}}/h \approx 35.1\,\text{GHz}$, as determined by spectroscopic measurements. The two characteristic energies E_J and E_C define the full level spectrum of the qubit where the eigenenergy of level l is approximately given as $E_l \simeq -E_J + \sqrt{8E_C E_J}(l + 1/2) - E_C/12(6l^2 + 6l + 3)$ [Koch07a]. The cavity is realized as a coplanar resonator with bare resonance frequency $\nu_r \approx 6.44\,\text{GHz}$ and photon decay rate $\kappa/2\pi \approx 1.6\,\text{MHz}$. Details of the sample design and fabrication can be found in Chapter 5. Optical microscope images of the sample are shown in Fig. 8.6 a. A simplified electrical circuit diagram of the setup, including the qusi-thermal photon source, is shown in Fig. 8.6 b.

8.3.2   Generalized Jaynes-Cummings model

The transmon qubit is a superconducting circuit with a nonlinear energy level spectrum. In many experiments the nonlinearity, which can be adjusted by circuit design and fabrication, is sufficient to correctly model it as a two level system. For the experimental results presented in this work it is however essential to treat the qubit as a multilevel system taking into account the coupling of all relevant transmon levels to the cavity photons. While in Section 8.2 it was sufficient to include only one additional transmon level, here we present a more general approach.

The physics of a multilevel artificial atom strongly coupled to a single mode of the electromagnetic field is described by a generalized Jaynes-Cummings model with the Hamiltonian

$$\hat{\mathscr{H}} = \hbar\omega_r\,\hat{a}^\dagger\hat{a} + \sum_{l=e,f,h,\dots}\left(\hbar\omega_l\hat{\sigma}_{l,l} + \hbar g_{l-1,l}\,(\hat{\sigma}^\dagger_{l-1,l}\,\hat{a} + \hat{a}^\dagger\hat{\sigma}_{l-1,l})\right). \tag{8.2}$$

Here, $\hbar\omega_l$ is the energy of the l'th excited state $|l\rangle$ of the multilevel artificial atom, ω_r is the frequency of the resonator field and $g_{l-1,l}$ is the coupling strength of the transition $l - 1 \to l$ and one photon. $\hat{a}^\dagger$ and $\hat{a}$ are the raising and lowering operators acting on the
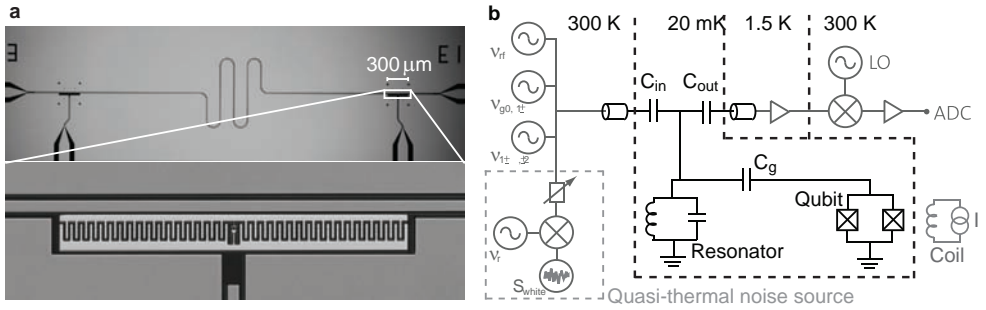
Figure 8.6: **Sample and experimental setup. a**, Optical images of the superconducting coplanar waveguide resonator (top) with the transmon type superconducting qubit embedded at the position indicated. The qubit of dimensions $300 \times 30\ \mu m^2$ is shown on the bottom. **b**, Simplified circuit diagram of the experimental setup. The qubit is capacitively coupled to the resonator through C_g and flux tuned with a current biased (I) external miniature superconducting coil. The resonator, represented by a parallel LC circuit, is coupled to input and output transmission lines via the capacitors C_{in} and C_{out}. A quasi thermal field can be generated by modulating a microwave carrier tone ν_r with a large bandwidth pseudo-random noise spectrum S_{white}. The noise signal is filtered, attenuated and added to pump ($\nu_{g0,1\pm}$, $\nu_{1\pm,2\pm}$) and probe (ν_{rf}) tones. The resulting microwave fields are further attenuated and applied to the resonator input. After amplification with an ultra low noise amplifier the transmitted probe signal ν_{rf} is downconverted with a local oscillator (LO) and digitized with an analog to digital converter (ADC).

field with photon number n and $\hat{\sigma}_{i,j} = |i\rangle\langle j|$ are the corresponding operators acting on the qubit states. In Fig. 8.7, a sketch of the energy level diagram of the resonantly coupled qubit-resonator system ($\nu_r = \nu_{g,e}$) is shown for up to three photons $n = 0,1,2,3$ and the first four transmon levels $l = g, e, f$ and h.

Considering the first two levels of the artificial atom at zero detuning ($\Delta \equiv \nu_r - \nu_{g,e} = 0$) the eigenstates of the coupled system are the symmetric $(|g,n\rangle + |e,n-1\rangle)/\sqrt{2} \equiv |n+\rangle$ and antisymmetric $(|g,n\rangle - |e,n-1\rangle)/\sqrt{2} \equiv |n-\rangle$ qubit-photon superposition states, see Fig. 8.7. For $n = 1$, the coupled one photon one atom eigenstates are split due to the dipole interaction [Agarwal84, Mondragon83]. The Jaynes-Cummings model predicts a characteristic nonlinear scaling of this frequency as $\sqrt{n}2g_{g,e}$ with the number of excitations n in the system. In the general multilevel case, the higher energy atomic levels renormalize the dipole coupled dressed state energies. This causes frequency shifts in the excitation spectrum as indicated by red dashed lines in Fig. 8.7 and the simple $\sqrt{n}$ scaling is slightly modified.

8.3.3 Thermal background field

Experimentally, the coupled circuit QED system is prepared in its ground state $|g,0\rangle$ by cooling it to temperatures below $< 20\,mK$ in a dilution refrigerator. Measuring the cavity transmission spectrum T in the anti-crossing region of the qubit transition frequency $\nu_{g,e}$ and the cavity frequency ν_r yields transmission maxima at frequencies corresponding to transitions from $|g,0\rangle$ to the first doublet $|1\pm\rangle$ of the Jaynes-Cummings ladder, see Fig. 8.8 a. On resonance, see Fig. 8.8 b, we extract the coupling strength of $g_{g,e}/2\pi = 133\,MHz$. This is a clear indication that the strong coupling limit $g_{g,e} \gg \kappa, \gamma$, with photon decay and qubit decoherence rates $\kappa/2\pi, \gamma/2\pi \sim 1\,MHz$, is realized. Solid lines in Fig. 8.8 a (and Fig. 8.9 a) are numerically calculated dressed state frequencies, see
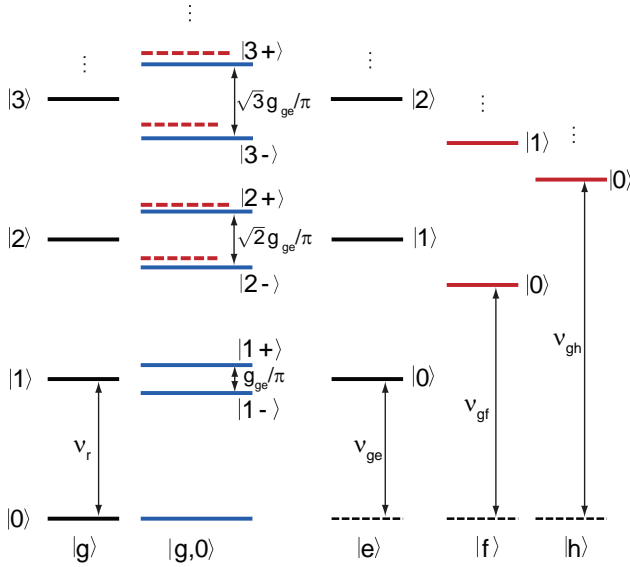
Figure 8.7: **Sketch of the energy level diagram of a resonant cavity QED system** ($v_r = v_{g,e}$)**.** The uncoupled qubit states $|g\rangle, |e\rangle, |f\rangle$ and $|h\rangle$ (from left to right) and the photon states $|0\rangle, |1\rangle, |2\rangle, |3\rangle, ...$ (from bottom to top) are shown with black and red solid lines. The dipole coupled dressed states are shown in blue and the shifts due to the $|f,0\rangle, |f,1\rangle$ and $|h,0\rangle$ levels are indicated by red dashed lines.

Fig. 8.8 c, with the qubit and resonator parameters as stated above. For the calculation, the qubit Hamiltonian is diagonalized exactly in the charge basis. The qubit states $|g\rangle$ and $|e\rangle$ and the flux dependent coupling constant $g_{g,e}$ are then incorporated in the Jaynes-Cummings Hamiltonian Eq. (8.2). Its numerical diagonalization yields the dressed states of the coupled system without any fit parameters.

In addition to the expected spectral lines corresponding to the transition from the ground state $|g,0\rangle$ to the first doublet states $|1\pm\rangle$, we observe three lines with very low intensities, see Figs. 8.8 a and b. These additional transitions are visible because the system is excited by a small thermal background field with a cavity photon number distribution given by the Bose-Einstein distribution. This thermal field is a consequence of incomplete thermalization of the room temperature black-body radiation at the input and output ports of the resonator. This effect can easily be avoided by adding additional cold attenuation to the input line of the setup.

A quantitative analysis taking into account the two photon states $|2\pm\rangle$ and the presence of the higher energy qubit levels f and h in Eq. (8.2) yields the transition frequencies indicated by yellow and red solid lines in Fig. 8.8. For this analysis the coupling constants $g_{e,f} = 184$ MHz and $g_{f,h} = 221$ MHz of higher energy qubit levels to the cavity mode, obtained from exact diagonalization of the qubit Hamiltonian, have been included. We thus identify two of the additional spectral lines as transitions between the first $|1\pm\rangle$ and second $|2\pm\rangle$ doublet states of the resonant Jaynes Cummings ladder, see Fig. 8.8 c. The lowest frequency additional spectral line corresponds to a transition from the antisymmetric
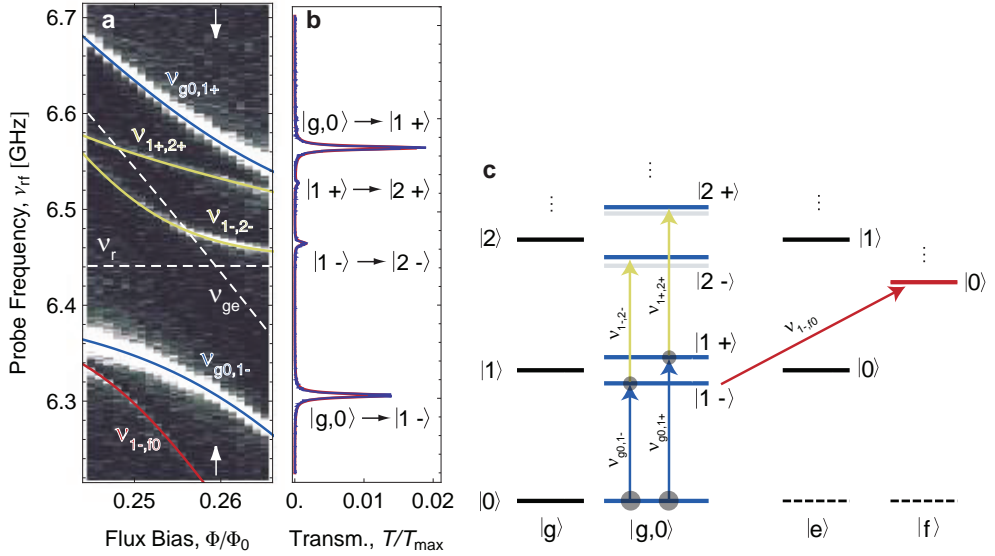
Figure 8.8: **Vacuum Rabi mode splitting with a weak coherent probe tone. a**, Measured resonator transmission spectra versus external flux Φ close to degeneracy. Black indicates low and white high transmission T. The solid lines show dressed state energies as obtained numerically and the dashed lines indicate the bare resonator frequency ν_r and the qubit transition frequency $\nu_{g,e}$. **b**, Resonator transmission T at degeneracy as indicated with arrows in panel (a), with a line fit to four Lorentzians in red. **c**, Corresponding energy level spectrum (similar to Fig. 8.7) with observed transitions indicated by arrows and small thermal population indicated with gray circles.

doublet state with one photon $|1-\rangle$ to the qubit f level without a photon $|f,0\rangle$.

The details of the thermally excited transmission spectrum can be used as a sensitive probe for the cavity field temperature, see Chapter 10 and [Fink10]. Analyzing the amplitudes of the Rabi splitting spectrum with a quantitative master equation model [Bishop09], leads to an estimated cavity field temperature of $T_c \simeq 0.2$ K which corresponds to a relatively high mean thermal occupation number of $n_{th} \simeq 0.3$ photons for the data presented in Fig. 8.8 a. Careful filtering and thermalization at the input and output ports results in a typical cavity field temperature of < 90 mK and < 54 mK ($n_{th} < 0.03$ and $n_{th} < 0.003$) as reported for example in Refs. [Fragner08] and [Bishop09], see also [Fink10] and Chapter 10.

8.3.4 Quasi-thermal excitation

In order to access the three photon doublet states $|3\pm\rangle$ of the coupled multi-photon multilevel-atom system we use externally applied broadband quasi-thermal fields. In this new approach the dressed eigenstates are populated according to a thermal distribution depending on the chosen thermal field temperature. This allows to investigate the flux dependence of all resolvable spectral lines for a given effective resonator mode temperature T_c in a single experimental run. The spectrum of a one dimensional black body

such as the considered cavity is given as $S_{1D}(\nu) = h\nu/[\exp(h\nu/k_B T_c) - 1]$. At a temperature of $T_c > h\nu_r/k_B \simeq 300$ mK this energy spectrum is flat with a variation of $< 5\%$ within a 500 MHz band centered at the cavity frequency $\nu_r \simeq 6.44$ GHz. It is therefore a very good approximation to make use of a white noise spectrum in the narrow frequency band of the experimentally investigated transition frequencies centered at ν_r, in order to generate quasi-thermal fields of temperatures $T_c > 300$ mK and populate the considered cavity mode with thermal photons.

In order to generate such a spectrum a carrier microwave tone at frequency ν_r is modulated with a low frequency large bandwidth quasi-random noise spectrum S_{white} using a mixer, see Fig. 8.6 b. This approximately yields a microwave frequency white noise spectrum with a bandwidth of 500 MHz centered symmetrically around the cavity frequency ν_r. Using tunable attenuators, we can adjust the noise power spectral density over a wide range of values. For this experiment we adjust it such that the thermal population of the cavity mode is on the order of $n_{\text{th}} \sim 0.9$ corresponding to a temperature of $T_c \sim 0.4$ K. This noise spectrum constitutes a reasonable approximation of a black body thermal noise source for the considered 1D cavity mode, temperature and frequency. At the same time, the chosen mean thermal population $n_{\text{th}} \sim 0.9$ allows to observe all allowed transitions between the ground state $|g\rangle$ and the three photon doublet states $|3\pm\rangle$.

In the presence of the thermal field, we probe the cavity transmission spectrum as a function of flux in the anticrossing region, see Fig. 8.9 a, with a weak coherent probe tone ν_{rf} in the linear response limit. In this limit the weak probe tone is only a small perturbation to the field and no multi-photon transitions are induced. In this measurement we
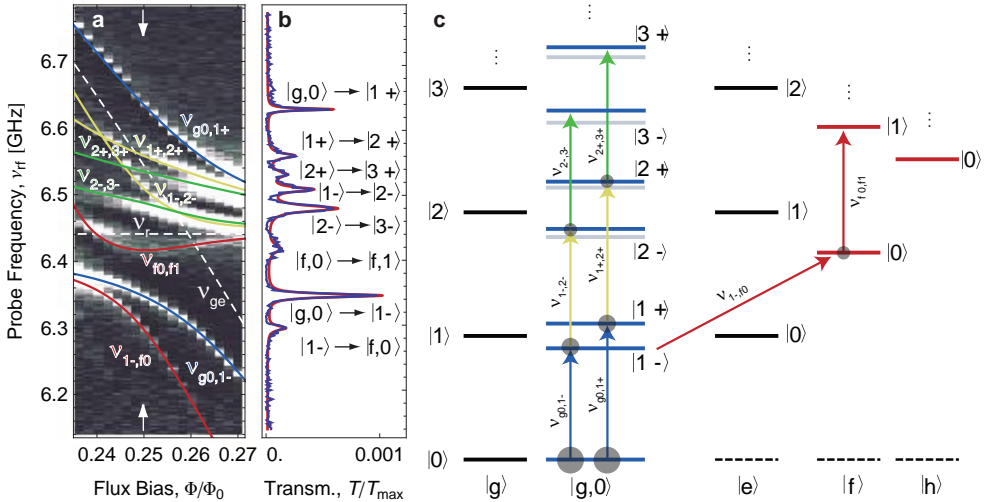
Figure 8.9: **Vacuum Rabi mode splitting in the presence of a thermal field. a**, Cavity transmission T as in Fig. 8.8 with an additional quasi-thermal field of temperature $T_c \sim 0.4$ K applied to the resonator input populating the $|1\pm\rangle$, $|2\pm\rangle$ and $|f,0\rangle$ states. **b**, Transmission spectrum at $\Phi/\Phi_0 = 0.25$, indicated by arrows in (a). **c**, Corresponding energy level spectrum (similar to Fig. 8.7) with observed transitions indicated by arrows and induced thermal population indicated with gray circles.

resolve all allowed transitions between the thermally occupied dipole coupled states in the generalized Jaynes-Cummings ladder. The solid lines are again the calculated dressed state transition energies which agree well with the observed spectral lines. In Fig. 8.9 b, a cavity transmission measurement at flux $\Phi/\Phi_0 = 0.25$ is shown. We identify 8 allowed transitions, compare with Fig. 8.9 c. It follows that the states $|1\pm\rangle$, $|2\pm\rangle$ and also $|f,0\rangle$ are thermally populated.

In the two-level-atom approximation, transitions between symmetric and antisymmetric doublet states are forbidden at degeneracy. In the generalized Jaynes-Cummings model the dressed state transition matrix elements are renormalized due to higher qubit levels. Numerical diagonalization shows that the matrix elements squared, which are related to the amplitude of the expected spectral lines, are 140 (6) times smaller for the symmetry changing transitions $|1-\rangle \rightarrow |2+\rangle$ ($|1+\rangle \rightarrow |2-\rangle$) than for the observed symmetry preserving transitions $|1-\rangle \rightarrow |2-\rangle$ ($|1+\rangle \rightarrow |2+\rangle$) at degeneracy. Similarly, for the transitions $|2-\rangle \rightarrow |3+\rangle$ ($|2+\rangle \rightarrow |3-\rangle$) the matrix elements squared are 235 (16) times smaller than the measured transitions $|2-\rangle \rightarrow |3-\rangle$ ($|2+\rangle \rightarrow |3+\rangle$) at degeneracy. Therefore transitions between symmetric and antisymmetric doublet states are not resolved in our experiment. Symmetry changing transitions populating the antisymmetric states $|2-\rangle$ and $|3-\rangle$ have larger matrix elements than symmetry changing transitions populating the symmetric states $|2+\rangle$ and $|3+\rangle$ because the former are closer in frequency to the qubit levels $|f,0\rangle$ and $|h,0\rangle$. Similarly, the matrix element for the transition $|1-\rangle \rightarrow |f,0\rangle$ is 34 times larger than for the transition $|1+\rangle \rightarrow |f,0\rangle$ at degeneracy. The latter is therefore also not observed in the experimental data. In addition to the transition $|1-\rangle \rightarrow |f,0\rangle$, also seen in the data presented in Fig. 8.8, we observe a transmission line which corresponds to the transition $|f,0\rangle \rightarrow |f,1\rangle$, see Fig. 8.9 b. A numerical calculation shows that the matrix element is 5 times larger at degeneracy than $|2-\rangle \rightarrow |f,1\rangle$ and 7 times larger than $|f,0\rangle \rightarrow |h,0\rangle$ which in principle could also have been observed. All transitions observed in the experimental data are in qualitative agreement with the calculated matrix elements stated above.

In Fig. 8.10 the full level spectrum reconstructed from the measured data of the bound photon/atom system up to the third excitation is shown. To calculate the absolute energies of the levels (blue dots) we extract the transition frequencies from data presented in Fig. 8.9 with Lorentzian line fits and add them accordingly. For the first doublet states $|1\pm\rangle$ we find excellent agreement with both a simple two-level atom Jaynes-Cummings model (dotted red lines) as well as the generalized multilevel Jaynes-Cummings model (solid red lines). In the case of the second $|2\pm\rangle$ and third doublet states $|3\pm\rangle$ we find considerable frequency shifts with regard to the two level model (compare dotted and solid red lines) but excellent agreement with the generalized model taking account the additional qubit levels, as expected from the results in Section 8.2 and Ref. [Fink08]. Furthermore it can be seen in Fig. 8.10 that the negative anharmonicity of the transmon qubit, together with the strong dipole coupling, causes large frequency shifts of the antisymmetric dressed levels $|2-\rangle$ and $|3-\rangle$ since they are closer in frequency to the qubit levels $|f,0\rangle$ and $|f,1\rangle$, $|h,0\rangle$. This leads to a small reduction of the $\sqrt{n}$ nonlinearity which is in agreement with the numerical results.

We extended our previous work presented in Section 8.2 and Ref. [Fink08] by introducing thermal fields to populate the dressed eigenstates in a resonant cavity QED system. In addition to the one and two photon/atom superposition states we report a measurement

of the three photon doublet using quasi-thermal fields. The results are in good agreement with a generalized multilevel-atom Jaynes-Cummings Hamiltonian without any fit parameters. It has been shown that cavity QED with superconducting circuits can be a sensitive probe for thermal fields. Refer to Chapter 10 and Ref. [Fink10] for further details on thermal field sensing.
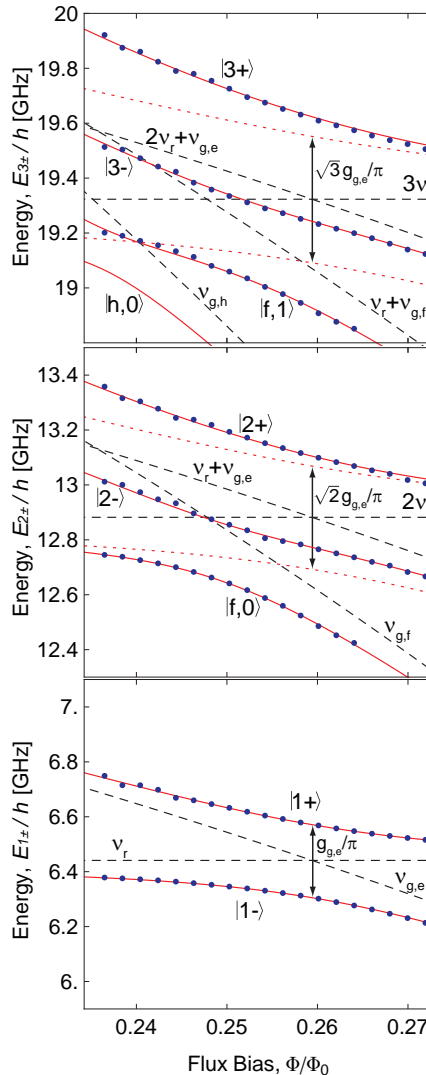
Figure 8.10: **Measured energy level diagram of the three-photon / artificial atom system.** Measured dressed state energies (blue dots) reconstructed from extracted transition frequencies from data in Fig. 8.9 compared to calculated uncoupled cavity and qubit levels (dashed black lines), the calculated dressed state energies in the qubit two-level approximation (dotted red lines) and to the corresponding calculation including four qubit levels (solid red lines).

8.4 Three photon pump and probe spectroscopy of dressed states

In order to probe the excitation spectrum of the two and three photon doublet states we extend the pump and probe spectroscopy scheme presented in Section 8.2 and Refs. [Thompson98, Fink08], where one of the first doublet states $|1\pm\rangle$ is coherently pumped and the transition to the states $|2\pm\rangle$ is probed, see also [Fink09a]. This technique avoids large intra-cavity photon numbers which are needed in high-drive and elevated temperature experiments. The results presented in this section have been measured using the sample introduced in Section 8.3.

In analogy to the previous experiments, we wait for the system to equilibrate with its cold environment to prepare the ground state $|g,0\rangle$. The qubit is then tuned close to degeneracy where $\Phi/\Phi_0 \approx 0.25$. We weakly probe the resonator transmission spectrum as shown in Fig. 8.11 (blue lines).

In a second step we apply a pump tone at frequency $\nu_{g0,1-}$ ($\nu_{g0,1+}$) populating the dressed state $|1-\rangle$ ($|1+\rangle$) and probe the system again, see Fig. 8.11 a (b) yellow line. Clearly the transitions $|1\pm\rangle \rightarrow |2\pm\rangle$ become visible at the calculated eigenenergy which is indicated with yellow vertical arrows in Figs. 8.11 a, b and c. We also note that the state $|f,0\rangle$ is populated by the probe tone via the transition $|1-\rangle \rightarrow |f,0\rangle$, see red arrows in Figs. 8.11 a and c.

In a last step we apply two pump tones at frequencies $\nu_{g0,1-}$ and $\nu_{1-,2-}$, see Fig. 8.11 a (green line), or at frequencies $\nu_{g0,1+}$ and $\nu_{1+,2+}$, see Fig. 8.11 b (green line) respectively.
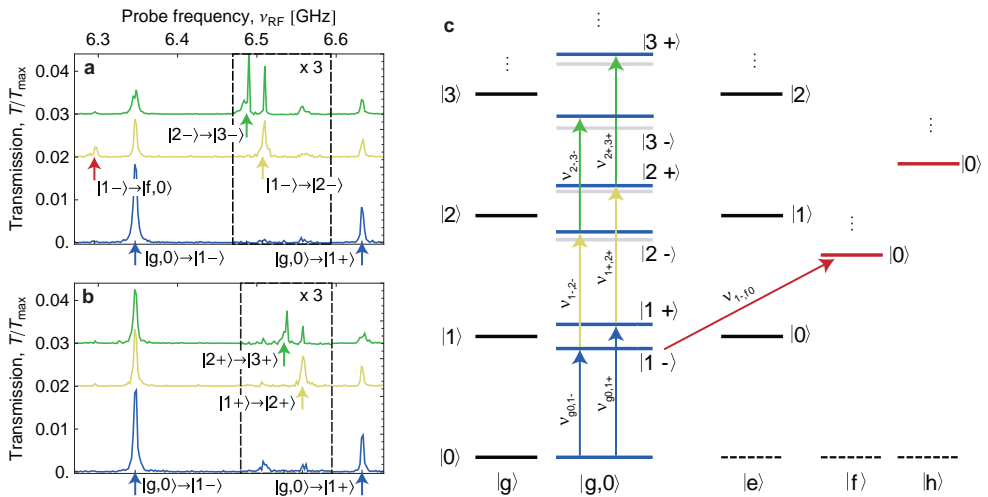
Figure 8.11: **Vacuum Rabi mode splitting with one probe tone and zero, one or two coherent pump tones at flux $\Phi/\Phi_0 \approx 0.25$ close to degeneracy. a**, Measured resonator transmission spectra T/T_{max} without a pump tone (blue) with one pump tone $\nu_{g0,1-}$ (yellow) and with two pump tones $\nu_{g0,1-}$ and $\nu_{1-,2-}$ (green) applied. The spectra are offset by 0, 0.02 and 0.03 T/T_{max} and the boxed area is scaled in amplitude by a factor of 3 for better visibility. Vertical arrows indicate numerically calculated transition frequencies. **b**, Similar measurement of resonator transmission T for the case of no (blue), $|1+\rangle$ (yellow) and both $|1+\rangle$ and $|2+\rangle$ symmetric dressed states pumped coherently. **c**, Energy level spectrum (similar to Fig. 8.7) with relevant transitions indicated by arrows.

The three-photon one-qubit dressed state transitions $|2\pm\rangle \rightarrow |3\pm\rangle$ become visible in the spectrum, see green vertical arrows. At the same time, transitions from the ground state are found to saturate considerably when the pump tones are turned on, compare the amplitudes of the spectral lines at the frequency indicated by the left blue arrow in Fig. 8.11 a, or similarly by the right blue arrow in figure Fig. 8.11 b. This is expected since the occupation probability of the ground state is reduced and the transition starts to be saturated when the pump tones are turned on.

Again, the observed transition frequencies are in good agreement with the calculated dressed state transition energies indicated by vertical arrows in Figs. 8.11 a and b. Additional spectral lines with low intensity, see Fig. 8.11 a and b blue lines, occur because of a small probability of occupation of the first doublet due to the residual thermal field, see Section 8.3. The transition $|f,0\rangle \rightarrow |f,1\rangle$ is not observed because the level $|f,0\rangle$ is neither thermally, nor coherently populated here.

8.5   Conclusion

Our experiments clearly demonstrate the quantum non-linearity of a system of one, two and three photons strongly coupled to a single artificial atom in a cavity QED setting. Both symmetric and antisymmetric superposition states involving two and three photons are resolved by tens of linewidths. In our circuit QED system, excited states $|n\pm\rangle$ with $n > 2$ are observable by pumping the system with thermal photons, by applying coherent drive fields in a pump and probe scheme and also by applying strong drive fields which induce multi-photon transitions, see [Bishop09]. We have also observed that higher excited states of the artificial atom induce energy shifts in the coupled atom-photon states. These shifts should also be observable in time-resolved measurements of Rabi-oscillations with photon number states.

The observed very strong nonlinearity on the level of single or few quanta could be used for the realization of a single photon transistor, parametric down-conversion, and for the generation and detection of individual microwave photons. A more detailed quantitative analysis of the thermally excited vacuum Rabi spectra could be of interest in the context of environmentally induced dissipation and decoherence, thermal field sensing and the cross-over from the quantum to the classical regime of cavity QED, see Chapter 10. Related results have been reported in an atomic system [Schuster08] and similar effects may be interesting to approach also in semiconducting cavity QED systems.

COLLECTIVE MULTI-QUBIT INTERACTION

We present an ideal realization of the Tavis-Cummings model in the absence of atom number and coupling fluctuations by embedding a discrete number of fully controllable superconducting qubits at fixed positions into a transmission line resonator. Measuring the vacuum Rabi mode splitting with one, two and three qubits strongly coupled to the cavity field, we explore both bright and dark dressed collective multi-qubit states and observe the discrete $\sqrt{N}$ scaling of the collective dipole coupling strength. Our experiments demonstrate a novel approach to explore collective states, such as the W-state, in a fully globally and locally controllable quantum system. Our scalable approach is interesting for solid-state quantum information processing and for fundamental multi-atom quantum optics experiments with fixed atom numbers.

9.1 Introduction

In the early 1950's, Dicke realized that under certain conditions a gas of radiating molecules shows the collective behavior of a single quantum system [Dicke54]. The idealized situation in which N two-level systems with identical dipole coupling are resonantly interacting with a single mode of the electromagnetic field was analyzed by Tavis and Cummings [Tavis68]. This model predicts the collective N-atom interaction strength to be $G_N = g_j\sqrt{N}$, where g_j is the dipole coupling strength of each individual atom j. In fact, in first cavity QED experiments the normal mode splitting, observable in the cavity transmission spectrum [Agarwal84, Leslie04], was demonstrated with on average $\bar{N} > 1$ atoms in optical [Raizen89, Zhu90] and microwave [Bernardot92] cavities to overcome the relatively weak dipole coupling g_j. The $\sqrt{N}$ scaling has been observed in the regime of a small mean number of atoms $\bar{N}$ with dilute atomic beams [Bernardot92, Childs96, Thompson98] and fountains [Münstermann00] crossing a high-finesse cavity. In these

experiments, spatial variations of the atom positions and Poissonian fluctuations in the atom number inherent to an atomic beam [Childs96, Carmichael99, Leslie04] are unavoidable. In a different limit where the cavity was populated with a very large number of ultra-cold ^{87}Rb atoms [Tuchman06] and more recently with Bose-Einstein condensates [Brennecke07, Colombe07] the $\sqrt{N}$ nonlinearity was also demonstrated. However, the number of interacting atoms is typically only known to about $\sim 10\%$ [Brennecke07].

Here we present an experiment in which the Tavis-Cummings model is studied for a discrete set of fully controllable artificial atoms at fixed positions and with virtually identical couplings to a resonant cavity mode. The investigated situation is sketched in Fig. 9.1 a, depicting an optical analog where three two-state atoms are deterministically positioned at electric field antinodes of a cavity mode where the coupling is maximum.

9.1.1 Experimental setup

In our circuit QED [Wallraff04, Schoelkopf08] realization of this configuration (Fig. 9.1 b), three transmon-type [Koch07a] superconducting qubits are embedded in a microwave resonator which contains a quantized radiation field. The cavity is realized as a coplanar waveguide resonator with a first harmonic full wavelength resonance frequency of $\omega_{\mathrm{r}}/2\pi = 6.729$ GHz and a photon decay rate of $\kappa/2\pi = 6.8$ MHz. The qubits are positioned at the antinodes of the first harmonic standing wave electric field. The transition frequency between ground $|g\rangle$ and first excited state $|e\rangle$ of qubit j, approximately given by $\omega_j \approx \sqrt{8E_{\mathrm{C}_j}E_{\mathrm{J}_j}(\Phi_j)}/\hbar - E_{\mathrm{C}_j}/\hbar$, is controllable through the flux dependent Josephson energy $E_{\mathrm{J}_j}(\Phi_j) = E_{\mathrm{J}\max_j}|\cos(\pi\Phi_j/\Phi_0)|$ [Koch07a]. Here E_{C_j} is the single electron charging energy, $E_{\mathrm{J}\max_j}$ the maximum Josephson energy at flux $\Phi_j = 0$ and Φ_0 the magnetic flux quantum. Effectively independent flux control of each qubit is achieved by applying magnetic fields with three external miniature current biased coils (Fig. 9.2 a) where we take
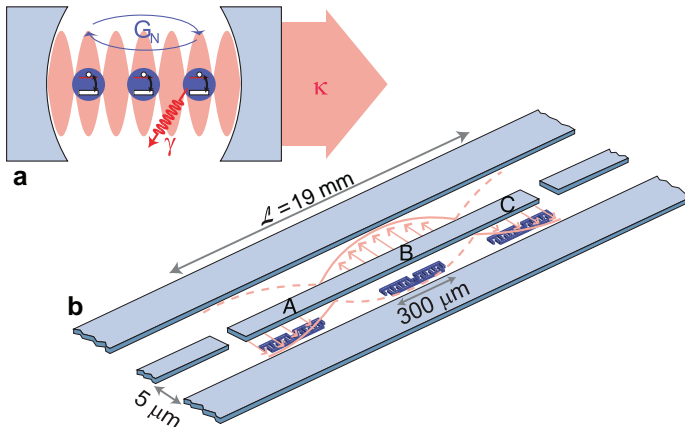
Figure 9.1: **Schematic of the experimental setup. a**, Optical analog. Three two-state atoms are identically coupled to a cavity mode with photon decay rate κ, atomic energy relaxation rate γ and collective coupling strength G_{N}. **b**, Schematic of the investigated system. The coplanar waveguide resonator is shown in light blue, the transmon qubits A, B and C in violet and the first harmonic of the standing wave electric field in red.

into account all cross-couplings, see Table 9.1, by inverting the full coupling matrix

$$\begin{pmatrix} \Phi_A \\ \Phi_B \\ \Phi_C \end{pmatrix} = \begin{pmatrix} 1/\Phi_{0_{aA}} & 1/\Phi_{0_{bA}} & 1/\Phi_{0_{cA}} \\ 1/\Phi_{0_{aB}} & 1/\Phi_{0_{bB}} & 1/\Phi_{0_{cB}} \\ 1/\Phi_{0_{aC}} & 1/\Phi_{0_{bC}} & 1/\Phi_{0_{cC}} \end{pmatrix} \begin{pmatrix} V_a \\ V_b \\ V_c \end{pmatrix} + \begin{pmatrix} \Phi_{off_A} \\ \Phi_{off_B} \\ \Phi_{off_C} \end{pmatrix}. \tag{9.1}$$

Optical images of the investigated sample are depicted in Fig. 9.2 b and c. The resonator was fabricated employing optical lithography and aluminum evaporation techniques on a Sapphire substrate. All qubits were fabricated with electron beam lithography and standard Al/AlO$_x$/Al shadow evaporation techniques. Table 9.2 states the individual qubit parameters obtained from spectroscopic measurements.

9.1.2 Tavis-Cummings model

The physics of our system is described by the Tavis-Cummings Hamiltonian [Tavis68]

$$\hat{\mathcal{H}}_{TC} = \hbar\omega_r \hat{a}^\dagger \hat{a} + \sum_j \left(\frac{\hbar}{2} \omega_j \hat{\sigma}_j^z + \hbar g_j (\hat{a}^\dagger \hat{\sigma}_j^- + \hat{\sigma}_j^+ \hat{a}) \right), \tag{9.2}$$

where g_j is the coupling strength between the field and qubit j. $\hat{a}^\dagger$ and $\hat{a}$ are the creation and annihilation operators of the field, $\hat{\sigma}_j^+$ and $\hat{\sigma}_j^-$ are the corresponding operators acting on the qubit j, and $\hat{\sigma}_j^z$ is a Pauli operator. The ground state $|g,g,g\rangle \otimes |0\rangle$ of the three-qubit/cavity system is prepared by cooling the microchip to a temperature of 20 mK in a dilution refrigerator.
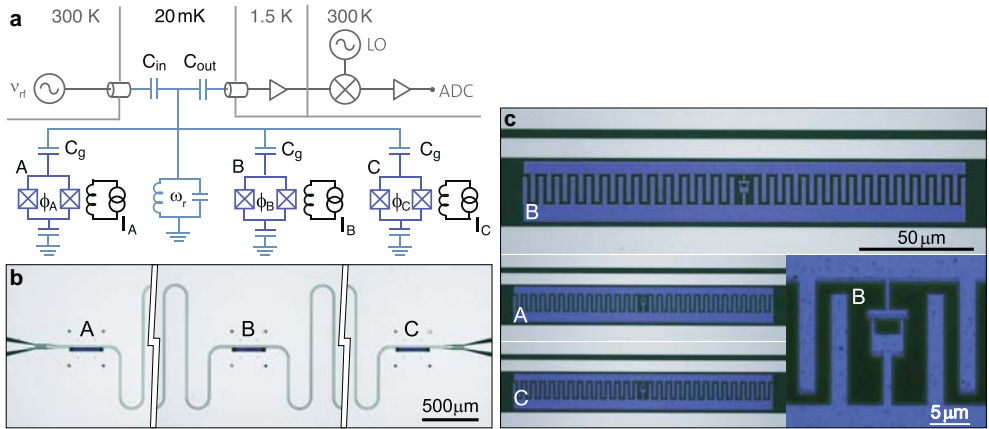
Figure 9.2: **Circuit diagram and false color optical images of the sample. a,** Simplified electrical circuit diagram of the experimental setup. The waveguide resonator operated at a temperature of 20 mK, indicated as LC oscillator with frequency ω_r, is coupled to input and output leads with the capacitors C_{in} and C_{out}. Qubits A, B and C are controlled with external current biased coils ($I_{A,B,C}$) and coupled to the resonator via identical capacitors C_g. A transmission measurement is performed by applying a measurement tone ν_{rf} to the input port of the resonator, amplifying the transmitted signal and digitizing it with an analog-to-digital converter (ADC) after down-conversion with a local oscillator (LO) in a heterodyne detection scheme. **b,** The coplanar microwave resonator is shown truncated in gray (substrate in dark green) and the locations of qubits A, B and C are indicated. **c,** Top, magnified view of transmon qubit B (violet) embedded between ground plane and center conductor of the resonator. Bottom left, qubits A and C, of same dimensions as qubit B, are shown at reduced scale. Bottom right, magnified view of SQUID loop of qubit B.

9.2   Collective dipole coupling

First we investigate the resonant coupling of the $|g\rangle$ to $|e\rangle$ transition of qubit A to the first harmonic mode of the resonator. We measure the anti-crossing between qubit A (ν_A) and the cavity (ν_r) by populating the resonator with much less than a photon on average. We record the resulting transmission spectrum T versus magnetic flux Φ_A controlled detuning of qubit A (Fig. 9.3 a). Qubits B and C remain maximally detuned from the resonator at $\Phi_B = \Phi_C = \Phi_0/2$ where they do not affect the measurement. At finite detuning (left hand side of Fig. 9.3 a) we observe a shift of the resonator spectrum which increases with decreasing detuning due to the dispersive interaction with qubit A.

On resonance ($\omega_j = \omega_r$) and in the presence of just one two level system ($N = 1$), Eq. (9.2) reduces to the Jaynes-Cummings Hamiltonian [Jaynes63]. The eigenstates $|N, n \pm\rangle$ of this system in the presence of a single excitation $n = 1$ are the symmetric and anti-symmetric qubit-photon superpositions $|1, 1\pm\rangle = 1/\sqrt{2}\,(|g, 1\rangle \pm |e, 0\rangle)$ (Fig. 9.4 a) where the excitation is equally shared between qubit and photon. Accordingly, we observe a clean vacuum Rabi mode splitting spectrum formed by the states $|1, 1\pm\rangle$ (Fig. 9.3 b). From analogous measurements performed on qubits B and C (not shown) we obtain the single qubit coupling constants g_j listed in Table 9.2. The magnitudes of the coupling strengths are virtually identical with a scatter of only a few MHz. The strong coupling of an individual photon and an individual two-level system has been observed in a wealth of different realizations of cavity QED both spectroscopically [Wallraff04, Boca04, Khitrova06] and in time-resolved experiments [Brune96, Hofheinz08]. The regime of multiple excitations n which proves field quantization in these systems has been reported both in the time-resolved results cited above and more recently also in spectroscopic measurements [Schuster08, Fink08, Bishop09].

In a next step, we maintain qubit A at degeneracy ($\nu_A = \nu_r$), where we observed the one-photon one-qubit doublet (see left part of Fig. 9.3 c). Qubit B remains far detuned ($\Phi_B = \Phi_0/2$) for the entire measurement. Qubit C is then tuned through the already cou-

Qubit	Φ_{0_a} (V)	Φ_{0_b} (V)	Φ_{0_c} (V)	$\Phi_{off}(\Phi_0)$
A	-6.55	7.36	-228	-0.018
B	-31.8	6.67	59.0	-0.027
C	250	5.47	5.28	-0.430

Table 9.1: Coil-coupling parameters and flux offsets of three qubits coupled to three superconducting coils. The stated values are obtained from flux dependent spectroscopy.

Qubit j	E_{C_j}/h (MHz)	$E_{J_{max\,j}}/h$ (GHz)	$g_j/2\pi$ (MHz)
A	283	224	83.7
B	287	226	-85.7
C	294	214	85.1

Table 9.2: Qubit and qubit-resonator coupling parameters. The single electron charging energy E_{C_j}, the maximum Josephson energy $E_{J_{max\,j}}$ extracted from spectroscopic measurements and the coupling strengths g_j obtained from resonator transmission measurements for qubits A, B and C.
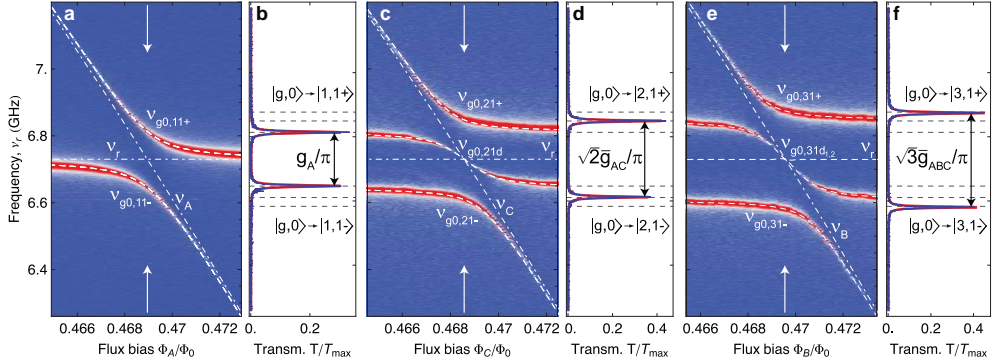
Figure 9.3: **Vacuum Rabi mode splitting with one, two and three qubits. a**, Measured resonator transmission spectrum T (blue, low and red, high transmission) versus normalized external flux bias Φ_A/Φ_0 of qubit A. Dash-dotted white lines indicate bare resonator ν_r and qubit ν_A frequencies and dashed white lines are calculated transition frequencies $\nu_{g0,Nn\pm}$ between $|g,0\rangle$ and $|N,n\pm\rangle$. **b**, Resonator transmission $T/T_{\max}$ at degeneracy normalized to the maximum resonator transmission $T_{\max}$ measured at $\Phi_{A,B,C} = \Phi_0/2$ (not shown), as indicated with arrows in panel a. Red line is a fit to two Lorentzians. **c**, Resonator transmission spectrum $T/T_{\max}$ versus external flux bias Φ_C/Φ_0 of qubit C with qubit A degenerate with the resonator ($\nu_A = \nu_r$). **d**, Transmission spectrum $T/T_{\max}$ at flux as indicated in panel c. **e**, Transmission spectrum versus flux Φ_B/Φ_0 with both qubits A and C at degeneracy ($\nu_A = \nu_C = \nu_r$). The white dashed line at frequency $\nu_{g0,31d_{1,2}} = \nu_r$ indicates the dark state occurring at degeneracy. **f**, Transmission spectrum $T/T_{\max}$ at flux indicated in panel e.

pled states from lower to higher values of flux Φ_C. In this case, the doublet states $|1,1\pm\rangle$ of qubit A are found to be dispersively shifted due to non-resonant interaction with qubit C (Fig. 9.3 c). When both qubits and the resonator are exactly in resonance, the transmission spectrum T (Fig. 9.3 d) shows only two distinct maxima corresponding to the doublet $|2,1\pm\rangle = 1/\sqrt{2}\,|g,g\rangle \otimes |1\rangle \pm 1/2\,(|e,g\rangle + |g,e\rangle) \otimes |0\rangle$ with eigenenergies $\hbar(\omega_r \pm G_2)$. Here a single excitation is shared between one photon, with probability $1/2$, and two qubits, with probability $1/4$ each (Fig. 9.4 b). Both states have a photonic component and can be excited from the ground state $|g,g,g\rangle \otimes |0\rangle$ by irradiating the cavity with light. These are thus referred to as bright states. In general we expect $N + n = 3$ eigenstates for two qubits and one photon. The third state $|2,1d\rangle = 1/\sqrt{2}(|e,g\rangle - |g,e\rangle) \otimes |0\rangle$ with energy $\hbar\omega_r$ at degeneracy has no matrix element with a cavity excitation and is referred to as a dark state. Accordingly we observe no visible population in the transmission spectrum at frequency ν_r at degeneracy. In this regime the two qubits behave like one effective spin with the predicted [López07a] coupling strength $G_2 = \sqrt{2}\,\overline{g}_{AC}$ with $\overline{g}_{AC} = \sqrt{1/2(g_A^2 + g_C^2)}$, which is indicated by dashed black lines in Fig. 9.3 d. This prediction is in very good agreement with our measurement.

Following the same procedure, we then flux tune qubit B through the already resonantly coupled states of qubits A, C and the cavity ($\nu_A = \nu_C = \nu_r$), (Fig. 9.3 e). We observe the energies of three out of $N + n = 4$ eigenstates, the fourth one being dark, for a range of flux values Φ_B. Starting with the dark state $|2,1d\rangle$ at frequency ν_r and the doublet $|2,1\pm\rangle$ (left part of Fig. 9.3 e), the presence of qubit B dresses these states and shifts the doublet $|2,1\pm\rangle$ down in frequency. Again one of these states turns dark as it approaches degeneracy where it is entirely mixed with qubit B. At degeneracy we identify two bright doublet states
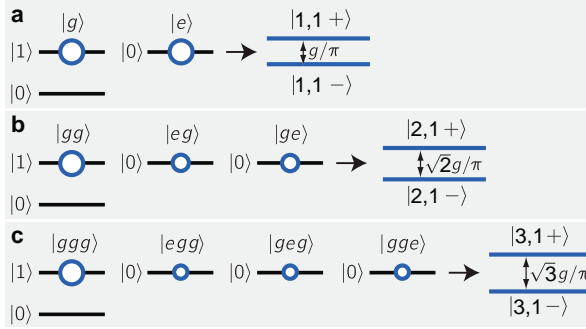
Figure 9.4: **Level diagram representing the total energy of one (a) two (b) and three qubits (c) resonantly coupled to a single photon.** Bare energy levels of the qubits $|g\rangle$, $|e\rangle$ and the cavity $|0\rangle$, $|1\rangle$ are shown in black. The bright dressed energy levels $|N, n\pm\rangle$, with N the number of qubits, n the number of excitations and $\pm$ indicating the symmetry of the state, are illustrated in blue. The areas of the circles indicate the relative population of the bare states in the eigenstates $|N, n\pm\rangle$.

$|3, 1\pm\rangle = 1/\sqrt{2}\,|g, g, g\rangle \otimes |1\rangle \pm 1/\sqrt{6}\,(|e, g, g\rangle - |g, e, g\rangle + |g, g, e\rangle) \otimes |0\rangle$ (Fig. 9.4 c). The part of the states $|3, 1\pm\rangle$ carrying the atomic excitation is a so called W-state, in which a single excitation is equally shared among all N qubits [Dür00]. Both $|3, 1\pm\rangle$ states are clearly visible in the transmission spectrum shown in Fig. 9.3 f.

In addition, there are two dark states $|3, 1d_1\rangle = 1/\sqrt{2}(|e, g, g\rangle - |g, g, e\rangle) \otimes |0\rangle$ and $|3, 1d_2\rangle = 1/\sqrt{2}(|g, e, g\rangle + |g, g, e\rangle) \otimes |0\rangle$ which do not lead to resonances in the transmission spectrum at degeneracy. In general all $N + n - 2$ dark states are degenerate at energy $\hbar\omega_r$. The symmetries of the dressed three-qubit states are determined by the signs of the coupling constants $g_A \approx -g_B \approx g_C$. While our measurement is not sensitive to the sign of coupling, it is a simple consequence of the phase shift of the electric field mode by π between the ends and the center of the resonator. Again, the observed transmission peak frequencies are in agreement with the calculated splitting of the doublet $G_3 = \sqrt{3}\,\overline{g}_{ABC}$ (dashed black lines in Fig. 9.3 f). Also at finite detunings the measured energies of all bright states are in excellent agreement with the predictions based on the Tavis-Cummings model (dashed white lines in Fig. 9.3 a, c, e) using the measured qubit and resonator parameters. We have also performed analogous measurements of all twelve one, two and three qubit anti-crossings (nine are not shown) and find equally good agreement.

In Fig. 9.5 all twelve measured coupling strengths (blue dots) for one, two and three qubits at degeneracy are plotted *vs.* N. Excellent agreement with the expected collective interaction strength $G_N = \sqrt{N}\,\overline{g}_{ABC}$ (red line) is found without any fit parameters and $\overline{g}_{ABC} = 84.8$ MHz.

9.3   Summary

Our spectroscopic measurements clearly demonstrate the collective interaction of a discrete number of quantum two-state systems mediated by an individual photon. All results are in good agreement with the predictions of the basic Tavis-Cummings model in
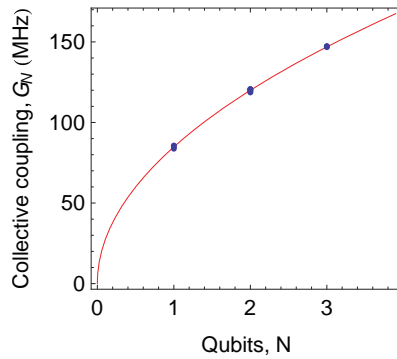
Figure 9.5: **Scaling of the collective dipole coupling strength.** Measured coupling constants (blue dots) extracted from Fig. 9.3 and nine similar data sets and theoretical scaling (red line).

the absence of any number, position or coupling fluctuations. The presented approach may enable novel investigations of super- and sub-radiant states of artificial atoms. Flux tuning on nanosecond timescales should furthermore allow the controlled generation of Dicke states [Stockton04, López07b] and fast entanglement generation via collective interactions [Tessier03, Retzker07], not relying on individual qubit operations. This could be used for quantum state engineering and an implementation of Heisenberg limited spectroscopy [Leibfried04] in the solid state.

QUANTUM-TO-CLASSICAL TRANSITION

The quantum properties of electromagnetic, mechanical or other harmonic oscillators can be revealed by investigating their strong coherent coupling to a single quantum two level system in an approach known as cavity quantum electrodynamics (QED). At temperatures much lower than the characteristic energy level spacing the observation of vacuum Rabi oscillations or mode splittings with one or a few quanta asserts the quantum nature of the oscillator. Here, we study how the classical response of a quantum cavity QED system emerges from the quantum one when its thermal occupation – or effective temperature – is raised gradually over 5 orders of magnitude. In this way we explore in detail the continuous quantum-to-classical cross-over in the spirit of Bohr's correspondence principle. We also demonstrate how to extract effective cavity field temperatures from both spectroscopic and time-resolved vacuum Rabi measurements.

10.1 Introduction

Cavity QED [Haroche06] enables the study of the nature of matter light interactions in exquisite detail. It realizes an open quantum system in which the coupling to the environment is highly controllable. In a circuit realization of cavity QED [Wallraff04], we carefully investigate the quantum-to-classical transition of a harmonic oscillator strongly coupled to a two level system by increasing the effective oscillator temperature. From measured vacuum Rabi splitting spectra and from time-resolved vacuum Rabi oscillations we consistently extract effective cavity field temperatures between 100 mK and a few Kelvin using a quantum master equation model as suggested in Ref. [Rau04]. The dissipative quantum-to-classical cross-over of a field mode coupled to a qubit was also studied theoretically in Ref. [Everitt09]. The emergence of classical physics from quantum mechanics

and the role of decoherence in this process is an important subject of current research [Schlosshauer07].

10.1.1 Experimental setup

In our experiments a superconducting artificial atom is strongly coupled to a coplanar transmission line resonator to realize a circuit QED system [Wallraff04]. The transmon qubit [Koch07a] consists of two superconducting aluminum thin films weakly connected by two Josephson tunnel junctions. Its ground $|g\rangle$ and excited state $|e\rangle$ differ by the specific charge configuration of the two superconducting islands. The transition frequency $\nu_{g,e} \simeq \sqrt{8E_C E_J(\Phi)} - E_C$ is determined spectroscopically. Here, $E_C/h \approx 0.502$ GHz is the single electron charging energy, $E_J(\Phi) = E_{J,max}|\cos(\pi\Phi/\Phi_0)|$ the flux controlled Josephson energy with $E_{J,max}/h \approx 14.4$ GHz and Φ_0 is the superconducting flux quantum. The cavity has a bare resonance frequency of $\nu_r \approx 6.44$ GHz and a coupling limited photon decay rate of $\kappa/(2\pi) \approx 3.2$ MHz. Optical microscope images of the sample are shown in Fig. 10.1 a.

In our experimental setup, see Fig. 10.1 b, the coupled qubit/cavity system is prepared in its ground state $|g,0\rangle$, see Fig. 10.2 a, with close to $n = 0$ photons in the resonator by cooling the sample to below 20 mK in a dilution refrigerator. Instead of increasing the physical temperature of the sample to control the thermal occupation of the cavity, we apply thermal radiation only at its input. We approximate the one-dimensional Planck spectrum of the thermal field as constant with a power spectral density S_n in the small relevant bandwidth around ν_r. S_n is controlled by applying broadband microwave frequency white noise of controlled amplitude. In this case, we can assign an intra-cavity thermal photon number $n_{th} = [\exp(\hbar\omega_r/k_B T_c) - 1]^{-1}$ and thus an equivalent cavity field temperature T_c to the externally applied white noise. Owing to the high internal quality factor of the resonator, the field does not thermalize on the chip, which allows us to control the effective temperature of the resonator field to up to $T_c \sim 100$ K. In addition our setup allows for the phase sensitive detection of the quadrature amplitudes of a weak coherent probe tone that populates the resonator with $n_{probe} \lesssim 0.1$ photons on average while effectively rejecting all uncorrelated thermal radiation from the detection system.
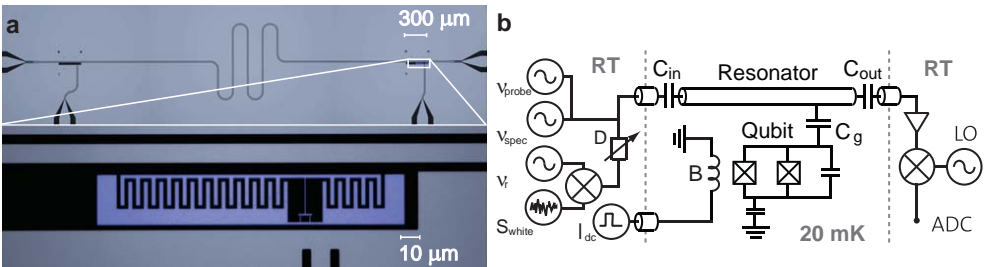
Figure 10.1: **Experimental setup. a**, Coplanar microwave resonator with two qubit slots and flux bias lines (top) and a single embedded qubit (violet) shown on an enlarged scale (bottom). **b**, Circuit diagram of setup. Input (left) is at room temperature (RT) with microwave sources for measurement (ν_{probe}), qubit spectroscopy and qubit drive (ν_{spec}), variable attenuation (D) quasi thermal field source (S_{white}) at ν_r and an arbitrary waveform generator for fast flux biasing (I_{dc}) through the on-chip flux line (B). At 20 mK the qubit is coupled via a capacitance C_g to the transmission line resonator between the capacitances C_{in} and C_{out}. The transmitted microwave tone is amplified, down-converted with a local oscillator (LO) and digitized (ADC).

10.1.2 Vacuum Rabi splitting

At the lowest measured cavity field temperature $T_c \sim 100\,\text{mK}$, a clear vacuum Rabi mode splitting is observed in a linear response cavity transmission measurement, see Fig. 10.2 c (dark blue lines). Two Lorentzian lines characteristic for the dressed states $|n, \pm\rangle = (|g, n\rangle \pm |e, n - 1\rangle)/\sqrt{2}$ with excitation number $n = 1$ separated by twice the dipole coupling strength $g_{g,e}/(2\pi) = 54\,\text{MHz}$ are clearly observed at the frequencies $\nu_{g0,1\pm}$. This indicates that the strong coupling regime, $g_{g,e} \gg \kappa,\ \gamma$, with the qubit relaxation rate $\gamma/(2\pi) \approx 0.6\,\text{MHz}$, is realized.

While the observation of the simple vacuum Rabi mode splitting for $n = 1$ could in principle be interpreted as a normal mode splitting using a semiclassical model, the observation of additional transitions to higher excited dressed states with coupling increased by a factor $\sqrt{n}$ [Schuster08, Fink08, Bishop09, Fink09a] is an unambiguous signature for the quantum nature of the system [Agarwal86, Agarwal91, Tian92], see also Chapter 8. In our experiment these transitions are observed at frequencies $\nu_{1\pm,2\pm}$, see the level diagram in Fig. 10.2 a and measurements in Fig. 10.2 c (green lines) [and Fig. 10.3 a (blue and green lines)], when slightly increasing the effective cavity temperature and thus populating excited states of the Jaynes-Cummings ladder. In this case the weak coherent probe tone excites transitions between higher levels.

10.2 Strong quasi-thermal excitation

At high temperatures the Jaynes-Cummings system is excited to high quantum numbers and many transitions can be accessed by the weak probe tone [Agarwal86, Agarwal91, Cirac91, Tian92, Rau04]. The resulting linear response transmission spectrum can be understood as a sum of individual level to level transitions that overlap. At a mean thermal photon number of $n_{th} > 1$ the transitions from the ground state $\nu_{g0,1\pm}$ are almost saturated and therefore only weakly contribute to the observed cavity transmission spectrum (Fig. 10.2 c, yellow lines). At even larger effective temperatures all available transition frequencies are densely spaced close to the resonator frequency, see level diagram in Fig. 10.2 b and measurement in Fig. 10.2 c (red lines). At these temperatures all transitions which would show the nonlinear $\sqrt{n}$ signature of the single qubit–photon interaction are saturated and the transmission spectrum does not carry any information about the intrinsic quantum nature of the system.

10.2.1 The high temperature limit

The resulting harmonic spectrum resembles that of two uncoupled linear oscillators, a situation where not the absolute energies but the energy differences of the system are degenerate [vandenBrink02, Rau04]. In contrast to the regime of strong coherent driving, where non-classicality can persist at large excitation numbers [Alsing91, Armen09], the phase noise of the thermal field used in our experiments renders the two high-excitation dressed-state ladders indistinguishable. As a result, at high temperatures the spectrum is that of a classical resonator and we find excellent agreement with a Lorentzian line fit of width $\kappa_{eff}/(2\pi) = 4\,\text{MHz}$ close to the intrinsic resonator line width (Fig. 10.2 c, black line).
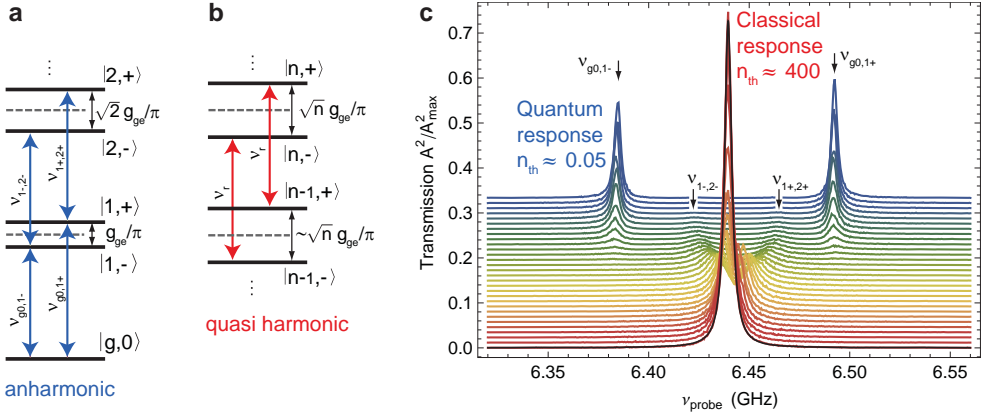
Figure 10.2: **Quantum-to-classical transition of the vacuum Rabi splitting spectrum. a**, Energy level diagram of dipole coupled dressed states $|n, \pm\rangle$ for excitation numbers $n = 0$, 1 and 2 (black lines), uncoupled qubit and cavity energies (grey dashed lines) and allowed transitions at frequencies $\nu_{g0,1\pm}$ and $\nu_{1\pm,2\pm}$ (blue arrows). **b**, Dressed state diagram for large excitation numbers $n > 280$ and allowed transitions at the resonator frequency ν_r (red arrows). **c**, Measured cavity transmission A^2/A_{max}^2 for intra-cavity thermal photon numbers 0.05 (blue) $\lesssim n_{th} \lesssim 400$ (red) and a fit to a Lorentzian line (black). Measured data sets are normalized to the transmission amplitude A_{max} obtained when the qubit is maximally detuned. The data is offset and colored for better visibility, see inset in Fig. 10.4 for color code.

10.2.2   Quantitative model

A quantitative understanding of the measured results is obtained by numerically solving the Markovian master equation

$$\mathscr{L}[\hat{\rho}] = -\frac{i}{\hbar}[\hat{\mathscr{H}}, \hat{\rho}] + (n_{th} + 1)\kappa\mathscr{D}[\hat{a}]\hat{\rho} + \gamma\,\mathscr{D}\left[\sum_{l=e,f,\dots}\frac{g_{l-1,l}}{g_{g,e}}\,\hat{\sigma}_{l-1,l}\right]\hat{\rho} + n_{th}\kappa\mathscr{D}[\hat{a}^\dagger]\hat{\rho}, \quad (10.1)$$

where the thermal photon number n_{th} or equivalently the cavity field temperature T_c is extracted as the only fit parameter. Here the coherent dynamics is described by the Jaynes-Cummings Hamiltonian $\hat{\mathscr{H}}$ with l transmon levels, see [Koch07a], and without a drive term, which is justified in the linear response limit. The three damping terms model the loss of cavity photons at rate κ, the intrinsic relaxation of the transmon excited state $|e\rangle$ at rate γ and the creation of cavity photons due to a thermal bath with occupation n_{th}. $\mathscr{D}$ is the usual Lindblad damping superoperator. Note that neither qubit dephasing nor an independent qubit thermal bath has significant influence on the agreement between the theory and the presented spectroscopic results. Therefore, these two terms have been omitted. Equation (10.1) is solved by exact diagonalization and the transmission spectrum is calculated as $A/A_{max} = (\kappa + \gamma)/2 \langle a^\dagger a\rangle / n_{th}$, using similar methods as in Ref. [Rau04].

We observe that the measured and calculated spectra agree very well over a large range of applied thermal noise powers (Fig. 10.3). This allows to extract the effective cavity field temperature (Fig. 10.4). However, for mean thermal photon numbers $n_{th} \gtrsim 30$ the accuracy of our numerical calculations is limited by the finite size of the Hilbert space spanned by 200 resonator states and 6 transmon states. In the large photon number limit the qubit
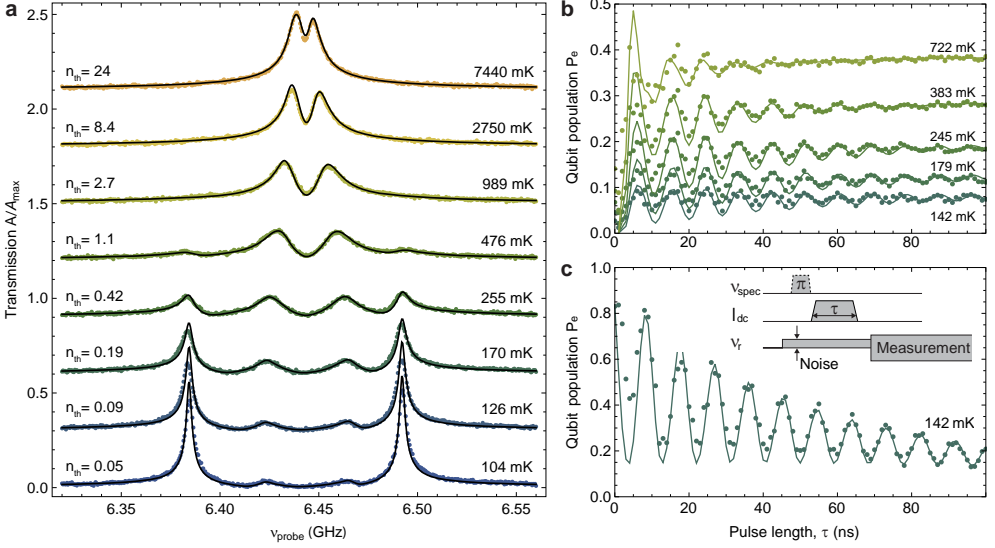
Figure 10.3: **Quantitative analysis of elevated temperature Rabi mode splittings and vacuum Rabi oscillations.** **a**, Measured (dots) and calculated (lines) cavity transmission (same data as in Fig. 2 c) shown for applied $S_n = -221.5$ dBm/Hz (bottom) to -190 dBm/Hz (top) in steps of 4.5 dBm/Hz. Extracted thermal photon numbers n_{th} and cavity temperatures T_c are indicated. **b**, Measured qubit excited state population P_e as a function of the resonant cavity interaction time τ (dots) and master equation simulation (lines) for $S_n = -214$ dBm/Hz to -202 dBm/Hz in steps of 3 dBm/Hz. **c**, Similar measurement as in (b) with qubit prepared in the excited state for $S_n = -214$ dBm/Hz. Inset: Vacuum Rabi pulse sequence.

only negligibly perturbs the empty cavity Lorentzian spectrum [Fig. 10.2 c], because the cavity and cavity dissipation terms in Eq. (10.1) scale linearly with n, while the qubit photon coupling term scales only with $\sqrt{n}$, see also [Savage89]. In the limit where the coupling is smaller than the damping $\sqrt{n}g_{g,e} < n\kappa$ the dominant terms in Eq. Eq. (10.1) describe a damped harmonic oscillator with a Lorentzian spectrum. A classical harmonic oscillator is furthermore a good description of our cavity QED system if the relative $\sqrt{n}$ nonlinearity, i.e. the frequency shift due to the qubit, is smaller than the relevant dissipation rate $2g_{g,e}(\sqrt{n+1} - \sqrt{n}) < \kappa$. For large photon numbers these two criteria are equivalent and in our experiment, the classical limit is entered for mean thermal photon numbers $n_{th} > (g_{g,e}/\kappa)^2 \approx 280$.

10.2.3 Time domain measurements

We have also performed time domain vacuum Rabi oscillation measurements in the presence of thermal photons. In these experiments, we first detune the qubit from the resonator by 0.5 GHz where the applied quasi thermal noise is both filtered and largely reflected from the resonator and does not affect the qubit state. We then apply an amplitude shaped current pulse I_{dc} via an on-chip flux line, see sample and setup in Fig. 10.1, to tune the qubit into resonance with the cavity field for a variable time τ, see pulse sequence in inset of Fig. 10.3 c. The qubit excited state population P_e is then determined in a dispersive measurement [Bianchetti09].

For the lowest cavity temperatures we observe low contrast, long coherence vacuum Rabi oscillations induced by the weak thermal field only, see Fig. 10.3 b. When the number of thermal photons is increased the amplitude of the coherent oscillations increases while their coherence time decreases, which is expected for a thermal distribution of photon numbers. At long interaction times τ, the qubit population shows a temperature dependent saturation that approaches the value of 0.5 when the qubit is strongly driven by the thermal field at high temperatures. We have repeated the experiment preparing the qubit initially in the excited state using a π-pulse and measuring vacuum Rabi oscillations at low applied noise power, see Fig. 10.3 c. In this case high contrast oscillations are observed albeit with a small offset in the qubit population visible at large τ caused by the thermal field. From these data the cavity temperature has been extracted by solving a time dependent master equation, see solid lines in Figs. 10.3 b and c. In this case 2 qubit states and up to 6 cavity states are considered and qubit dephasing is included. The deviations at short times τ are due to imperfections in the qubit flux tuning pulses.

10.2.4   Extraction of the effective field temperature

The cavity field temperatures T_c extracted from both spectroscopic (full dots) and time-resolved measurements (crosses) plotted on a logarithmic scale versus the applied noise spectral density S_n are in close agreement (Fig. 10.4). Both data sets are explained consistently considering that the cavity thermal photon number $n_{th} = S_n/\hbar\omega + n_0$ is the sum of the applied quasi thermal noise $S_n/\hbar\omega$ expressed as a photon number and a small thermal background field of $n_0 = 0.04$ photons[1] ($T_0 = 95$ mK). The measured intra-cavity photon number n_{th} is consistent with the noise applied to the input of our setup and the expected attenuation of the line and also with calibration measurements based on the known qubit ac-Stark shift [Schuster05]. The background photon number is due to incomplete thermalization of the input line and can easily be decreased by adding additional cold attenuation.

The inset of Fig. 10.4 shows an extrapolation of the temperature to the largest applied noise powers and provides a calibration for the measurements shown in Fig. 10.2 c where the same color code is used (also used in Figs. 10.3 and 10.4). Accordingly, the measurements at the highest temperatures were conducted with approximately ~ 370 thermal photons in the cavity. This corresponds to an effective cavity temperature of $T_c \sim 115$ K. We clearly observe the transition to a classical harmonic resonator at $n_{th} \approx 370 > (g_{g,e}/\kappa)^2 \approx 280$ as indicated by the Lorentzian spectrum in Fig.10.2 c.

10.3   Conclusion

We have demonstrated a quantitative understanding of the transition from the quantum to the classical response of a cavity QED system. Moreover, we have presented a viable approach to measure the temperature of an electromagnetic field in a cavity over a wide

---

[1]In more recent experiments an additional attenuation of -10 dB was added on the resonator input line at 20 mK, see setup in Fig. 4.1. This reduced the background photon number by almost one order of magnitude. In fact, in the measured transmission spectrum we cannot resolve any two photon dressed states. Using the model Eq. (10.1) we therefore can only state an upper bound of $n_0 \lesssim 0.005$.
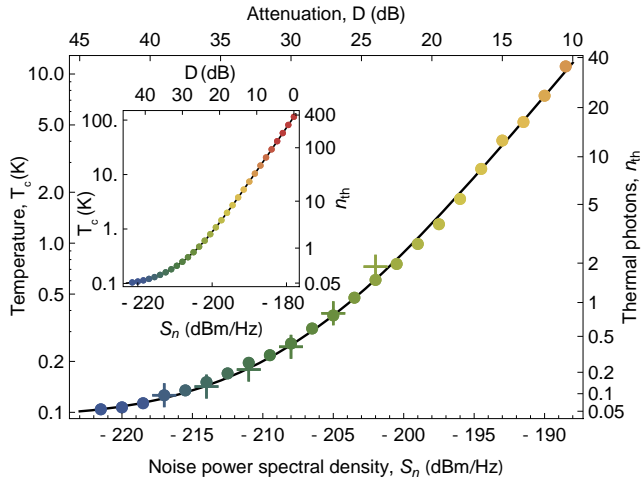
Figure 10.4: **Temperature sensing measurement.** Resonator field temperature T_c and photon number n_{th} extracted from measured Rabi spectra (full dots) and Rabi oscillations (crosses) versus noise power spectral density S_n or equivalently attenuation D. Theory (black line). Inset: extrapolation to higher T_c provides temperature scale (color coded) for the measurements shown in Figs. 10.2 c and 10.3.

range. A different approach to extract the resonator temperature in the dispersive regime of circuit QED has been proposed [Clerk07] and measurements of the qubit temperature have been demonstrated [Palacios-Laloy09]. Related experiments have been performed in the optical domain using a semiconductor cavity QED system [Laucht09]. In these systems, entanglement and decoherence at elevated temperatures can be studied in future experiments in the context of quantum information.

CONCLUSION AND PROSPECTS

We have successfully installed and characterized the experimental infrastructure necessary to perform circuit QED experiments in the *Quantum Device Laboratory (QuDev)* at ETH Zurich. Various qubit samples have been fabricated and analyzed in spectroscopic and time-resolved resonator transmission measurements.

The main focus of the presented work was the study of the resonant interaction of individual superconducting qubits and single photons. We showed the first direct spectroscopic measurement of both matter-light superposition states of a single (artificial) atom and two photons [Fink08]. We also investigated the nonlinear spectrum of three photon superposition states with both coherent and thermal fields [Fink09a]. Furthermore, we showed the nonlinear scaling of the collective dipole coupling strength with the number of artificial atoms without ensemble averaging for up to three qubits [Fink09b]. Finally, we demonstrated a quantitative understanding of the quantum-to-classical transition in an open quantum system by controlling the system temperature. In addition, a detailed simulation of the resonator transmission spectrum allowed the sensing of thermal fields over more than 2 orders of magnitude in temperature [Fink10].

During the completion of this thesis contributions have also been made to other experiments such as the observation of Berry's phase [Leek07], the Lamb shift [Fragner08] and Autler-Townes and Mollow transitions [Baur09]. In addition, fabrication of qubits for experiments aimed towards the goal of quantum computing [Leek09, Leek10, Bianchetti09, Bianchetti10b] as well as fabrication of SQUIDs for frequency tunable quantum limited parametric amplification and squeezing was part of this thesis. More recently, qubit devices used for single photon correlation measurements [Bozyigit10c, Lang10], the observation of microwave photon antibunching [Bozyigit10b], as well as for studying the potential of time-resolved resonant three qubit quantum state synthesis, see for example Ref. [Haack10], have been fabricated.

The rapid conceptual, experimental and technological progress in circuit QED opens up a wealth of new research directions. This is also reflected by the large number of circuit QED related proposals that are being published.

Increasing the number of qubits in our system promises to extend the domain of ultra strong coupling [Bourassa09, Niemczyk10, Forn-Díaz10, Nataf10b] to the domain where the Dicke superradiant quantum phase transition is predicted to occur [Chen07, Lambert09, Nataf10a]. Using a chain of superconducting qubits coupled to light also promises new insights in related quantum many body physics models [Larson10, Tian10, Tomadin10]. Utilizing the recently implemented fast local qubit flux bias control enables the study of the dynamics of few qubit collective spin states [Keeling09]. These collective modes could potentially be used to realize quantum computing with a small qubit spin ensemble, similar to Ref. [Wesenberg09]. More realistic is their application for resonant quantum gates and efficient quantum state generation [Haack10], which would be useful also for one way quantum computing. Other cooperative phenomena that should be readily observable in our circuit QED system are superradiance [Scully09] and multiphase stability [Delanty10] as well as the collective Lamb shift [Scully10].

A natural extension of current circuit QED experiments would be to study arrays of resonators coupled to superconducting qubits. Such setups have been suggested as potential candidates to realize Bose and Jaynes-Cummings Hubbard models [Schmidt09, Silver10, Leib10] and probe the superfluid to Mott insulator transition of light [Koch09]. It has also been pointed out that time-reversal symmetry breaking [Koch10] and localization and self-trapping of photons in circuit QED photon lattices [Schmidt10] could be investigated. Cavity grids would complement the research with cold atomic gases. Circuit QED with coupled cavity arrays has also been suggested for scalable quantum computing and quantum communication [Giampaolo09, Lin09, Helmer09].

Another interesting direction is in part already pursued in our laboratory. Making use of the tuning capabilities and SQUIDs and qubits enables to in-situ tune the resonance frequency of microwave resonators [Sandberg08a, Sandberg08b]. Rapidly tunable resonators and qubits have been suggested [Dodonov09, De Liberato09, Johansson09, Johansson10, Dodonov10] to be used for the parametric generation of photons and the observation [Wilson10] of vacuum radiation in analogy to the dynamical Casimir effect.

The nonlinearities provided by SQUIDs and qubits can also be used to develop parametric amplifiers for quantum limited amplification and squeezing [Yurke87, Yurke89, Castellanos-Beltran07, Yamamoto08, Castellanos-Beltran08]. A quantum limited amplifier would be extremely useful not only for efficient single shot qubit readout and field state tomography of itinerant microwave photons [Eichler10a] with a high signal to noise ratio, it also allows to engineer one and multi-mode squeezed field states [Eichler10b]. For the future even continuous variable quantum computing may be envisaged.

A better signal to noise ratio will complement our recently implemented improvements in the data acquisition hard- and software, used for single photon source antibunching correlation measurements [Bozyigit10b]. Using two single photon sources it should be possible to observe microwave photon-photon interference in a Hong-Ou-Mandel type experiment. We have already found evidence for related quantum optics effects such as the predicted dressing of dressed states [Shamailov10, Lang10] and the spontaneous dressed state polarization in the strong driving limit of resonant cavity QED

[Alsing91, Armen09, Delanty10]. Once the parametric amplifier is well integrated into our data acquisition circuit one can also start to think about real-time control and feedback of solid state quantum systems. Advanced implementations of teleportation and optimal control techniques will benefit from these capabilities.

While basic quantum computing algorithms involving up to two qubits have already been demonstrated in circuit QED [DiCarlo09], a demonstration of scalability and an implementation of quantum error correction codes is still lacking. An in-depth analysis of decoherence mechanisms, novel designs [Manucharyan09, Steffen10], fabrication techniques, as well as clever strategies to efficiently control multi-qubit systems will be essential. Hopefully more applicable, capable and useful quantum computing algorithms will be developed in the near future. It appears that the quantum simulation of problems which are hard to solve by classical means, such as quantum many body physics problems, may be a fruitful pathway to approach quantum information processing.

Another promising development is the new trend to investigate hybrid quantum systems [Rabl06, Rabl07, Wesenberg09, Imamoglu09, Marcos10, Twamley10]. These systems would have the potential to combine the fast gate operation times and the large coupling strengths attainable in circuit QED, with the long coherence times demonstrated for example in trapped ion and neutral atom as well as nuclear spin and color center implementations of quantum computing. In addition, mechanical transducers or plasmonic devices could potentially be used to form a link between the microwave and the optical domain such that long distance quantum communication between superconducting circuits or other solid states qubits may be envisaged.

The circuit QED architecture clearly provides an excellent playground for curiosity driven experimental research. There are numerous technological as well as conceptual challenges waiting to be solved and there are a lot of interesting quantum optics, quantum information processing and solid state physics phenomena to be unveiled on this path. Quantum engineering with superconducting circuits will continue to test and push the boundaries and the size of truly quantum mechanical systems further and further.

APPENDICES
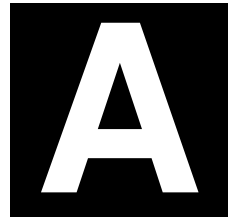
ASPECTS OF THE CRYOGENIC SETUP

In this chapter we summarize a number of important aspects of the infrastructure required to successfully operate a dilution refrigerator at its lowest temperatures for high sensitivity microwave frequency measurements.

A.1   Dimensioning He vacuum pumping lines

We decided to install the vacuum pumps and compressors required to operate the dilution refrigerators *Kelvinox 400 HA* from *Oxford Instruments* and the prototypical cryogen free system from *VeriCold* not directly in the laboratory, due to the mechanical vibrations, noise and dirt which is potentially generated. This requires longer pumping lines which can reduce the effective pumping speed. Since the cooling power and to some extent also the base temperature are connected to the effective ^{3}He and ^{4}He pumping speeds on the *still* and *1K-pot* pumping lines respectively, the question arose which tubing diameters are necessary to compensate the extra lengths of tubing such that the nominal pumping speeds are not significantly reduced.

   The most important parameter for such a dimensioning is the actual pressure of the gas directly before the roots (BOC EH 500), rotary vane (RV12) or turbo pump (TPH 1201 P). This pressure can vary over a large range of typically $0.01\,\text{mbar} < p < 10\,\text{mbar}$ on the *still* and $1\,\text{mbar} < p < 10\,\text{mbar}$ on the *1K-pot*, depending on the system and operation mode [OxfordInstr06]. From our calculations we will see that at the higher end of this pressure range practical tube dimensions are not limiting the nominal pumping speeds.[1]

---

[1]In case the turbo pump is used, the pump itself will be the limiting factor at larger pressures since its nominal pumping speed at $0.001\,\text{mbar}$ is already decreased by about two orders of magnitude at a pressure of $0.1\,\text{mbar}$. This pressure dependence is not as dramatic in case of the roots pump and the rotary vane pump is actually designed for optimal operation at pressures above one millibar.

The interesting situation in terms of tube dimensioning is therefore the *still* line operated at a low pressure which we take to be $p_s = 5\,\text{Pa}$. The typical flow or throughput Q in the Oxford system is on the order of 125 sccm (standard cubic centimeter per minute) if the dilution refrigerator is operated at base temperature and about 800 sccm if the cooling power test is performed at 100 mK [OxfordInstr06]. At pressure p_s this corresponds to a required pumping speed $S = Q/p_s$ of at least $0.04\,\text{m}^3/\text{s}$ and $0.27\,\text{m}^3/\text{s}$ respectively.

Starting with the nominal pumping speed of the Oxford Instruments cryostat *roots still pump*, i.e. $S_n \sim 0.1\,\text{m}^3/\text{s}$ (Vericold *turbo pump* $S_n \sim 0.2\,\text{m}^3/\text{s}$) at $p_s = 5\,\text{Pa}$, we calculate the reduced pumping speed at the cryostat S_{cryo} due to the pumping line consisting of two back to back pipes of lengths $l_1 = 1\,\text{m}$, $l_2 = 6.5\,\text{m}$ and radii $r_1 = 0.025\,\text{m}$, $r_2 = 0.05\,\text{m}$ as

$$S_{\text{cryo}} = \frac{1}{\frac{1}{S_n} + \frac{1}{C_{\text{tot}}}} \tag{A.1}$$

where

$$C_{\text{tot}} = \frac{1}{\frac{1}{C_1} + \frac{1}{C_2}} \tag{A.2}$$

is the total conductance value of the two tubes with the individual conductance values $C_{1,2}$ operated in series. The associated total pressure drop between the cryostat and the the pump is

$$\Delta p = \frac{Q}{C_{\text{tot}}} \tag{A.3}$$

with the total gas throughput Q. Additional sections of tubes and other constrictions like bends or baffles installed in series need to be added according to Eq. (A.2). In order to determine the two tube conductances $C_{1,2}$ we first need to determine if laminar ($R_e < 1100$) or turbulent flow ($R_e > 2100$) occurs. The Reynolds number R_e is defined as the ratio of inertial forces and viscous forces which can be calculated as

$$R_e = \rho v \frac{2r_1}{\eta} \approx 1.4, \tag{A.4}$$

with the density

$$\rho = \frac{Mp_s}{R_0 T} \approx 6 \cdot 10^{-6}\,\text{kg}/\text{m}^3 \tag{A.5}$$

the average speed

$$v = \frac{S_n}{r_1^2 \pi} \approx 12\,\text{m/s} \tag{A.6}$$

and the dynamic viscosity of the gas [Richardson88]

$$\eta = \frac{2}{3}\sqrt{\frac{MR_0 T}{N_A^2 \pi^3 (2r_1)^4}} \approx 1.1 \cdot 10^{-5}\,\frac{\text{kg}}{\text{m s}}. \tag{A.7}$$

Here, $M = 0.003\,\text{kg/mol}$ is the atomic mass of ^3He, $R_0 = 8.31\,\text{J}/(\text{K mol})$ the gas constant, $T \approx 300\,\text{K}$ the temperature and $N_A \approx 6.022 \cdot 10^{23}\,\text{1/mol}$ the Avogadro constant. Clearly we are in the limit of laminar flow where $R_e \ll 1100$ even by taking into account the smaller tube diameter $2r_1$ as the characteristic length scale.

In the laminar flow regime the conductance value can be dominated by internal friction caused by particle particle collisions. This is the regime of continuous or viscous flow where the conductance is proportional to the mean gas pressure (Kn > 110). The other extreme is the regime of molecular flow (Kn < 1) where the conduction is dominated by friction caused by particles colliding with the walls and constrictions of the tubes which is independent of the gas pressure. In our case we realize the intermediate or Knudsen flow (1 < Kn < 110) characterized by the Knudsen number given as

$$\text{Kn} = \frac{2r_1}{L} \approx 49, \tag{A.8}$$

where $2r_1$ is the characteristic length scale and

$$L = R_0 \frac{T}{\sqrt{2}\pi d^2 N_A p_s} \approx 3.85 \cdot 10^{-3}\,\text{m}, \tag{A.9}$$

the mean free path[2] of a helium particle with a hard sphere diameter [Kennard38] taken to be $d \sim 2.2 \cdot 10^{-10}$ m. We therefore need to take into account the contributions of both, continuous flow and molecular flow.

In the regime of laminar continuous flow the conduction of a long smooth pipe can be calculated according to the law of Hagen-Poiseuille

$$C_{\text{cont }1,2} = \frac{\pi r_{1,2}^4}{8\eta l_{1,2}} p_s. \tag{A.10}$$

For the molecular flow on the other hand the conduction is given as [Roth76]

$$C_{\text{mol }1,2} = \frac{r_{1,2}^3 \pi}{l_{1,2}} \sqrt{\frac{\pi R_0 T}{2M}}, \tag{A.11}$$

see also [PfeifferVacuum10]. In the relevant intermediate regime it is given as [Roth76]

$$C_{\text{int }1,2} = C_{\text{cont }1,2} + \sqrt{\frac{2\pi R_0 T}{M}} \frac{4r_{1,2}^3}{3l_{1,2}} \frac{1 + \sqrt{M/(R_0 T)}\, 2r_{1,2} p_s/\eta}{1 + 1.24\sqrt{M/(R_0 T)}\, 2r_{1,2} p_s/\eta}. \tag{A.12}$$

Note furthermore that there exists an upper bound for the conduction value

$$C_{\text{max}} \le c_s r_1^2 \pi \approx 9\,\text{m}^3/\text{s}, \tag{A.13}$$

which is limited by the speed of sound of the fluid $c_s = \sqrt{\gamma R_0 T/M} \approx 1.2 \cdot 10^3$ m/s with the adiabatic index $\gamma = c_p/c_v = (f+2)/f \approx 1.67$ for $f = 3$ degrees of freedom of the monatomic ^{3}He gas.

For the above mentioned configuration of two back to back tubes we obtain the conductances $C_{\text{int }1} \approx 0.13\,\text{m}^3/\text{s}$, $C_{\text{int }2} \approx 0.28\,\text{m}^3/\text{s}$ and the total conductance of $C_{\text{tot}} \approx 0.09\,\text{m}^3/\text{s}$. This corresponds to a pumping speed at the cryostat of $S_{\text{cryo}} \approx 0.05\,\text{m}^3/\text{s}$ which

---

[2]Using the mean free path and the mean particle speed of $v_p = \sqrt{8R_0 T/(M\pi)}$ one can also obtain the dynamic viscosity as $\eta = Mpv_p L/(3R_0 T)$.

relates to a pressure drop of $\Delta p = S_{\text{cryo}} p_s / C_{\text{tot}} \approx 2.8\,\text{Pa}$ and a reduction of the nominal pumping speed $S_{\text{n}} \approx 0.1\,\text{m}^3/\text{s}$ by about 50% due to the tubing. If our configuration is compared to the original layout of pumping lines the loss in pumping speed is however not as dramatic. In addition, the throughput expected when operated at base temperature, i.e. $0.04\,\text{m}^3/\text{s}$ at 5 Pa can still be accomplished. After installation the specified cooling power could be demonstrated and a lowest base temperature of $< 6\,\text{mK}$ was achieved and analyzed using a nuclear orientation thermometer [Pobell06].

A.2   Mechanical vibration measurements

Before setting up the cryostat we analyzed the mechanical vibration spectrum on 1) the laboratory floor which has a base separated from the rest of the building and 2) the cryostat frame which is mounted on the laboratory ceiling. We make use of 3 geophone sensors *GS-20DX-2C* from *Geo Space Corporation* with a natural resonance frequency of $f_{\text{n}} = 10\,\text{Hz}$ and an internal coil resistance of $r = 630\,\Omega$. The geophones detect vibrations longitudinal to their cases. They are firmly mounted in a solid aluminum holder in order to sense the vibrations in the vertical and both horizontal directions. This holder is then attached firmly to the object of interest.

The operation principle of a geophone sensor is based on the relative movement between a coil and a magnetic field. Typically the magnetic field is generated by a permanent magnet held by a spring and the coil is fixed with respect to the housing of the sensor. The relative movement of the coil in the magnetic field due to external vibrations then induce a voltage at its leads. The excitation frequency f dependent voltage response $E(f)$ in V/(m/s) of the used sensor can be calculated as

$$E(f) = \frac{G\frac{R}{r+R}\left(\frac{f}{f_n}\right)^2}{\sqrt{\left(1 - \left(\frac{f}{f_n}\right)^2\right)^2 + 4b_t^2\left(\frac{f}{f_n}\right)^2}}, \qquad (A.14)$$

with the intrinsic voltage sensitivity $G = 34.6\,\text{V}/(\text{m}/\text{s})$. This is the geophone sensitivity without any damping shunt resistance across the two geophone terminals R. The geophone total damping expressed as a fraction of the critical damping is suggested to be in the range $0.6 < b_t < 0.7$. In this regime the intrinsic sensitivity is only slightly lowered while the overall voltage response is close to constant in the excitation frequency, see Fig. A.1 a. The necessary shunt resistance to achieve this can be calculated as $R = (D/(b_t - b_{\text{to}}) - r)$ with $D = 868$ the damping constant and $b_{\text{to}} = 0.3$ the open circuit damping. However, for the presented measurements we did not use a shunt resistor and worked with the open circuit damping of $b_t = 0.3$ where $R \to \infty$.

The voltage signal is directly detected and Fourier transformed using the spectrum analyzer *SR785* from *Stanford Research Systems*. The peak acceleration plotted in Fig. A.1 b-d is calculated from the measured peak voltage V_{pk} using $A_{\text{pk}}(f) = 2\pi f V_{\text{pk}}(f)/(E(f)g)$ with $g = 9.81\,\text{m}/\text{s}^2$. For the measurements we used a bandwidth of 0.25 Hz, 800 FFT lines, BMH windowing and 10 rms averages. The spectra between 10 Hz and 100 Hz are found to be peaked at a value below $10\,\mu g\,\text{Hz}$, $900\,\mu g\,\text{Hz}$ and $1000\,\mu g\,\text{Hz}$ for the vertical direction,

10 µg Hz, 1000 µg Hz and 20000 µg Hz for vibrations in the horizontal longitudinal direction of the cryostat support frame and 10 µg Hz, 2000 µg Hz and 50000 µg Hz for vibrations in the horizontal transverse direction. Here, the first number is measured on the laboratory floor (red curves in Fig. A.1), the second on the support frame (blue curves) and the third is obtained from the measurements on the frame after it was hit by hand (green curves). The peaked spectrum at 150 Hz in Fig. A.1 b is likely to be due to an electrical resonance.

In summary we can state that the laboratory base is very well isolated in terms of mechanical vibrations. With the largest accelerations below 10 µg, the vibration spectrum is comparable to measurements conducted with an accelerometer in Donald Eigler's lab at IBM. We furthermore observe that the situation at the ceiling is substantially worse, typically by one to two orders of magnitude. In case the support frame is excited we observe an
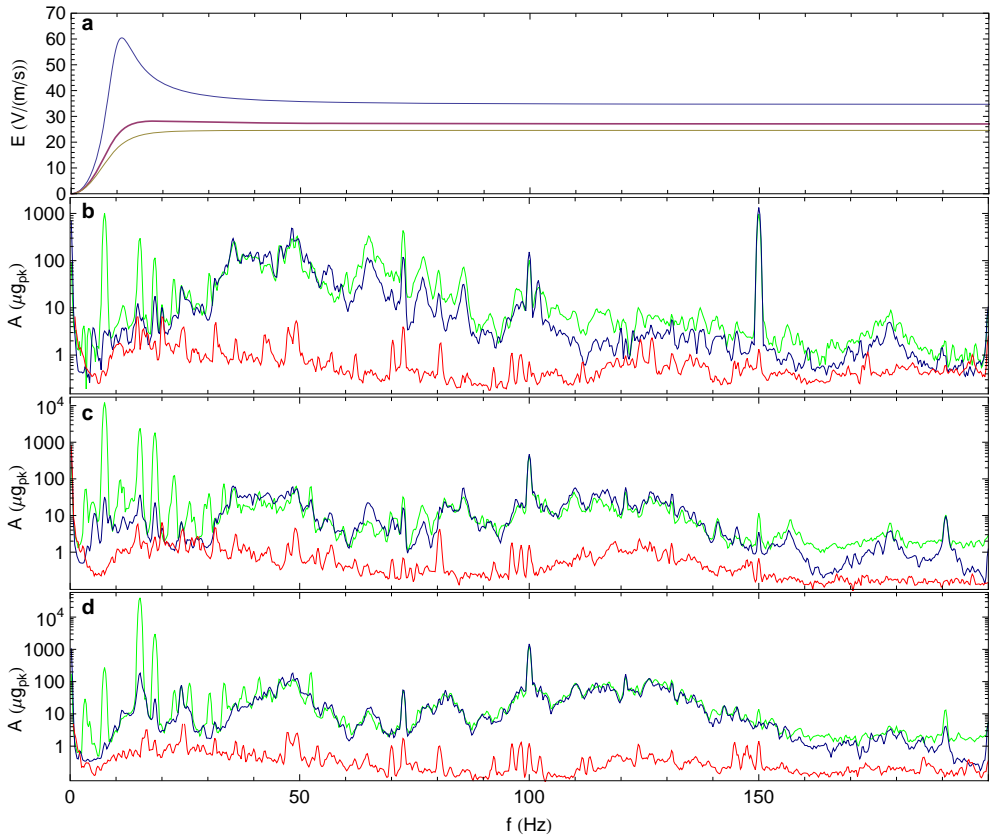
Figure A.1: **Vibration measurements. a**, Calculated voltage response spectrum for different dampings $b_t = 0.7, 0.6, 0.3$ (yellow, red, blue). The blue spectrum is used to convert the measured voltage spectrum to a velocity. **b**, Vibration spectrum measured in vertical direction on the lab floor (red), the support frame (blue) and the support frame excited with a manual hit (green). **c**, Vibrations measured in horizontal longitudinal direction of the rectangular support frame. **d**, Vibrations measured in horizontal transverse direction of the support frame.

additional set of low frequency resonances. In the subsequent frame designs a more stiff layout has been implemented to reduce these resonances. At higher frequencies there is however no substantial deviation between these two cases. For practical reasons the cryostats were however all mounted on the ceiling with the option to supporting them from the floor if required.

A.3   Double gimbal vibration isolation

In order to minimize mechanical vibrations transmitted from the vacuum pumps to the cryostat through the pumping lines, we implemented one meter of each pumping line using flexible tubes. In the middle of this section the flexible tubes were firmly attached to a solid wall. In order to further reduce the amount of vibrations on the still line which is quite stiff due to its large diameter, we in addition designed a double gimbal vibration isolation device, as proposed in Ref. [Kirk78].

The double gimbal design, see Fig. A.2, basically prevents the mechanical contraction of the flexible bellows due to the vacuum and thus keeps them flexible. At the same time, the gimbals ability to pivot about two axes minimizes the restoring forces on the cryostat side caused by small mechanical deflections on the pumping side. Such a decoupling is possible because the resonance frequency of the construction < 1 Hz is much smaller than the expected vibration frequency. The effect is therefore similar to that of a very flexible pumping line only, which is not applicable at large pipe diameters of $\gtrsim 50\,\text{mm}$. The implemented design has also been argued to have a superior isolation performance compared to the frequently used *crossed-bellow design* which requires 4 flexible bellows [Kirk78].

Figure A.2: **Double gimbal vibration isolation.** The pumping side (top) is connected to the cryostat *still line* (right) using two flexible stainless steel bellows. The bellows are elongated to their nominal length using steel ropes suspended at two gimbals. The two gimbals are fixed at two rings which are free to pivot around one axis relative to the two inner rings. The inner rings themselves are also free to pivot about the orthogonal axis. The connections were implemented with a set of 16 tight fitted axial deep grove ball bearings.

NANO FABRICATION RECIPES

Here we give a point by point list of process steps for the fabrication of a typical set of superconducting qubit devices based on aluminum shadow evaporation.

B.1 Chip preparation

A careful inspection of the processed chip is strongly advised. All critical resonator features including the alignment marks should be well resolved. Carefully rinse and dry all glass ware before use. For every spinning layer use a new pipette. Both, the pipette and the chip should be cleaned with the N_2 gun to remove residual dust before the deposition of resist. Try to avoid resist flowing across the chip edge. If it happened remove resist sticking on the bottom of the chip before baking such that good thermal contact between chip and hotplate is assured.

Process step	Description	Comments
Chip cleaning	O_2 plasma ashing for 120 s, 150 W, 0.7 Torr	Dicing protection resist needs to have been removed already
	Acetone ultrasonic bath for 2 min, 50°C, US power 2	Take care that moving chips do not scratch each other
	Isopropanol ultrasonic bath for 2 min, 50°C, US power 2	Take care that moving chips do not scratch each other
	N_2 blow dry chip carefully	Inspect chip under opt. microscope

Spinning	Prebake on hotplate for 5 min at 120°C	
	Cool down for 5 min	
	Cover entire chip with P(MMA-MAA) pure	Wait 5 − 10 sec before starting to spin
	Spin for 60 sec at 3000 rpm	Ramp up time 3 sec
	Bake on hotplate for 300 s at 180°C	
	Cool down for 5 min	Thickness should be 630 ± 10 nm
	Cover entire chip with PMMA 950k 2:1 in ethyl lactate	Wait 5 − 10 sec before starting to spin
	Spin for 60 s at 4000 rpm	Ramp up time 4 sec
	Bake on hotplate for 900 s at 180°C	
	Cool down for 5 min	Inspect resist and edge bead. Thickness of second resist layer should be 115 ± 10 nm
Charge layer	Mount chips in evaporator	Clamp chips from the side
	Deposit 10 nm aluminum	Use Alpure and check currents and rate stability

B.2   Electron beam lithography

The typical SQUID Josephson junction geometry is defined in the CAD file by two bridges of width 100 nm and length 200 nm. Typical exposure doses are $\sim 400\,\mu C/cm^2$ for small structures like the Josephson junctions, $\sim 350\,\mu C/cm^2$ for larger structures that could become instable such as the transmon finger capacitors and $\sim 100\,\mu C/cm^2$ for undercut boxes where only the copolymer layer should be developed.

Process step	Description	Comments
Chip loading	Mount monitor and resonator chips on waver holder	Sketch their positions and check chip orientations
	Clamp the chips from the top at one of the corners with caution	Use clean in house made beryllium copper or phosphor bronze clamps
	Carefully scratch the resist on the monitor chip a few times on lower left corner	Sharp tweezers or small screw driver are suitable

	N_2 blow dry chip carefully	Also check and clean the electrical contact of the waver holder
	Start EBL loading procedure	
EBL setup	Set $10\,\mu m$ aperture and 30 kV gun voltage	Ramp up the voltage starting from 21 kV with 1 kV/min
	Go to the Faraday cup (FC) closest to the chips	
	Set previous stigmator and aperture values	These are the values of the last person who used the same aperture and voltage
	Set the write-field to $500\,\mu m$	corresponds to an magnification of 720k
	Choose SE2 detector and coarsely focus on FC	
	Correct all user positions	All FC's are scanned, their coordinates are corrected and saved
Chip alignment	Go to lower left corner of monitor chip	No critical chip regions should be imaged before exposure
	Coarse focus, origin correction, angle correction	Set the middle of the monitor chip as $(U, V) = (0, 0)$
	Improve focus on a scratch or dirt particle feature $< 30\,nm$	Needs optimization of focus, stigmatism and aperture corrections, save values
	Manual stage based write-field alignment	Start with large scan size and small deflection and iteratively improve accuracy
	Burn a circular contamination dot of diameter $20 - 30\,nm$	Needs optimization of focus, stigmatism and aperture corrections, save values, try at different positions
JJ exposure	Measure beam current ($\sim 28\,pA$)	Correct dwell time, check beam speed and base dose of $100\,\mu C/cm^2$
	Check position list, exposure layers, working field settings and positions on waver map	Also check patterns, geometries and doses
	Go to origin and start exposure of the position list	Exposure details: $\sim 8\,nm$ step size (1 pixel), 20 ms waiting time, fly back factor 0.15, beam drag correction on
Pads exposure	Set $120\,\mu m$ aperture	Load saved correction values

	Measure beam current ($\sim 4.9\,$nA)	Correct dwell time, check beam speed and base dose of $100\,\mu$C/cm^2
	Check position list, exposure layers, working field settings and positions on waver map	Also check patterns, geometries and doses
	Go to origin and start exposure of the position list	Exposure details: $\sim 150\,$nm (19 pixel), $20\,$ms waiting time, fly back factor 0.15, beam drag correction on
Qubit exposure	Set $10\,\mu$m aperture	Load previous correction values
	Go to lower left corner of resonator chip	Again, no critical chip regions should be imaged before exposure
	Temporary origin correction	Set lower left corner as $(U,V) = (0,0)$
	Find closest qubit alignment mark with caution	Set center of qubit alignment marks as origin
	Careful 3 point chip alignment	Use the 3 alignment marks most separated on the chip
	Burn a circular contamination dot of diameter $20-30\,$nm on top of one of the inner qubit alignment marks	Requires only small optimization of focus, stigmatism and aperture corrections, save values
	Measure beam current ($\sim 28\,$pA)	Correct dwell time, check beam speed and base dose of $100\,\mu$C/cm^2
	Check position list, exposure layers, working field settings and positions on waver map	Also check patterns, geometries and doses
	Go to origin and start exposure of the position list	Exposure details: $\sim 8\,$nm step size (1 pixel), $20\,$ms waiting time, fly back factor 0.15, beam drag correction on
	Before qubit exposure perform the beam based write-field alignment two or three times	Center the cross hair in at least 3 of the 4 scans on the qubit alignment mark and confirm the correction

B.3 Development

The stated development times should tried to be met as accurately as possible. Carefully rinse and dry all glass ware before use. During the process steps the chip is slowly moved inside the liquids to provide steady liquid flow across the chip surface. Note that freshly mixed developer can have a reduced temperature which leads to a slower development rate.

Process step	Description	Comments
Al removal	10 % NaOH in H_2O for 30 s	Move chip steadily in the liquid
	H_2O for 10 s	Move chip steadily in the liquid
	Blow dry extra carefully and make sure the chip and the tweezers are completely dry	Residual H_2O can substantially alter the subsequent development. Check that all aluminum is removed.
Development	MIBK in isopropanol (1:3) for 50 s	Move chip in the liquid steadily. Note, freshly mixed developer can develop at a lower rate.
	Isopropanol for 10 s	Move chip steadily in the liquid
	Blow dry carefully	Check structure under optical microscope

B.4   Shadow evaporation

In the process described below we obtain Josephson energies between 60 and 20 GHz for oxidation times between 6 and 40 minutes. This is the case for two Josephson junctions with a typical size of 250 by 200 nm^2.

Process step	Description	Comments
Preliminaries	Mount chips on special holder with slider clamps	Rotate sample holder such that resist bridges are aligned to the sample stage tilt direction
	Standard load lock pump down	
	Purge ArO_2 gas line	Vent load lock with ArO_2 gas (10 Torr)
	Pump down	Start pump down and pause process for at least 1 h (up to 15 h)
Evaporation	20 nm aluminum at 0.5 nm/s in perpendicular direction (0°)	Typical beam current 270-300 mA, use material *Alpure*
Oxidation	Oxidation with 15 % O_2 in Ar at 9 Torr	Typical transmon oxidation times are in the range of 10 to 20 minutes, measure pressure with baratron sensor
Evaporation	80 nm aluminum at 20° and 0.5 nm/s	Sign of evaporation angle is typically chosen such that the top layer junction fingers overlap the bottom layer part of the SQUID

Passivation	Oxidation with O_2 pure at 10 Torr for 15 minutes	

B.5 Resist stripping

For the liftoff procedure we clamp the chips at one corner by means of teflon clamp. The chip holder is placed on a teflon base that gives space to a magnetic stirrer below the base. Base and holder are dipped into an acetone filled glass. This glass is heated in hot water which also contains a magnetic stirrer.

Process step	Description	Comments
Liftoff	Heat acetone filled glass in water to 50 degree Celsius on a hotplate	Water and acetone glass contain a magnetic stirrer
	Mount chips vertically on a holder	
	Place holder on a base and dip both in hot acetone	Place holder close to the perimeter of the glass
	Wait for 1-2 hours at a rotation speed of about 300 rpm	
	Use a pipette to blow off the aluminum layer in one piece	Never remove the chip from the solvent before the aluminum layer is completely removed
	Wait for another ~10 minutes	
Inspection	Relocate the chips to a shallow glass filled with isopropanol	Do this step quickly such that the chip does not dry
	Check liftoff under optical microscope	Take a close look at the liftoff of the SQUIDs and chip edges in particular
	Remove residues with pipette or tweezers with caution (if necessary)	If absolutely necessary apply ultrasonic power 2 in a bath of acetone for a short time. This should not be required and can remove part of the qubit metallization!
	Rinse in isopropanol and blow dry carefully	
	Optical imaging and DC resistance measurements	

BIBLIOGRAPHY

Abdumalikov10   A. A. Abdumalikov, O. Astafiev, A. M. Zagoskin, Y. A. Pashkin, Y. Nakamura & J. S. Tsai. Electromagnetically induced transparency on a single artificial atom. *Phys. Rev. Lett.*, **104** 193601 (2010).   *(Cited on page 8)*

Agarwal84   G. S. Agarwal. Vacuum-field Rabi splittings in microwave absorption by Rydberg atoms in a cavity. *Phys. Rev. Lett.*, **53** 1732 (1984).   *(Cited on pages 91 and 99)*

Agarwal86   G. Agarwal, R. Bullougha & G. Hildred. Exact finite temperature quantum statistics of single atom electrodynamics in a cavity of arbitrary Q. *Opt. Commun.*, **59** 23 (1986).   *(Cited on page 109)*

Agarwal91   G. Agarwal, R. Bullough & N. Nayak. Probing the dressed states of an atom interacting with a quantized field. *Opt. Commun.*, **85** 202 (1991).   *(Cited on page 109)*

Al-Saidi01   W. A. Al-Saidi & D. Stroud. Eigenstates of a small Josephson junction coupled to a resonant cavity. *Phys. Rev. B*, **65** 014512 (2001).   *(Cited on page 7)*

Allen87   L. Allen & J. Eberly. *Optical resonance and two-level atoms.* Dover (1987). *(Cited on pages 16, 75, and 76)*

Alsing91   P. Alsing & H. J. Carmichael. Spontaneous dressed-state polarization of a coupled atom and cavity mode. *Quantum Opt.*, **3** 13 (1991).   *(Cited on pages 109 and 117)*

Ambegaokar63   V. Ambegaokar & A. Baratoff. Tunneling between superconductors. *Phys. Rev. Lett.*, **10** 486 (1963).   *(Cited on page 51)*

Ansmann09   M. Ansmann, H. Wang, R. C. Bialczak, M. Hofheinz, E. Lucero, M. Neeley, A. D. O'Connell, D. Sank, M. Weides, J. Wenner, A. N. Cleland & J. M. Martinis. Violation of Bell's inequality in Josephson phase qubits. *Nature*, **461** 504 (2009).   *(Cited on page 8)*

Armen09   M. A. Armen, A. E. Miller & H. Mabuchi. Spontaneous dressed-state polarization in the strong driving regime of cavity QED. *Phys. Rev. Lett.*, **103** 173601 (2009).   *(Cited on pages 109 and 117)*

Astafiev07   O. Astafiev, K. Inomata, A. O. Niskanen, T. Yamamoto, Y. A. Pashkin, Y. Nakamura & J. S. Tsai. Single artificial-atom lasing. *Nature*, **449** 588 (2007).   *(Cited on page 7)*

Astafiev10a   O. Astafiev, A. M. Zagoskin, J. Abdumalikov, A. A., Y. A. Pashkin, T. Yamamoto, K. Inomata, Y. Nakamura & J. S. Tsai. Resonance fluorescence of a single artificial atom. *Science*, **327** 840 (2010).   *(Cited on page 8)*

Astafiev10b   O. V. Astafiev, A. A. Abdumalikov, A. M. Zagoskin, Y. A. Pashkin, Y. Nakamura & J. S. Tsai. Ultimate on-chip quantum amplifier. *Phys. Rev. Lett.*, **104** 183603 (2010).   *(Cited on page 8)*

Bardeen57   J. Bardeen, L. Cooper & J. Schrieffer. Theory of superconductivity. *Physical Review*, **108** 1175 (1957).   *(Cited on page 51)*

Baur07   M. Baur. *Quantum Electrodynamics with Superconducting Circuits: Measurement of the Cavity Photon Number using Ramsey Interference.* Master's thesis, ETH Zurich (2007).   *(Cited on page 20)*

Baur09   M. Baur, S. Filipp, R. Bianchetti, J. M. Fink, M. Goppl, L. Steffen, P. J. Leek, A. Blais & A. Wallraff. Measurement of Autler-Townes and Mollow transitions in a strongly driven superconducting qubit. *Phys. Rev. Lett.*, **102** 243602 (2009).   *(Cited on pages 8 and 115)*

Bernardot92   F. Bernardot, P. Nussenzveig, M. Brune, J. M. Raimond & S. Haroche. Vacuum Rabi splitting observed on a microscopic atomic sample in a microwave cavity. *Europhys. Lett.*, **17** 33 (1992).
                                                                                        (Cited on page 99)

Bertet02   P. Bertet, S. Osnaghi, P. Milman, A. Auffeves, P. Maioli, M. Brune, J. M. Raimond & S. Haroche. Generating and probing a two-photon Fock state with a single atom in a cavity. *Phys. Rev. Lett.*, **88** 143601 (2002).   *(Cited on pages 83 and 85)*

Bethe47   H. A. Bethe.   The electromagnetic shift of energy levels.   *Phys. Rev.*, **72** 339 (1947).
                                                                                        (Cited on page 3)

Bialczak10   R. C. Bialczak, M. Ansmann, M. Hofheinz, M. Lenander, E. Lucero, M. Neeley, A. D. O'Connell, D. Sank, H. Wang, M. Weides, J. Wenner, T. Yamamoto, A. N. Cleland & J. M. Martinis. Demonstration of a tuneable coupler for superconducting qubits using coherent, time domain, two-qubit operations. arXiv:1007.2219 (2010).   *(Cited on page 77)*

Bianchetti09   R. Bianchetti, S. Filipp, M. Baur, J. M. Fink, M. Göppl, P. J. Leek, L. Steffen, A. Blais & A. Wallraff. Dynamics of dispersive single-qubit readout in circuit quantum electrodynamics. *Phys. Rev. A*, **80** 043840 (2009).   *(Cited on pages 22, 23, 72, 75, 76, 111, and 115)*

Bianchetti10a   R. Bianchetti. *Control and readout of a superconducting artificial atom*. Ph.D. thesis, ETH Zurich (2010).   *(Cited on pages 36, 43, and 76)*

Bianchetti10b   R. Bianchetti, S. Filipp, M. Baur, J. M. Fink, C. Lang, L. Steffen, M. Boissonneault, A. Blais & A. Wallraff. Control and tomography of a three level superconducting artificial atom. Phys. Rev. Lett. (in print) (2010).   *(Cited on pages 23, 32, 69, 72, 75, 76, and 115)*

Bishop09   L. S. Bishop, J. M. Chow, J. Koch, A. A. Houck, M. H. Devoret, E. Thuneberg, S. M. Girvin & R. J. Schoelkopf. Nonlinear response of the vacuum Rabi resonance. *Nat. Phys.*, **5** 105 (2009).
                                                                    (Cited on pages 8, 84, 93, 98, 102, and 109)

Bishop10a   L. S. Bishop. *Circuit Quantum Electrodynamics: Volume II*. Ph.D. thesis, Yale University (2010).   *(Cited on page 11)*

Bishop10b   L. S. Bishop, E. Ginossar & S. M. Girvin. Response of the strongly driven Jaynes-Cummings oscillator. *Phys. Rev. Lett.*, **105** 100505 (2010).   *(Cited on pages 23, 69, and 72)*

Blais03   A. Blais, A. M. van den Brink & A. M. Zagoskin. Tunable coupling of superconducting qubits. *Phys. Rev. Lett.*, **90** 127901 (2003).   *(Cited on page 7)*

Blais04   A. Blais, R.-S. Huang, A. Wallraff, S. M. Girvin & R. J. Schoelkopf. Cavity quantum electrodynamics for superconducting electrical circuits: An architecture for quantum computation. *Phys. Rev. A*, **69** 062320 (2004).   *(Cited on pages 5, 7, 11, 18, 84, and 86)*

Blais07   A. Blais, J. Gambetta, A. Wallraff, D. I. Schuster, S. M. Girvin, M. H. Devoret & R. J. Schoelkopf. Quantum-information processing with circuit quantum electrodynamics. *Phys. Rev. A*, **75** 032329 (2007).   *(Cited on pages 7 and 24)*

Boca04   A. Boca, R. Miller, K. M. Birnbaum, A. D. Boozer, J. McKeever & H. J. Kimble. Observation of the vacuum Rabi spectrum for one trapped atom. *Phys. Rev. Lett.*, **93** 233603 (2004).
                                                                                        (Cited on pages 85 and 102)

Bocquillon09   E. Bocquillon, C. Couteau, M. Razavi, R. Laflamme & G. Weihs. Coherence measures for heralded single-photon sources. *Phys. Rev. A*, **79** 035801 (2009).   *(Cited on page 85)*

Boissonneault08   M. Boissonneault, J. M. Gambetta & A. Blais. Nonlinear dispersive regime of cavity qed: The dressed dephasing model. *Phys. Rev. A*, **77** 305 (2008).   *(Cited on page 75)*

Boissonneault10   M. Boissonneault, J. M. Gambetta & A. Blais. Improved superconducting qubit readout by qubit-induced nonlinearities. *Phys. Rev. Lett.*, **105** 100504 (2010).   *(Cited on pages 23, 69, and 72)*

Bolesch10   C. Bolesch. Ultra low noise amplifiers and their DC wiring. Semester thesis, ETH Zurich (2010).   *(Cited on page 44)*

Bouchiat98   V. Bouchiat, D. Vion, P. Joyez, D. Esteve & M. H. Devoret. Quantum coherence with a single Cooper pair. *Phys. Scr.*, **T76** 165 (1998).   *(Cited on pages 13, 51, 86, and 90)*

Bourassa09   J. Bourassa, J. M. Gambetta, J. A. A. Abdumalikov, O. Astafiev, Y. Nakamura & A. Blais. Ultra-strong coupling regime of cavity QED with phase-biased flux qubits. *Phys. Rev. A*, **80** 032109 (2009).   *(Cited on pages 21 and 116)*

Boyer75   T. H. Boyer. Random electrodynamics: The theory of classical electrodynamics with classical electromagnetic zero-point radiation. *Phys. Rev. D*, **11** 790 (1975).   *(Cited on page 4)*

Bozyigit08   D. Bozyigit. Design and development of an high performance signal processing platform for qubit readout (2008).   *(Cited on pages 45 and 77)*

Bozyigit10a   D. Bozyigit. *Correlation function measurements of a microwave frequency single photon source*. Master's thesis, ETH Zurich (2010).   *(Cited on pages 33, 43, 45, and 77)*

Bozyigit10b   D. Bozyigit, C. Lang, L. Steffen, J. M. Fink, M. Baur, R. Bianchetti, P. J. Leek, S. Filipp, M. P. da Silva, A. Blais & A. Wallraff. Antibunching of microwave frequency photons observed in correlation measurements using linear detectors. Nat. Phys. (in print) (2010).   *(Cited on pages 4, 8, 32, 33, 44, 46, 75, 115, and 116)*

Bozyigit10c   D. Bozyigit, C. Lang, L. Steffen, J. M. Fink, M. Baur, R. Bianchetti, P. J. Leek, S. Filipp, M. P. da Silva, A. Blais & A. Wallraff. Measurements of the correlation function of a microwave frequency single photon source. arXiv:1002.3738 (2010).   *(Cited on pages 5, 8, 32, 75, 76, and 115)*

Brennecke07   F. Brennecke, T. Donner, S. Ritter, T. Bourdel, M. Kohl & T. Esslinger. Cavity QED with a Bose-Einstein condensate. *Nature*, **450** 268 (2007).   *(Cited on page 100)*

Brown56   R. H. Brown & R. Q. Twiss. Correlation between photons in coherent beams of light. *Nature*, **177** 27 (1956).   *(Cited on page 4)*

Brune94   M. Brune, P. Nussenzveig, F. Schmidt-Kaler, F. Bernardot, A. Maali, J. M. Raimond & S. Haroche. From Lamb shift to light shifts: Vacuum and subphoton cavity fields measured by atomic phase sensitive detection. *Phys. Rev. Lett.*, **72** 3339 (1994).   *(Cited on page 20)*

Brune96   M. Brune, F. Schmidt-Kaler, A. Maali, J. Dreyer, E. Hagley, J. M. Raimond & S. Haroche. Quantum Rabi oscillation: A direct test of field quantization in a cavity. *Phys. Rev. Lett.*, **76** 1800 (1996).   *(Cited on pages 4, 83, 85, and 102)*

Buisson01   O. Buisson & F. Hekking. Entangled states in a Josephson charge qubit coupled to a superconducting resonator. In D. V. Averin, B. Ruggiero & P. Silvestrini, eds., *Macroscopic Quantum Coherence and Quantum Computing*. Kluwer, New York (2001).   *(Cited on page 7)*

Burkard04   G. Burkard, R. H. Koch & D. P. DiVincenzo. Multilevel quantum description of decoherence in superconducting qubits. *Phys. Rev. B*, **69** 064503 (2004).   *(Cited on page 11)*

Büttiker87   M. Büttiker. Zero-current persistent potential drop across small-capacitance Josephson junctions. *Phys. Rev. B*, **36** 3548 (1987).   *(Cited on page 13)*

Carmichael96   H. J. Carmichael, P. Kochan & B. C. Sanders. Photon correlation spectroscopy. *Phys. Rev. Lett.*, **77** 631 (1996).   *(Cited on pages 83, 84, and 85)*

Carmichael99   H. J. Carmichael & B. C. Sanders. Multiatom effects in cavity QED with atomic beams. *Phys. Rev. A*, **60** 2497 (1999).   *(Cited on page 100)*

Castellanos-Beltran07   M. A. Castellanos-Beltran & K. W. Lehnert. Widely tunable parametric amplifier based on a superconducting quantum interference device array resonator. *Appl. Phys. Lett.*, **91** 083509 (2007).   *(Cited on page 116)*

Castellanos-Beltran08   M. A. Castellanos-Beltran, K. D. Irwin, G. C. Hilton, L. R. Vale & K. W. Lehnert. Amplification and squeezing of quantum noise with a tunable Josephson metamaterial. *Nat. Phys.*, **4** 929 (2008).   *(Cited on page 116)*

Chen07   G. Chen, Z. Chen & J. Liang. Simulation of the superradiant quantum phase transition in the superconducting charge qubits inside a cavity. *Phys. Rev. A*, **76** 055803 (2007).
                                                                                           (Cited on page 116)

Childs96   J. J. Childs, K. An, M. S. Otteson, R. R. Dasari & M. S. Feld. Normal-mode line shapes for atoms in standing-wave optical resonators. *Phys. Rev. Lett.*, **77** 2901 (1996).   *(Cited on pages 99 and 100)*

Chiorescu04   I. Chiorescu, P. Bertet, K. Semba, Y. Nakamura, C. J. P. M. Harmans & J. E. Mooij. Coherent dynamics of a flux qubit coupled to a harmonic oscillator. *Nature*, **431** 159 (2004).
                                                                                           (Cited on pages 7 and 83)

Chow10a   J. M. Chow, L. DiCarlo, J. M. Gambetta, F. Motzoi, L. Frunzio, S. M. Girvin & R. J. Schoelkopf. Implementing optimal control pulse shaping for improved single-qubit gates (2010).   *(Cited on pages 8 and 16)*

Chow10b   J. M. Chow, L. DiCarlo, J. M. Gambetta, A. Nunnenkamp, L. S. Bishop, L. Frunzio, M. H. Devoret, S. M. Girvin & R. J. Schoelkopf. Detecting highly entangled states with a joint qubit readout. *Phys. Rev. A*, **81** 062325 (2010).   *(Cited on page 8)*

Cirac91   J. I. Cirac, H. Ritsch & P. Zoller. Two-level system interacting with a finite-bandwidth thermal cavity mode. *Phys. Rev. A*, **44** 4541 (1991).   *(Cited on page 109)*

Clarke08   J. Clarke & F. K. Wilhelm. Superconducting quantum bits. *Nature*, **453** 1031 (2008).
                                                                                           (Cited on page 13)

Clauser74   J. F. Clauser. Experimental distinction between the quantum and classical field-theoretic predictions for the photoelectric effect. *Phys. Rev. D*, **9** 853 (1974).   *(Cited on page 4)*

Clerk07   A. A. Clerk & D. W. Utami. Using a qubit to measure photon-number statistics of a driven thermal oscillator. *Phys. Rev. A*, **75** 042302 (2007).   *(Cited on page 113)*

Cohen-Tannoudji89   C. Cohen-Tannoudji, J. Dupont-Roc & G. Grynberg. *Photons & Atoms - Introduction to Quantum Electrodynamics*. Wiley (1989).   *(Cited on pages 3, 5, and 17)*

Cohen-Tannoudji98   C. Cohen-Tannoudji, J. Dupont-Roc & G. Grynberg. *Atom-Photon Interactions: Basic Processes and Applications*. Wiley Science Paperback Series (1998).   *(Cited on page 17)*

Colombe07   Y. Colombe, T. Steinmetz, G. Dubois, F. Linke, D. Hunger & J. Reichel. Strong atom-field coupling for Bose-Einstein condensates in an optical cavity on a chip. *Nature*, **450** 272 (2007).
                                                                                           (Cited on page 100)

Cottet02   A. Cottet, D. Vion, A. Aassime, P. Joyez, D. Esteve & M. H. Devoret. Implementation of a combined charge-phase quantum bit in a superconducting circuit. *Physica C*, **367** 197 (2002).
                                                                                           (Cited on page 15)

Court08   N. A. Court, A. J. Ferguson, R. Lutchyn & R. G. Clark. Quantitative study of quasiparticle traps using the single-cooper-pair transistor. *Phys. Rev. B*, **77** 100501 (2008).   *(Cited on pages 51 and 63)*

daSilva10   M. P. da Silva, D. Bozyigit, A. Wallraff & A. Blais. Schemes for the observation of photon correlation functions in circuit QED with linear detectors. *Phys. Rev. A*, **82** 043804 (2010).
                                                                                           (Cited on page 46)

De Liberato09   S. De Liberato, D. Gerace, I. Carusotto & C. Ciuti. Extracavity quantum vacuum radiation from a single qubit. *Phys. Rev. A*, **80** 053810 (2009).   *(Cited on page 116)*

Delanty10   M. Delanty, S. Rebic & J. Twamley. Superradiance and phase multistability in circuit quantum electrodynamics. arXiv:1007.2231 (2010).   *(Cited on pages 116 and 117)*

Deleglise08   S. Deleglise, I. Dotsenko, C. Sayrin, J. Bernu, M. Brune, J.-M. Raimond & S. Haroche. Reconstruction of non-classical cavity field states with snapshots of their decoherence. *Nature*, **455** 510 (2008).   *(Cited on page 84)*

Deppe08   F. Deppe, M. Mariantoni, E. P. Menzel, A. Marx, S. Saito, K. Kakuyanagi, H. Tanaka, T. Meno, K. Semba, H. Takayanagi, E. Solano & R. Gross. Two-photon probe of the Jaynes-Cummings model and controlled symmetry breaking in circuit QED. *Nat. Phys.*, **4** 686 (2008).   *(Cited on page 8)*

Deutsch85   D. Deutsch. Quantum theory, the Church-Turing principle and the universal quantum computer. *Proc. R. Soc. Lond. A*, **400** 97 (1985).   *(Cited on page 12)*

Deutsch92   D. Deutsch & R. Jozsa. Rapid solution of problems by quantum computation. *Proc. R. Soc. Lond.*, **439** 553 (1992).   *(Cited on page 12)*

Devoret97   M. H. Devoret. Quantum fluctuations in electrical circuits. In S. Reynaud, E. Giacobino & J. Zinn-Justin, eds., *Quantum Fluctuations: Les Houches Session LXIII*, pp. 351–386. Elsevier (1997).   *(Cited on pages 11 and 13)*

Devoret03   M. H. Devoret & J. M. Martinis. Quantum entanglement and information processing. In J.-M. Raimond, J. Dalibard & D. Esteve, eds., *Les Houches Session LXXIX*, pp. 443–485. Elsevier (2003).   *(Cited on page 15)*

Devoret04   M. H. Devoret, A. Wallraff & J. M. Martinis. Superconducting qubits: A short review. cond-mat/0411174v1 (2004).   *(Cited on page 13)*

Devoret07   M. Devoret, S. Girvin & R. Schoelkopf. Circuit-QED: How strong can the coupling between a Josephson junction atom and a transmission line resonator be? *Ann. Phys.*, **16** 767 (2007).   *(Cited on page 21)*

DiCarlo09   L. DiCarlo, J. M. Chow, J. M. Gambetta, L. S. Bishop, B. R. Johnson, D. I. Schuster, J. Majer, A. Blais, L. Frunzio, S. M. Girvin & R. J. Schoelkopf. Demonstration of two-qubit algorithms with a superconducting quantum processor. *Nature*, **460** 240 (2009).   *(Cited on pages 5, 8, 23, and 117)*

DiCarlo10   L. DiCarlo, M. D. Reed, L. Sun, B. R. Johnson, J. M. Chow, J. M. Gambetta, L. Frunzio, S. M. Girvin, M. H. Devoret & R. J. Schoelkopf. Preparation and measurement of three-qubit entanglement in a superconducting circuit. *Nature*, **467** 574 (2010).   *(Cited on pages 8 and 23)*

Dicke54   R. H. Dicke. Coherence in spontaneous radiation processes. *Phys. Rev.*, **93** 99 (1954).   *(Cited on page 99)*

Dirac27   P. Dirac. The quantum theory of the emission and absorption of radiation. *Proc. R. Soc. Lond.*, **A 114** 243 (1927).   *(Cited on page 3)*

DiVincenzo00 D. P. DiVincenzo. The physical implementation of quantum computation. *Fortschr. Phys.*, **48** 771 (2000).   *(Cited on page 12)*

Dodonov09   A. V. Dodonov. Photon creation from vacuum and interactions engineering in nonstationary circuit QED. *J. Phys.: Conf. Ser.*, **161** 012029 (2009).   *(Cited on page 116)*

Dodonov10   V. V. Dodonov. Current status of the dynamical Casimir effect. *Phys. Scr.*, **82** 038105 (2010).   *(Cited on page 116)*

Dolan88   G. Dolan & J. Dunsmuir. Very small (20 nm) lithographic wires, dots, rings, and tunnel junctions. *Physica B*, **152** 7 (1988).   *(Cited on page 60)*

Dür00   W. Dür, G. Vidal & J. I. Cirac. Three qubits can be entangled in two inequivalent ways. *Phys. Rev. A*, **62** 062314 (2000).   *(Cited on page 104)*

Eberly80   J. H. Eberly, N. B. Narozhny & J. J. Sanchez-Mondragon. Periodic spontaneous collapse and revival in a simple quantum model. *Phys. Rev. Lett.*, **44** 1323 (1980).   *(Cited on page 4)*

Eichler10a   C. Eichler, et al. & A. Wallraff. Field state tomography of itinerant microwave photons (2010). In preperation.   *(Cited on page 116)*

Eichler10b   C. Eichler, et al. & A. Wallraff. Gaussian state reconstruction of a two-mode squeezed state (2010). In preperation.   *(Cited on page 116)*

Englund07   D. Englund, A. Faraon, I. Fushman, N. Stoltz, P. Petroff & J. Vuckovic. Controlling cavity reflectivity with a single quantum dot. *Nature*, **450** 857 (2007).   *(Cited on pages 83 and 85)*

Enss05   C. Enss & S. Hunklinger. *Low-Temperature Physics*. Springer-Verlag (2005). *(Cited on page 39)*

Everitt09   M. J. Everitt, W. J. Munro & T. P. Spiller. Quantum-classical crossover of a field mode. *Phys. Rev. A*, **79** 032328 (2009).   *(Cited on page 107)*

Fermi32   E. Fermi. Quantum theory of radiation. *Rev. Mod. Phys.*, **4** 87 (1932).   *(Cited on page 3)*

Feynman71   R. Feynman, M. Sands & R. Leighton. *The Feynman Lectures on Physics Vol.3.* Addison-Wesley (1971).   *(Cited on page 3)*

Feynman82   R. P. Feynman. Simulating physics with computers. *Int. J. Theor. Phys.*, **21** 467 (1982).   *(Cited on page 12)*

Filipp09   S. Filipp, P. Maurer, P. J. Leek, M. Baur, R. Bianchetti, J. M. Fink, M. Göppl, L. Steffen, J. M. Gambetta, A. Blais & A. Wallraff. Two-qubit state tomography using a joint dispersive readout. *Phys. Rev. Lett.*, **102** 200402 (2009).   *(Cited on pages 23 and 76)*

Fink07   J. M. Fink. *Single qubit control and observation of Berry's phase in a superconducting quantum circuit*. Master's thesis, Universität Wien and ETH Zurich (2007).   *(Cited on page 76)*

Fink08   J. M. Fink, M. Göppl, M. Baur, R. Bianchetti, P. J. Leek, A. Blais & A. Wallraff. Climbing the Jaynes-Cummings ladder and observing its nonlinearity in a cavity QED system. *Nature*, **454** 315 (2008).   *(Cited on pages 4, 5, 8, 81, 84, 95, 97, 102, 109, and 115)*

Fink09a   J. M. Fink, M. Baur, R. Bianchetti, S. Filipp, M. Göppl, P. J. Leek, L. Steffen, A. Blais & A. Wallraff. Thermal excitation of multi-photon dressed states in circuit quantum electrodynamics. *Phys. Scr.*, **T137** 014013 (2009).   *(Cited on pages 32, 81, 85, 97, 109, and 115)*

Fink09b   J. M. Fink, R. Bianchetti, M. Baur, M. Goppl, L. Steffen, S. Filipp, P. J. Leek, A. Blais & A. Wallraff. Dressed collective qubit states and the Tavis-Cummings model in circuit QED. *Phys. Rev. Lett.*, **103** 083601 (2009).   *(Cited on pages 8, 32, 82, and 115)*

Fink10   J. M. Fink, L. Steffen, P. Studer, L. S. Bishop, M. Baur, R. Bianchetti, D. Bozyigit, C. Lang, S. Filipp, P. J. Leek & A. Wallraff. Quantum-to-classical transition in cavity quantum electrodynamics. *Phys. Rev. Lett.*, **105** 163601 (2010).   *(Cited on pages 8, 32, 82, 85, 93, 96, and 115)*

Forn-Díaz10   P. Forn-Díaz, J. Lisenfeld, D. Marcos, J. J. GarcÃa-Ripoll, E. Solano, C. J. P. M. Harmans & J. E. Mooij. Observation of the Bloch-Siegert shift in a qubit-oscillator system in the ultrastrong coupling regime. arXiv:1005.1559v1 (2010).   *(Cited on pages 21 and 116)*

Fragner08   A. Fragner, M. Göppl, J. M. Fink, M. Baur, R. Bianchetti, P. J. Leek, A. Blais & A. Wallraff. Resolving vacuum fluctuations in an electrical circuit by measuring the Lamb shift. *Science*, **322** 1357 (2008).   *(Cited on pages 8, 22, 72, 93, and 115)*

Frey08   T. Frey. Design of microwave beam splitters for photon correlation measurements. Semster thesis, ETH Zurich (2008).   *(Cited on page 33)*

Frunzio05   L. Frunzio, A. Wallraff, D. Schuster, J. Majer & R. Schoelkopf. Fabrication and characterization of superconducting circuit QED devices for quantum computation. *IEEE T. Appl. Supercon.*, **15** 860 (2005).   *(Cited on page 33)*

Gambetta06   J. Gambetta, A. Blais, D. I. Schuster, A. Wallraff, L. Frunzio, J. Majer, M. H. Devoret, S. M. Girvin & R. J. Schoelkopf. Qubit-photon interactions in a cavity: Measurement-induced dephasing and number splitting. *Phys. Rev. A*, **74** 042318 (2006).   *(Cited on pages 22 and 74)*

Gardiner91   C. W. Gardiner & P. Zoller. *Quantum Noise*. Springer (1991).   *(Cited on page 3)*

Gerry05   C. Gerry & P. L. Knight. *Introductory Quantum Optics*. Cambridge University Press (2005).
          (Cited on page 19)

Ghosh87   R. Ghosh & L. Mandel. Observation of nonclassical effects in the interference of two photons. *Phys. Rev. Lett.*, **59** 1903 (1987).   *(Cited on page 4)*

Giampaolo09   S. M. Giampaolo & F. Illuminati. Long-distance entanglement and quantum teleportation in coupled-cavity arrays. *Phys. Rev. A*, **80** 050301 (2009).   *(Cited on page 116)*

Glauber63a   R. J. Glauber. Coherent and incoherent states of the radiation field. *Phys. Rev.*, **131** 2766 (1963).   *(Cited on page 4)*

Glauber63b   R. J. Glauber. The quantum theory of optical coherence. *Phys. Rev.*, **130** 2529 (1963).
          (Cited on page 4)

Gleyzes07   S. Gleyzes, S. Kuhr, C. Guerlin, J. Bernu, S. Deleglise, U. Busk Hoff, M. Brune, J.-M. Raimond & S. Haroche. Quantum jumps of light recording the birth and death of a photon in a cavity. *Nature*, **446** 297 (2007).   *(Cited on pages 20 and 84)*

Göppert-Mayer31   M. Göppert-Mayer. Über Elementarakte mit zwei Quantensprüngen. *Ann. Phys.*, **9** 273 (1931).
          (Cited on pages 5 and 17)

Göppl08   M. Göppl, A. Fragner, M. Baur, R. Bianchetti, S. Filipp, J. M. Fink, P. J. Leek, G. Puebla, L. Steffen & A. Wallraff. Coplanar waveguide resonators for circuit quantum electrodynamics. *J. Appl. Phys.*, **104** 113904 (2008).   *(Cited on pages 9, 10, 33, and 68)*

Göppl09   M. Göppl. *Engineering Quantum Electronic Chips - Realization and Characterization of Circuit Quantum Electrodynamics Systems*. Ph.D. thesis, ETH Zurich (2009).   *(Cited on pages 33, 53, 67, and 76)*

Grajcar08   M. Grajcar, S. H. W. van der Ploeg, A. Izmalkov, E. Il'ichev, H.-G. Meyer, A. Fedorov, A. Shnirman & G. Schon. Sisyphus cooling and amplification by a superconducting qubit. *Nat. Phys.*, **4** 612 (2008).   *(Cited on page 8)*

Grangier86   P. Grangier, G. Roger & A. Aspect. Experimental evidence for a photon anticorrelation effect on a beam splitter: A new light on single-photon interferences. *Europhys. Lett.*, **1** 173 (1986).
          (Cited on page 4)

Grover96   L. K. Grover. A fast quantum mechanical algorithm for database search. In *Proceedings of the twenty-eighth annual ACM symposium on theory of computing*, pp. 212–219. ACM, Philadelphia, Pennsylvania (1996).   *(Cited on page 12)*

Guerlin07   C. Guerlin, J. Bernu, S. Deleglise, C. Sayrin, S. Gleyzes, S. Kuhr, M. Brune, J.-M. Raimond & S. Haroche. Progressive field-state collapse and quantum non-demolition photon counting. *Nature*, **448** 889 (2007).   *(Cited on pages 20, 84, and 85)*

Haack10   G. Haack, F. Helmer, M. Mariantoni, F. Marquardt & E. Solano. Resonant quantum gates in circuit quantum electrodynamics. *Phys. Rev. B*, **82** 024514 (2010).   *(Cited on pages 115 and 116)*

Haroche89   S. Haroche & D. Kleppner. Cavity quantum electrodynamics. *Phys. Today*, **42** 24 (1989).
          (Cited on page 4)

Haroche92   S. Haroche. *Fundamental Systems in Quantum Optics*, chap. Cavity quantum electrodynamics, p. 767. Elsevier (1992).   *(Cited on page 19)*

Haroche06   S. Haroche & J.-M. Raimond. *Exploring the Quantum: Atoms, Cavities, and Photons*. OUP Oxford (2006).   *(Cited on pages 4, 18, and 107)*

Helmer09   F. Helmer, M. Mariantoni, A. G. Fowler, J. von Delft, E. Solano & F. Marquardt. Cavity grid for scalable quantum computation with superconducting circuits. *Europhys. Lett.)*, **85** 50007 (2009).   *(Cited on pages 77 and 116)*

Hennessy07   K. Hennessy, A. Badolato, M. Winger, D. Gerace, M. Atature, S. Gulde, S. Falt, E. L. Hu & A. Imamoglu. Quantum nature of a strongly coupled single quantum dot-cavity system. *Nature*, **445** 896 (2007).   *(Cited on pages 83 and 85)*

Henzen08   D. Henzen. Measurement and analysis of superconducting microwave beam splitters. Semster thesis, ETH Zurich (2008).   *(Cited on page 33)*

Hofheinz08   M. Hofheinz, E. M. Weig, M. Ansmann, R. C. Bialczak, E. Lucero, M. Neeley, A. D. O'Connell, H. Wang, J. M. Martinis & A. N. Cleland. Generation of Fock states in a superconducting quantum circuit. *Nature*, **454** 310 (2008).   *(Cited on pages 5, 8, 84, 85, and 102)*

Hofheinz09   M. Hofheinz, H. Wang, M. Ansmann, R. C. Bialczak, E. Lucero, M. Neeley, A. D. O'Connell, D. Sank, J. Wenner, J. M. Martinis & A. N. Cleland. Synthesizing arbitrary quantum states in a superconducting resonator. *Nature*, **459** 546 (2009).   *(Cited on pages 5, 8, and 84)*

Holmqvist08   T. Holmqvist, M. Meschke & J. P. Pekola. Double oxidation scheme for tunnel junction fabrication. *J. Vac. Sci. Technol. B*, **26** 28 (2008).   *(Cited on page 65)*

Houck07   A. Houck, D. Schuster, J. Gambetta, J. Schreier, B. Johnson, J. Chow, L. Frunzio, J. Majer, M. Devoret, S. Girvin & R. Schoelkopf. Generating single microwave photons in a circuit. *Nature*, **449** 328 (2007).   *(Cited on pages 5 and 7)*

Houck08   A. A. Houck, J. A. Schreier, B. R. Johnson, J. M. Chow, J. Koch, J. M. Gambetta, D. I. Schuster, L. Frunzio, M. H. Devoret, S. M. Girvin & R. J. Schoelkopf. Controlling the spontaneous emission of a superconducting transmon qubit. *Phys. Rev. Lett.*, **101** 080502 (2008).
                                                                                                      (Cited on page 13)

Imamoglu09   A. Imamoglu. Cavity QED based on collective magnetic dipole coupling: Spin ensembles as hybrid two-level systems. *Phys. Rev. Lett.*, **102** 083602 (2009).   *(Cited on page 117)*

Ithier05   G. Ithier, E. Collin, P. Joyez, P. J. Meeson, D. Vion, D. Esteve, F. Chiarello, A. Shnirman, Y. Makhlin, J. Schriefl & G. Schon. Decoherence in a superconducting quantum bit circuit. *Phys. Rev. B*, **72** 134519 (2005).   *(Cited on page 13)*

Jaynes63   E. Jaynes & F. Cummings. Comparison of quantum and semiclassical radiation theories with application to the beam maser. *Proc. IEEE*, **51** 89 (1963).   *(Cited on pages 4, 18, and 102)*

Jeurgens02   L. P. H. Jeurgens, W. G. Sloof, F. D. Tichelaar & M. E. J. Growth kinetics and mechanisms of aluminum-oxide films formed by thermal oxidation of aluminum. *J. Appl. Phys.*, **92** 1649 (2002).   *(Cited on page 65)*

Johansson06   J. Johansson, S. Saito, T. Meno, H. Nakano, M. Ueda, K. Semba & H. Takayanagi. Vacuum Rabi oscillations in a macroscopic superconducting qubit LC oscillator system. *Phys. Rev. Lett.*, **96** 127006 (2006).   *(Cited on pages 7, 83, 84, and 85)*

Johansson09   J. R. Johansson, G. Johansson, C. M. Wilson & F. Nori. Dynamical Casimir effect in a superconducting coplanar waveguide. *Phys. Rev. Lett.*, **103** 147003 (2009).   *(Cited on page 116)*

Johansson10   J. R. Johansson, G. Johansson, C. M. Wilson & F. Nori. The dynamical Casimir effect in superconducting microwave circuits. arXiv:1007.1058 (2010).   *(Cited on page 116)*

Johnson10   B. R. Johnson, M. D. Reed, A. A. Houck, D. I. Schuster, L. S. Bishop, E. Ginossar, J. M. Gambetta, L. DiCarlo, L. Frunzio, S. M. Girvin & R. J. Schoelkopf. Quantum non-demolition detection of single microwave photons in a circuit. *Nat. Phys.*, **6** 663 (2010).   *(Cited on pages 8 and 20)*

Josephson62   B. D. Josephson. Possible new effects in superconductive tunnelling. *Physics Letters*, **1** 251 (1962).   *(Cited on pages 13 and 50)*

Keeling09   J. Keeling. Quantum corrections to the semiclassical collective dynamics in the Tavis-Cummings model. *Phys. Rev. A*, **79** 053825 (2009). *(Cited on page 116)*

Kennard38   E. H. Kennard. *Kinetic Theory of Gases*. Mc (1938). *(Cited on page 123)*

Khitrova06   G. Khitrova, H. M. Gibbs, M. Kira, S. W. Koch & A. Scherer. Vacuum Rabi splitting in semiconductors. *Nat. Phys.*, **2** 81 (2006). *(Cited on page 102)*

Kimble77   H. J. Kimble, M. Dagenais & L. Mandel. Photon antibunching in resonance fluorescence. *Phys. Rev. Lett.*, **39** 691 (1977). *(Cited on page 4)*

Kirk78   W. P. Kirk & M. Twerdochlib. Improved method for minimizing vibrational motion transmitted by pumping lines. *Rev. Sci. Instrum.*, **49** 6 (1978). *(Cited on pages 39 and 126)*

Koch07a   J. Koch, T. M. Yu, J. Gambetta, A. A. Houck, D. I. Schuster, J. Majer, A. Blais, M. H. Devoret, S. M. Girvin & R. J. Schoelkopf. Charge-insensitive qubit design derived from the Cooper pair box. *Phys. Rev. A*, **76** 042319 (2007). *(Cited on pages 15, 16, 48, 73, 86, 89, 90, 100, 108, and 110)*

Koch07b   R. Koch, D. DiVincenzo & J. Clarke. Model for l/f flux noise in SQUIDs and qubits. *Phys. Rev. Lett.*, **98** 267003 (2007). *(Cited on pages 13, 21, 22, and 72)*

Koch09   J. Koch & K. Le Hur. Superfluid – Mott-insulator transition of light in the Jaynes-Cummings lattice. *Phys. Rev. A*, **80** 023811 (2009). *(Cited on page 116)*

Koch10   J. Koch, A. A. Houck, K. L. Hur & S. M. Girvin. Time-reversal-symmetry breaking in circuit-QED-based photon lattices. *Phys. Rev. A*, **82** 043811 (2010). *(Cited on page 116)*

Koppinen07   P. J. Koppinen, L. M. Vaisto & I. J. Maasilta. Complete stabilization and improvement of the characteristics of tunnel junctions by thermal annealing. *Appl. Phys. Lett.*, **90** 053503 (2007). *(Cited on pages 61 and 65)*

Ladd10   T. D. Ladd, F. Jelezko, R. Laflamme, Y. Nakamura, C. Monroe & J. L. O'Brien. Quantum computers. *Nature*, **464** 45 (2010). *(Cited on pages 5 and 12)*

Lamb47   W. E. Lamb & R. Retherford. Fine structure of the hydrogen atom by a microwave method. *Physical Review*, **72** 241 (1947). *(Cited on page 3)*

Lambert09   N. Lambert, Y. nan Chen, R. Johansson & F. Nori. Quantum chaos and critical behavior on a chip. *Phys. Rev. B*, **80** 165308 (2009). *(Cited on page 116)*

Landauer91   R. Landauer. Information is physical. *Physics Today*, **44** 23 (1991). *(Cited on page 12)*

Lang09   C. Lang. Read-out strategies for multi-qubit states in circuit quantum electrodynamics. Diploma thesis, LMU Munich (2009). *(Cited on pages 45 and 77)*

Lang10   C. Lang, et al. & A. Wallraff. Observation of photon blockade and dressing of dressed states (2010). In preperation. *(Cited on pages 32, 33, 115, and 116)*

Larson10   J. Larson. Circuit QED scheme for the realization of the Lipkin-Meshkov-Glick model. *Europhys. Lett.*, **90** 54001 (2010). *(Cited on page 116)*

Laucht09   A. Laucht, N. Hauke, J. M. Villas-Bôas, F. Hofbauer, G. Böhm, M. Kaniber & J. J. Finley. Dephasing of exciton polaritons in photoexcited InGaAs quantum dots in GaAs nanocavities. *Phys. Rev. Lett.*, **103** 087405 (2009). *(Cited on page 113)*

Leek07   P. J. Leek, J. M. Fink, A. Blais, R. Bianchetti, M. Göppl, J. M. Gambetta, D. I. Schuster, L. Frunzio, R. J. Schoelkopf & A. Wallraff. Observation of Berry's phase in a solid-state qubit. *Science*, **318** 1889 (2007). *(Cited on pages 8, 75, and 115)*

Leek09   P. J. Leek, S. Filipp, P. Maurer, M. Baur, R. Bianchetti, J. M. Fink, M. Göppl, L. Steffen & A. Wallraff. Using sideband transitions for two-qubit operations in superconducting circuits. *Phys. Rev. B*, **79** 180511 (2009). *(Cited on pages 8, 23, 74, 75, 76, and 115)*

Leek10   P. J. Leek, M. Baur, J. M. Fink, R. Bianchetti, L. Steffen, S. Filipp & A. Wallraff. Cavity quantum
                electrodynamics with separate photon storage and qubit readout modes. *Phys. Rev. Lett.*, **104**
                100504 (2010).   *(Cited on pages 8, 32, 75, and 115)*

Leib10   M. Leib & M. J. Hartmann. Bose-Hubbard dynamics of polaritons in a chain of circuit quan-
                tum electrodynamics cavities. *New J. Phys.*, **12** 093031 (2010).   *(Cited on page 116)*

Leibfried04   D. Leibfried, M. D. Barrett, T. Schaetz, J. Britton, J. Chiaverini, W. M. Itano, J. D. Jost, C. Langer
                & D. J. Wineland. Toward Heisenberg-limited spectroscopy with multiparticle entangled
                states. *Science*, **304** 1476 (2004).   *(Cited on page 105)*

Leslie04   S. Leslie, N. Shenvi, K. R. Brown, D. M. Stamper-Kurn & K. B. Whaley. Transmission spectrum
                of an optical cavity containing N atoms. *Phys. Rev. A*, **69** 043805 (2004).   *(Cited on pages 99
                and 100)*

Lin09   G. W. Lin, X. B. Zou, X. M. Lin & G. C. Guo. Scalable, high-speed one-way quantum computer
                in coupled-cavity arrays. *Appl. Phys. Lett.*, **95** 224102 (2009).   *(Cited on page 116)*

Lisenfeld10   J. Lisenfeld, C. Müller, J. H. Cole, P. Bushev, A. Lukashenko, A. Shnirman & A. V. Ustinov. Rabi
                spectroscopy of a qubit-fluctuator system. *Phys. Rev. B*, **81** 100511 (2010). *(Cited on page 72)*

Littich09   G. Littich. Superconducting Mach-Zehnder interferometers for circuit quantum electrody-
                namics. Semester thesis, ETH Zurich (2009).   *(Cited on page 33)*

Lloyd05   S. Lloyd. The computational universe: Quantum gravity from quantum computation. quant-
                ph/0501135 (2005).   *(Cited on page 12)*

López07a   C. E. López, H. Christ, J. C. Retamal & E. Solano. Effective quantum dynamics of interacting
                systems with inhomogeneous coupling. *Phys. Rev. A*, **75** 033818 (2007).   *(Cited on page 103)*

López07b   C. E. López, J. C. Retamal & E. Solano. Selective control of the symmetric Dicke subspace in
                trapped ions. *Phys. Rev. A*, **76** 033413 (2007).   *(Cited on page 105)*

Lucero10   E. Lucero, J. Kelly, R. C. Bialczak, M. Lenander, M. Mariantoni, M. Neeley, A. O´Connell,
                D. Sank, H. Wang, M. Weides, J. Wenner, T. Yamamoto, A. Cleland & J. Martinis. Reduced
                phase error through optimized control of a superconducting qubit. arXiv:1007.1690 (2010).
                                                                                    (Cited on pages 8 and 16)

Mabuchi02   H. Mabuchi & A. C. Doherty. Cavity quantum electrodynamics: Coherence in context. *Sci-
                ence*, **298** 1372 (2002).   *(Cited on pages 4
                and 83)*

Majer07   J. Majer, J. M. Chow, J. M. Gambetta, J. Koch, B. R. Johnson, J. A. Schreier, L. Frunzio, D. I.
                Schuster, A. A. Houck, A. Wallraff, A. Blais, M. H. Devoret, S. M. Girvin & R. J. Schoelkopf.
                Coupling superconducting qubits via a cavity bus. *Nature*, **449** 443 (2007). *(Cited on pages 5
                and 8)*

Makhlin01   Y. Makhlin, G. Schön & A. Shnirman. Quantum-state engineering with Josephson-junction
                devices. *Rev. Mod. Phys.*, **73** 357 (2001).   *(Cited on pages 7 and 13)*

Mallet09   F. Mallet, F. R. Ong, A. Palacios-Laloy, F. Nguyen, P. Bertet, D. Vion & D. Esteve. Single-shot
                qubit readout in circuit quantum electrodynamics. *Nat. Phys.*, **5** 791 (2009). *(Cited on page 8)*

Mandel95   L. Mandel & E. Wolf. *Optical Coherence and Quantum Optics*. Cambridge University Press
                (1995).   *(Cited on page 3)*

Manucharyan09   V. E. Manucharyan, J. Koch, L. I. Glazman & M. H. Devoret. Fluxonium: Single Cooper-pair
                circuit free of charge offsets. *Science*, **326** 113 (2009).   *(Cited on page 117)*

Marcos10   D. Marcos, M. Wubs, J. M. Taylor, R. Aguado, M. D. Lukin & A. S. Sorensen. Coupling nitrogen
                vacancy centers in diamond to superconducting flux qubits. Phys. Rev. Lett. (in print) (2010).
                                                                                    (Cited on page 117)

Marquardt01   F. Marquardt & C. Bruder. Superposition of two mesoscopically distinct quantum states: Coupling a Cooper-pair box to a large superconducting island. *Phys. Rev. B*, **63** 054514 (2001).
(Cited on page 7)

Marx09   S. Marx. Optimization of the microwave properties of a cryostat sample holder. Semester thesis, ETH Zurich (2009). *(Cited on page 36)*

Mondragon83   J. J. S. Mondragon, N. B. Narozhny & J. H. Eberly. Theory of spontaneous-emission line shape in an ideal cavity. *Phys. Rev. Lett.*, **51** 550 (1983). *(Cited on page 91)*

Motzoi09   F. Motzoi, J. M. Gambetta, P. Rebentrost & F. K. Wilhelm. Simple pulses for elimination of leakage in weakly nonlinear qubits. *Phys. Rev. Lett.*, **103** 110501 (2009). *(Cited on pages 8 and 16)*

Münstermann00   P. Münstermann, T. Fischer, P. Maunz, P. W. H. Pinkse & G. Rempe. Observation of cavity-mediated long-range light forces between strongly coupled atoms. *Phys. Rev. Lett.*, **84** 4068 (2000). *(Cited on page 99)*

Nahum93   M. Nahum & J. M. Martinis. Ultrasensitive-hot-electron microbolometer. *Appl. Phys. Lett.*, **63** 3075 (1993). *(Cited on page 64)*

Nakamura99   Y. Nakamura, Y. A. Pashkin & J. S. Tsai. Coherent control of macroscopic quantum states in a single-Cooper-pair box. *Nature*, **398** 786 (1999). *(Cited on pages 7 and 13)*

Nakamura01   Y. Nakamura, Y. A. Pashkin & J. S. Tsai. Rabi oscillations in a Josephson-junction charge two-level system. *Phys. Rev. Lett.*, **8724** 246601 (2001). *(Cited on page 75)*

Nataf10a   P. Nataf & C. Ciuti. No-go theorem for superradiant quantum phase transitions in cavity QED and counter-example in circuit QED. *Nat. Commun.*, **1** 72 (2010). *(Cited on page 116)*

Nataf10b   P. Nataf & C. Ciuti. Vacuum degeneracy of a circuit QED system in the ultrastrong coupling regime. *Phys. Rev. Lett.*, **104** 023601 (2010). *(Cited on page 116)*

Neeley08   M. Neeley, M. Ansmann, R. C. Bialczak, M. Hofheinz, N. Katz, E. Lucero, A. O'Connell, H. Wang, A. N. Cleland & J. M. Martinis. Process tomography of quantum memory in a josephson-phase qubit coupled to a two-level state. *Nat. Phys.*, **4** 523 (2008). *(Cited on page 72)*

Neeley10   M. Neeley, R. C. Bialczak, M. Lenander, E. Lucero, M. Mariantoni, A. D. O/'Connell, D. Sank, H. Wang, M. Weides, J. Wenner, Y. Yin, T. Yamamoto, A. N. Cleland & J. M. Martinis. Generation of three-qubit entangled states using superconducting phase qubits. *Nature*, **467** 570 (2010). *(Cited on page 8)*

Nielsen00   M. A. Nielsen & I. L. Chuang. *Quantum Computation and Quantum Information*. Cambridge University Press (2000). *(Cited on pages 5, 12, and 84)*

Niemczyk10   T. Niemczyk, F. Deppe, H. Huebl, E. P. Menzel, F. Hocke, M. J. Schwarz, J. J. Garcia-Ripoll, D. Zueco, T. Hummer, E. Solano, A. Marx & R. Gross. Circuit quantum electrodynamics in the ultrastrong-coupling regime. *Nat. Phys.*, **6** 772 (2010). *(Cited on pages 21 and 116)*

O´Connell10   A. D. O´Connell, M. Hofheinz, M. Ansmann, R. C. Bialczak, M. Lenander, E. Lucero, M. Neeley, D. Sank, H. Wang, M. Weides, J. Wenner, J. M. Martinis & A. N. Cleland. Quantum ground state and single-phonon control of a mechanical resonator. *Nature*, **464** 697 (2010). *(Cited on page 8)*

OxfordInstr06   OxfordInstr.   Private communication with Ricardo Viana, Oxford Instruments (2006). *(Cited on pages 121 and 122)*

Palacios-Laloy09   A. Palacios-Laloy, F. Mallet, F. Nguyen, F. Ong, P. Bertet, D. Vion & D. Esteve. Spectral measurement of the thermal excitation of a superconducting qubit. *Phys. Scr.*, **T137** 014015 (2009). *(Cited on page 113)*

Paul63   H. Paul.   Induzierte Emission bei starker Einstrahlung.   *Ann. Phys.*, **466** 1521 (1963). *(Cited on page 4)*

Peter05   E. Peter, P. Senellart, D. Martrou, A. Lemaitre, J. Hours, J. M. Gerard & J. Bloch. Exciton-photon strong-coupling regime for a single quantum dot embedded in a microcavity. *Phys. Rev. Lett.*, **95** 067401 (2005).   *(Cited on pages 83 and 85)*

PfeifferVacuum10 PfeifferVacuum.   Introduction to vacuum technology, fundamentals, conductivities. http://www.pfeiffer-vacuum.de/en/know-how/container.action (2010). *(Cited on page 123)*

Plastina03   F. Plastina & G. Falci. Communicating Josephson qubits. *Phys. Rev. B*, **67** 224514 (2003).   *(Cited on page 7)*

Pobell06   F. Pobell.   *Matter and Methods at Low Temperatures*.   Springer, 3rd edition, (2006).   *(Cited on pages 39, 42, and 124)*

Pozar93   D. M. Pozar.   *Microwave Engineering*.   Addison-Wesley Publishing Company (1993).   *(Cited on pages 9, 10, 12, 43, and 68)*

Puebla08   G. Puebla. Dual channel power supply. Tech. rep., Quantum Device Lab, ETH Zurich (2008).   *(Cited on page 44)*

Rabl06   P. Rabl, D. DeMille, J. M. Doyle, M. D. Lukin, R. J. Schoelkopf & P. Zoller. Hybrid quantum processors: Molecular ensembles as quantum memory for solid state circuits. *Phys. Rev. Lett.*, **97** 033003 (2006).   *(Cited on page 117)*

Rabl07   P. Rabl & P. Zoller. Molecular dipolar crystals as high-fidelity quantum memory for hybrid quantum computing. *Phys. Rev. A*, **76** 042308 (2007).   *(Cited on page 117)*

Raimond01   J. M. Raimond, M. Brune & S. Haroche. Manipulating quantum entanglement with atoms and photons in a cavity. *Rev. Mod. Phys.*, **73** 565 (2001).   *(Cited on pages 4 and 83)*

Raizen89   M. G. Raizen, R. J. Thompson, R. J. Brecha, H. J. Kimble & H. J. Carmichael. Normal-mode splitting and linewidth averaging for two-state atoms in an optical cavity. *Phys. Rev. Lett.*, **63** 240 (1989).   *(Cited on page 99)*

Rau04   I. Rau, G. Johansson & A. Shnirman.   Cavity quantum electrodynamics in superconducting circuits: Susceptibility at elevated temperatures. *Phys. Rev. B*, **70** 054521 (2004).   *(Cited on pages 107, 109, and 110)*

Reed10a   M. D. Reed, L. DiCarlo, B. R. Johnson, L. Sun, D. I. Schuster, L. Frunzio & R. J. Schoelkopf. High-fidelity readout in circuit quantum electrodynamics using the Jaynes-Cummings nonlinearity. *Phys. Rev. Lett.*, **105** 173601 (2010).   *(Cited on pages 23, 69, and 72)*

Reed10b   M. D. Reed, B. R. Johnson, A. A. Houck, L. DiCarlo, J. M. Chow, D. I. Schuster, L. Frunzio & R. J. Schoelkopf. Fast reset and suppressing spontaneous emission of a superconducting qubit (2010).   *(Cited on page 13)*

Reithmaier04   J. P. Reithmaier, G. Sek, A. Loffler, C. Hofmann, S. Kuhn, S. Reitzenstein, L. V. Keldysh, V. D. Kulakovskii, T. L. Reinecke & A. Forchel. Strong coupling in a single quantum dot-semiconductor microcavity system. *Nature*, **432** 197 (2004).   *(Cited on pages 83 and 85)*

Rempe87   G. Rempe, H. Walther & N. Klein. Observation of quantum collapse and revival in a one-atom maser. *Phys. Rev. Lett.*, **58** 353 (1987).   *(Cited on pages 4 and 83)*

Retzker07   A. Retzker, E. Solano & B. Reznik. Tavis-Cummings model and collective multiqubit entanglement in trapped ions. *Phys. Rev. A*, **75** 022312 (2007).   *(Cited on page 105)*

Richardson88   R. C. Richardson & E. N. Smith. *Experimental Techniques in Condensed Matter Physics at Low Temperatures*. Addison-Wesley Publishing Company (1988).   *(Cited on pages 39 and 122)*

Roth76   A. Roth. *Vacuum technology*. North-Holland Publishing Company (1976). *(Cited on pages 39 and 123)*

Sandberg08a   M. Sandberg, C. M. Wilson, F. Persson, T. Bauch, G. Johansson, V. Shumeiko, T. Duty & P. Delsing. Tuning the field in a microwave resonator faster than the photon lifetime. *Appl. Phys. Lett.*, **92** 203501 (2008).   *(Cited on page 116)*

Sandberg08b   M. Sandberg, C. M. Wilson, F. Persson, G. Johansson, V. Shumeiko, T. Bauch, T. Duty & P. Delsing. Fast tuning of superconducting microwave cavities. *AIP Conf. Proc.*, **1074** 12 (2008).
(Cited on page 116)

Savage89   C. M. Savage. Resonance fluorescence spectrum of an atom strongly coupled to a cavity. *Phys. Rev. Lett.*, **63** 1376 (1989). *(Cited on page 111)*

Schlosshauer07   M. Schlosshauer. *Decoherence and the Quantum-to-Classical Transition*. Springer (2007).
(Cited on page 108)

Schmidlin08   S. Schmidlin. Design and characterization of microwave printed circuit boards for circuit QED experiments. Semester thesis, ETH Zurich (2008). *(Cited on page 34)*

Schmidlin09   S. Schmidlin. *Generation of amplitude and phase controlled microwave pulses for qubit manipulation in circuit QED*. Master's thesis, ETH Zurich (2009). *(Cited on page 38)*

Schmidt09   S. Schmidt & G. Blatter. Strong coupling theory for the Jaynes-Cummings-Hubbard model. *Phys. Rev. Lett.*, **103** 086403 (2009). *(Cited on page 116)*

Schmidt10   S. Schmidt, D. Gerace, A. A. Houck, G. Blatter & H. E. Türeci. Nonequilibrium delocalization-localization transition of photons in circuit quantum electrodynamics. *Phys. Rev. B*, **82** 100507 (2010). *(Cited on page 116)*

Schoelkopf08   R. Schoelkopf & S. Girvin. Wiring up quantum systems. *Nature*, **451** 664 (2008).
(Cited on pages 5, 7, 87, and 100)

Schreier08   J. Schreier, A. Houck, J. Koch, D. I. Schuster, B. Johnson, J. Chow, J. Gambetta, J. Majer, L. Frunzio, M. Devoret, S. Girvin & R. Schoelkopf. Suppressing charge noise decoherence in superconducting charge qubits. *Phys. Rev. B*, **77** 180502(R) (2008). *(Cited on pages 13, 16, 72, 73, 86, and 90)*

Schuster05   D. I. Schuster, A. Wallraff, A. Blais, L. Frunzio, R.-S. Huang, J. Majer, S. M. Girvin & R. J. Schoelkopf. AC Stark shift and dephasing of a superconducting qubit strongly coupled to a cavity field. *Phys. Rev. Lett.*, **94** 123602 (2005). *(Cited on pages 7, 22, 72, 73, 74, 86, and 112)*

Schuster07a   D. I. Schuster. *Circuit Quantum Electrodynamics*. Ph.D. thesis, Yale University (2007).
(Cited on pages 33 and 46)

Schuster07b   D. I. Schuster, A. A. Houck, J. A. Schreier, A. Wallraff, J. M. Gambetta, A. Blais, L. Frunzio, J. Majer, B. Johnson, M. H. Devoret, S. M. Girvin & R. J. Schoelkopf. Resolving photon number states in a superconducting circuit. *Nature*, **445** 515 (2007). *(Cited on pages 7, 22, 72, 74, 84, and 85)*

Schuster08   I. Schuster, A. Kubanek, A. Fuhrmanek, T. Puppe, P. W. H. Pinkse, K. Murr & G. Rempe. Nonlinear spectroscopy of photons bound to one atom. *Nat. Phys.*, **4** 382 (2008). *(Cited on pages 4, 84, 98, 102, and 109)*

Schwabl02   F. Schwabl. *Quantenmechanik*. Springer-Verlag, Berlin Heidelberg New York (2002).
(Cited on page 10)

Scully97   M. O. Scully & M. S. Zubairy. *Quantum Optics*. Cambridge University Press (1997).
(Cited on pages 3, 4, 16, and 17)

Scully09   M. O. Scully & A. A. Svidzinsky. The super of superradiance. *Science*, **325** 1510 (2009).
(Cited on page 116)

Scully10   M. O. Scully & A. A. Svidzinsky. The Lamb shift – yesterday, today, and tomorrow. *Science*, **328** 1239 (2010). *(Cited on page 116)*

Shamailov10   S. Shamailov, A. Parkins, M. Collett & H. Carmichael. Multi-photon blockade and dressing of the dressed states. *Opt. Commun.*, **283** 766 (2010). *(Cited on page 116)*

Shor97   P. W. Shor. Polynomial-time algorithms for prime factorization and discrete logarithms on a quantum computer. *SIAM J. Sci. Stat. Comp.*, **26** 1484 (1997). *(Cited on page 12)*

Sillanpää07   M. A. Sillanpää, J. I. Park & R. W. Simmonds. Coherent quantum state storage and transfer between two phase qubits via a resonant cavity. *Nature*, **449** 438 (2007).   *(Cited on page 8)*

Silver10   A. O. Silver, M. Hohenadler, M. J. Bhaseen & B. D. Simons. Bose-Hubbard models coupled to cavity light fields. *Phys. Rev. A*, **81** 023617 (2010).   *(Cited on page 116)*

Simmonds04   R. W. Simmonds, K. M. Lang, D. A. Hite, S. Nam, D. P. Pappas & J. M. Martinis. Decoherence in Josephson phase qubits from junction resonators. *Phys. Rev. Lett.*, **93** 077003 (2004).
     (Cited on page 72)

Simons01   R. N. Simons. *Coplanar waveguide circuits, components and systems*. Wiley Series in Microwave and Optical Engineering. Wiley Inter-Science (2001).   *(Cited on pages 9, 34, 35, and 68)*

Spiller06   T. P. Spiller, K. Nemoto, S. L. Braunstein, W. J. Munro, P. van Loock & G. J. Milburn. Quantum computation by communication. *New J. Phys.*, **8** 30 (2006).   *(Cited on page 5)*

Srinivasan10   S. Srinivasan, A. Hoffman & H. Andrew. Straddling regime of a transmon qubit. Abstract, APS March Meeting (2010).   *(Cited on page 22)*

Steffen07   L. Steffen. Spin echo measurements in a superconducting qubit. Semester thesis, ETH Zurich (2007).   *(Cited on page 76)*

Steffen08   L. Steffen. *Local Qubit Control in Circuit Quantum Electrodynamics*. Master's thesis, ETH Zurich (2008).   *(Cited on pages 33 and 43)*

Steffen10   M. Steffen, S. Kumar, D. P. DiVincenzo, J. R. Rozen, G. A. Keefe, M. B. Rothwell & M. B. Ketchen. High-coherence hybrid superconducting qubit. *Phys. Rev. Lett.*, **105** 100502 (2010).
     (Cited on page 117)

Steinbach01   A. Steinbach, P. Joyez, A. Cottet, D. Esteve, M. H. Devoret, M. E. Huber & J. M. Martinis. Direct measurement of the Josephson supercurrent in an ultrasmall Josephson junction. *Phys. Rev. Lett.*, **87** 137003 (2001).   *(Cited on page 51)*

Stockton04   J. K. Stockton, R. van Handel & H. Mabuchi. Deterministic Dicke-state preparation with continuous measurement and control. *Phys. Rev. A*, **70** 022106 (2004).   *(Cited on page 105)*

Tanzilli05   S. Tanzilli, W. Tittel, M. Halder, O. Alibart, P. Baldi, N. Gisin & H. Zbinden. A photonic quantum information interface. *Nature*, **437** 116 (2005).   *(Cited on page 5)*

Tavis68   M. Tavis & F. W. Cummings. Exact solution for an N-molecule-radiation-field Hamiltonian. *Phys. Rev.*, **170** 379 (1968).   *(Cited on pages 99 and 101)*

Tessier03   T. Tessier, I. H. Deutsch, A. Delgado & I. Fuentes-Guridi. Entanglement sharing in the two-atom Tavis-Cummings model. *Phys. Rev. A*, **68** 062316 (2003).   *(Cited on page 105)*

Thompson92   R. J. Thompson, G. Rempe & H. J. Kimble. Observation of normal-mode splitting for an atom in an optical cavity. *Phys. Rev. Lett.*, **68** 1132 (1992).   *(Cited on page 85)*

Thompson98   R. J. Thompson, Q. A. Turchette, O. Carnal & H. J. Kimble. Nonlinear spectroscopy in the strong-coupling regime of cavity QED. *Phys. Rev. A*, **57** 3084 (1998).   *(Cited on pages 84, 85, 97, and 99)*

Tian92   L. Tian & H. J. Carmichael. Incoherent excitation of the Jaynes-Cummings system. *Quantum Opt.*, **4** 131 (1992).   *(Cited on page 109)*

Tian10   L. Tian. Circuit QED and sudden phase switching in a superconducting qubit array. *Phys. Rev. Lett.*, **105** 167001 (2010).   *(Cited on page 116)*

Tinkham96   M. Tinkham. *Introduction to Superconductivity*. McGraw-Hill International Editions (1996).
     (Cited on pages 13 and 14)

Tomadin10   A. Tomadin & R. Fazio. Many-body phenomena in qed-cavity arrays. *J. Opt. Soc. Am. B*, **27** A130 (2010).   *(Cited on page 116)*

Tuchman06   A. K. Tuchman, R. Long, G. Vrijsen, J. Boudet, J. Lee & M. A. Kasevich. Normal-mode splitting with large collective cooperativity. *Phys. Rev. A*, **74** 053821 (2006).   *(Cited on page 100)*

Twamley10   J. Twamley & S. D. Barrett. Superconducting cavity bus for single nitrogen-vacancy defect centers in diamond. *Phys. Rev. B*, **81** 241202 (2010).   *(Cited on page 117)*

vandenBrink02   A. M. van den Brink & A. M. Zagoskin. Liouville invariance in quantum and classical mechanics. *Quantum Inf. Process.*, **1** 55 (2002).   *(Cited on page 109)*

Varcoe00   B. T. H. Varcoe, S. Brattke, M. Weidinger & H. Walther. Preparing pure photon number states of the radiation field. *Nature*, **403** 743 (2000).   *(Cited on pages 83 and 85)*

Vion02   D. Vion, A. Aassime, A. Cottet, P. Joyez, H. Pothier, C. Urbina, D. Esteve & M. H. Devoret. Manipulating the quantum state of an electrical circuit. *Science*, **296** 886 (2002).   *(Cited on pages 13 and 16)*

Vion03   D. Vion, A. Aassime, A. Cottet, P. Joyez, H. Pothier, C. Urbina, D. Esteve & M. H. Devoret. Rabi oscillations, Ramsey fringes and spin echoes in an electrical circuit. *Fortschr. der Phys.*, **51** 462 (2003).   *(Cited on page 75)*

Wallraff04   A. Wallraff, D. I. Schuster, A. Blais, L. Frunzio, R. S. Huang, J. Majer, S. Kumar, S. M. Girvin & R. J. Schoelkopf. Strong coupling of a single photon to a superconducting qubit using circuit quantum electrodynamics. *Nature*, **431** 162 (2004).   *(Cited on pages 5, 7, 45, 83, 85, 86, 87, 100, 102, 107, and 108)*

Wallraff05   A. Wallraff, D. I. Schuster, A. Blais, L. Frunzio, J. Majer, S. M. Girvin & R. J. Schoelkopf. Approaching unit visibility for control of a superconducting qubit with dispersive readout. *Phys. Rev. Lett.*, **95** 060501 (2005).   *(Cited on pages 7, 22, 72, 75, and 76)*

Wallraff07   A. Wallraff, D. I. Schuster, A. Blais, J. M. Gambetta, J. Schreier, L. Frunzio, M. H. Devoret, S. M. Girvin & R. J. Schoelkopf. Sideband transitions and two-tone spectroscopy of a superconducting qubit strongly coupled to an on-chip cavity. *Phys. Rev. Lett.*, **99** 050501 (2007).   *(Cited on pages 7, 72, and 74)*

Wallraff08   A. Wallraff. Quantenmechanik mit Schaltkreisen: Photonen und Qubits auf einem supraleitenden Mikrochip. *Physik Journal*, **7** 39 (2008).   *(Cited on page 7)*

Walls94   D. Walls & G. Milburn. *Quantum optics*. Spinger-Verlag, Berlin (1994).   *(Cited on pages 3, 45, and 83)*

Walther06   H. Walther, B. T. H. Varcoe, B.-G. Englert & T. Becker. Cavity quantum electrodynamics. *Rep. Prog. Phys.*, **69** 1325 (2006).   *(Cited on pages 4 and 83)*

Wang09   H. Wang, M. Hofheinz, J. Wenner, M. Ansmann, R. C. Bialczak, M. Lenander, E. Lucero, M. Neeley, A. D. O'Connell, D. Sank, M. Weides, A. N. Cleland & J. M. Martinis. Improving the coherence time of superconducting coplanar resonators. *Appl. Phys. Lett.*, **95** 233508 (2009).   *(Cited on page 34)*

Wentzel26   G. Wentzel. Zur Theorie des photoelektrischen Effekts. *Z. Phys.*, **40** 574 (1926).   *(Cited on page 3)*

Wentzel27   G. Wentzel. Über die Richtungsverteilung der Photoelektronen. *Z. Phys.*, **41** 828 (1927).   *(Cited on page 3)*

Wesenberg09   J. H. Wesenberg, A. Ardavan, G. A. D. Briggs, J. J. L. Morton, R. J. Schoelkopf, D. I. Schuster & K. Mølmer. Quantum computing with an electron spin ensemble. *Phys. Rev. Lett.*, **103** 070502 (2009).   *(Cited on pages 116 and 117)*

White02   G. K. White & P. J. Meeson. *Experimental Techniques in Low-Temperature Physics*. Oxford University Press (2002).   *(Cited on pages 39 and 42)*

Wilk07   T. Wilk, S. C. Webster, A. Kuhn & G. Rempe. Single-atom single-photon quantum interface. *Science*, **317** 488 (2007).   *(Cited on page 5)*

Wilson10   C. Wilson, T. Duty, M. Sandberg, F. Persson & P. Shumeiko, V. Delsing. Photon genera-
                tion in an electromagnetic cavity with a time-dependent boundary. arXiv:1006.2540 (2010).
                                                                                                      (Cited on page 116)

Woolley03   R. G. Woolley. *Handbook of Molecular Physics and Quantum Chemistry*. Wiley (2003).
                                                                                                       (Cited on page 17)

Yamamoto99   Y. Yamamoto & A. Imamoglu. *Mesoscopic Quantum Optics*. Wiley (1999).   *(Cited on pages 3
                and 17)*

Yamamoto08   T. Yamamoto, K. Inomata, M. Watanabe, K. Matsuba, T. Miyazaki, W. D. Oliver, Y. Nakamura
                & J. S. Tsai. Flux-driven Josephson parametric amplifier. *Appl. Phys. Lett.*, **93** 042510 (2008).
                                                                                                      (Cited on page 116)

Yang03   C.-P. Yang, S.-I. Chu & S. Han.   Possible realization of entanglement, logical gates, and
                quantum-information transfer with superconducting-quantum-interference-device qubits
                in cavity QED. *Phys. Rev. A*, **67** 042311 (2003).   *(Cited on page 7)*

Ye08   J. Ye, H. J. Kimble & H. Katori.   Quantum state engineering and precision metrology using
                state-insensitive light traps. *Science*, **320** 1734 (2008).   *(Cited on page 4)*

Yoshie04   T. Yoshie, A. Scherer, J. Hendrickson, G. Khitrova, H. M. Gibbs, G. Rupper, C. Ell, O. B. Shchekin
                & D. G. Deppe.   Vacuum Rabi splitting with a single quantum dot in a photonic crystal
                nanocavity. *Nature*, **432** 200 (2004).   *(Cited on pages 83 and 85)*

You03   J. Q. You & F. Nori. Quantum information processing with superconducting qubits in a mi-
                crowave field. *Phys. Rev. B*, **68** 064509 (2003).   *(Cited on page 7)*

Yurke87   B. Yurke. Squeezed-state generation using a Josephson parametric amplifier. *J. Opt. Soc. Am.
                B*, **4** 1551 (1987).   *(Cited on page 116)*

Yurke89   B. Yurke, L. R. Corruccini, P. G. Kaminsky, L. W. Rupp, A. D. Smith, A. H. Silver, R. W. Simon &
                E. A. Whittaker. Observation of parametric amplification and deamplification in a Josephson
                parametric amplifier. *Phys. Rev. A*, **39** 2519 (1989).   *(Cited on page 116)*

Zagoskin07   A. Zagoskin & A. Blais. *Physics in Canada / La Physique au Canada*, vol. 63, chap. Supercon-
                ducting qubits. CAP (2007).   *(Cited on page 13)*

Zhu90   Y. Zhu, D. J. Gauthier, S. E. Morin, Q. Wu, H. J. Carmichael & T. W. Mossberg. Vacuum Rabi
                splitting as a feature of linear-dispersion theory: Analysis and experimental observations.
                Phys. Rev. Lett., **64** 2499 (1990).   *(Cited on pages 83, 85, and 99)*

Zurek03   W. H. Zurek. Decoherence, einselection, and the quantum origins of the classical. *Rev. Mod.
                Phys.*, **75** 715 (2003).   *(Cited on page 12)*

ACKNOWLEDGEMENTS

CURRICULUM VITAE

Name: Johannes Martin Fink

Contact: www.finkjohannes.com

DOB: 21st of December 1981 in Bregenz, Austria.

Education: 1996 – 2001   *HTL Bregenz* – higher technical school for mechanical engineering and automation technology. Thesis: 'Heat-dissipation by Convection at Cylindrical Bodies' in cooperation with *Liebherr Aerospace*.

2002 – 2007   Study of physics at the *University of Vienna*, the *Macquarie University* in Sydney and at *ETH Zürich*. Thesis: 'Single Qubit Control and Observation of Berry's Phase in a Superconducting Quantum Circuit' conducted in the Quantum Device Laboratory at *ETH Zürich*. Graduation with distinction at the *University of Vienna* (Mag. rer. nat.). Examiners: Prof. Andreas Wallraff and Prof. Anton Zeilinger.

2007 – 2010   Ph.D. studies at *ETH Zürich*. Thesis: 'Quantum Nonlinearities in Strong Coupling Circuit QED'. Graduation as a Doctor of Sciences. Examiners: Prof. Andreas Wallraff and Prof. Ataç İmamoğlu.

Employment: 1997 – 2005   Construction, design and simulation (7 months) as well as machining and assembling (3 months) for *Meusburger*, *Doppelmayr* and *Liebherr Aerospace*.

2001 – 2002   Mandatory national service (7 months).

2006 – 2010   Research associate and teaching assistant at *ETH Zürich*, Department of Physics, Laboratory for Solid State Physics.

Zürich, September 2010